



17 September 2010 | \$10

# Science

 AAAS



## EDITORIAL

- 1441** Young Leaders for Biology in India  
*Shubha Tole and Ronald D. Vale*  
>> *Policy Forum* p. 1471

## NEWS OF THE WEEK

- 1450** With Stem Cells in Court, a History Primer  
**1453** China Clamps Down on Illegal Fossil Trading  
**1453** From the *Science* Policy Blog  
**1454** No Meeting of Minds on XMRV's Role in Chronic Fatigue, Cancer  
**1455** From *Science's* Online Daily News Site  
**1456** Genentech Scientist to Take the Helm at Rockefeller University  
**1457** Physicist Tapped to Turn Embattled Institute Into a Fully Fledged University

## NEWS FOCUS

- 1458** Has China Outgrown the One-Child Policy? Of Population Projections and Projectiles  
>> *Science Podcast*  
**1462** No Vaccines in the Time of Cholera  
**1464** 11th International Conference of Archaeozoology  
Score One for Hunting at Olduvai  
Burying Man's Best Friend, With Honor  
In a Cold Snap, Farmers Turned to Milk

## LETTERS

- 1466** Battling the Paper Glut  
*D. Siegel and P. Baveye*  
India's Courteous Creativity  
*T. N. Narasimhan*  
Archaeology Augments Tibet's Genetic History  
*P. J. Brantingham et al.*  
Response  
*X. Yi et al.*

- 1467** CORRECTIONS AND CLARIFICATIONS

## BOOKS ET AL.

- 1469** Whistling Vivaldi  
*C. M. Steele, reviewed by W. von Hippel*  
**1469** BROWSINGS  
**1470** Nanotechnologies for Future Mobile Devices  
*T. Ryhänen et al., Eds.*

## POLICY FORUM

- 1471** Achieving Scientific Eminence Within Asia  
*A. S. Huang and C. Y. H. Tan*  
>> *Editorial* p. 1441

## PERSPECTIVES

- 1473** New Roles for Codon Usage  
*I. Weygand-Durasevic and M. Ibba*  
>> *Report* p. 1534  
**1474** Aerosols in Clearer Focus  
*U. Baltensperger*  
>> *Research Article* p. 1488; *Report* p. 1513  
**1475** A Never-Ending Story  
*B.-M. Sjöberg*  
>> *Report* p. 1526  
**1477** Quantum Walks Through a Waveguide Maze  
*M. Hillery*  
>> *Report* p. 1500  
**1478** Should Confidence Be Trusted?  
*H. Lau and B. Maniscalco*  
>> *Report* p. 1541  
**1479** Seismic Images of the Biggest Crash on Earth  
*R. Kind and X. Yuan*

## REVIEW

- 1481** Tyrannosaur Paleobiology: New Research on Ancient Exemplar Organisms  
*S. L. Brusatte et al.*

CONTENTS continued >>



page 1458



page 1470



## COVER

Topographic map of the Moon based on measurements from the Lunar Orbiter Laser Altimeter, showing the boundary between Oceanus Procellarum, a smooth, relatively young mare region on the western nearside (upper right), and the older, more heavily cratered highlands (center and lower left). Colors indicate increasing elevation from blue to red. The crescent-shaped Lorentz crater (center) is ~312 kilometers in diameter. See the Reports on pages 1504, 1507, and 1510.

Image: NASA/LRO/LOLA/GSFC/MIT/Brown

## DEPARTMENTS

- 1437** This Week in *Science*  
**1442** Editors' Choice  
**1446** *Science* Staff  
**1449** Random Samples  
**1544** New Products  
**1545** *Science* Careers

## BREVIA

- 1487** Island Biogeography Reveals the Deep History of SIV  
*M. Worobey et al.*  
 Separation of the island of Bioko from West Africa about 10,000 years ago dates the origins of simian immunodeficiency virus.

## RESEARCH ARTICLES

- 1488** Hemispheric Aerosol Vertical Profiles: Anthropogenic Impacts on Optical Depth and Cloud Nuclei  
*A. Clarke and V. Kapustin*  
 Vertical profiles of atmospheric aerosols from throughout the Pacific region show the influence of anthropogenic combustion.  
 >> *Perspective p. 1474; Report p. 1513*
- 1492** Evidence for an Alternative Glycolytic Pathway in Rapidly Proliferating Cells  
*M. G. Vander Heiden et al.*  
 Characterization of cancer cell metabolism provides evidence for a previously uncharacterized metabolic pathway.

## REPORTS

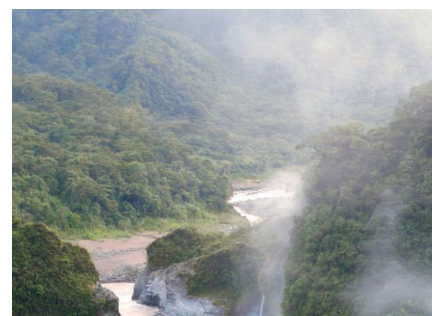
- 1500** Quantum Walks of Correlated Photons  
*A. Peruzzo et al.*  
 Pairs of correlated photons retain their quantum-mechanical correlations as they propagate through a waveguide maze.  
 >> *Perspective p. 1477*
- 1504** Global Distribution of Large Lunar Craters: Implications for Resurfacing and Impactor Populations  
*J. W. Head III et al.*  
 An analysis of high-resolution global topography data advances our understanding of the impact history of the Moon.
- 1507** Global Silicate Mineralogy of the Moon from the Diviner Lunar Radiometer  
*B. T. Greenhagen et al.*
- 1510** Highly Silicic Compositions on the Moon  
*T. D. Glotch et al.*  
 Remote thermal emission spectroscopy reveals the existence of complex igneous processes on the Moon.
- 1513** Rainforest Aerosols as Biogenic Nuclei of Clouds and Precipitation in the Amazon  
*U. Pöschl et al.*  
 The majority of cloud condensation nuclei in the Amazon during the wet season are derived from biogenic precursors.  
 >> *Perspective p. 1474; Research Article p. 1488*
- 1516** Melting of Peridotite to 140 Gigapascals  
*G. Fiquet et al.*  
 High-temperature and high-pressure experiments reveal details about how and where the mantle melts.

- 1518** A Test of the Snowball Theory for the Rate of Evolution of Hybrid Incompatibilities  
*D. R. Matute et al.*
- 1521** Hybrid Incompatibility "Snowballs" Between *Solanum* Species  
*L. C. Moyle and T. Nakazato*  
 Two studies support the theory that the number of genes involved in hybrid incompatibility increases faster than linearly.
- 1523** The Ecological Significance of Tool Use in New Caledonian Crows  
*C. Rutz et al.*  
 Stable isotope analysis reveals the nutritional benefits of tool use in wild New Caledonian crows.  
 >> *Science Podcast*
- 1526** Structural Basis for Activation of Class Ib Ribonucleotide Reductase  
*A. K. Boal et al.*  
 A single protein activates two different metallofactors by distinct chemistries.  
 >> *Perspective p. 1475*
- 1530** Bifurcation of Toll-Like Receptor 9 Signaling by Adaptor Protein 3  
*M. Sasai et al.*  
 Compartmentalization of signaling components allows induction of distinct pathways downstream of a pathogen receptor.
- 1534** Differential Arginylation of Actin Isoforms Is Regulated by Coding Sequence-Dependent Degradation  
*F. Zhang et al.*  
 The translational speed of proteins influences whether they are cotranslationally degraded after arginylation.  
 >> *Perspective p. 1473*
- 1537** MiR-16 Targets the Serotonin Transporter: A New Facet for Adaptive Responses to Antidepressants  
*A. Baudry et al.*  
 The uptake transporter for a key neurotransmitter is regulated by a microRNA, yielding new insight into how Prozac functions.
- 1541** Relating Introspective Accuracy to Individual Differences in Brain Structure  
*S. M. Fleming et al.*  
 Individual differences in the capacity for introspection are reflected in structural variation in the frontal lobe.  
 >> *Perspective p. 1478*

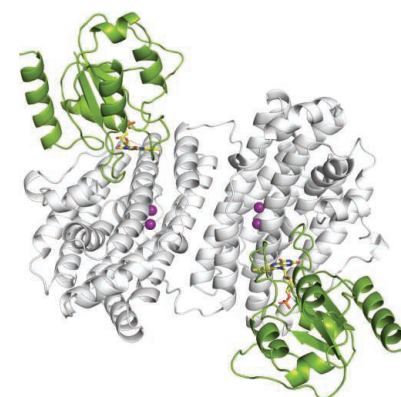
CONTENTS continued &gt;&gt;



page 1487



pages 1474, 1488, &amp; 1513



pages 1475 &amp; 1526

## SCIENCEONLINE

## SCIENCEEXPRESS

[www.sciencexpress.org](http://www.sciencexpress.org)

### Family Planning and the Millennium Development Goals

W. Cates Jr. et al.

To alleviate global poverty, investments and partnerships in family planning are needed.  
10.1126/science.1197080

### Fast Vesicle Fusion in Living Cells Requires at Least Three SNARE Complexes

R. Mohrmann et al.

Membrane fusion proteins cooperate to promote rapid secretory vesicle exocytosis from neuroendocrine cells.  
10.1126/science.1193134

### Impeding *Xist* Expression from the Active X Chromosome Improves Mouse Somatic Cell Nuclear Transfer

K. Inoue et al.

Efficiency of mouse nuclear transfer was improved by correcting aberrant gene expression on the active X chromosome.  
10.1126/science.1194174

### IDH2 Mutations in Patients with D-2-Hydroxyglutaric Aciduria

M. Kranendijk et al.

A mutation that changes the specificity of an enzyme in human cancer is also found in an inherited metabolic disorder.  
10.1126/science.1192632

### Propane Respiration Jump-Starts Microbial Response to a Deep Oil Spill

D. L. Valentine et al.

Hydrocarbon gases were the first compounds that bacteria degraded in deep underwater petroleum plumes.  
10.1126/science.1196830

>> *Science Podcast*

## SCIENCENOW

[www.sciencenow.org](http://www.sciencenow.org)

Highlights From Our Daily News Coverage

### How to Train Your Robot (to Lie)

Researchers create fibbing machines in the lab.

### Fast-Growing Boys Have More Sex as Men

Research supports the idea that early infant experiences shape adult attributes.

### Physicists Fashion the Ultimate Peashooter Out of Laser Light

A "light pipe" delivers tiny objects across the room with hair's breadth accuracy.

## SCIENCE SIGNALING

[www.sciencesignaling.org](http://www.sciencesignaling.org)

The Signal Transduction Knowledge Environment

## EVOLUTION OF SIGNALING SYSTEMS

EDITORIAL GUIDE: Focus Issue—

### Evolution III—Domains for Change

N. R. Gough

Domains provide evolution with tools for the creation of new functions.

### RESEARCH ARTICLE: Characterization of the Extrinsic Apoptotic Pathway in the Basal Chordate *Amphioxus*

S. Yuan et al.

Death domain-dependent signaling in the basal chordate *amphioxus* suggests that extrinsic apoptotic signaling is not restricted to vertebrates.

### PERSPECTIVE: Domain Recombination—A Workhorse for Evolutionary Innovation

G. Apic and R. B. Russell

Firm evidence for domain shuffling as a means of evolving new functions may lead us to the creation of combinations of practical benefit.

### PERSPECTIVE: Signals—Tinkering with Domains

E. Bornberg-Bauer

Binding domains in signaling proteins can tolerate sequence variation but still bind ligands and be structurally stable.

### REVIEW: ABL Tyrosine Kinases—Evolution of Function, Regulation, and Specificity

J. Colicelli

Insight into the regulation of ABL-family tyrosine kinases could facilitate development of therapies for malignancies driven by ABL fusion proteins.

## SCIENCE CAREERS

[www.sciencereers.org/career\\_magazine](http://www.sciencereers.org/career_magazine)

Free Career Resources for Scientists

### Tooling Up: A Job-Search Plan for the Person Without One (Part 2)

D. Jensen

The key to a successful job hunt is to precisely target particular jobs.

### Expanding the Genetic Code

E. Pain

Trained as a chemist, Jason Chin is rewriting central dogmas of biology by coaxing cells to make proteins containing novel amino acids.

## SCIENCE TRANSLATIONAL MEDICINE

[www.sciencetranslationalmedicine.org](http://www.sciencetranslationalmedicine.org)

Integrating Medicine and Science

### PERSPECTIVE: GIP—No Longer the Neglected Incretin Twin?

R. N. Kulkarni

The incretin hormone gastric inhibitory polypeptide may be a promising therapeutic target for type 2 diabetes.

### COMMENTARY: A Multi-Level Systems Perspective for the Science of Team Science

K. Börner et al.

Understanding how teams function is vital, because they are increasingly dominating the production of high-impact science.



SCIENCE SIGNALING  
Evolving domains.

### RESEARCH ARTICLE: Personalized Epigenomic Signatures That Are Stable Over Time and Covary with Body Mass Index

A. P. Feinberg et al.

Epigenetic signatures akin to genetic fingerprints may correlate with a common genetic trait.

### RESEARCH ARTICLE : Disruption at the *PTCHD1* Locus on Xp22.11 in Autism Spectrum Disorder and Intellectual Disability

A. Noor et al.

Mutations of the X-linked gene *PTCHD1* are associated with autism spectrum disorders and intellectual disability.

## SCIENCE PODCAST

[www.sciencemag.org/multimedia/podcast](http://www.sciencemag.org/multimedia/podcast)  
Free Weekly Show

Download the 17 September *Science* Podcast to hear about 30 years of China's one-child policy, hydrocarbon-degrading bacteria in the Gulf of Mexico, tool-making crows, and more.

## SCIENCE INSIDER

[news.sciencemag.org/scienceinsider](http://news.sciencemag.org/scienceinsider)  
Science Policy News and Analysis

**SCIENCE** (ISSN 0036-8075) is published weekly on Friday, except the last week in December, by the American Association for the Advancement of Science, 1200 New York Avenue, NW, Washington, DC 20005. Periodicals Mail postage (publication No. 484460) paid at Washington, DC, and additional mailing offices. Copyright © 2010 by the American Association for the Advancement of Science. The title **SCIENCE** is a registered trademark of the AAAS. Domestic individual membership and subscription (51 issues): \$146 (\$74 allocated to subscription). Domestic institutional subscription (51 issues): \$910; Foreign postage extra: Mexico, Caribbean (surface mail) \$55; other countries (air assist delivery) \$85. First class, airmail, student, and emeritus rates on request. Canadian rates with GST available upon request, GST #1254 88122. Publications Mail Agreement Number 1069624. Printed in the U.S.A.

**Change of address:** Allow 4 weeks, giving old and new addresses and 8-digit account number. **Postmaster:** Send change of address to AAAS, P.O. Box 96178, Washington, DC 20090-6178. **Single-copy sales:** \$10.00 current issue, \$15.00 back issue prepaid includes surface postage; bulk rates on request. **Authorization to photocopy** material for internal or personal use under circumstances not falling within the fair use provisions of the Copyright Act is granted by AAAS to libraries and other users registered with the Copyright Clearance Center (CCC) Transactional Reporting Service, provided that \$20.00 per article is paid directly to CCC, 222 Rosewood Drive, Danvers, MA 01923. The identification code for *Science* is 0036-8075. *Science* is indexed in the *Reader's Guide to Periodical Literature* and in several specialized indexes.



ADVANCING SCIENCE, SERVING SOCIETY





Shubha Tole is an associate professor at the Tata Institute of Fundamental Research, Mumbai, India; a member of the IndiaBioscience Committee; and a former YIM organizer. E-mail: shubhatole@gmail.com.



Ronald D. Vale is a professor at the University of California, San Francisco; an Investigator with the Howard Hughes Medical Institute; and a member of the YIM and IndiaBioscience committees. E-mail: vale@cmp.ucsf.edu.

## Young Leaders for Biology in India

MANY DEVELOPING COUNTRIES IN ASIA ARE RAPIDLY BUILDING NEW RESEARCH INSTITUTES, EAGER to establish a vibrant and progressive scientific enterprise on a nationwide scale. As Huang and Tan point out in the Policy Forum on p. 1471, this buildup of scientific infrastructure must be combined with changes in culture that promote innovation and collaboration, which are required ingredients for recruiting a new generation of outstanding scientists. India, a nation faced with such challenges, is engaged in a promising grassroots experiment aimed at attracting back talented young researchers and fostering a new scientific culture in the biological sciences.

In recent years, India has made considerable investments in life-science research (the current budget is approximately double that of 5 years ago). The new resources have been directed primarily toward creating new institutes, revitalizing older ones, and expanding the number of research and teaching positions. Thus far, India has not adopted China's and Singapore's strategy of offering lavish resources to established U.S. or European scientists to either move to or create outpost laboratories in Asia. Instead, India is reaching out to its young scientists who have mostly trained abroad, hoping to entice them to return home. To facilitate repatriation, the government has established several grant programs to support postdoctoral work and new independent laboratories within India (such as the Wellcome Trust/Department of Biotechnology India Alliance and other prestigious fellowships). But the major challenge is to change the mindset of expatriate scientists whose picture of Indian science is often one of poor laboratory facilities remembered from their undergraduate days.

For the past 2 years, bioscientists in India have been involved in a community-building effort directed at uniting its young scientists to promote their success. The centerpiece is an annual Young Investigator Meeting (YIM) that brings together ~40 postdoctoral fellows who are considering establishing careers in India with a similar number of young faculty who are already facing the realities of setting up a research program in India. Mid-career and junior scientists from across the country organize the meeting, which is held in a different region of India each year. Leading international scientists, senior Indian faculty, and government leaders are also invited to provide mentorship on both India-specific as well as more universal hurdles facing those setting up a research program. The topics under discussion include how to obtain grants, pick research problems, publish papers, guide trainees, and resolve conflicts.

This meeting offers a forum in which junior scientists unite and gain a sense of their important roles and responsibilities in building Indian biology. Social networking is strongly encouraged as a means of sharing solutions to problems and creating research collaborations. The postdoctoral fellows who attend obtain a realistic picture of the challenges and prospects in India, while forming a network with their prospective colleagues. This creative nationwide initiative is aimed at recruiting scientists into multiple institutions, thereby benefiting the country as a whole.

To complement this effort, a central IndiaBioscience Web portal ([www.indiabioscience.org](http://www.indiabioscience.org)) has been created to provide information on grants, jobs, and special programs, as well as opinion pieces on issues such as managing family and work, combining teaching with research, and hiring couples. Both the meeting and the Web site, managed by junior/mid-career faculty, help to instill a sense of responsibility among India's younger scientists to take ownership of their future and lead efforts to improve the scientific environments at their home institutions.

These initiatives represent a model that can be translated to other countries. Scientific success cannot emerge from new buildings and equipment alone. The best guarantee for future success is to imbue young scientists with a sense of a mission, to nurture not just the science but a culture that fuels the will to succeed in countries long thought of as second-choice options for research careers.

— Shubha Tole and Ronald D. Vale

10.1126/science.1196967





**1200 New York Avenue, NW  
Washington, DC 20005**  
Editorial: 202-326-6550, FAX 202-289-7562  
News: 202-326-6581, FAX 202-371-9227  
**Bateman House, 82-88 Hills Road  
Cambridge, UK CB2 1LQ**  
+44 (0) 1223 326500, FAX +44 (0) 1223 326501

**SUBSCRIPTION SERVICES** For change of address, missing issues, new orders and renewals, and payment questions: 866-434-AAAS (2227) or 202-326-6417, FAX 202-842-1065. Mailing addresses: AAAS, P.O. Box 96178, Washington, DC 20090-6178 or AAAS Member Services, 1200 New York Avenue, NW, Washington, DC 20005

**INSTITUTIONAL SITE LICENSES** please call 202-326-6755 for any questions or information

**REPRINTS:** Author Inquiries 800-635-7181  
Commercial Inquiries 803-359-4578

**PERMISSIONS** 202-326-7074, FAX 202-682-0816

**MEMBER BENEFITS** AAAS/Barnes&Noble.com bookstore www.aaas.org/bn; AAAS Online Store www.apisource.com/aaas/ code MKB6; AAAS Travels: Betchart Expeditions 800-252-4910; Apple Store www.apple.com/epstore/aaas; Bank of America MasterCard 1-800-833-6262 priority code FAA3YU; Cold Spring Harbor Laboratory Press Publications www.cshlpress.com/affiliates/aaas.htm; GEICO Auto Insurance www.geico.com/landingpage/go51.htm?logo=17624; Hertz 800-654-2200 CDP#343457; Office Depot https://bsd.officedepot.com/portalllogin.do; Seabury & Smith Life Insurance 800-424-9883; Subaru VIP Program 202-326-6417; VIP Moving Services www.vipmayflower.com/domestic/index.html; Other Benefits: AAAS Member Services 202-326-6417 or www.aaasmember.org.

science\_editors@aaas.org (for general editorial queries)  
science\_letters@aaas.org (for queries about letters)  
science\_reviews@aaas.org (for returning manuscript reviews)  
science\_bookrevs@aaas.org (for book review queries)

Published by the American Association for the Advancement of Science (AAAS), *Science* serves its readers as a forum for the presentation and discussion of important issues related to the advancement of science, including the presentation of minority or conflicting points of view, rather than by publishing only material on which a consensus has been reached. Accordingly, all articles published in *Science*—including editorials, news and comment, and book reviews—are signed and reflect the individual views of the authors and not official points of view adopted by AAAS or the institutions with which the authors are affiliated.

AAAS was founded in 1848 and incorporated in 1874. Its mission is to advance science, engineering, and innovation throughout the world for the benefit of all people. The goals of the association are to: enhance communication among scientists, engineers, and the public; promote and defend the integrity of science and its use; strengthen support for the science and technology enterprise; provide a voice for science on societal issues; promote the responsible use of science in public policy; strengthen and diversify the science and technology workforce; foster education in science and technology for everyone; increase public engagement with science and technology; and advance international cooperation in science.

## INFORMATION FOR AUTHORS

See pages 352 and 353 of the 15 January 2010 issue or access www.sciencemag.org/about/authors

EDITOR-IN-CHIEF **Bruce Alberts**  
EXECUTIVE EDITOR **Monica M. Bradford**  
NEWS EDITOR **Colin Norman**

MANAGING EDITOR, RESEARCH JOURNALS **Katrina L. Knelser**  
DEPUTY EDITORS **R. Brooks Hanson, Barbara R. Jasny, Andrew M. Sugden**

**EDITORIAL SENIOR EDITORS/COMMENTARY** Lisa D. Chong, Brad Wible; **SENIOR EDITORS** Gilbert J. Chin, Pamela J. Hines, Paula A. Kiberstis (Boston), Marc S. Lavine (Toronto), Beverly A. Purnell, L. Bryan Ray, Guy Riddihough, H. Jesse Smith, Phillip D. Szuroni (Tennessee), Valda Vinson, Jake S. Yeston; **ASSOCIATE EDITORS** Kristen L. Mueller, Jelena Stajic, Nicholas S. Wigginton, Laura M. Zahn; **RESEARCH ASSOCIATE** Alexis Wynne Mogul; **BOOK REVIEW EDITOR** Sherman J. Suter; **ASSOCIATE LETTERS EDITOR** Jennifer Sills; **EDITORIAL MANAGER** Cara Tate; **SENIOR COPY EDITORS** Jeffrey E. Cook, Cynthia Howe, Harry Jach, Lauren Kimec, Barbara P. Ordway, Trista Wagoner; **COPY EDITOR** Chris Filibartre; **EDITORIAL COORDINATORS** Carolyn Kyle, Beverly Shields; **PUBLICATIONS ASSISTANTS** Ramatoulaye Diop, Joi S. Granger, Emily Guise, Jeffrey Hearn, Michael Hicks, Lisa Johnson, Scott Miller, Jerry Richardson, Jennifer A. Seibert, Brian White, Anita Wynn; **EDITORIAL ASSISTANTS** Emily C. Horton, Patricia M. Moore, Miriam Weinberg; **EXECUTIVE ASSISTANT** Alison Crawford; **ADMINISTRATIVE SUPPORT** Maryrose Madrid; **EDITORIAL FELLOW** Melissa R. McCartney

**EDITORIAL DIRECTOR, WEB AND NEW MEDIA** Stewart Wills; **SENIOR WEB EDITOR** Tara S. Marathe; **WEB EDITOR** Robert Frederic; **WEB DEVELOPMENT MANAGER** Martyn Green; **WEB DEVELOPER** Andrew Whitesell; **INTERN** Sophia Cai  
**NEWS DEPUTY NEWS EDITORS** Robert Coontz, David Grimm, Eliot Marshall, Jeffrey Mervis, Leslie Roberts; **CONTRIBUTING EDITORS** Elizabeth Culotta, Polly Shulman; **NEWS WRITERS** Yudhith Bhattacharjee, Adrian Cho, Jennifer Couzin, Jocelyn Kaiser, Richard A. Kerr, Eli Kintisch, Greg Miller, Elizabeth Pennisi, Lauren Schenkenman, Robert F. Service (Pacific NW), Erik Stokstad (Online); **WEB DEVELOPER** Daniel Berger; **INTERN** Kristen Minogue; **CONTRIBUTING CORRESPONDENTS** Jon Cohen (San Diego, CA), Daniel Ferber, Ann Gibbons, Sam Kean, Robert Koenig, Andrew Lawler, Mitch Leslie, Charles C. Mann, Virginia Morell, Gary Taubes; **COPY EDITORS** Linda B. Felaco, Melvin Gatling, Melissa Raimondi; **ADMINISTRATIVE SUPPORT** Scherraine Mack; **BUREAUS** San Diego, CA: 760-942-3252, FAX 760-942-4979; Pacific Northwest: 503-963-1940

**PRODUCTION DIRECTOR** James Landry; **SENIOR MANAGER** Wendy K. Shank; **ASSISTANT MANAGER** Rebecca Doshi; **SENIOR SPECIALISTS** Steve Forrester, Chris Redwood, Anthony Rosen; **PREFLIGHT DIRECTOR** David M. Tompkins; **MANAGER** Marcus Spiegler; **SPECIALIST** Jason Hillman  
**ART DIRECTOR** Yael Fitzpatrick; **ASSOCIATE ART DIRECTOR** Laura Creveling; **SENIOR ILLUSTRATORS** Chris Bickel, Katharine Sutliff; **ILLUSTRATOR** Yana Hammond; **ART ASSISTANTS** Holly Bishop, Preston Huey, Nayomi Kevitiyagala; **ART ASSOCIATES** Kay Engman, Matthew Twombly; **PHOTO EDITOR** Leslie Blizard

## SCIENCE INTERNATIONAL

**EUROPE** (science@science-int.co.uk) **EDITORIAL: INTERNATIONAL MANAGING EDITOR** Andrew M. Sugden; **SENIOR EDITOR/COMMENTARY** Julia Fahrenkamp-Uppenbrink; **SENIOR EDITORS** Caroline Ash, Stella M. Hurtle, Ian S. Osborne, Peter Stern; **ASSOCIATE EDITOR** Maria Cruz; **LOCUM EDITOR** Helen Pickersgill; **EDITORIAL SUPPORT** Rachel Roberts, Alice Whaley; **ADMINISTRATIVE SUPPORT** John Cannell, Janet Clements, Louise Hartwell; **NEWS: EUROPE NEWS EDITOR** John Travis; **DEPUTY NEWS EDITOR** Daniel Clery; **CONTRIBUTING CORRESPONDENTS** Michael Balter (Paris), John Bohannon (Vienna), Martin Enserink (Amsterdam and Paris), Gretchen Vogel (Berlin); **INTERN** Sarah Reed

**LATIN AMERICA CONTRIBUTING CORRESPONDENT** Antonio Regalado

**ASIA** Japan Office: Asca Corporation, Tomoko Furusawa, Rustic Bldg. 7F, 77 Tenjin-cho, Shinjuku-ku, Tokyo 162-0808, Japan; +81 3 6802 4616, FAX +81 3 6802 4615, inquiry@sciencemag.jp; **ASIA NEWS EDITOR** Richard Stone (Beijing: rstone@aaas.org); **CONTRIBUTING CORRESPONDENTS** Dennis Normile [Japan: +81 (0) 3 3391 0630, FAX +81 (0) 3 5936 3531; dnormile@gol.com]; Hao Xin [China: cindyhao@gmail.com]; Pallava Bagla [South Asia: +91 (0) 11 2271 2896; pbagla@vsnl.com]

EXECUTIVE PUBLISHER **Alan I. Leshner**  
PUBLISHER **Beth Rosner**

**FULFILLMENT SYSTEMS AND OPERATIONS** (membership@aaas.org); **DIRECTOR** Waylon Butler; **CUSTOMER SERVICE SUPERVISOR** Pat Butler; **SPECIALISTS** Latoya Casteel, LaVonda Crawford, Vicki Linton, April Marshall; **DATA ENTRY SUPERVISOR** Cynthia Johnson; **SPECIALISTS** Shirlene Hall, Tarrika Hill, William Jones

**BUSINESS OPERATIONS AND ADMINISTRATION DIRECTOR** Deborah Rivera-Wienhold; **BUSINESS SYSTEMS AND FINANCIAL ANALYSIS DIRECTOR** Randy Yi; **MANAGER, BUSINESS ANALYSIS** Eric Knott; **MANAGER, BUSINESS OPERATIONS** Jessica Tierney; **FINANCIAL ANALYST** Priti Pannani, Celeste Troxler; **RIGHTS AND PERMISSIONS: ADMINISTRATOR** Emilie David; **ASSOCIATE** Elizabeth Sandler; **MARKETING DIRECTOR** Ian King; **MARKETING MANAGERS** Allison Pritchard, Alison Chandler, Julianne Wielga; **MARKETING ASSOCIATES** Aimee Aponte, Mary Ellen Crowley, Wendy Wise; **SENIOR MARKETING EXECUTIVE** Jennifer Reeves; **DIRECTOR, SITE LICENSING** Tom Ryan; **DIRECTOR, CORPORATE RELATIONS** Eileen Bernadette Moran; **PUBLISHER RELATIONS, eRESOURCES SPECIALIST** Kiki Forsythe; **SENIOR PUBLISHER RELATIONS SPECIALIST** Catherine Holland; **PUBLISHER RELATIONS, EAST COAST** Phillip Smith; **PUBLISHER RELATIONS, WEST COAST** Philip Tsolakis; **FULFILLMENT SUPERVISOR** Iquo Edim; **FULFILLMENT COORDINATOR** Carrie MacDonald; **MARKETING MANAGER** Christina Schlecht; **MARKETING ASSOCIATE** Laura Tutino; **ELECTRONIC MEDIA: MANAGER** Elizabeth Harman; **PROJECT MANAGER** Trista Snyder; **ASSISTANT MANAGER** Lisa Stanford; **SENIOR PRODUCTION SPECIALISTS** Ryan Atkins, Christopher Coleman, **COMPUTER SPECIALIST** Walter Jones, Kai Zhang; **PRODUCTION SPECIALISTS** Angela Forest, Nichole Johnston, Kimberly Oster; **DIRECTOR, WEB AND NEW MEDIA** Will Collins

**ADVERTISING DIRECTOR, WORLDWIDE AD SALES** Bill Moran

**COMMERCIAL EDITOR** Sean Sanders: 202-326-6430

**ASSISTANT COMMERCIAL EDITOR** Tianna Hicklin 202-326-6463

**PROJECT DIRECTOR, OUTREACH** Brianna Blaser

**PRODUCT** (science\_advertising@aaas.org); **MIDWEST** Rick Bongiovanni: 330-405-7080, FAX 330-405-7081; **EAST COAST/ E. CANADA** Laurie Faraday: 508-747-9395, FAX 617-507-8189; **WEST COAST/W. CANADA** Lynne Stickrod: 415-931-9782, FAX 415-520-6940; **UK/EUROPE/ASIA** Roger Goncalves: TEL/FAX +41 43 243 1358; **JAPAN** ASCA Corporation, Nanako Ide +81 (0) 3 6802 4616, FAX +81 (0) 3 6802 4615; ads@sciencemag.jp; **SENIOR TRAFFIC ASSOCIATE** Deandra Simms

**WORLDWIDE ASSOCIATE DIRECTOR OF SCIENCE CAREERS** Tracy Holmes: +44 (0) 1223 326525, FAX +44 (0) 1223 326532

**CLASSIFIED** (advertise@sciencemag.org); **U.S.: MIDWEST/WEST COAST/ SOUTH CENTRAL/CANADA** Tina Burks: 202-326-6577; **EAST COAST/INDUSTRY** Elizabeth Early: 202-326-6578; **ADVERTISING OPERATIONS MANAGER** Kate Panganiban **SALES COORDINATORS** Rohan Edmonson, Shirley Young; **EUROPE/ROW SALES** Susanne Kharraz, Dan Pennington, Alex Palmer; **SALES ASSISTANT** Lisa Patterson; **JAPAN** ASCA Corporation, Jie Chin +81 (0) 3 6802 4616, FAX +81 (0) 3 6802 4615; careerads@sciencemag.jp; **ADVERTISING SUPPORT MANAGER** Karen Foote: 202-326-6740; **ADVERTISING PRODUCTION OPERATIONS MANAGER** Deborah Tompkins; **SENIOR PRODUCTION SPECIALIST/GRAPHIC DESIGNER** Amy Hardcastle; **PRODUCTION SPECIALIST** Yuse Lajiminmuhip; **SENIOR TRAFFIC ASSOCIATE** Christine Hall

**AAAS BOARD OF DIRECTORS** RETIRING PRESIDENT, CHAIR Peter C. Agre; **PRESIDENT** Alice Huang; **PRESIDENT-ELECT** Nina Fedoroff; **TREASURER** David E. Shaw; **CHIEF EXECUTIVE OFFICER** Alan I. Leshner; **BOARD LINDA P. B. Katchi, Nancy Knowlton, Stephen Mayo, Cherry A. Murray, Julia M. Phillips, Sue V. Rosser, David D. Sabatini, Thomas A. Woolsey**



ADVANCING SCIENCE. SERVING SOCIETY

## SENIOR EDITORIAL BOARD

**John I. Brauman**, Chair, Stanford Univ.  
**Richard Losick**, Harvard Univ.  
**Linda Partridge**, Univ. College London  
**Michael S. Turner**, University of Chicago

## BOARD OF REVIEWING EDITORS

**Adriano Aguzzi**, Univ. Hospital Zürich  
**Takuzo Aida**, Univ. of Tokyo  
**Sonia Altizer**, Univ. of Georgia  
**David Altschuler**, Broad Institute  
**Arturo Alvarez-Buylla**, Univ. of California, San Francisco  
**Richard Amasino**, Univ. of Wisconsin, Madison  
**Angelika Amon**, MIT  
**Kathryn Anderson**, Memorial Sloan-Kettering Cancer Center  
**Siv G. E. Andersson**, Uppsala Univ.  
**Peter Andolfatto**, Princeton Univ.  
**Meinrat O. Andreae**, Max Planck Inst., Mainz  
**John A. Bargh**, Yale Univ.  
**Ben Barres**, Stanford Medical School  
**Marisa Bartolomei**, Univ. of Penn. School of Med.  
**Jordi Bascompte**, Estación Biológica de Doñana, CSIC  
**Facundo Batista**, London Research Inst.  
**Ray H. Baughman**, Univ. of Texas, Dallas  
**Yasmine Belkaid**, NIAID, NIH  
**Stephen J. Benkovic**, Penn State Univ.  
**Gregory C. Beroza**, Stanford Univ.  
**Ton Bisseling**, Lawrence Berkeley National Lab  
**Mina Bissell**, Lawrence Berkeley National Lab  
**Peer Bork**, EMBL  
**Robert W. Boyd**, Univ. of Rochester  
**Paul M. Brakefield**, Leiden Univ.  
**Christian Büchel**, Universitätsklinikum Hamburg-Eppendorf  
**Joseph A. Burns**, Cornell Univ.  
**William P. Butz**, Population Reference Bureau  
**Mats Carlsson**, Univ. of Oslo  
**Mildred Cho**, Stanford Univ.  
**David Clapham**, Children's Hospital, Boston  
**David Clark**, Oxford University  
**J. M. Claverie**, CNRS, Marseille  
**Jonathan D. Cohen**, Princeton Univ.  
**Andrew Cossins**, Univ. of Liverpool  
**Robert H. Crabtree**, Yale Univ.

**Wolfgang Cramer**, Potsdam Inst. for Climate Impact Research  
**F. Fleming Crim**, Univ. of Wisconsin  
**Jeff L. Dangl**, Univ. of North Carolina  
**Stanislas Dehaene**, Collège de France  
**Edward DeLong**, MIT  
**Emmanouil T. Dermizakis**, Univ. of Geneva Medical School  
**Robert Desimone**, MIT  
**Claude Desplan**, New York Univ.  
**Dennis Discher**, Univ. of Pennsylvania  
**Scott C. Doney**, Woods Hole Oceanographic Inst.  
**Jennifer A. Doudna**, Univ. of California, Berkeley  
**Julian Downward**, Cancer Research UK  
**Bruce Dunn**, Univ. of California, Los Angeles  
**Christopher Dye**, WHO  
**Michael B. Elowitz**, Calif. Inst. of Technology  
**Gerhard Ertl**, Fritz-Haber-Institut, Berlin  
**Mark Estelle**, Indiana Univ.  
**Barry Everitt**, Univ. of Cambridge  
**Paul G. Falkowski**, Rutgers Univ.  
**Ernst Fehr**, Univ. of Zurich  
**Tom Fenchel**, Univ. of Copenhagen  
**Alain Fischer**, INSERM  
**Wulfam Gerstner**, EPFL Lausanne  
**Charles Godfray**, Univ. of Oxford  
**Diane Griffin**, Johns Hopkins Bloomberg School of Public Health  
**Christian Haass**, Ludwig Maximilians Univ.  
**Steven Hahn**, Fred Hutchinson Cancer Research Center  
**Gregory J. Hannon**, Cold Spring Harbor Lab.  
**Niels Hansen**, Technical Univ. of Denmark  
**Dennis L. Hartmann**, Univ. of Washington  
**Chris Hawkesworth**, Univ. of St Andrews  
**Martin Heimann**, Max Planck Inst., Jena  
**James A. Hendler**, Rensselaer Polytechnic Inst.  
**Janet G. Hering**, Swiss Fed. Inst. of Aquatic Science & Technology  
**Ray Hilborn**, Univ. of Washington  
**Michael E. Himmel**, National Renewable Energy Lab.  
**Kei Hirose**, Tokyo Inst. of Technology  
**David Hoegh-Guldberg**, Univ. of Queensland  
**Lora Hooper**, UT Southwestern Medical Ctr at Dallas  
**Ronald R. Hoy**, Cornell Univ.  
**Jeffrey A. Hubbell**, EPFL Lausanne  
**Steven Jacobsen**, Univ. of California, Los Angeles  
**Peter Jonas**, Universität Freiburg

**Barbara B. Kahn**, Harvard Medical School  
**Daniel Kahne**, Harvard Univ.  
**Bernhard Keimer**, Max Planck Inst., Stuttgart  
**Robert Kingston**, Harvard Medical School  
**Hanna Kokko**, Univ. of Helsinki  
**Alberto R. Kornblitt**, Univ. of Buenos Aires  
**Leonid Kruglyak**, Princeton Univ.  
**Lee Kump**, Penn State Univ.  
**Mitchell A. Lazar**, Univ. of Pennsylvania  
**David Lazer**, Harvard Univ.  
**Virginia Lee**, Univ. of Pennsylvania  
**Julian Lewis**, Cancer Research UK  
**Olle Lindvall**, Univ. Hospital, Lund  
**Marcia C. Linn**, Univ. of California, Berkeley  
**John S. Lilly**, Cornell Univ.  
**Richard Losick**, Harvard Univ.  
**Ke Lu**, Chinese Acad. of Sciences  
**Laura Machuga**, CRUK Beatson Inst. for Cancer Research  
**Andrew P. Mackenzie**, Univ. of St Andrews  
**Anne Magurran**, Univ. of St Andrews  
**Oscar Marin**, CSIC & Univ. Miguel Hernández  
**Charles Marshall**, Univ. of California, Berkeley  
**Martin M. Matzuk**, Baylor College of Medicine  
**Graham Medley**, Univ. of Warwick  
**Virginia Miller**, Washington Univ.  
**Yasushi Miyashita**, Univ. of Tokyo  
**Richard Morris**, Univ. of Edinburgh  
**Edward Moser**, Norwegian Univ. of Science and Technology  
**Sean Munro**, MRC Lab. of Molecular Biology  
**Naoto Nagaosa**, Univ. of Tokyo  
**James Nelson**, Stanford Univ. School of Med.  
**Timothy W. Nilsen**, Case Western Reserve Univ.  
**Pär Nordlund**, Karolinska Inst.  
**Helga Nowinski**, European Research Advisory Board  
**Stuart H. Orkin**, Dana-Farber Cancer Inst.  
**Christine Ortiz**, MIT  
**Elinor Ostrom**, Indiana Univ.  
**Andrew Oswald**, Univ. of Warwick  
**Jonathan T. Overpeck**, Univ. of Arizona  
**P. David Pearson**, Univ. of California, Berkeley  
**John Pendry**, Imperial College  
**Reginald M. Penner**, Univ. of California, Irvine  
**John H. J. Petriani**, Memorial Sloan-Kettering Cancer Center  
**Simon Philpott**, Univ. of Florida  
**Philippe Poulin**, CNRS

**Colin Renfrew**, Univ. of Cambridge  
**Trevor Robbins**, Univ. of Cambridge  
**Barbara A. Romanowicz**, Univ. of California, Berkeley  
**Jens Rostrup-Nielsen**, Haldor Topsøe  
**Edward M. Rubin**, Lawrence Berkeley National Lab  
**Shimon Sakaguchi**, Kyoto Univ.  
**Michael J. Sanderson**, Univ. of Arizona  
**Jürgen Sandkühler**, Medical Univ. of Vienna  
**Randy Seeley**, Univ. of Cincinnati  
**Christine Seidman**, Harvard Medical School  
**David Sibley**, Washington Univ.  
**Joseph Silk**, Univ. of Oxford  
**Montgomery Slatkin**, Univ. of California, Berkeley  
**Davor Solter**, Inst. of Medical Biology, Singapore  
**Allan C. Spradling**, Carnegie Institution of Washington  
**Jonathan Sprent**, Garvan Inst. of Medical Research  
**Elisbeth Stern**, ETH Zürich  
**Yoshiko Takahashi**, Univ. of Science and Technology  
**Jürg Tschopp**, Univ. of Lausanne  
**Herbert Virgin**, Washington Univ.  
**Bert Vogelstein**, Johns Hopkins Univ.  
**Bruce D. Walker**, Harvard Medical School  
**Christopher A. Walsh**, Harvard Medical School  
**David A. Wardle**, Swedish Univ. of Agric Sciences  
**Colin Watts**, Univ. of Dundee  
**Detlef Weigel**, Max Planck Inst., Tübingen  
**Jonathan Weissman**, Univ. of California, San Francisco  
**Sue Wessler**, Univ. of Georgia  
**Ian A. Wilson**, The Scripps Res. Inst.  
**Timothy D. Wilson**, Univ. of Virginia  
**Xiaoliang Sunney Xie**, Harvard Univ.  
**John R. Yates III**, The Scripps Res. Inst.  
**Jan Zaenen**, Leiden Univ.  
**Mayana Zatz**, University of Sao Paulo  
**Huda Zoghbi**, Baylor College of Medicine  
**Maria Zuber**, MIT

## BOOK REVIEW BOARD

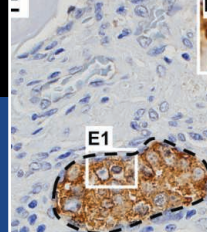
**John Aldrich**, Duke Univ.  
**David Bloom**, Harvard Univ.  
**Angela Creager**, Princeton Univ.  
**Richard Sweder**, Univ. of Chicago  
**Ed Wasserman**, DuPont  
**Lewis Wolpert**, Univ. College London





Protecting China's fossil beds

1453



XMRV: No meeting of the minds

1454

SCIENCE AND THE LAW

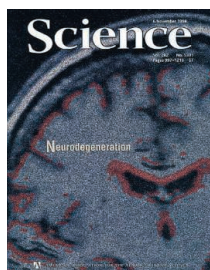
## With Stem Cells in Court, A History Primer

For those working with human embryonic stem cells (hESCs)—or even those following the research—the past 4 weeks have been tumultuous. In August, a District of Columbia (D.C.) judge temporarily barred federal funding for hESC research. The ruling threw labs and funding agencies into turmoil and generated much debate over whether current stem cell guidelines violate a 1996 rule that prohibits harming human embryos. An appeals court temporarily lifted the funding ban last week, and the National Institutes of Health (NIH) has resumed funding the work, but the case against hESC research is moving forward, with more legal filings expected this month and next that could again interrupt funding. In the end, resolution may need to come from Congress, where a handful of politicians are considering bills to more explicitly allow federal funding for hESC work. Whether they'll become law before the midterm elections in November remains to be seen.

Although this particular court case dates only to the summer of 2009, the hESC story stretches back 15 years, even before the cells were first isolated. *Science* assembled a timeline to capture this long road, whose end is still uncertain.

—GRETCHEN VOGEL AND  
JENNIFER COUZIN-FRANKEL

**26 January 1996:** Responding in part to an order from the Clinton Administration allowing some embryo research, the Republican-led Congress passes the Dickey-Wicker Amendment. The amendment, named for then-representatives Jay Dickey and Roger Wicker (now a U.S. senator), bars “research in which a human embryo or embryos are destroyed, discarded, or knowingly subjected to risk of injury or death greater than that allowed for research on fetuses in utero” (*Science*, 9 December 1994, p. 1634).



**6 November 1998:**

James Thomson and colleagues at the University of Wisconsin, Madison, report that they have isolated hESCs and kept them growing for months without differentiating. Thomson had walled off his embryo research from any public funding, setting up a separate lab in a building across campus from where he does NIH-funded research (*Science*, 6 November 1998, p. 1014).



**19 January 1999:** Then-NIH Director Harold Varmus (above) announces at a meeting of the National Bioethics Advisory Commission that “current law permits federal funds to be used for research using human pluripotent stem cells.” Varmus bases his announcement on a memo by Harriet Rabb, general counsel to the Department of Health and Human Services (HHS). It concluded that because hESCs are not embryos, research using them does not violate the Dickey-Wicker Amendment (*Science*, 22 January 1999, p. 465).

**23 August 2000:** NIH issues guidelines for hESC research. Before any grants are funded, however, President George W. Bush is inaugurated in January 2001. He orders

a new review of the NIH policy, putting all grant reviews on hold (*Science*, 1 September 2000, p. 1442). (In an ironic twist for supporters of the research, Jay Dickey was one of the few incumbents who lost his seat in the November 2000 election.)

**8 May 2001:** While Bush reviews the policy, researchers join forces with high-profile individuals affected by conditions for which hESCs are considered promising, including actor Christopher Reeve, paralyzed by a spinal cord injury. They ask the U.S. District Court for the District of Columbia to declare that the NIH guidelines are legal and to compel NIH to fund research on the cells (*Science*, 25 May 2001, p. 1463).

**9 August 2001:** Bush announces that NIH will fund research only on cell lines derived before this date. Ultimately, 78 cell lines are included in the NIH registry, but only 21 are actually available for research. Many submitted lines fail to grow without differentiating; others are not shipped by the labs that made them. One was withdrawn by the embryo donors.

**18 July 2006:** The Senate passes a bill sponsored by representatives Diana DeGette (D-CO) (below) and Michael Castle (R-DE) and previously endorsed by the House of Representatives. It would allow research on hESCs provided the cells are derived from embryos left over after fertility treatments and donated to research. The next day, Bush vetoes the bill.



CREDITS (CHRONOLOGICAL): © STEVE GSCHEISSNER/SCIENCE PHOTO LIBRARY/CORBIS; SCIENCE 262, 5391 (6 NOVEMBER 1998); © MARTIN H. SIMON/CORBIS; AP IMAGES

Downloaded from [www.sciencemag.org](http://www.sciencemag.org) on September 16, 2010





**25 August 2006:** Shinya Yamanaka of the University of Kyoto in Japan (left) reports in *Cell* a technique called cellular reprogramming, which turns mouse fibroblast cells into pluripotent cells that can become any cell

type. The induced pluripotent stem cells are heralded as a noncontroversial alternative to hESCs and potentially more powerful than adult stem cells.



**7 June 2007:** Congress tries again, authorizing NIH research on hESCs regardless of when they were derived. Two weeks later, on 20 June, Bush (above) vetoes the bill for a second time.



**9 March 2009:** President Barack Obama (above) issues an executive order stating that NIH “may support and conduct responsible, scientifically worthy human stem cell research, including human embryonic stem cell research, to the extent permitted by law.” The order requires NIH to develop new guidelines to govern the research within 4 months.

**9 April 2009:** NIH releases draft guidelines that would permit federal funding for research on hESCs but not for their derivation. Over the next 2 months, it receives more than 49,000 comments in response.

**7 July 2009:** Under acting Director Raynard Kington (right), new NIH guidelines go into effect. They establish criteria for hESC lines in NIH-funded projects and a registry of approved lines. For lines derived before 7 July, a committee must review the informed-consent documents used to donate the embryos. Cell lines derived later must comply with the informed-consent requirements laid out in the guidelines (*Science*, 10 July 2009, p. 131).



**19 August 2009:** A raft of plaintiffs, including an embryo adoption agency, embryos, and adult stem cell scientists James Sherley (left) and Theresa Deisher, file a lawsuit against HHS and NIH arguing that federal funding for hESC research is illegal because it violates the Dickey-Wicker Amendment. The two researchers were recruited to the suit by attorneys for those opposing hESC research and didn’t meet each other until earlier this month.

**27 October 2009:** Chief Judge Royce Lamberth of the U.S. District Court in Washington, D.C., dismisses the case, arguing that the plaintiffs don’t have legal standing to bring the lawsuit, largely because they aren’t being harmed by the current hESC guidelines.

**28 October 2009:** The plaintiffs appeal.

**25 June 2010:** U.S. Court of Appeals for the District of Columbia Circuit reverses Lamberth’s ruling as it pertains to the standing of Sherley and Deisher. In August, the court sends the case back to Lamberth and orders that it be allowed to proceed.

**23 August 2010:**

Lamberth grants the plaintiffs’ request for a preliminary injunction that blocks federal funding for hESC research until the case is decided. NIH, led by Francis Collins (right), immediately freezes grant reviews. One week later, NIH halts all hESC research inside its institutes (*Science*, 3 September, p. 1132).



**9 September 2010:**

After a flurry of filings on both sides, the D.C. Court of Appeals temporarily blocks Lamberth’s (right) ruling, allowing federal funding to continue for now.



**9 September 2010:** The plaintiffs, Sherley and Deisher, file a motion for summary judgment, telling Lamberth there’s enough evidence for him to rule in their favor without holding a trial.

**Next:** By 20 September, both sides must file briefs on the preliminary injunction, currently halted, to ban hESC funding. The court’s decision will determine whether funding can continue while the case proceeds. In October, Lamberth will probably rule on the case itself. Any decision is likely to be appealed. On the congressional front, Senator Tom Harkin (D-IA) was expected to hold a hearing this week to discuss hESC funding and the legal landscape.



## PALEONTOLOGY

# China Clamps Down on Illegal Fossil Trading

**BEIJING**—China's powerful State Council issued a regulation last week designed to rein in rampant pillaging of the country's magnificent fossil beds, which have yielded the first feathered dinosaurs and other blockbuster finds. The new rules will change the way excavation permits are issued and impose hefty fines for infractions. Paleontologists are generally pleased, but they will pay a price for the stepped-up protection: potential loss of sovereignty over important fossils they unearth.

By law, all fossils are state property. In practice, farmers scour known sites and sell their finds to dealers, some of whom alert paleontologists to fossils of potential scientific value. However, many dealers are not so conscientious, and premier specimens end up in private collections. With so much money sloshing around the fossil trade, venal officials are known to turn a blind eye to illegal fossil collection while withholding permission for scientific digs.

The regulation is meant to tackle this systemic rot, but when a draft emerged last year, scientists cried foul: It would have given local authorities even more say in issuing excavation permits (*Science*, 21 August 2009, p. 924). To researchers' relief, the much-anticipated final rule, set to go into effect on 1 January, should wrest control of important dig sites from local officials and put it in the hands of the central government. And paleontologists will no longer need permits for small-scale fossil collecting for teaching and research—defined as using hand tools and no heavy equipment—as long as they file a plan beforehand. “This is major progress,” says Zhou Zhonghe, director of the Institute of Vertebrate Paleontology and Paleoanthropology in Beijing.

Also reassuring to researchers, the regulation casts a protective net over fossil beds bearing the most valuable specimens: holotypes, for which a species is named; com-

plete vertebrate fossils; aggregates of invertebrates or plants; and imprints like dinosaur tracks. The Ministry of Land and Resources will now have sole authority to issue permits for excavating high-priority fossils. Scientists will provide critical input: The State Council will forward excavation applications to a national paleontological committee for review. Provincial authorities will continue to oversee excavation of low-priority fossils, such as single specimens of invertebrates or plants. (Early human remains and Ice Age

fossils are protected by other statutes.) Adding an element of uncertainty, the regulation states that excavations must be “supervised” by the land ministry's county offices. “If they have basic scientific knowledge and know what a fossil is and understand this regulation, then our work can go well. Otherwise, they can stop us at any time,” says Jiang

Da-yong, an expert on marine reptiles at Peking University.

The regulation contains one bitter pill for researchers. The land ministry will be the sole arbiter of where high-

priority fossils should be deposited: in the institution that collects them, or, for example, in a museum. This means researchers could lose control of the most important fossils they unearth, says Zhou. Overseas collaborations could suffer too: Only the ministry may decide which specimens can be sent abroad for research, and for how long—stripping authority from institutions.

The regulation sidesteps one key issue: the legality of existing private fossil collections. But it sets substantial fines for infractions—up to \$1.5 million for excavating high-priority fossils without the land ministry's permission—that may deter illicit activity in the future. Still, it's far from certain that the regulation will end up improving the protection of China's magnificent fossils. “We will see,” says Zhou. He and others don't underestimate the will of shadier dealers to stay in business.

—RICHARD STONE



**Site visit.** Zhou Zhonghe examines a Cretaceous-era fish.

## ScienceInsider

### From the *Science* Policy Blog



A new report from the Massachusetts Institute of Technology lays out steps to triple the world's **nuclear energy** output by 2050, to more than a terawatt. Funding loan guarantees to bring on the latest generation of reactors is a priority, the report says, as is increasing yearly U.S. federal R&D spending to roughly \$1 billion. The key step, the report says, is to “preserve our options” through research aimed at determining whether spent fuel rods can be used as a fuel source rather than constituting waste that needs to be buried. [http://bit.ly/nuke\\_report](http://bit.ly/nuke_report)

NASA has failed to tamp down media coverage of a reanalysis of data on **soil samples from Mars**. Despite heavy caveats in a NASA press release put out just before the long Labor Day weekend, media outlets heralded the possibility of finding organic compounds—and the faint chance of life itself—on Mars in the future. But those reports failed to make clear that any organics that may someday be found on the planet could have arrived there by asteroid. [http://bit.ly/mars\\_life](http://bit.ly/mars_life)

The **imperiled Russian seed bank at Pavlovsk Experimental Station** outside St. Petersburg may have been issued a reprieve. In August, a Russian court approved the transfer of 29 hectares of fields to the Russian Housing Development Foundation. Now the foundation will postpone selling the plots and appoint a commission to assess their scientific value. [http://bit.ly/plants\\_reprieve](http://bit.ly/plants_reprieve)

The European Parliament has approved regulations to limit some **animal research**. They allow experiments on macaques and other monkeys but prohibit research on great apes. [http://bit.ly/animal\\_studies](http://bit.ly/animal_studies)

Biologist Elizabeth Goodwin, who **pleaded guilty to making false statements** on a federal grant report, has been ordered by a judge to pay a \$500 fine and \$50,000 in restitution to the U.S. government and \$50,000 to the University of Wisconsin, where she used to work. [http://bit.ly/goodwin\\_sentenced](http://bit.ly/goodwin_sentenced)

For more science policy news, visit <http://news.sciencemag.org/scienceinsider>.

## VIROLOGY

# No Meeting of Minds on XMRV's Role in Chronic Fatigue, Cancer

**BETHESDA, MARYLAND**—For the past few years, researchers have been tantalized by reports linking a new retrovirus to some cases of prostate cancer and, more recently—and more controversially—the mysterious illness chronic fatigue syndrome (CFS). With the excitement over discovering a possible new cause for these diseases, however, has come skepticism, as some groups have found scarcely a trace of the novel virus, called XMRV. Many hoped a 1.5-day workshop\* here last week would help resolve the controversy. Instead, the field remains mired in “a zone of chaos,” concluded co-organizer and retrovirologist John Coffin of Tufts University in Boston and the National Cancer Institute (NCI) in Frederick, Maryland. “We don’t have agreement on almost anything.”

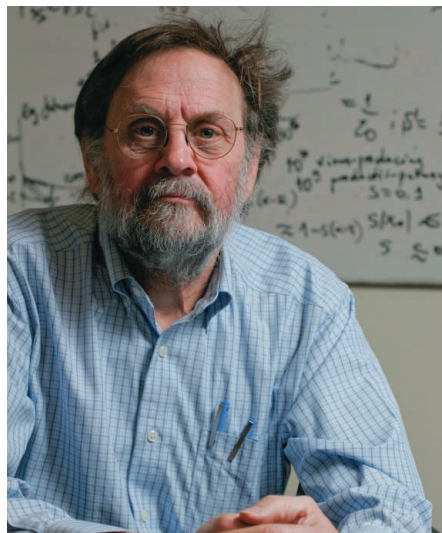
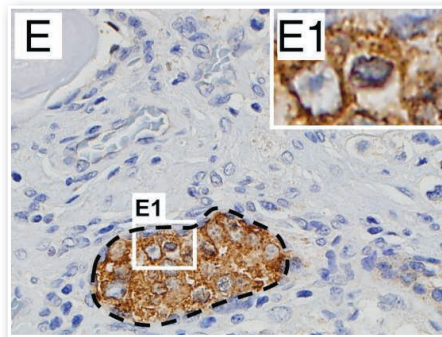
Still, in spirited discussions, sometimes frustrated-sounding researchers had a chance to air their findings and discuss ways to move forward. At the meeting Francis Collins, director of the National Institutes of Health, announced that NIH is funding a new study that could help resolve whether the presence of XMRV varies with geography or whether differences in how labs prepare and test samples explain the varying results.

XMRV, which resembles a mouse retrovirus, was discovered in 2006 in a group of men with a hereditary form of prostate cancer. Some groups have since confirmed the finding, but others, particularly in Europe, have not. Then a year ago, a report in *Science* linked XMRV to CFS, a disease involving fatigue and muscle pain mostly in middle-age women (*Science*, 9 October 2009, p. 215). Although patient groups were ecstatic to finally have a potential cause for what some people consider not a true disease, the study, led by Judy Mikovits of the Whittemore Peterson Institute (WPI) in Reno, Nevada, met with doubts as other groups failed to confirm it (*Science*, 15 January, p. 254).

This summer, scientists at the U.S. Centers for Disease Control and Prevention (CDC) found no XMRV in blood from CFS patients, while a team at the Food and Drug Administration (FDA) and NIH reported finding genes from a group of viruses closely related to XMRV, dubbed MLV-related viruses, in 87% of 37 blood samples from CFS patients and in 7% of healthy people (*Science*, 27 August,

p. 1000). Differences in virus-detection methods or in how patients were diagnosed or recruited could help explain the discrepancies, the two sets of authors suggested.

At last week’s workshop, 220 scientists and others ran through many of the published studies, as well as some new unpublished ones. For example, Mikovits has now found XMRV in patients in England with CFS. She



**In disarray.** Discussions over XMRV (above in prostate cancer cells) remain in “chaos,” says John Coffin.

defended her group’s original findings: “We have independent confirmation from three groups,” she said at the workshop. But some participants raised concerns about possible sources of stray mouse DNA, from knives for slicing tumors to the heparin sometimes used to stabilize blood samples. Tufts immunologist Brigitte Huber reported that her lab initially found almost no XMRV in CFS patient samples, but when they tested more samples from patients and healthy people prepared a different way, many were positive. These

samples turned out to contain endogenous mouse retrovirus DNA, probably from a contaminated reagent, said Huber: “It’s a false positive in our hands.”

One underlying issue is that the polymerase chain reaction assay used to detect XMRV—the assay copies and amplifies pieces of DNA—is so sensitive that it can detect extremely small traces of viral sequences, the amount in a milliliter of water from a swimming pool in which a drop of mouse blood has been mixed, Coffin said. This makes it easy to pick up contaminant mouse viral DNA. Even if XMRV is present in some tumors, the reported levels are so low that it’s unclear how it could contribute to the development of cancer, says pathologist Angelo De Marzo of Johns Hopkins University in Baltimore, Maryland. “The data [are] very noncompelling,” says De Marzo, whose lab, working with NCI’s Alan Rein, failed to find XMRV in nearly 800 prostate tumor samples.

Some meeting participants said the only way to establish that XMRV actually causes CFS and isn’t simply a “passenger” virus that doesn’t contribute to the illness is to treat CFS patients with antiretroviral drugs. Coffin cautioned that it would be “premature” to do so without an assay to monitor the amount of XMRV in a patient’s blood, as is now done with AIDS patients on antiviral therapy. But if such a test is developed, “I would not be averse to doing very small studies under tightly controlled clinical conditions,” he said.

Hoping to figure out what’s going on, a federal working group involving labs at FDA, CDC, WPI, and elsewhere has compared results for blood samples to which various amounts of XMRV had been added. (All six labs detected it.) The group has also tested four WPI samples from CFS patients but isn’t ready to discuss the results because “we’re still confused by them,” says Coffin, who is part of the working group.

More answers could come from the study Collins announced. National Institute of Allergy and Infectious Diseases Director Anthony Fauci has asked Columbia University epidemiologist W. Ian Lipkin to collect blood samples from 100 CFS patients from four parts of the United States and 100 healthy people and send blinded samples to the FDA, CDC, and WPI labs for testing. “We’re interested in settling a discrepant observation,” Fauci says.

Chaos may still reign, but Coffin thinks order may emerge over the next year. If nothing else, he says, “people left the meeting talking to each other when they weren’t always before. I hope that will continue.”

—JOCELYN KAISER

\*1st International Workshop on XMRV, 7–8 September 2010, Bethesda, Maryland.



## From *Science's* Online Daily News Site

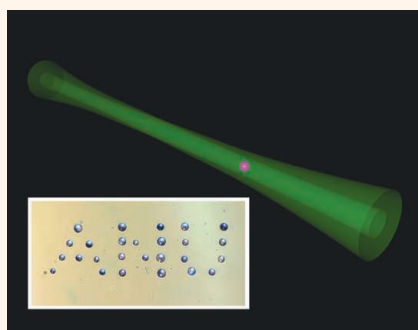
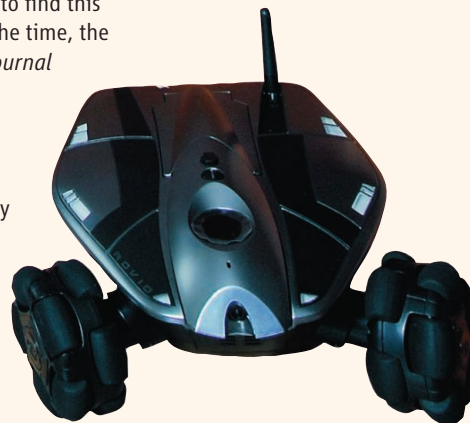
### The Real Decepticons

Don't trust this robot. It's been programmed to lie.

Computer scientists Alan Wagner and Ronald Arkin of the Georgia Institute of Technology in Atlanta designed an algorithm that taught a two-wheeled, camera-equipped robot to cheat in a simple game of hide-and-seek. First, the robot chooses one of three compartments in which to conceal itself. The pathway to each is blocked by a green, red, or blue marker. So, ostensibly, whichever way the robot goes, it knocks down a marker that gives a clue to its hiding place. But when programmed to deceive, the robot knocked over one marker and then turned around and hid somewhere

else. A "finder" robot programmed to find this "hider" failed in its quest 75% of the time, the team reports in the *International Journal of Social Robotics*.

Wagner says he's aware people might be leery of creating deceitful robots. But he thinks robots that know how to lie could benefit society in the long run. "There are a lot of important situations in which humans deceive for the better of the other person," he says. "Deception is not necessarily nefarious." <http://bit.ly/robot-lies>



### A Laser Peashooter

Who needs a straw? Physicists have devised a tunnel of laser light that can shoot small particles across a room.

Vladlen Shvedov, Andrei Rode, and colleagues at Australian National University in Canberra relied on a bit of physics called the photophoretic force, which arises when light warms a particle in air and essentially shoves it in a particular direction. To put this force to work, the researchers formed a tube of laser light called a vortex beam. They then fed into the tube either bits of carbon or tiny glass

spheres coated with carbon. When a particle would wander away from the dark hole in the middle of the beam, the light would warm one side of it and push it back toward the center. And because the light in the beam was flowing in one direction, it would gently push the particle down the pipe, for distances as far as 1.5 meters, the team reports in an upcoming paper in *Physical Review Letters*.

The technique should allow researchers to transport proteins or even cells over large distances without touching or contaminating them, Rode says. Others envision taking the rig out of the lab, perhaps to sniff out contraband by snaring molecules out of the air. <http://bit.ly/peashooter>

### A Better Way to Monitor Preemies?

Babies born too early often struggle to survive. But doctors can have a hard time telling which preemies are going to develop serious health problems, such as respiratory failure, and which ones are going to be fine.

To create a better diagnostic, researchers including Anna Penn, a neonatologist at

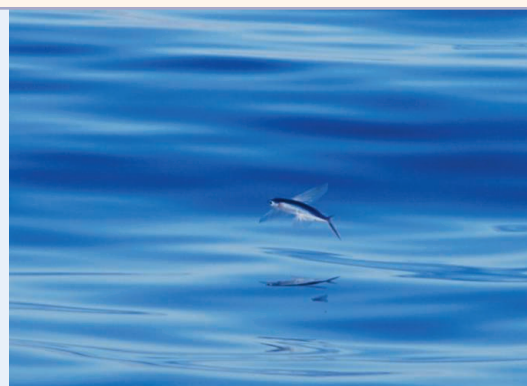
Lucile Packard Children's Hospital in Palo Alto, California and Daphne Koller, a computer scientist at Stanford University, examined physiological data routinely collected in the first 3 hours of life by bedside monitors, such as heart rate, respiratory rate, and the amount of oxygen in the blood. When they modeled these data, they observed signatures in sick babies that were different from the ones they observed in healthy ones. They used these differences to develop a scoring system, called PhysiScore. As the researchers report in *Science Translational Medicine*, they were able to predict serious complications with an accuracy of between 91% and 98%—far better than current approaches, such as the so-called Apgar score.

Penn says the same techniques might also work to identify high-risk surgical patients or adults most likely to suffer complications following a heart attack. <http://bit.ly/physiscore>

Read the full postings, comments, and more at <http://news.sciencemag.org/sciencenow>.

### Flying Fish Match Birds at Gliding

Strictly speaking flying fish don't fly—they glide. But these fork-tailed swimmers found in tropical and subtropical oceans still outperform some veteran fliers. When researchers placed the fish—caught in the wild, killed, and stuffed with foam—in a wind tunnel, they found that their fins achieved better lift and less drag than the wings of many insects, and did just as well as some birds, like hawks and wood ducks. That may explain why the fish are able to glide over the water for distances as far as 200 meters, the team reports in the *Journal of Experimental Biology*. Of course, hawks and butterflies don't have to be great gliders—they can just flap their wings to keep from crashing to the ground. <http://bit.ly/flying-fish>



## NEWSMAKER INTERVIEW

# Genentech Scientist to Take the Helm at Rockefeller University

Last week, Rockefeller University announced that it has selected Marc Tessier-Lavigne to be its next president. Tessier-Lavigne, 50, is currently executive vice president for research and chief scientific officer at Genentech, the San Francisco Bay-area biotech company. He replaces outgoing president Paul Nurse, who will return to his native United Kingdom to head both the 350-year-old Royal Society and the nascent UK Centre for Medical Research and Innovation in London (*Science*, 23 July, p. 380).

Born in Canada, Tessier-Lavigne studied physics at McGill University in Montreal and physiology and philosophy at the University of Oxford as a Rhodes scholar before earning a Ph.D. in physiology at University College London. Early in his career, he made a name for himself by identifying molecular signals that guide axons to their targets in the embryonic brain, work with potentially important implications for developing therapies to regenerate damaged nerves. He held faculty positions at the University of California, San Francisco, and at Stanford University before joining Genentech in 2003. After the Swiss pharmaceutical giant Roche acquired Genentech last year, Tessier-Lavigne became second in charge of research, reporting to former Stanford colleague Richard Scheller, who heads Genentech as an independent research center (*Science*, 1 May 2009, p. 583).

Tessier-Lavigne will assume his new position in March 2011. He spoke with *Science* last week about the transition. His remarks have been edited for brevity.

—GREG MILLER

**Q:** Many people expect the Roche takeover to kill the famously innovative culture at Genentech, and Roche recently said it is looking for new ways to cut costs. To what extent was this a factor in your decision?

**M.T.L.:** It had absolutely nothing to do with my decision. Roche, when they acquired Genentech, promised that they would maintain research and early clinical development as an autonomous group that reports directly to the CEO. Roche has been absolutely true to their word, and as a result not a single member of the senior research leadership has left. I'm the first to leave, but it's because I was presented with a once-in-a-

lifetime opportunity. It was a difficult decision. I think the prospects at Genentech have never been better, but I had to choose.

**Q:** Genentech prides itself on fostering an academic environment, and Rockefeller is an academic institution devoted to biomedicine. Do you expect your new job to be all that different from your old job?

**M.T.L.:** In many ways, this is a very similar type of enterprise. In coming to Rocke-



*"I think the prospects at Genentech have never been better, but I had to choose."*

—MARC TESSIER-LAVIGNE,  
GENENTECH

efeller, I see many of the same strengths: a relentless focus on basic science and a real interest in science that is relevant and applicable to disease. There's more emphasis on the basic science, but it's really a question of weighting.

**Q:** Are there important differences?

**M.T.L.:** Genentech is more of a collaborative research enterprise across the institution. Here [at Rockefeller], the institute supports 70 labs to pursue what the lab heads believe

are the most important directions. The role of the president is to help enable the faculty to maximize their impact.

**Q:** Have you had time to think about your goals and priorities for the university?

**M.T.L.:** My first priority is to listen and learn what the secret sauce is that's made Rockefeller so successful for over a century. Some ingredients seem clear. First, it's a small institution with no departments. Because of the structure, there are very few distractions [such as] departmental affairs and undergraduate teaching. And that's why people can remain productive late into their careers. You may have seen that Paul Greengard, who's 84 years old, just had a beautiful article in *Nature* [2 September] on an important regulator of the amyloid precursor protein that's important for Alzheimer's disease.

**Q:** Will you have your own lab?

**M.T.L.:** Yes. The university has a strong tradition of presidents maintaining an active research lab, and that was a major appeal of the job.

**Q:** You had a recent *Nature* paper on Alzheimer's disease yourself [19 February 2009], hinting at an alternative to the most popular explanation of the disease. Where do things stand with the amyloid hypothesis?

**M.T.L.:** The amyloid hypothesis is a strong hypothesis. It's equally important to focus on additional mechanisms that are upstream of amyloid formation and mechanisms downstream that are involved in the actual degenerative processes within neurons. One important lesson in drug discovery is don't put all your eggs in one basket.

**Q:** We recently wrote about the challenges of drug discovery in neuroscience [*Science*, 30 July, p. 502]. What does the future look like to you?

**M.T.L.:** The unmet need is still huge. There are no disease-modifying treatments for neurodegenerative diseases. The same is true of psychiatric illnesses, many of which are poorly treated. The prospects for drug discovery are entirely based on understanding the biological mechanisms that go awry. Our knowledge is accelerating, particularly for neurodegenerative diseases. It's breaking open in the way that cancer did in the early 1990s. I'm guardedly optimistic that we're on the cusp of great breakthroughs in understanding the mechanisms, and that's what's essential for rational drug discovery.





**Physical fitness.** Jonathan Dorfan will strengthen physics and math at OIST.



## NEWSMAKER INTERVIEW

# Physicist Tapped to Turn Embattled Institute Into a Fully Fledged University

**ONNA VILLAGE, JAPAN**—Can a world-class research university thrive on a subtropical island lacking a scientific tradition? Physicist Jonathan Dorfan intends to make that happen. Appointed president-elect of the Okinawa Institute of Science and Technology this summer, Dorfan will steer OIST through the final phase of start-up and enroll its first graduate students in 2012. He was chosen because of his stature and experience from 1999 to 2007 as director of the Stanford Linear Accelerator Center, now the SLAC National Accelerator Laboratory in Menlo Park, California, where he oversaw a staff of 1500 and an annual budget of \$300 million.

Conceived almost a decade ago, OIST is intended to break the Japanese university mold by emphasizing interdisciplinary research, filling at least half its faculty positions with foreigners, and conducting all instruction in English. It is also charged with fostering economic development in Okinawa, one of Japan's poorest prefectures.

OIST opened as a research institute in September 2005 with Nobel laureate Sydney Brenner as its first president. Dorfan will take over when OIST officially becomes a university next year. In the meantime, he must lead curriculum development, add physicists and mathematicians to a life sciences-heavy faculty, and win accreditation. He must also secure funding from a government determined to rein in a ballooning public debt while fending off skepticism in Japan's parliament over OIST's merits. Last spring, a governmental waste-hunting task force grilled Brenner over OIST's expenditures on its Nobel laureate-packed board of governors: reportedly \$350,000 a year for honoraria and first-class tickets to biannual meetings. Brenner promised to economize. Dorfan says he wants to meet critics in person to make OIST's case. —DENNIS NORMILE

**Q: Why did you take up this challenge?**

**J.D.:** To a large extent, it is the boldness of the endeavor and the goals, which are to promote international research and education. In addition, I saw an opportunity to provide support to researchers in an environment that's unfettered.

**Q: What is going to distinguish your approach to interdisciplinary research?**

**J.D.:** Let me acknowledge that "interdisciplinary" is a buzzword. It is something that some of the best institutions in the world have taken on aggressively. One challenge in a traditional university is that faculty normally are based in departments. They have teaching duties in their departments. Academic support is departmental. Here we can organize in a way that is much freer than that. Our teaching is at the graduate level. That lessens the load on researchers. It gives you more freedom to create the kinds of interactions that lead to interdisciplinary research.

Secondly, there's been a great deal of thought in the layout of the labs. Principal investigators are in groups of eight. They must bump into each other [and] talk to each other. A lot of thought has gone into the dynamic that generates interdisciplinary discussions, and you hope ideas will follow.

**Q: What about the educational component?**

**J.D.:** We need to produce researchers who have a strong base in a discipline—with well-identified skills and capabilities. On the other hand, we can [add] multidisciplinary aspects. An example might be a course on measurement. Not how do you make measurements specific to a particular biological area, but what is the essence of measurements. To be frank, we're still developing these ideas.

**Q: Until now the focus here has been on life sciences. How will you broaden the scientific efforts?**

**J.D.:** Now that we have established a core in life sciences, we will start to build up physical sciences and mathematics. We are also very open to people who are strong in specialized instrumentation. I hope that new instrumentation will be a hallmark of this institution.

**Q: Will you be able to recruit top people?**

**J.D.:** I came here with great enthusiasm, attracted by the research and educational possibilities. ... It's a beautiful island. It's a very welcoming culture. Now, I am also realistic. We will have to compete with the best for the best. I'm confident that we are going to win enough encounters that this place will flourish.

**Q: This institute is also supposed to contribute to the sustainable development of Okinawa. How will you fulfill that role?**

**J.D.:** Building an exceptional faculty, bringing in the best young researchers, and having an outstanding student body is really the essence of what we need. Then many things follow. The cultural opportunities are also great. An internationally constituted scientific community appreciates creativity. So we will bring in performers, artists, and shows that will sit alongside the island's already very rich artistic aura.

Finally, what we talk about the most is technology transfer. You certainly know examples of technology clusters, one of which started with a farm in a town called Palo Alto, and you see what you have there now. We have to do it here. A series of discussions will [help] us formulate a strategy over time.

**Q: Given the Japanese government's fiscal situation, will you try fundraising?**

**J.D.:** It's an absolutely clear certainty. It's going to be one of my early pushes. I was the first director at SLAC who brought in donor money. I want to use that experience and my connections to generate private support. That takes a while. You don't just go out on the street with a sign.



# Has China Outgrown The One-Child Policy?

**Thirty years ago, China launched an unprecedented attempt to put the brakes on population growth. Some social scientists now argue that it's time to scrap the one-child policy altogether**

**SHANGHAI, CHINA**—Elementary schools converted into nursing homes. Lonely only children coddled by parents and grandparents. A generation in which men seriously outnumber women. China's one-child policy may have slowed population growth in the world's most populous country. But it has also produced a rapidly aging population, a shrinking labor force, and a skewed sex ratio at birth, perils that many demographers say could threaten China's economy and social fabric.

As the most spectacular demographic experiment in history, the one-child policy is unprecedented in its scope and extremity. The measure is so sacrosanct that officials who have dared in the past to hint at its dissolution have been quickly silenced. But a growing number of experts contend that the policy, which turns 30 next week, has run its course. "It's time to start experimenting and looking at how to phase out the policy," says Wang Feng, a demographer at the University of California (UC), Irvine.

Over the past decade, Wang and two dozen other Chinese-born demographers, sociologists, and former government officials

have been pushing quietly for the policy's abolition. They have looked at what would happen if birth targets were lifted, and they have put forth schemes for dismantling the policy step by step. At times this informal anti-one-child advocacy group has veered close to heresy, debunking some of the government birth-control lobby's most cherished claims. But they have been left mostly undisturbed to continue their work. "Chinese policymakers have increasingly accepted the fact that fertility has dropped to below replacement level," explains Wang, who is also affiliated with Fudan University here. An internal government debate about the policy's future, he says, has been "going on for some time."

When the country's leaders unveiled the one-child policy in an open letter to members of the Communist Party and Communist Youth League on 25 September 1980, the intervention was not meant to last forever. They foresaw a life span of one generation, explaining that "in 30 years, when the problem of population growth that is especially serious at present has been mitigated," the government could adopt a new policy.

Now, as children of the one-child generation marry and have babies, Wang and his colleagues are taking their campaign public to draw attention to that expiration date. In recent months, they have held seminars, published widely in the Chinese press, and released a study showing that many couples in one part of China are choosing to have only one child, even when given the chance to have another—evidence, they say, that the one-child policy is obsolete.

They have their work cut out for them. They're up against decades of bad science, central government leaders preoccupied with short-term stability, and a bureaucracy of staggering proportions: the National Population and Family Planning Commission, a half-million-person-strong agency responsible for implementing the one-child policy. The quest is taking longer than expected, says Gu Baochang, a demographer at Renmin University in Beijing and former adviser to a Family Planning Commission minister. But his group has a powerful ally: empirical evidence. "We went into the field," Gu says.

## Birth police

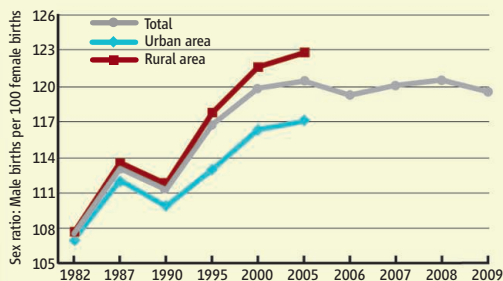
In the 1970s, China emerged from the Cultural Revolution with the memory of famine still acute. Poor central planning had helped cause food shortages, but now attention focused on population as the culprit, and Chairman Mao Zedong, who had once encouraged large families, shifted course.

He wasn't alone in worrying about population growth. In Western countries, too, public health breakthroughs and falling mortality rates had led to a fear of overpopulation, sparking a wave of neo-Malthusianism that culminated in the controversial 1972 report *The Limits to Growth* by the Club of Rome, an international group of scientists. Doomsday projections found their way to China. "Developed countries spread Club of Rome thinking to the developing world," says Liang Zhongtang, an economist at the Shanghai Academy of Social Sciences who participated in deliberations over the one-child policy.

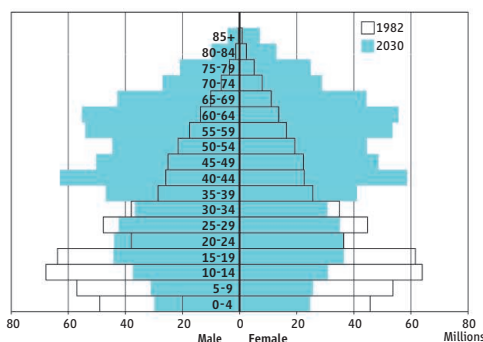
In China, neo-Malthusianism resonated with a government intent on boosting economic growth. The aim was to manipulate population dynamics under the planned economy. China experimented with birth planning throughout the 1970s, when the government pushed a "later, longer, fewer" approach that encouraged Chinese to marry later, wait longer between children, and have fewer babies. As a result, according to World Bank estimates, the country's total fertility rate declined from 5.5 in 1970 to 2.7 in 1979.



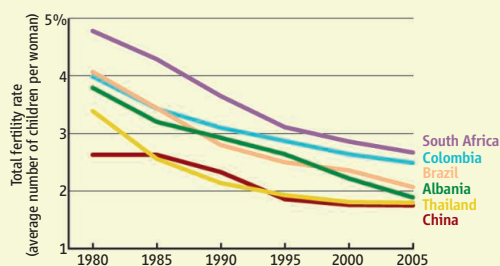
## Too Many Boys?



## A Graying Population



## Having Fewer Babies Anyway



**Serious consequences.** Chinese couples' desire to make their one child a son has led to sex-selective abortions, skewing the sex ratio (*top*). Declining fertility rates will result in a lopsided age structure by 2030 (*middle*); other countries saw similar drops without strict birth planning (*bottom*).

SOURCES: (TOP TO BOTTOM) SHUZHUO LI; CAI YONG/UNIVERSITY OF NORTH CAROLINA; WORLD BANK

The advocacy group calls this the “golden age” of China’s fertility transition: a successful, moderate policy with a low impact on age structure and sex ratio at birth. But at the time, the country lacked trained demographers who could point to the wisdom of staying the course. So when missile scientists put forth wild projections of a population explosion by 2080 (see sidebar, p. 1460), policymakers responded with an extreme plan.

The one-child policy was a group decision reached under Deng Xiaoping, China’s paramount leader from 1978 to 1992. The open letter called for bringing China’s natural growth rate, or the difference between its

crude birth and death rates, down to 0.5% by 1985—a precipitously low goal for a young country.

To implement the policy, the government beefed up its birth planning infrastructure, adding thousands of workers and launching propaganda campaigns. Enforcement was flawed from the beginning: The central government assigned stringent birth quotas to local governments but left them to shoulder a portion of the costs. Some local officials intent on meeting targets forced pregnant women to abort and sterilized men against their will. Others issued offending parents outrageous fines to recover program costs.

The drive sparked a backlash, fueling discontent among peasants. It also led to a rash of female infanticide among Chinese hoping to make their sole child a boy—a prelude to sex-selective abortions that later became widespread. The central government responded in 1984 by issuing *Document 7*, which handed provincial governments the power to adapt the policy to local circumstances.

That decentralized structure, which still stands, has yielded a clunky policy that is comparable in complexity to the U.S. tax code, says Wang. To discourage sex-selective abortion, many provinces allow rural parents whose first child is a girl to try again for a boy, an exception sometimes called the “1.5-child policy.” All told, there are 22 exceptions qualifying a couple for more children, ranging from one partner being disabled to one being a miner. The policy’s intricacies help explain, in part, why few within China’s scientific community tried to combat it for the first half of its life. Then in the late 1990s, a generation of young scholars trained abroad came of age, and China finally had world-class demographers. They began to speak up.

China’s rapidly aging population was an early theme. The country has benefited from a “demographic dividend”—a surfeit of young workers born during a 1960s baby boom—that will dry up as China gets old before it gets rich. From 2010 to 2020, the number of Chinese aged 20 to 24 will drop by a whopping 45%, from 125 million to 68 million. “The U.S., Japan, and Europe are talking about a pension crisis,” says Cai Yong, a demographer at the University of North Carolina, Chapel Hill, and a member of the advocacy group. “China’s situation is going to be much worse, because it will happen at a faster pace and with much less cushion.”

Other scholars turned their attention to the skewed sex ratio at birth. Shortly after the one-child policy was introduced, ultrasound machines became widely available across China, allowing pregnant women to scan the sex of their fetuses and abort females. The government outlawed sex identification and sex-selective abortion, but enforcement took a back seat to birth targets, and local officials often looked the other way when late-term pregnancies ended inexplicably. China’s ratio of male to female births—now 119 boys born for every 100 girls—has been “really intensified by the family-planning policy,” says Shuzhuo Li, a demographer at Xi’an Jiaotong University. The gender imbalance is projected to yield 30 million more men than women by 2030, heightening the risk of social instability.

Such concerns spurred the advocacy group’s formation in 2000. The time was ripe for a full-scale critique. The expiration date laid out by the open letter was nearing, allowing the scholars and former officials to argue that by pushing for the policy’s abolition, they were remaining true to its architects’ original vision. But the deadline also led to a new question: What next?

## Baby boom time?

The group coalesced from conversations among Wang, Gu, Peking University demographer Guo Zhigang, and others. Eventually, their discussions turned on what would happen demographically if the policy were lifted.

Government leaders assumed that the one-child policy had avoided hundreds of millions of births, and that if it were relaxed it would lead to a baby boom that would strain schools, hospitals, and the future job market. But China’s shrinking birthrate had coincided with a rapid drop in fertility rates in many other developing countries. From 1970 to 1990, World Bank data shows that China’s fertility rate fell from 5.5 to 2.3, Thailand’s

dropped from 5.6 to 2.1, and Brazil’s from 5.0 to 2.8. The scholars suspected that the one-child policy was not primarily responsible for China’s rapid

fertility drop. But they wanted tangible evidence, one way or the other.

In 2001, they called together experts for a meeting here. Some participants objected to the coercion and human-rights abuses carried out in enforcing the policy. (Forced abortions had become rarer, but they still occurred in isolated areas.) Others worried about how the sex ratio at birth and lopsided age struc-

## Online

sciencemag.org

Podcast interview with author Mara Hvistendahl.

ture might affect the country's stability. Still others believed birth planning remained necessary but that China needed to overhaul its existing policy.

In the years that followed, Gu, Wang, Guo, and retired Family Planning Commission official Zhang Erli collected data from all of China's 450 prefectures. Wading through the 22 policy exceptions, they calculated how many couples in each prefecture were eligible to have more than one child. They found that the

term "1.5-child policy" was misleading; 63% of couples were still restricted to one.

A thornier question was the actual fertility rate. China's 1992 National Fertility Survey found a total fertility rate for the previous year of 1.65 children per woman. When all the exceptions are taken into account, the policy implies a target rate of 1.47, and the 1992 figure meant China was close to achieving that. But over the following decade, political incentives for concealing further declines grew,

because continuing the one-child policy rested in part on a high fertility rate. In recent years, even as Chinese left farms in droves and settled into middle-class lifestyles, China's reported total fertility rate went up—supposedly to account for couples who had second children and did not register them. In 2009, U.N. estimates drawn from a government survey listed a rate of 1.77 children per woman.

By comparing official statistics with school registration data and other methods of retroactively estimating births, Gu and colleagues determined that the Family Planning Commission's fertility rates were inflated by an average of 25%. China's actual fertility level, Gu says, is closer to 1.5, putting it between those of countries like Switzerland and Canada.

Even as they claim a high birthrate, Chinese officials argue that 3 decades of birth planning have avoided 400 million births—a number touted at last year's climate summit in Copenhagen as one of China's environmental contributions. The advocacy group says this figure assumes China's fertility rate had stayed at its 1970 level instead of falling steadily over the 1970s. The actual number of births avoided over 30 years is closer to 100 million, says Cai.

The advocacy group now had evidence to debunk critical arguments used in defense of the policy: that most Chinese were no longer subject to the policy and that it had not yet achieved its goal. They assumed leaders would respond to empirical reasoning. But the policy is "not rational," asserts Joan Kaufman, a former Ford Foundation and U.N. Population Fund representative in China who has advised the group. Criticizing it is tricky, she warns: "They're all operating at a certain amount of professional risk."

### Overcoming inertia

In 2004, the advocacy group distributed a report detailing its findings within the Family Planning Commission and other agencies. The document, whose 18 signatories included the former head of statistics for Shanghai's family-planning commission, the vice president of the Shanghai Academy of Social Sciences, and seven directors of university demography programs, detailed the results of the group's years of fact-finding. Graphs depicted the aging population and skewed sex ratio at birth in stark detail.

The group hoped the proposal would lead to experimental zones in which couples could have two children. Instead, the government response, says Gu, was "not very

## Of Population Projections and Projectiles

China's one-child policy may appear to be a case of ideology trumping science. But the policy was based on the projections of a 1970s missile scientist and adopted in an atmosphere of renewed faith in empiricism and openness to the West.

A key figure in the policy's adoption was Song Jian, a Soviet-trained military scientist and specialist in cybernetics, or the control of machine systems. A former People's Liberation Army soldier, Song was a protégé of Qian Xuesen, Mao Zedong's trusted science adviser. Qian's backing helped Song rise to an influential post in China's Ministry of National Defense.

From his perch in the Seventh Ministry of Machine Building, a missile laboratory, Song moved into the unlikely field of population analysis—in part because other Chinese scientists had been persecuted during the Cultural Revolution. Sociology and demography were "essentially demolished under Mao," explains Susan Greenhalgh, an anthropologist at the University of California, Irvine, who outlines Song's story in the book *Just One Child: Science and Policy in Deng's China*. But "most defense scientists were able to continue working."

Beginning in 1970, China encouraged late marriage and childbirth spacing and asked couples to stop at two children. The approach was remarkably effective, halving China's birthrate over the next decade. However, says Greenhalgh, China's leaders wanted to be on par with the industrialized world—by reducing the number of mouths they had to feed.

A critical moment came in 1975, when Song joined a Chinese delegation to Europe. At the University of Twente in Enschede, the Netherlands, he met Geert Jan Olsder, a specialist in differential game theory. Over beers at a pub, Olsder told Song about a series of equations he had developed to control population on a fictional island. The key variable, calculated per time unit, was number of births. "He immediately became enthusiastic," recalls Olsder, who says his equations were theoretical. Olsder gave Song a paper explaining the equations, *Population Planning: a Distributed Time Optimal Control Problem*.

Song put the methods of Olsder and other European mathematicians to use. By 2080, they predicted, China's population would top 4 billion—a projection resting on unreliable data, says Greenhalgh. But it wowed Chinese leaders, propelling them toward another of the team's prognoses: that the only way to avert catastrophe was to reduce fertility to one child by 1985 and maintain that level for 20 to 40 years.

Liang Zhongtang, a Shanghai Academy of Social Sciences economist who took part in early discussions about the one-child policy, corroborates much of Greenhalgh's account but says she assigns too much importance to Song. "Many people felt the one-child policy was China's only choice at the time," says Liang, who was among the plan's few critics in the 1970s. Song's group provided data to justify the policy, Liang says, but they "weren't the ones who came up with it." He agrees, however, that Song's calculations dazzled policymakers, making the policy appear to be good science.

Song went on to become president of the Chinese Academy of Engineering. Olsder says the two kept in touch, last meeting in the Netherlands in 2004, but he never realized the role he had inadvertently played in the adoption of the one-child policy until a journalist alerted him to Greenhalgh's book in 2008.

—M.H.



**Population bomb maker.** Missile scientist Song Jian, shown here with Geert Jan Olsder (right) in 2004.







成员名单



PUBLIC HEALTH

## No Vaccines in the Time of Cholera

The threat of a major cholera epidemic looms over flood-stricken Pakistan. So why is a new, relatively cheap vaccine unlikely to make a difference?

With millions of people homeless, clean drinking water in short supply, and the infrastructure in tatters, water-borne diseases are one of the biggest threats in the Pakistani regions ravaged by floods. Experts are particularly worried about cholera, a disease that can cause explosive and lethal outbreaks. So you'd think this is the time to deploy the inexpensive new oral cholera vaccine, produced especially for the developing world in neighboring India by a company called Shantha Biotechnics.

But you'd be wrong.

The International Vaccine Institute (IVI) in Seoul, which helped develop the vaccine, is lobbying for production to be ramped up, and Shantha says it is ready to do so. But so far, the Pakistani government has no plans for a mass vaccination campaign, and the World Health Organization (WHO) does not advocate one. Vaccinating millions of homeless people would be an "extreme challenge" for the country's overburdened health system, says WHO spokesperson Paul Garwood. One key problem: The vaccine requires two doses, given 2 weeks apart, which is nearly impossible to do in a massive population on the move, says Garwood.

The debate is just the latest in an ongoing tussle about exactly how useful the new vaccine, called Shanchol—and an older, more expensive vaccine called Dukoral—is. In 2008–09, WHO came under fire for not using vaccines to help control a massive cholera

outbreak in Zimbabwe. IVI Director John Clemens—who has worked on cholera vaccines for a quarter-century—says immunization could have made a big difference in the 11-month outbreak, which claimed more than 4000 lives. But WHO and aid organizations say that a rapid vaccination campaign was not feasible in the impoverished nation.

Even the use of Shanchol under nonemergency circumstances is debated. Developed for the world's poorest, the vaccine costs only \$3.70 for two doses. That may not be much, but it doesn't make the shots a shoo-in for endemic countries and foreign donors. There are other control options, such as improving access to clean water, which helps prevent a panoply of diseases. And the cholera vaccine has to compete with vaccines for other agents, such as pneumococcus and rotavirus, that promise more bang for the buck than a cholera vaccine. Even India, the only country where Shanchol is available on the private market, doesn't have plans yet for a government-run vaccination campaign. "We are very disappointed," says Raman Rao, Shantha's vice president for R&D.

### Fast and violent

Whether a major cholera outbreak is imminent in Pakistan—or already under way—is difficult to say. More than 600,000 people have sought treatment for acute watery diarrhea, but little testing has been done to confirm the

cause. So far, WHO has not received formal reports of cholera from the Pakistani government, says Garwood. But Zulfiqar Bhutta of the Aga Khan University in Karachi says his enteric diseases lab has found cholera in over 50% of samples from diarrhea patients in the Khairpur District and has notified the government and WHO.

Although it's the massive outbreaks that make headlines, cholera kills many more people in smaller outbreaks in the more than 50 endemic countries. Some 4000 to 6000 deaths are reported to WHO annually, but most experts believe the true number is at least 100,000 and rising. Death from cholera can be fast and violent. When it colonizes the gut, *Vibrio cholerae* produces a toxin that causes massive leakage of water and electrolytes into the small intestine. In extreme cases, the resulting dehydration kills patients within 6 hours after the first symptoms.

Scientists started making cholera vaccines in the 19th century by injecting killed *V. cholerae*. But studies in the 1960s showed that these offered modest protection at best and had considerable side effects; WHO stopped recommending them in 1973. Since then, the focus has been on oral vaccines, which trigger immunity where *V. cholerae* attacks: in the gut.

Dukoral, developed in the 1970s by Jan Holmgren of the University of Gothenburg in Sweden, consists of killed *Vibrio* microbes,



**Troubled water.** Boys in a flooded village in Pakistan search for drinking water.

plus the so-called B-subunit, a part of the microbe's toxin protein produced via recombinant DNA technology. Studies have shown that the vaccine offers about 85% protection. The downside is that protection from cholera drops rapidly, so a booster shot is required every 2 years.

Although Holmgren's dream was to develop a vaccine for the developing world, and major phase III trials were done in slums in Bangladesh and with the Peruvian military, Dukoral has remained a "traveler's vaccine" for people from rich countries. Its cost—upward of \$40 in Western countries—is prohibitive in the developing world. And because the B-subunit easily disintegrates in the stomach, vaccinees have to swallow 150 milliliters of a raspberry-flavored buffer solution—an addition that makes the vaccine bulky and expensive to ship.

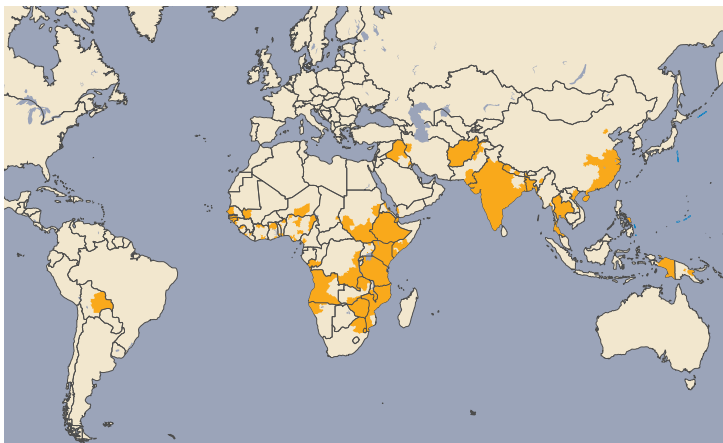
In the late 1980s, Dang Duc Trach, then deputy director of the National Institute of Hygiene and Epidemiology in Hanoi, decided to make a cheap cholera vaccine for use in Vietnam. Because the recombinant subunit was too expensive to produce, the killed cells alone would have to do the job, Trach reasoned. The Swedish government and Holmgren helped transfer the technology to Hanoi, where a company called VA Biotech now makes the vaccine. It has been given to about 20 million Vietnamese children at risk in annual campaigns.

Initially, it wasn't clear how well it worked. But in mid-1990s, IVI's Clemens, then at the U.S. National Institutes of Health, accepted Trach's invitation to see the program up close. He discovered that Trach had carried out a big efficacy study in 1992 that had never been published. "It was just sitting there in a drawer," says Clemens. "We thought, we've got to get this into print." The result was a 1997 paper in *The Lancet* showing that two doses of the vaccine provided about 66% protection.

Shanchol is the result of Clemens's tireless efforts to reproduce the Vietnamese recipe internationally. A team at IVI, which has its own lab in Seoul, refined the Vietnamese vaccine and adapted it to currently circulating strains and then transferred the technology to Shantha in Hyderabad. An interim analysis of a phase III trial among 70,000 people

in Calcutta, published last year, showed that Shanchol protects as well as the Vietnamese vaccine. India's regulatory agency approved the vaccine last year, and it has been submitted for approval to WHO; that would open the doors to use in many other countries.

For the current crisis in Pakistan, Shantha's parent company, Sanofi Aventis in France, has offered 74,000 doses for free. But with millions of people at risk, that's a drop in a bucket, says Claire-Lise Chaignat, head of WHO's Global Task Force on Cholera Control; ethical decisions about who gets the vaccine will be tricky, she says. And emergency vaccination campaigns can be very difficult, she adds: After the 2004 tsunami, a campaign to vaccinate people in the Indonesian province of Aceh with Dukoral took 6 months—4 months longer than planned—and cost more than \$8 per person, not counting the cost of the vaccine itself.



**Disease of poverty.** Cholera—reported in these areas between 2007 and 2009—strikes primarily people without access to clean drinking water and sanitation.

But Clemens says Aceh was an extreme case and that vaccination in Pakistan would be easier. "I would love for WHO to set up an emergency meeting of experts to come up with vaccination strategies," he says. Not vaccinating in cholera hot spots is a "high-risk gamble," adds Bhutta, who's also a member of WHO's Strategic Advisory Group of Experts on Immunization.

### Competition

Using the vaccine in regular vaccination campaigns—without the chaos of war or natural disasters—is far easier, but even then, researchers would need to prove that Shanchol is worth the money. Cholera is notoriously unpredictable, and in many endemic countries, the annual number of cases is too low to warrant mass vaccination. Moreover, governments and donors need to spend their money wisely, and drilling wells to improve the water

supply or providing people with filtering systems at home may prevent more cases at the same cost and protect against other diseases as well.

To help make the case for Shanchol, IVI has hired economist Dale Whittington of the University of North Carolina, Chapel Hill, to perform cost-benefit analyses. In a paper last year, Whittington compared vaccination scenarios in cities in Bangladesh, Indonesia, India, and Mozambique. He found that in most instances, vaccination would be "cost effective" under the arbitrary but often-used criterion that the cost of every life-year saved is less than three times the gross domestic product per capita in that country.

The analyses are based on complex models, however, and small changes in the underlying assumptions can make a big difference. One reason the vaccine does well in the analyses is that researchers believe there is a big

"herd immunity" effect: From a reanalysis of the 1980s study of Dukoral in Bangladesh, researchers concluded in 2005 that even if only half of the population gets vaccinated, the total number of cases drops by 93%. Whether this will hold up in other parts of the world is an open question, however.

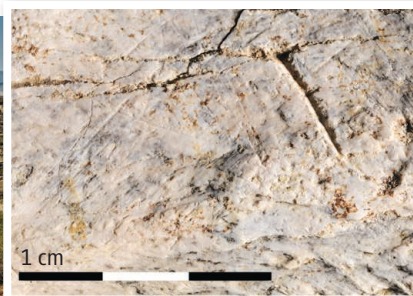
What's more, Shanchol has to compete for donor and country support with new vaccines against several other diseases. The Global Alliance for Vaccines and Immunisation, for instance, has decided not to fund cholera vaccines until at least 2013, choosing to focus

instead on new vaccines against pneumococcus and rotavirus—two major childhood killers—which it expects to be a better investment. Other donors have yet to step forward.

What the world really needs is a good one-dose vaccine, says Chaignat. IVI and Shantha hope to start a trial in Calcutta next year to see if Shanchol offers reasonable protection after just a single dose. IVI is also working on a new vaccine candidate, called Peru-15, which consists not of killed but of live, weakened *Vibrio*. But it could easily be another decade before it hits the market, says Clemens. "We can't let the perfect be the enemy of the good."

Still, he says he's not discouraged by the lack of enthusiasm for the current vaccines. "I've been working on this for 25 years, and I have seen several situations where these vaccines could have been used," Clemens says. "I have become a patient man. I think it will happen."

—MARTIN ENSERINK



**Hunting haven?** Cut marks on animal bones (*inset*) suggest that Olduvai Gorge hominins weren't scavengers.

## Score One for Hunting at Olduvai

Many anthropologists think meat eating was essential for the evolution of bigger human brains (*Science*, 15 June 2007, p. 1558). But were early humans mighty hunters, or did they get their pound of flesh from scavenging carcasses left behind by carnivores such as hyenas? The answer has implications for everything from our ancestors' subsistence strategies to their social structure.

Louis Leakey, who with his wife, Mary, excavated Tanzania's fossil-rich Olduvai Gorge in the 1950s and '60s, concluded from finds of human and animal bones closely associated with stone tools that hominins had been active hunters there at least 1.8 million years ago. But beginning in the late 1970s, other scientists began to argue that the pat-

terns of cut marks and tooth marks on the animal bones were more consistent with scavenging (*Science*, 25 May 1984, p. 861).

The argument is far from settled. Over the past several years, two teams currently working at Olduvai, one led by prehistorian Manuel Domínguez-Rodrigo of Complutense University of Madrid and the other by anthropologist Robert Blumenshine of Rutgers University in New Brunswick, New Jersey, have sparred in journals over the issue. In Paris, the hunting partisans, led by Domínguez-Rodrigo, fired their latest salvo.

Domínguez-Rodrigo presented evidence from a 1.3-million-year-old Olduvai site called BK—which was explored but not fully

excavated by the Leakeys—that, he says, argues against the scavenging hypothesis. Adding new data to an argument presented in the *Journal of Human Evolution* (*JHE*) last year, Domínguez-Rodrigo reported an analysis of more than 1000 pieces of animal bone from four hominin occupation layers at BK, including the remains of about 30 wild cattle from the genus *Pelorovis* and two *Sivattherium*, a large ruminant related to the giraffe. Both of these now-extinct animals weighed at least 400 kilograms. The team found 181 bones with cut marks apparently made by hominins and 172 percussion marks from hammering on the bones with stones or other objects, but only 45 carnivore tooth marks. Moreover, Domínguez-Rodrigo said at the meeting, the cut marks, especially on the cattle, were all over the animals' bodies, suggesting that the carcasses had been butchered whole by hominins at the BK site. If they had been scavenged, only the meatiest parts of the carcasses would have been transported to BK from carnivore kills farther away. "We are finding cut marks in anatomical areas that should not be found if hominins had only secondary access to the remains," Domínguez-Rodrigo said.

## Burying Man's Best Friend, With Honor

Dogs are famously loyal to their masters, and many dog owners repay this loyalty by burying their pets carefully in backyards or in pet cemeteries. According to the first-ever systematic literature survey of dog burials, this practice may have roots deep in prehistory. In a talk greeted enthusiastically, graduate student Angela Perri of Durham University in the United Kingdom suggested that the practice might be correlated with the use of dogs as hunting partners when the world warmed in the post-Ice Age Holocene period about 10,000 years ago.

Researchers have debated just when dogs were domesticated, but most agree that it had happened by 14,000 years ago. Yet the earliest dog burials are dated only to about

9000 years ago, at least a millennium after the Holocene began. So far Perri has identified more than 400 sites that comprise a total of more than 1200 reported dog burials. To be sure that she counts only instances when dogs were given special treatment in their own right and weren't incidental to human internments, Perri is considering only "primary" burials, during which dogs were buried separately from humans or other animals. For example, at the famous 7000-year-old site of Skateholm in Sweden, hunter-gatherers dug a pit and arranged a dog in it on its side (see photo); there were several such burials at that site.

So far Perri has come up with 263 cases, all clustered in three geographic areas: the southern United States, northern Europe, and Japan. In each area, Perri said at the meeting, primary dog burials came to an end in prehistory once agriculture was adopted,

even though farming appeared at different times in each region. Perri is now exploring the hypothesis that dogs gained special status as hunting partners when forests in these areas expanded in the Holocene warmth, and



**Top dog.** Prehistoric hunter-gatherers at Skateholm in Sweden buried their canines carefully.



As for who was doing the hunting, Domínguez-Rodrigo said that during the 2010 field season the team found some skeletal remains tentatively identified as *Homo ergaster*, the African version of *H. erectus*. How the BK hominins, who were armed with stone tools such as flakes, handaxes, and hammerstones, hunted these imposing beasts is unclear, but Domínguez-Rodrigo noted that they might have cornered the animals rather than chased them across the landscape. And he suggested that by 1.3 million years ago, cultural and demographic changes, such as larger social groups, might have enhanced their ability to hunt larger animals.

Sabine Gaudzinski-Windheuser, an archaeozoologist at Johannes Gutenberg University in Mainz, Germany, says that Domínguez-Rodrigo made a “convincing case” that hominins did indeed hunt at Olduvai. Scavenging proponents were not at the meeting, including Blumenshine, who was in the field and could not be reached for comment. But anthropologist James O’Connell of the University of Utah in Salt Lake City—who has debated the issue with Domínguez-Rodrigo in the pages of *JHE*—told *Science* he’s not persuaded by the new bone analyses. He says they do not rule out “aggressive scavenging,” in which hominins chase off the predators that killed a large animal and take the carcass. Living hunter-gatherers, such as the Hadza people of Tanzania, acquired much of their meat in just this way, he notes, citing studies by him and others. The debate is likely to go on as new data accumulate; Domínguez-Rodrigo said his team will continue digging at BK “for quite a few years.” —M.B.

forest prey became available to their hunter-gatherer masters. But when hunter-gatherers turned to farming, the role of the dog might have been downgraded or shifted.

Although Perri stressed that her work is preliminary, she was peppered with queries about various burials during the question-and-answer session and mobbed by researchers wanting to talk after she stepped down. “It is very interesting that no one has seen this pattern or suggested this hypothesis before now,” says archaeologist Virginia Butler of Portland State University in Oregon. “It is a great example of [archaeological] records ... staring us in the face, but we simply didn’t put all the pieces together.” Butler adds that if the geographic pattern holds up, climate change and human adaptations to it, rather than local cultural practices, might explain the rise and fall of dog burials in prehistory. —M.B.



Climate clues. Excavations at Syria’s Tell Sabi Abyad show changes in animal use after 8200 B.P.

## In a Cold Snap, Farmers Turned to Milk

Today, the threat of global warming hangs over humanity and our planet, but prehistoric humans often faced the opposite problem: global cooling (*Science*, 22 January, p. 404). One much-discussed climate event took place about 8200 years ago, when a sudden shift of North Atlantic currents plunged the Northern Hemisphere into a short cold and dry spell. Many researchers have argued that this so-called 8200 B.P. event affected cultures around the globe, in different ways depending on locale.

But the evidence has not been clear-cut, and archaeologists have long debated the role of climate, in part because few sites offer a continuous record before and after 8200 B.P. At the meeting, archaeologist Anna Russell of Leiden University in the Netherlands presented what is perhaps the best case yet for the cold snap’s effect on human activity, finding a marked shift in how farmers at a site in northern Syria exploited animals after 8200 B.P.

The 8200 B.P. event was short-lived—perhaps no more than 200 years—but it shows up in Greenland ice cores and other proxy indicators of climate change, lowering winter temperatures an estimated 2° to 4°C and triggering aridity throughout the Northern Hemisphere. In the Near East, where agriculture was getting started, archaeologists have found tantalizing suggestions of the event’s impact: New farming sites sprout in central Turkey, although they are relatively small, and on Cyprus farming disappears entirely for a millennium. Meanwhile, farmers began for the first time to move into southeastern Europe, possibly seeking more favorable conditions.

To explore the event’s effects, Russell

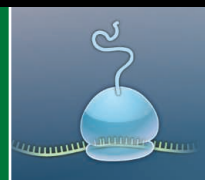
analyzed 15,000 animal bones from the early farming site of Tell Sabi Abyad, where Leiden archaeologist Peter Akkermans leads excavations. The site was occupied between about 8900 and 7300 years ago and is one of the few to fully straddle the event.

Russell said at the meeting that after 8200 B.P., pig farming, which had been a major source of subsistence, gave way to cattle raising, and the number of domesticated sheep and goats rose. In addition, milk products—detected by traces of lipids in pottery—suddenly showed up in the archaeological record, and the number of spindles, used to spin animal fibers into textiles, increased as well. The people apparently began to rely more on so-called secondary products, such as milk and textiles, which can be stored longer and might have helped them cope in a time of climatic stress, Russell said.

She pointed out that a few other Neolithic sites in the Near East also show changes in subsistence around 8200 B.P. At Çatalhöyük in Turkey, for example, residents apparently abandoned one settlement and founded a smaller, less dense one across a river.

Archaeobiologist Melinda Zeder of the Smithsonian National Museum of Natural History in Washington, D.C., cautions that the 8200 B.P. event may have been one of a “wide range of factors”—including possibly increased social stratification—that led to changes in animal use. But archaeologist Virginia Butler of Portland State University in Oregon says that although she agrees that “correlation is not causation,” Russell’s talk was “a great example of trying to link changes in the faunal record to a known global [climate] event.”

—MICHAEL BALTER



## LETTERS

edited by Jennifer Sills

## Battling the Paper Glut

THE ACADEMIC COMMUNITY CONTINUES TO BELIEVE THAT THE FORMAL SCHOLARLY PUBLISHING process separates sound research from shoddy or biased counterparts. Unfortunately, scholarly publishing may not be able to effectively fulfill its role as a gatekeeper much longer.

As soon as the “publish or perish” concept (the imperative to publish work constantly to further or sustain an academic career) surfaced in the United States in the early 1950s, academics criticized it openly as a recipe for disaster (1, 2). Nevertheless, in the early to mid-1980s, administrators in universities systematically began to use the number of articles published per year by individual faculty members as a measure of their productivity.

The shift transformed scholarly publishing. Researchers began “salami slicing” their manuscripts in ever smaller “least publishable units” and began rushing manuscripts to publication before proper replication or evaluation of results. Multi-authored manuscripts increased, regardless of true contribution to the work. Doctoral students began to write dissertations as a series of publishable chapters, some submitted even before the defense. As a result, the quantity of articles published in scholarly journals increased on average by about 200 to 300% from the early 1980s to the late 1990s (3).

Researchers in countries such as China and India are subjected to a numbers game similar to that in the West, sometimes with the added incentive of monetary rewards for articles published in “top” journals. In 2008, China passed the United States to become the second scholarly producer (in total number of articles) after Europe.

Researchers have reacted to this publication glut by developing bibliometric indices, such as the h- and g-indexes, based on citation counts, to evaluate a researcher’s impact in their discipline. Perhaps these indexes do evaluate impact better than counting annual number of articles. However, in various ways, they also encourage researchers to publish more articles to directly inflate their own citations or to cite friends who then cite them in return.

The top journals now are flooded with numbers of manuscripts beyond most editors’ capacity to handle. Reviewers are solicited to scrutinize not just manuscripts but also research proposals and governmental reports. Yet, peer-reviewing is rarely, if ever, valued by academic institutions as a fruitful way for researchers to spend their time, so finding good reviewers has become more and more difficult.

Researchers need to fight to contain the current paper glut. The number of articles published per year should never be used, under any circumstance, as a criterion in tenure or promotion decisions, or to rank academic institutions. As the medical community proposed 25 years ago (4), researchers should never be allowed to include more than three publications per year in activity reports; in research proposals, principal investigators should cite no more than 10 papers. University administrators should consider peer-reviewing as not only legitimate, but a

vitaly important way for researchers to contribute to scholarship, and should reward it as such. One way to accomplish this would be a new generation of review impact indexes, based on information provided by publishers (3, 5). Effectiveness in peer-reviewing should be viewed as an essential skill to acquire for Ph.D. students, worldwide. Journals should demand that for every paper submitted, an author provide three reviews of other manuscripts. Perhaps if authors knew that their reviewing workload would increase dramatically with the number of papers they submit, they would craft fewer and better papers, ultimately benefiting all involved.

DONALD SIEGEL<sup>1\*</sup> AND PHILIPPE BAVEYE<sup>2</sup>

<sup>1</sup>Department of Earth Sciences, Syracuse University, Syracuse, NY 13244, USA. <sup>2</sup>SIMBIOS Centre, Abertay University, Dundee DD1 1HG, UK.

\*To whom correspondence should be addressed. E-mail: disiegel@syr.edu

## References

1. L. Hurt, *Coll. Engl.* **23**, 5 (1961).
2. R. W. Beard, *J. Higher Ed.* **36**, 455 (1965).
3. P. Baveye, *J. Scholarly Pub.* **41**, 191 (2010).
4. M. Angell, *Ann. Int. Med.* **104**, 261 (1985).
5. P. C. Baveye, J. T. Trevors, *Water Air Soil Pollut.*, 10.1007/s11270-010-0355-7 (2010).

## India’s Courteous Creativity

IN HIS EDITORIAL “IRREVERENCE AND INDIAN science” (30 April, p. 547), R. A. Mashelkar observes that Indian science lacks adventure and a spirit of questioning established ideas. He suggests that the situation has deep roots in Indian culture and tradition.

I disagree. Creativity can and does exist in a society that values decorum over irreverence, such as India. In fact, a healthy skepticism, an ability to be introspective, and an urge to revisit and reexamine existing ideas have always been part of India’s intellectual tradition. Take, for example, literary works known as bhashyas, which are commen-







Photons take  
a random walk

1477



Cognitive  
certainty

1478

taries or interpretations of classical works. Bhashyas contain interpretations from opposing perspectives by different commentators. The body of work, collectively known as Upanishads, is considered by many to be a collaborative exploration of knowledge by student and teacher. In a culture that usually gives an exalted position to the teacher, questioning authority is permissible, albeit with decorum.

Ideally, education should strike a balance between sound training in the fundamentals and motivation to critically question those fundamentals in order to advance knowledge. C. V. Raman (who discovered the Raman effect), Megnad Saha (distinguished astrophysicist), and Jagdish Chandra Bose and Satyen Bose (both renowned physicists), who functioned during the Indian colonial rule, were not only well trained in the fundamentals of science but also capable of questioning established ideas. It is not clear that the lack of an adventurous spirit in modern Indian science, or for that matter, in the humanities and the social sciences, can be readily attributed to India's cultural roots.

T. N. NARASIMHAN

Department of Materials Science and Engineering, University of California at Berkeley, Berkeley, CA 94720-1760, USA. E-mail: tnnarasimhan@LBL.gov

## Archaeology Augments Tibet's Genetic History

T. S. SIMONSON *ET AL.* ("GENETIC EVIDENCE for high-altitude adaptation in Tibet," Reports, 2 July, p. 72) and especially X. Yi *et al.* ("Sequencing of 50 human exomes reveals adaptation to high altitude," Reports, 2 July, p. 75) estimate that the genetic divergence of Tibetan populations with unique high-altitude adaptations occurred as late as ~2750 years ago. We have investigated this same problem from an archaeological perspective. Our results partly support the genetic-based scenario but suggest some contradictions between the two data sets. We currently have no evidence of permanent occupations on the Qinghai-Tibet Plateau before the middle Holocene, ~7000 years before the present (yr B.P.) (1), contrary to claims of occupations as old as 30,000 yr B.P. (2, 3). Mobile foragers did exploit the Plateau mar-

gins up to 3300 m by ~15,000 yr B.P. (4). Directly dated sites documenting human presence above 4000 m are younger still, at ~11,000 to 8000 yr B.P. (1). These early sites represent intermittent, seasonal occupations by populations who most likely spent much of their time at lower elevations. Foragers may have established more permanent occupations on the Plateau margins as high as 3300 m after ~7000 yr B.P. (5-7), but these groups interacted extensively with agricultural populations in low-elevation environments. Year-round occupation above 4000 m likely became possible only after 4000 yr B.P. with the emergence of dedicated pastoralist adaptations centered on domesticated yaks (6, 8). If the genetic traits suggested by Simonson *et al.* and Yi *et al.* evolved in response to selection on populations living exclusively above 4000 m, then the genetic divergence dates of ~2750 yr B.P. reasonably agrees with the archaeological evidence. If selection for these traits occurred among populations below 4000 m (2), where most Tibetans currently

live, then more complex population dynamics are indicated. Understanding the archaeological chronology behind the peopling of the Qinghai-Tibet Plateau is critical to evaluating the tempo of selection operating on contemporary human populations.

P. JEFFREY BRANTINGHAM,<sup>1\*</sup> DAVID RHODE,<sup>2</sup> DAVID B. MADSEN<sup>3</sup>

<sup>1</sup>Department of Anthropology, University of California, Los Angeles, Los Angeles, CA 90095, USA. <sup>2</sup>Desert Research Institute, Reno, NV 89512, USA. <sup>3</sup>Texas Archaeological Research Laboratory, University of Texas at Austin, Austin, TX 78758, USA.

\*To whom correspondence should be addressed. E-mail: branting@ucla.edu

### References

1. P. J. Brantingham *et al.*, in *Human Adaptation to Climate Change in Arid China*, D. B. Madsen, F. H. Chen, X. Gao, Eds. (Elsevier, Amsterdam, 2007), pp. 129-150.
2. C. M. Beall *et al.*, *Proc. Natl. Acad. Sci. U.S.A.* **107**, 11459 (2010).
3. M. Zhao *et al.*, *Proc. Natl. Acad. Sci. U.S.A.* **106**, 21230 (2009).
4. D. B. Madsen *et al.*, *J. Archaeol. Sci.* **33**, 1433 (2006).
5. M. S. Aldenderfer, in *Human Adaptation to Climate Change in Arid China*, D. B. Madsen, F. H. Chen, X. Gao, Eds. (Elsevier, Amsterdam, 2007), pp. 151-165.
6. D. Rhode *et al.*, *J. Archaeol. Sci.* **34**, 600 (2007).
7. D. Rhode *et al.*, *Quat. Int.* **218**, 29 (2010).
8. R. K. Flad, J. Yuan, S. C. Li, in *Human Adaptation to Climate Change in Arid China*, D. B. Madsen, F. H. Chen, X. Gao, Eds. (Elsevier, Amsterdam, 2007), pp. 167-203.

## Response

WE THANK BRANTINGHAM *ET AL.* FOR THEIR interest in our study; we agree that both molecular and archaeological evidence should be

## CORRECTIONS AND CLARIFICATIONS

**News Focus:** "From pigs to people: The emergence of a new superbug" by D. Ferber (27 August, p. 1010). Tara Smith's affiliation is the University of Iowa in Iowa City.

**Reports:** "Down-regulation of a host microRNA by a *Herpesvirus saimiri* noncoding RNA" by D. Cazalla *et al.* (18 June, p. 1563). The third author should have been listed as Joan A. Steitz. The correction has been made in the HTML version online.

**Reports:** "Evolution of an expanded sex-determining locus in *Volvox*" by P. Ferris *et al.* (16 April, p. 351). The legend for figure S12 (Alternative splicing of female and male MAT3) in the Supporting Online Material should include the citation A. Kianianmomeni *et al.*, *Plant Cell* **20**, 2399 (2008), which reported two instances of unregulated intron retention (corresponding to E1\_3.3, E3\_5.4) and one instance of unregulated alternative splice site usage (corresponding to E13\_16.5) in female MAT3. A revised Supporting Online Material has been posted online at [www.sciencemag.org/cgi/content/full/328/5976/351/DC1](http://www.sciencemag.org/cgi/content/full/328/5976/351/DC1).

**Reports:** "N-doping of graphene through electrothermal reactions with ammonia" by X. Wang *et al.* (8 May 2009, p. 768). After publication, the authors discovered that the graphene sheet (GS) sample used to take the x-ray photoelectron spectroscopy (XPS) and nanometer-scale secondary ion mass spectroscopy data in Fig. 4 was unintentionally oxidized by air from a leak that had not been detected during the experiment. The NH<sub>3</sub> annealing environment for the GS sample in Fig. 4 should be corrected to ~800 mtorr of NH<sub>3</sub> and an estimated partial pressure of oxygen of tens of millitorr.

Later, the authors found that as-made GSs annealed in NH<sub>3</sub> without any oxygen showed little n-doping within the detection limit of XPS, which is much lower than the doping level for the gas-phase-oxidized GS in Fig. 4. In a systematic study, they used XPS to observe n-doping and covalent N incorporation into the lattice of pre-oxidized GSs upon annealing in NH<sub>3</sub> [X. Li *et al.*, *J. Am. Chem. Soc.* **131**, 15939 (2009)]. They found that graphene oxide (with reduced oxidation and defect densities by stepwise thermal treatment) showed reduced n-doping levels upon NH<sub>3</sub> annealing [X. Li *et al.*, *J. Am. Chem. Soc.* **131**, 15939 (2009)], suggesting that the degree of n-doping scales with the degree of oxidation or concentration of defects in the graphene lattice.

The above findings are consistent with each other and do not change the main conclusions of the original publication—i.e., that annealing of graphene in NH<sub>3</sub> affords n-doping most likely at the edges and defect sites. The sample in Fig. 4 with unintended oxidation showed higher N signals than later samples without oxidation after similar NH<sub>3</sub> annealing, because gas-phase oxidation generated more defects and oxygen groups in the GS and increased its reactivity, allowing for large amounts of n-dopants to be incorporated into the GS. This finding is consistent with the authors' original suggestion and also shows that a higher defect density in graphene introduced by gas-phase oxidation allows for higher n-doping.

used to understand the demographic history of the Tibetan people. Our Report focused not on the demographic history of the Tibetan population, but rather the selection acting on specific putatively adaptive mutations segregating in the Tibetan population. We included some limited demographic analyses because they helped illuminate our results regarding natural selection. The real demographic model is clearly likely to be more complex than the simple models of two populations diverging from each other. For example, Zhao *et al.* (1) used mitochondrial DNA to argue that late settlers of the Tibetan plateau may not have entirely replaced the original population but that a small proportion of them carry mitochondrial DNA lineages tracing back to

Late Paleolithic inhabitants on the plateau. If this is the case, even if the EPAS1 variant was present in the early inhabitants of Tibet, strong selection would be needed to increase its frequency in the modern Tibetan gene pool. The understanding that the majority of the current population of the Tibetan plateau may trace their genetic ancestry back to quite recent immigrants into Tibet, even though humans have lived in Tibet for a much longer time—possibly with some continuity of culture—is important for understanding the difference between inferences based on archaeology and inferences based on genetics.

XIN YI,<sup>1,2</sup> YU LIANG,<sup>1,2</sup> EMILIA HUERTA-SANCHEZ,<sup>3</sup>  
XIN JIN,<sup>1,4</sup> ZHA XI PING CUO,<sup>2,5</sup> JOHN E. POOL,<sup>3,6</sup>  
XUN XU,<sup>1</sup> HUI JIANG,<sup>1</sup> NICOLAS VINCKENBOSCH,<sup>3</sup>  
THORFINN SAND KORNELIUSSEN,<sup>7</sup> HANCHENG  
ZHENG,<sup>1,4</sup> TAO LIU,<sup>1</sup> WEIMING HE,<sup>1,8</sup> KUI LI,<sup>2,5</sup>  
RUIBANG LUO,<sup>1,4</sup> XIFANG NIE,<sup>1</sup> HONGLONG WU,<sup>1,9</sup>  
MEIRU ZHAO,<sup>1</sup> HONGZHI CAO,<sup>1,9</sup> JING ZOU,<sup>1</sup> YING  
SHAN,<sup>1,4</sup> SHUZHENG LI,<sup>1</sup> QI YANG,<sup>1</sup> ASAN,<sup>1,2</sup> PEIXI-  
ANG NI,<sup>1</sup> GENG TIAN,<sup>1,2</sup> JUNMING XU,<sup>1</sup> XIAO LIU,<sup>1</sup>  
TAO JIANG,<sup>1,9</sup> RENHUA WU,<sup>1</sup> GUANGYU ZHOU,<sup>1</sup>  
MEIFANG TANG,<sup>1</sup> JUNJIE QIN,<sup>1</sup> TONG WANG,<sup>1</sup> SHUI-  
JIAN FENG,<sup>1</sup> GUOHONG LI,<sup>1</sup> HUASANG,<sup>1</sup> JIANGBAI  
LUOSANG,<sup>1</sup> WEI WANG,<sup>1</sup> FANG CHEN,<sup>1</sup> YADING  
WANG,<sup>1</sup> XIAOGUANG ZHENG,<sup>1,2</sup> ZHUO LI,<sup>1</sup> ZHUOMA  
BIANBA,<sup>10</sup> GE YANG,<sup>10</sup> XINPING WANG,<sup>11</sup> SHUHUI

TANG,<sup>11</sup> GUOYI GAO,<sup>12</sup> YONG CHEN,<sup>5</sup> ZHEN LUO,<sup>5</sup>  
LAMU GUSANG,<sup>5</sup> ZHENG CAO,<sup>1</sup> QINGHUI ZHANG,<sup>1</sup>  
WEIHAN OUYANG,<sup>1</sup> XIAOLI REN,<sup>1</sup> HUIQING LIANG,<sup>1</sup>  
HUISONG ZHENG,<sup>1</sup> YEBO HUANG,<sup>1</sup> JINGXIANG LI,<sup>1</sup>  
LARS BOLUND,<sup>1</sup> KARSTEN KRISTIANSEN,<sup>1,7</sup> YIN-  
GRUI LI,<sup>1</sup> YONG ZHANG,<sup>1</sup> XIUQING ZHANG,<sup>1</sup> RUIQ-  
IANG LI,<sup>1,7</sup> SONGGANG LI,<sup>1</sup> HUANMING YANG,<sup>1</sup>  
RASMUS NIELSEN,<sup>1,3,7\*</sup> JUN WANG,<sup>1,7\*</sup> JIAN WANG<sup>1\*</sup>

<sup>1</sup>BGI-Shenzhen, Shenzhen 518083, China. <sup>2</sup>The Graduate University of Chinese Academy of Sciences, Beijing 100062, China. <sup>3</sup>Department of Integrative Biology and Department of Statistics, University of California Berkeley, Berkeley, CA 94820, USA. <sup>4</sup>Innovative Program for Undergraduate Students, School of Bioscience and Biotechnology, South China University of Technology, Guangzhou 510641, China. <sup>5</sup>The People's Hospital of the Tibet Autonomous Region, Lhasa 850000, China. <sup>6</sup>Department of Evolution and Ecology, University of California Davis, Davis, CA 95616, USA. <sup>7</sup>Department of Biology, University of Copenhagen, DK-1165 Copenhagen, Denmark. <sup>8</sup>Innovative Program for Undergraduate Students, School of Science, South China University of Technology, Guangzhou 510641, China. <sup>9</sup>Genome Research Institute, Shenzhen University Medical School, Shenzhen 518060, China. <sup>10</sup>The People's Hospital of Lhasa, Lhasa, 850000, China. <sup>11</sup>The Military General Hospital of Tibet, Lhasa, 850007, China. <sup>12</sup>The Hospital of XiShuangBanNa Dai Nationalities, Autonomous Jinghong 666100, Yunnan, China.

\*To whom correspondence should be addressed. E-mail: wangjian@genomics.org.cn (Ji.W.); wangj@genomics.org.cn (Ju.W.); rasmus\_nielsen@berkeley.edu (R.N.)

#### Reference

1. M. Zhao *et al.*, *Proc. Natl. Acad. Sci. U.S.A.* **106**, 21230 (2009).

## Letters to the Editor

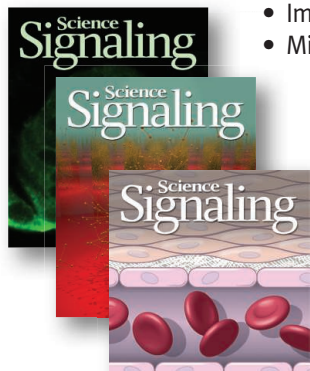
Letters (~300 words) discuss material published in *Science* in the previous 3 months or issues of general interest. They can be submitted through the Web ([www.submit2science.org](http://www.submit2science.org)) or by regular mail (1200 New York Ave., NW, Washington, DC 20005, USA). Letters are not acknowledged upon receipt, nor are authors generally consulted before publication. Whether published in full or in part, letters are subject to editing for clarity and space.

## Call for Papers

## Science Signaling

**Science Signaling**, from the publisher of **Science**, AAAS, features top-notch, peer-reviewed, original research weekly. Submit your manuscripts in the following areas of cellular regulation:

- Biochemistry
- Bioinformatics
- Cell Biology
- Development
- Immunology
- Microbiology
- Molecular Biology
- Neuroscience
- Pharmacology
- Physiology and Medicine
- Systems Biology



**Science Signaling** is indexed in CrossRef and MEDLINE.

Submit your research at:  
[www.sciencesignaling.org/about/help/research.dtl](http://www.sciencesignaling.org/about/help/research.dtl)

Subscribing to **Science Signaling** ensures that you and your lab have the latest cell signaling resources. For more information visit [www.ScienceSignaling.org](http://www.ScienceSignaling.org)

#### Chief Scientific Editor

**Michael B. Yaffe, M.D., Ph.D.**

Associate Professor, Department of Biology  
Massachusetts Institute of Technology

#### Editor

**Nancy R. Gough, Ph.D.**

AAAS

**Science Signaling**





## PSYCHOLOGY

# Performance Sapped by Stereotypes

William von Hippel

As a reader of *Science*, you probably regard yourself as intellectually curious and nonviolent. But what if others didn't see you that way? What if people doubted your intellectual capacity and were visibly anxious in your presence? How would you cope with this situation and what effect might it have on you? This is the problem that Brent Staples faced as a young African-American graduate student, when he noticed that people were afraid of him as he passed them on the street at night in Chicago's Hyde Park. Staples learned to escape this stereotype by whistling Vivaldi, a strategy that put passersby at ease and inspired the title of Claude Steele's new book on how stereotypes affect us.

In *Whistling Vivaldi*, Steele (a social psychologist at Columbia University) describes the groundbreaking work that he and his colleagues conducted over the past 20 years on stereotype threat, the psychological threat of confirming or being reduced to a negative stereotype. Empirical work on this topic began when Steele and Steve Spencer found that they could dramatically improve women's math scores simply by telling them that the test they were about to take shows no gender differences in performance [research described in (1)]. Steele and Joshua Aronson

then went on to show that the performance of black students could be similarly improved if they were told that a test was not a measure of intellectual achievement (2). Indeed, Steele and Aronson also found that African Americans performed more poorly on a challenging verbal test if they were first asked to indicate their race, thereby highlighting their stereotyped identity. This result was later extended by Margaret Shih and her colleagues, who found that Asian-American women did worse on a math test after indicating their gender but better after indicating their race (3).

As Steele takes pains to note, two surprising facts about stereotype threat are that members of any group can experience it and that there need not be a prejudiced perpetrator to cause it. Rather, it can be set off by subtle environmental cues, such as seeing very few members of one's own group in a performance setting. Steele describes feeling stereotype threat himself when in a Silicon Valley workplace where everyone else was twenty-something. The environment exuded youth through the music people played and the bicycles hung over the work cubicles, and these cues were enough to make Steele feel old and out of place. If Steele were employed in this setting, research on stereotype threat suggests that

his concerns about being stereotyped would likely consume valuable cognitive resources, resulting in poorer job performance.

As this example from the book indicates, people need only worry that others might stereotype them, and this worry alone can disrupt performance, despite (and sometimes because of) extraordinary efforts to prove the stereotype wrong. This worry can also lead

to long-term disengagement from stereotyped domains, as people tire of the Sisyphean task of continuously trying to prove that the stereotypes don't apply to them.

Superbly written and engaging, *Whistling Vivaldi* presents research on stereotype threat in the form of an historical narrative. Readers need no scientific

expertise to follow the story, and those who are already familiar with the research are likely to be intrigued by the events, ideas, and people that influenced theory development and experimentation. Despite the book's focus on the negative consequences of feeling stereotyped, Steele remains optimistic in his emphasis on how stereotype threat can be ameliorated. For example, he describes an intervention by Geoffrey Cohen and his colleagues in which students in racially integrated seventh-grade classrooms were randomly assigned to either reflect on their important values or discuss values that another person might find important (4). This former process, known as self-affirmation and based on Steele's earlier research (5), reduces the impact of a variety of different types of psychological threats. Cohen and colleagues thought that self-affirmation might ameliorate the stereotype threat experienced by African Americans in the classroom. Consistent with their reasoning, this brief affirmation reduced the gap between black and white students by 40% over the course of the term, and the benefit of this intervention was still apparent two years later.

In this sense, *Whistling Vivaldi* is a social scientist's dream, as the book demonstrates how slight changes in an individual's situation or experience can lead to dramatic reductions in the magnitude of various group differences that were (and often still are) portrayed as largely genetic and biological. Indeed, a recent meta-analysis (6) reveals that stereotype threat depresses the performance of women and minorities by more than a third of a standard deviation when they take difficult tests like the SAT—that's over 40 points on each section of a test that can determine admission or rejection at some of the most selective universities in the United States. Prior to Steele's theorizing

## Whistling Vivaldi

And Other Clues to How Stereotypes Affect Us

by Claude M. Steele

Norton, New York, 2010.

256 pp. \$25.95, C\$32.50.

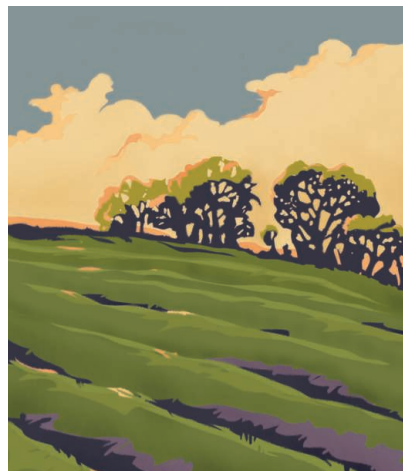
ISBN 9780393062496.

The reviewer is at the School of Psychology, McElwain Building, University of Queensland, St. Lucia, QLD 4072, Australia. E-mail: billvh@psy.uq.edu.au

## BROWSINGS

**The Field Guide to Fields: Hidden Treasures of Meadows, Prairies, and Pastures.** Bill Laws. National Geographic, Washington, DC, 2010. 224 pp. Paper, \$21.95, C\$26.95. ISBN 9781426205088. **Fields.** HarperCollins, London. £15.99. ISBN 9780007358199. Collins Field Guide.

Despite the title, this is not a field guide—the identification sections cover only a small, eclectic sample of flora and fauna. Instead, Laws celebrates the natural and human histories of rural landscapes where crops and animals have been (and are) raised. Rice paddies, water meadows, paddocks, vineyards, and plains of grain are among the pastoral scenes he offers armchair travelers while weaving aspects of culture, food, and folklore into the text. The artwork includes 25 expressive, full-page, woodcut-style illustrations, such as this depiction of a traditional ridge-and-furrow field.



and experimentation, none of us would have guessed that such small differences in instruction or setting could lead to such dramatic effects on performance.

#### References

1. S. J. Spencer, C. M. Steele, D. Quinn, *J. Exp. Soc. Psychol.* **35**, 4 (1999).
2. C. M. Steele, J. Aronson, *J. Pers. Soc. Psychol.* **69**, 797 (1995).
3. M. Shih, T. L. Pittinsky, N. Ambady, *Psychol. Sci.* **10**, 80 (1999).
4. G. L. Cohen, J. Garcia, N. Apfel, A. Master, *Science* **313**, 1307 (2006).
5. C. M. Steele, in *Advances in Experimental Social Psychology*, L. Berkowitz, Ed. (Academic Press, San Diego, CA, 1988), pp. 261–302.
6. H.-H. D. Nguyen, A. M. Ryan, *J. Appl. Psychol.* **93**, 1314 (2008).

10.1126/science.1194619

## TECHNOLOGY

# What Would A. G. Bell Say Now?

Marc Lavine

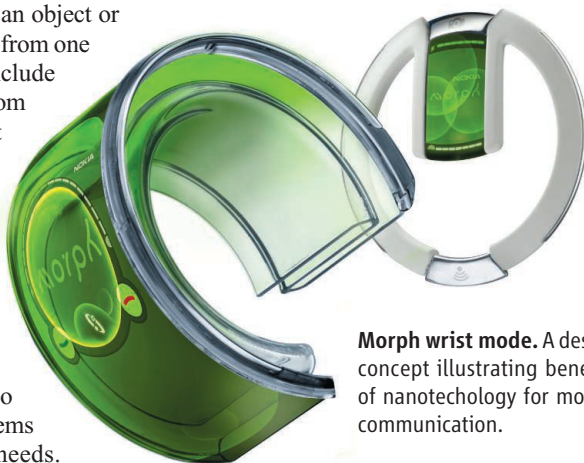
In fictional or science-fictional literature, technologies and devices are often invented in order to solve a problem that might otherwise detract from the storytelling, such as the need to move an object or a piece of information quickly from one place to another. Examples include the transporter and tricorder from *Star Trek* to the two-way wrist radio and two-way wrist TV of Dick Tracy fame. Although the instantaneous transporting of a person may not be realized soon, small-scale sensing, analysis, and communication are now commonplace.

Advances in technology also come about to solve real problems or in anticipation of future needs. The evolution of technology is not unidirectional, as new capabilities allow for the creation of new markets. Following on from workshops held with researchers from the University of Cambridge, Nokia, and Helsinki University of Technology, editors Tapani Ryhänen, Mikko Uusitalo, Olli Ikkala, and Asta Kärkkäinen offer a vision of how nanotechnology will be used to create future mobile devices. This may seem like a recipe for a dry, academic text, but *Nanotechnologies for Future Mobile Devices* more broadly explores the impact of new technologies and devices on manufacturing approaches, value

networks, innovation models, and the broader society. Our ability to connect with individuals across the planet at close to light speed has made the world both larger and smaller at the same time.

The volume starts with a vision of the growing interconnectedness of the world as seen by Ryhänen, Uusitalo, and Kärkkäinen (all of whom are at the Nokia Research Center, Helsinki). Even though the picture they paint is highly idealized, one can see how the needs of an aging population or the desires for an immersive three-dimensional virtual environment will shape the way future technologies are shaped. Beyond simple communication devices or the ability of a doctor to evaluate and treat a patient remotely, there are possibilities such as handheld devices capable of tracking seismic data or the presence of potential chemical hazards and conveying that information to the necessary authorities in real time.

Subsequent chapters survey a number of promising research areas, including nanocomposites, self-assembly, biomimicry and biological materials, and the development of



**Morph wrist mode.** A design concept illustrating benefits of nanotechnology for mobile communication.

functional surfaces. Although not exhaustive, the chapters' reference lists appear to contain the majority of key recent papers. The drive to new materials and fabrication technologies is in part due to some existing methods and materials coming up against fundamental limitations—particularly in the areas of energy and computation. Compare this with the areas of sensing, actuation, and communication and display technologies, where tremendous progress continues to be made (so that we can be bombarded with entertainment and advertising in airports, elevators,

gas stations, and taxis).

The volume's last two chapters make it stand out from other overviews and reviews. The first ("Manufacturing and open innovation"), from Tim Minshall *et al.* (a team of engineers at the University of Cambridge), looks at changes in manufacturing methods and the development of open innovation, in which

companies look beyond their own boundaries for methods to create, develop, and market new products and technologies. One might argue that such a distributed process of innovation already occurs to a large extent, either in the form of partnerships among corporations and the world of academia or through the aggressive acquisition of small startup companies. Increasingly, one finds that these startups come from university research that is promoted into its own entity, so as to better mesh with the goals of the corporate world.

The second ("Seeing beyond the hype") comes from Tom Crowley, Laura Juvonen, and Pekka Koponen at Spinverse, a company that commercializes and markets new technologies. They describe two frameworks for analyzing technology development: the S-curve (which maps the performance of a new technology over time) and the hype cycle (*I*), in which a trigger is followed successively by an initial "peak of inflated expectations," a "trough of disillusionment," a "slope of enlightenment," and lastly the "plateau of productivity." They also compare the evolution and marketing of Internet technologies with the current state of nanotechnology. Anyone looking to develop and commercialize promising emergent scientific and engineering advances—even researchers working outside the core areas covered in the volume—will certainly find this chapter worth reading.

To some extent, the technologies employed in the future are limited by our ability to design and manufacture the necessary devices. But as the fictional literature shows, the starting point is seeing and understanding a fundamental need and then working toward its solution. *Nanotechnologies for Future Mobile Devices*, the product of an unusual and productive collaboration, offers an interesting vision of our growing interconnectedness and the technologies that are likely to change this in the future.

#### References

1. J. Fenn, "When to leap on the hype cycle" (Gartner Group, Stamford, CT, 1995).

10.1126/science.1195196



# Achieving Scientific Eminence Within Asia

Alice S. Huang<sup>1,2\*</sup> and Chris Y. H. Tan<sup>3</sup>

Will Asia be a strong science partner in the 21st century? Our future depends on solving critical problems, many of which require scientific or technical solutions. Asia, which contains two-thirds of the world's population, should be a source of considerable talent for tackling these problems. It has the advantage of geographic size, a youthful population, and increasing wealth. Scholarly activity has been widely respected in Asian cultures throughout their history. Over 400,000 Asian students enrolled in U.S. universities come from Asia (1). In the past, many of these students remained in the United States, but recently an increasing number are returning to their homelands. In response, several Asian countries are attempting to build fundamental research establishments to accommodate these returnees and to increase science capacity (2).

Asian nations are extraordinarily diverse, from small city-states to the most populous countries in the world. Some of these, most notably China, India, South Korea, Taiwan, Hong Kong, and Singapore, have greatly improved their economies and have begun to invest heavily in their educational and research institutions. Japan, one of the wealthiest Asian countries, has had a continuous research establishment for more than a hundred years and yet is also recognizing the need to reform and build. Even the emergent economies of Malaysia, Thailand, Indonesia, and Vietnam aspire to build their own research capacity, especially in the areas of discovery and innovation.

However, we sense that Asian countries share some aspects of mindset and culture that limit their aspirational reach. Here, we cite common problems that we think can be avoided or overcome. Our perspective is that of practicing scientists and administrators who have worked mostly in the West, but who also have an understanding of Asia's cultures and rich history [e.g., C.Y.H.T. is founding director of Singapore's Institute of Molecular and Cell Biology (IMCB)] (3). We believe

success can be enhanced in each Asian country by following the eight recommendations in the table.

Asian investment in modern fundamental science did not begin until roughly 25 years ago. Unlike manufacturing, which is based on low cost labor and materials, fundamental research depends on the discovery of new knowledge that could lead to valuable new products. After considerable investment in buildings and equipment, Asian countries have come to appreciate that more is needed to build a vibrant research culture that is capable of world-class competitive research (4).

In the past, there was also a lack of cooperation and interaction among Asian research institutes, especially across national lines. For example, despite its developed economy, Japan's science establishment had very little interaction with the rest of Asian science. But since the 1990s, with newly established ties developed through science, we have seen a spirit of camaraderie among scientists in Taiwan's Institute of Molecular Biology, Singapore's IMCB, Hong Kong's University of Science and Technology, China's Beijing University and Institute of Biochemistry (Shanghai), Japan's Institute of Medical Science at the University of Tokyo, Indonesia's Eijkman Institute, Korea's Seoul National University, Australia's University of Queensland, and New Zealand's University of Otago. The recent mapping of human genomes in Asia was accomplished with the collaboration of 40 institutions throughout Asia (5). Also, scientists from 14 countries, with shared values and vision, joined to form an Asian-Pacific International Molecular Biology Network (A-IMBN; [www.a-imbn.org/](http://www.a-imbn.org/)) in 1997. A-IMBN is a grassroots organization that may well be the beginning of pan-Asian partnerships among scientists throughout Asia, similar to the European Molecular Biology Organization. These unprecedented developments demonstrate the potential capabilities already building in Asia.

Passive rote learning served China and

Asian countries are poised to help solve modern biological problems, but some policies and practices need reform.

- 1 Reform rote education by teaching active learning starting with the very young.
- 2 Establish a culture that rewards creative thinking and innovation.
- 3 Provide independence for young investigators immediately after their training.
- 4 Fund a large number of independent small and midsize groups to build a large base for innovative research.
- 5 Nurture young scientists in an open environment that encourages international collaborations.
- 6 Use the wisdom of experienced older scientists who understand the country's culture to create clear career paths and astute national science policies.
- 7 Establish transparent systems of competitive research funding based on merit.
- 8 Establish a culture that insists on scientific integrity and honesty.

India well for 3000 years. Civil servants were selected through tough imperial examinations based on how well they could recite from rote. Rote learning is entrenched and ingrained to this day in many areas of Asia (6). For example, in China and Japan, primary school students spend hours practicing calligraphy: the proper positioning and writing of each word within a box. This is not an environment that encourages "outside-of-the-box" thinking. The Indian Institute of Technology (IIT) is legendary for conducting rigorous entrance examinations, where 320,000 may take the exam, and only 8000 are accepted. But IIT may not always challenge the exceptional student once admitted (7). We believe that this is also true of many other institutions of higher learning throughout Asia. To compete internationally, Asia must establish a culture that rewards creative thinking and innovation. To do so, the mindset must change to promote active learning. But this takes time. In the interim, some of the best "teaching" may be via the Internet. But despite good Internet access, there is concern regarding censorship and control.

One way for countries to increase creative thinking in science is to attract their own scientists who have trained abroad to return. Ray Wu, a professor from Cornell University, made an agreement with China in 1980 to select young graduates from China's top universities and send them to leading American universities to obtain their graduate degrees in biology and biochemistry. Selected students were put on a crash course to speak and

<sup>1</sup>Division of Biology, California Institute of Technology, Pasadena, CA 91125, USA. <sup>2</sup>President, American Association for the Advancement of Science, Washington, DC 20005, USA.

<sup>3</sup>Calidris Therapeutics, Vancouver, BC, V6S1B2, Canada

\*Author for correspondence: [alice.huang@caltech.edu](mailto:alice.huang@caltech.edu)

write English before they entered the United States. By 1989, 422 students from China were training for their Ph.D.'s through this China–United States Biochemistry Examination and Application (CUSBEA) program (8). Within a decade, CUSBEA students changed the landscape of American research laboratories. For the first time, a large number of students from China in the United States were coauthors of outstanding publications in international journals. Many stayed in the United States and established excellent independent reputations.

Both China and Singapore have focused on this group, hoping to attract them back to Asia. At least 30 successful CUSBEA graduates and other Chinese professionals in the United States have recently given up major professorships to return to China (9, 10). Singapore's IMCB has also hired several CUSBEA graduates. Although it may be too early to judge, their return to Asia suggests that competitive scientific research may be built within a generation when enthusiastic, well-trained young scientists are given the opportunity to establish independent research programs.

It is difficult to “leap frog” to excellence, however, just by writing large checks in support of science. There are many gaps to be filled despite good intentions. Our observation of science in Asia reveals a remarkable similarity in policy-making. Science policy is typically a top-down process involving senior politicians and civil servants. Few have science discovery backgrounds, and middle-level bureaucrats accustomed to counting returns on investment carry out implementation. These individuals tend to adapt their version of metrics to measure productivity and success in science. Many Asian bureaucrats are finding out that scientific discovery is not readily quantifiable by returns on financial investment within their years of service. Such disappointments can lead to reprioritization of government support, interfering with and jeopardizing newly founded laboratories and often destabilizing careers.

The present Asian research community can be grossly divided into a majority of older, local scientists, with a minority of younger returnees and visiting scientists from the West. In Singapore there is an additional group, a small group of senior Western scientists recruited into part-time or full-time positions and entrusted to lead the science effort. Many of these expatriate scientists are well past retirement age. Managing these different groups of scientists at any one time is difficult, especially through a top-down, decision-making process.

Centralized, top-down control will con-

tinue to affect the development of science in Asia. It has generated debate about whether “big science” is the wave of the future or small, independent laboratories would provide the innovative science that is needed. Inherently, big science is accompanied by “big politics.” It is easier to sell big science not only because it is fashionable, but also because of its many easily measureable tangibles, such as modern buildings and expensive hardware. It would be alarming if Asia's newfound wealth goes largely to support big science because large facilities, instruments, and popular trends wear out and the rapid pace of discovery renders them obsolete. Worse, it reduces the base of innovations that Asia desperately needs to expand.

In Singapore, the debate is whether it is wiser to depend on established, Western senior scientists to lead (11) or better to grow a science leadership with younger returnees. A balance is needed, although we believe that younger returnees should be given the lead (3, 12, 13). Senior scientists, with their breadth of experience, provide the perspective needed for internal policy development and mentoring of young scientists. But young researchers in their prime are a better bet for innovation. They are likely to have the cutting-edge research knowledge, as well as ambition and energy, to be highly successful.

Asia can blaze a trail for encouraging innovative research by supporting large numbers of young returning scientists with access to funding that does not depend on cronyism and is competitively awarded on the basis of merit and productivity. If there are no clear career paths for scientists in Asia, the best and brightest will not be attracted to and remain in science as a career. One example of the failure to protect a bright scientist from changing administrative policies is that of a Stanford Ph.D. now making a living as a taxi driver in Singapore (14). Several Western-trained Asian returnees, including CUSBEA scientists have left Singapore for China.

The polemics between the traditional and the new continue, especially in Japan. Ken-ichi Arai, returning from Stanford, fought hard to reform the top-down, hierarchical system of life science research in Japan (15). One curious end product, derived from the reform movement there, was the birth of a new institute in Okinawa. Because Singapore's success story with IMCB was reported throughout Asia, Koji Omi, who was then both Japanese Minister of State for Science and Technology Policy, and also Minister of State for Okinawa, decided to build the world's best research institution in Okinawa. English would be the common language. Breaking

with Japanese tradition, he appointed Sydney Brenner, an English Nobel laureate, to be the president of this entity, the Okinawa Institute of Science and Technology (OIST). During OIST's first year, Yomiuri Shimbun, a major Japanese newspaper, wrote critically of the OIST president (16) but missed the opportunity to discuss the reform of science in Japan. Resistance to reform is not particularly a Japanese problem. It is inherent in cultures with long, proud histories. OIST teaches an important lesson: It takes more than inviting a few high-powered scientists from abroad to get acceptance for science reform.

Unfortunately, throughout Asia, the respect for scholarship has translated to a virtual worship of the Nobel Prize and branding opportunities offered by top universities. Nobelists and professors from well-known Western universities represent the ultimate intellectual authority. Huge sums of money have been and are being spent in the hope of fast-tracking scientific institutions in Asia by associating with famous universities abroad. As an example, Singapore tried several expensive partnerships with U.S.-based Johns Hopkins University and the Massachusetts Institute of Technology (17, 18).

How can Asia nurture its own scientific leadership with such a lack of confidence in its own talent? If not corrected, intellectual colonialism can become a serious barrier to Asia's quest to build capacity in science. Asia's ambition to build competitive institutions can still be achieved if educated, enlightened politicians and scientific leadership arise in, or return to, each country and are empowered to serve each region's best interests.

## References and Notes

1. Institute of International Education (IIE), [press release] 16 November 2008; <http://opendoors.iienetwork.org/?p=131590>.
2. National Science Board, Globalization of science and engineering research: A companion to science and engineering indicators (NSB, Arlington, VA, 2010).
3. J. Maddox, *Nature* **374**, 403 (1995).
4. *Economist* **24**, 43 (2010).
5. M. A. Abdulla et al., *Science* **326**, 1541 (2009).
6. L. Bao et al., *Science* **323**, 586 (2009).
7. F. Zakaria, *The Post-American World* (Norton, New York, 2009).
8. Y. S. Zhang, *IUBMB Life* **61**, 549 (2009).
9. Z. Chang, *IUBMB Life* **61**, 555 (2009).
10. S. LaFraniere, *New York Times*, 6 January 2010, p. A1.
11. S. Luman, *Wired* (12.08) (2004).
12. Y. Shi, Y. Rao, China's research culture, *Science* **329**, in press.
13. S. Tole, R. D. Vale, Young leaders for Indian Biology, *Science* **329**, in press.
14. A. Gunasingham, *Straits Times*, 19 August 2009.
15. K. Arai et al., *The Golden Helix: Big Bang for Frontier of Biomedicine* (Nikkei Press, Tokyo, 1997).
16. Y. Bhattacharjee, *Science* **314**, 1665 (2006).
17. N. Chourc et al., *MIT News*, **19**, 1 (2006).
18. I. Fuyuno, *Nature* **442**, 493 (2006).

10.1126/science.1190145



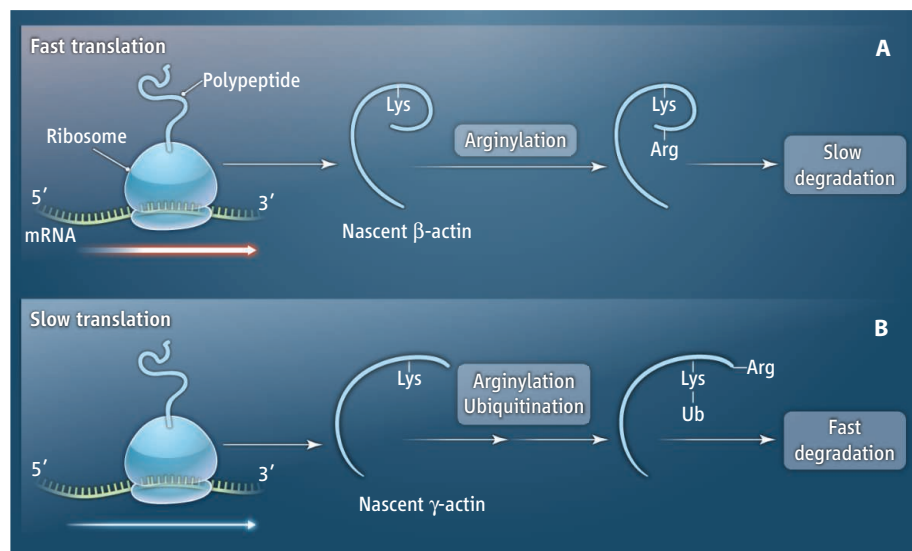
## CELL BIOLOGY

## New Roles for Codon Usage

Ivana Weygand-Durasevic<sup>1</sup> and Michael Ibba<sup>2</sup>

How do two proteins with almost indistinguishable amino acid sequences have different functions in the cell? A single amino acid change can dictate a property as complex as the topology of a membrane protein (1), but other examples are less easy to explain. One such puzzle relates to the mammalian cytoskeletal proteins  $\beta$ - and  $\gamma$ -actin, whose amino acid sequences are 98% identical.  $\beta$ -Actin is modified by the addition of arginine, whereas  $\gamma$ -actin is not, resulting in distinct roles for each in the cell. Identifying what exactly distinguishes  $\beta$ - from  $\gamma$ -actin has proved perplexing because the marginal differences in their amino-terminal sequences are not sufficient to explain why one is modified and the other is not. On page 1534 of this issue, Zhang *et al.* (2) show that the modification of  $\beta$ - and  $\gamma$ -actin is dictated by the codons—the triplets of nucleic acids that encode amino acids—rather than the specific amino acids themselves in the amino termini of these proteins. This is an unexpected example of proteins whose properties are determined at the nucleotide rather than the amino acid level, forcing a reassessment of what defines a synonymous change in a gene sequence.

Arginylation of certain proteins occurs after translation of their amino termini. Although discovered more than 40 years ago (3), the effects of protein arginylation have remained less well understood than many other posttranslational modifications. Proteins are arginylated during normal cell growth and in response to stress, and arginylation has been associated with protein degradation in the proteasome (4). One prominent group of substrates is the actin family. For example, arginylation of  $\alpha$ -actin in cardiac muscle affects myofibril development and function and regulates muscle contractility (5). But not all actins are arginylated. Despite their high amino acid similarity, only the  $\beta$ -, but not the  $\gamma$ - isoform of actin, is found arginylated at its amino terminus *in vivo* (6). Selective modification of actins is important for normal cell morphology and migration, because the absence of arginylation substantially decreases intracellular actin polymer levels and changes its spatial segre-



**Fast start, slow end.** (A) For  $\beta$ -actin, fast translation allows only arginylation, thereby stabilizing the protein. (B) Slow translation of  $\gamma$ -actin allows both arginylation and ubiquitination, leading to rapid degradation.

gation (7).  $\beta$ -Actin preferentially localizes at the protruding leading edge of a migrating cell, where rapid actin polymerization pushes the cell's front forward. There,  $\beta$ -actin is present as a loose and branched arrangement of relatively short actin filaments. By contrast,  $\gamma$ -actin is found in the cell body in dense non-branched networks and long contractile stress fibers that impart morphological stability and support cell adhesion.

Zhang *et al.* sought to determine what differentiates  $\beta$ - from  $\gamma$ -actin, thereby allowing these two almost identical proteins to exist in differently modified states and play such distinct roles in the cell. Given that the amino acid sequences of  $\beta$ - and  $\gamma$ -actin are not different enough to allow the selective arginylation of one protein over the other, the authors wondered if instead both isoforms might be modified with arginine immediately after they are translated. Indeed, the authors found that both nascent polypeptides are arginylated, but the critical difference between them is stability: Unlike arginylated  $\beta$ -actin, arginylated  $\gamma$ -actin only exists transiently and is rapidly degraded by the proteasome.

Why is  $\gamma$ -actin so much less stable? A striking difference in codon usage is the culprit. The amino terminus of the gene encoding  $\gamma$ -actin contains a high frequency of codons predicted to slow the rate of translation of its corresponding mRNA into protein. The same region of the gene encoding  $\beta$ -actin uses alter-

Nucleotide coding of actin is linked to the rate of translation, polypeptide modification, and stability.

nate codons to specify the same amino acids. Other recent studies have also identified codon usage, particularly at the amino terminus, as a key regulator of gene expression (8, 9). The pivotal role of the nucleotide sequence was confirmed by recoding the amino terminus of  $\gamma$ -actin with codons found in the same region of the  $\beta$ -actin gene. Without altering a single amino acid, codon changes alone stabilized  $\gamma$ -actin. In the reverse experiment,  $\beta$ -actin was destabilized. Zhang *et al.* further noted that the differences in codon usage determined whether or not the isoform was degraded. A critical residue, Lys<sup>18</sup>, is found in both  $\beta$ - and  $\gamma$ -actin. Lys<sup>18</sup> is normally buried in the core of fully folded  $\beta$ -actin protein, but slowing the rate of protein synthesis via codon changes transiently exposes this residue and prompts modification of Lys<sup>18</sup> with ubiquitin. This mark targets  $\gamma$ -actin for proteasomal degradation (see the figure).

The exact effects of slowing protein synthesis remain unclear. Zhang *et al.* suggest that  $\beta$ -actin may be translated faster than  $\gamma$ -actin, resulting in faster folding and cotranslational processing (10). The key parts of actin examined in this study are all within the first 18 amino acids translated, suggesting that the nascent  $\beta$ - and  $\gamma$ -actin polypeptides, which differ by four conservative replacements, would have to fold differently while still inside the ribosomal tunnel, so that when they emerge from the ribosome, each

<sup>1</sup>Department of Chemistry, Faculty of Science, University of Zagreb, HR-10000 Zagreb, Croatia. <sup>2</sup>Department of Microbiology, The Ohio State University, Columbus, OH 43210, USA. E-mail: ibba.1@osu.edu

can then engage distinct protein modification pathways. While such a mechanism would be unusual, it is not completely unprecedented. Recent work on the eukaryotic signal recognition particle also points to the potential importance of nascent proteins folding within the ribosomal tunnel (11). Whatever the exact mechanism, the discovery of Zhang *et al.* that synonymous codon changes can so profoundly change the role of a protein adds a

new level of complexity to how we interpret the genetic code.

#### References and Notes

1. S. Seppälä, J. S. Slusky, P. Lloris-Garcera, M. Rapp, G. von Heijne, *Science* **328**, 1698 (2010).
2. F. Zhang, S. Saha, S. Shabalina, A. Kashina, *Science* **329**, 1534 (2010).
3. A. Kaji, H. Kaji, G. D. Novelli, *Biochem. Biophys. Res. Commun.* **10**, 406 (1963).
4. C. C. Wong *et al.*, *PLoS Biol.* **5**, e258 (2007).
5. R. Rai *et al.*, *Development* **135**, 3881 (2008).
6. M. Karakozova *et al.*, *Science* **313**, 192 (2006).
7. A. S. Kashina, *Trends Cell Biol.* **16**, 610 (2006).
8. T. Tuller *et al.*, *Cell* **141**, 344 (2010).
9. G. Cannarozzi *et al.*, *Cell* **141**, 355 (2010).
10. G. Kramer, D. Boehringer, N. Ban, B. Bukau, *Nat. Struct. Mol. Biol.* **16**, 589 (2009).
11. U. Berndt, S. Oellerer, Y. Zhang, A. E. Johnson, S. Rospert, *Proc. Natl. Acad. Sci. U.S.A.* **106**, 1398 (2009).
12. Supported by NIH (GM65183) and the Unity through Knowledge Fund of Croatia (10/07).

10.1126/science.1195567

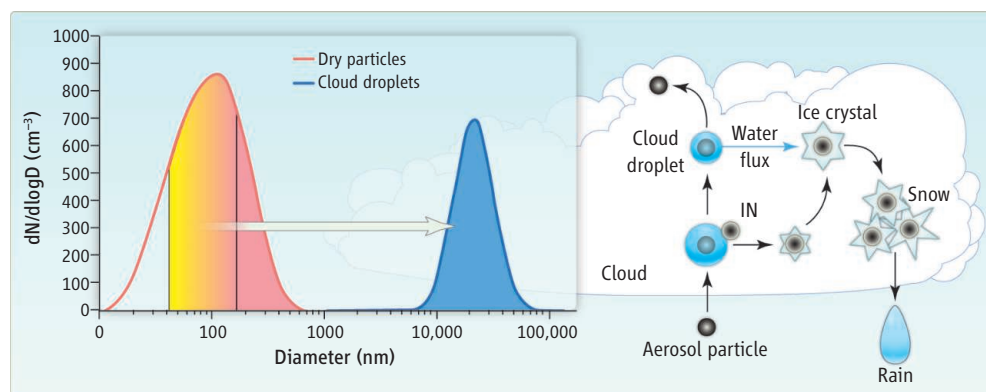
## ATMOSPHERIC SCIENCE

# Aerosols in Clearer Focus

Urs Baltensperger

Atmospheric aerosols—microscopic liquid or solid particles suspended in Earth's atmosphere—can harm human health (1) as well as influence climate by absorbing and reflecting solar radiation and modifying cloud formation (2). Our ability to fully describe the role of aerosols in the climate system, however, has been limited by uncertainty surrounding aerosol distribution and characteristics. Two papers in this issue help reduce this uncertainty by providing data from two regions where coverage was poor. On page 1488, Clarke and Kapustin (3) detail aerosol profiles from both relatively pristine and polluted areas over the Pacific Ocean. On page 1513, Pöschl *et al.* (4) report on aerosols and cloud formation over the Amazon, where conditions may approximate those that existed in preindustrial times.

Health-related monitoring typically focuses on measuring aerosol mass concentrations, but a suite of additional variables comes into play when dealing with climate issues. Climate researchers, for instance, want to know how aerosols scatter or absorb light to calculate aerosol optical depth (AOD), an important measure of atmospheric transparency, which can directly affect climate. They also want to know how many cloud condensation nuclei (CCN) are available to form cloud droplets; the radiative properties of clouds are influenced by the CCN concentration, an effect known as the indirect aerosol effect on climate (5). Clarke and Kapustin present data on AOD and a CCN proxy (the number



**Aerosols into cloud droplets.** (Left) The red curve presents a typical number size distribution of dry aerosol particles from the mountain site Jungfraujoch, Switzerland (11). The red shaded area represents particles that are activated to cloud droplets at a very low supersaturation (0.1%); orange and yellow areas represent activated particles for increasing supersaturation up to 1%. Critical diameters for Jungfraujoch aerosols can vary slightly with water solubility, surface tension, or mixing state (12); however, size is the most important parameter (13). The blue distribution represents an example of the size distribution of cloud droplets measured at the Jungfraujoch (7). (Right) When ice crystals are formed, water vapor is transported from the cloud droplets to the ice crystals because of the lower saturation vapor pressure over ice than over liquid water. This eventually results in evaporation of the cloud droplets, and the radiative properties of the cloud are no longer influenced by the number of CCN but only by the properties of the ice nuclei (IN) and ice crystals.

of particles surviving a 1- to 2-s exposure to 300°C) from about 1000 vertical profiles collected over 13 years. The data show that, in the Pacific regions most influenced by anthropogenic activities such as the burning of fossil fuels and biomass, AOD, CCN, and all other measured aerosol variables are higher—by more than an order of magnitude—than in cleaner regions. They conclude that increased aerosols from combustion are directly and indirectly influencing climate.

Andreae (6) argues that prehuman aerosol levels were very similar over continents and oceans. He concludes that, before the onset of human-induced pollution, the microphysical properties of clouds that formed over the continents resembled those that formed over the oceans. Today, however, cloud processes over most continents are shaped

by the effects of human perturbation.

Pöschl *et al.* report on cloud formation over one region where preindustrial conditions may still occur: the Amazon during the wet season. They characterized aerosols in air masses that moved over the region for an 11-day period in March 2008. They found that the majority of CCN were composed of secondary organic material formed by oxidation of gaseous biogenic precursors (apparently from forest biota). They showed that aerosol-cloud interactions in this environment are distinctly different from those in polluted regions. In particular, they suggest that cloud formation over the pristine Amazon is limited by the number of available aerosol particles; in contrast, in polluted regions the formation of cloud droplets is limited by the velocity of the updrafts that carry particles into the

Paul Scherrer Institute, 5232 Villigen PSI, Switzerland.  
E-mail: urs.baltensperger@psi.ch



higher atmosphere, where they “activate” into cloud droplets.

Pöschl *et al.* report that low aerosol concentrations resulted in cloud droplet number concentrations that were nearly independent of the updraft velocity of a convective cloud, and substantially higher supersaturation levels than found in polluted areas. This in turn meant that particles could activate to cloud droplets at a lower (smaller) critical diameter than in polluted areas. This modeling result is confirmed by measurements at the high-altitude (3580 m) station Jungfraujoch, Switzerland. There, the median of the activation diameter decreased from about 100 nm for particle concentrations (with diameter  $D > 100$  nm) greater than  $100\text{ cm}^{-3}$  to about 65 nm for particle concentrations below  $100\text{ cm}^{-3}$  (7). The effect of varying supersaturation is illustrated in the figure: At high supersaturation, a much higher fraction of the aerosol particles is activated to cloud droplets than at low supersaturation.

Pöschl *et al.* also report on ice nuclei (IN),

particles that initiate ice formation at a temperature considerably above the freezing temperature of water (roughly  $-40^\circ\text{C}$ ). Supermicron-sized particles over the Amazon consisted mostly of primary biological aerosol particles that showed substantial IN activity. Precipitation occurs when these supermicron particles act as “giant” CCN (in warm rain) or IN (when ice formation is involved). The impact of aerosol particles on precipitation is different for warm and cold clouds. In warm clouds, increased CCN concentrations slow the conversion of cloud droplets into raindrops by nucleating larger concentrations of smaller drops, which are slower to coalesce into raindrops (8). In cold clouds, the situation is much more complex. The saturation vapor pressure is lower over ice than over liquid water; this transports water vapor from the cloud droplets to the ice crystals as soon as ice crystals form in liquid clouds (the so-called Wegener-Bergeron-Findeisen process) (9). This results in evaporation of the cloud droplets and a very low fraction of activated

CCN (10). In these clouds, the radiative properties of the cloud are no longer influenced by the number of CCN but only by the properties of the IN and ice crystals. These processes are important for both the hydrological cycle and the radiative properties of clouds and clearly call for more research.

#### References

1. C. A. Pope, D. W. Dockery, *J. Air Waste Manage. Assoc.* **56**, 709 (2006).
2. IPCC, *Contribution of Working Group I to the Fourth Assessment Report of the Intergovernmental Panel on Climate Change*, S. Solomon *et al.*, Eds. (Cambridge Univ. Press, Cambridge, UK), [www.ipcc.ch/ipccreports/ar4-wg1.htm](http://www.ipcc.ch/ipccreports/ar4-wg1.htm) (2007).
3. A. Clarke, V. Kapustin, *Science* **329**, 1488 (2010).
4. U. Pöschl *et al.*, *Science* **329**, 1513 (2010).
5. S. Twomey, *J. Atmos. Sci.* **34**, 1149 (1977).
6. M. O. Andreae, *Science* **315**, 50 (2007).
7. S. Henning *et al.*, *Tellus* **54B**, 82 (2002).
8. D. Rosenfeld *et al.*, *Science* **321**, 1309 (2008).
9. W. Findeisen, *Meteorol. Z.* **55**, 121 (1938).
10. B. Verheggen *et al.*, *J. Geophys. Res.* **112**, D23202 (2007).
11. E. Weingartner, S. Nyeki, U. Baltensperger, *J. Geophys. Res.* **104**, 26809 (1999).
12. G. McFiggans *et al.*, *Atmos. Chem. Phys.* **6**, 2593 (2006).
13. U. Dusek *et al.*, *Science* **312**, 1375 (2006).

10.1126/science.1192930

## BIOCHEMISTRY

# A Never-Ending Story

Britt-Marie Sjöberg

More than 50 years ago, Reichard and colleagues elucidated how cells make their DNA building blocks—the deoxyribonucleotides or dNTPs (1). They found that the enzyme ribonucleotide reductase (RNR) converts ribonucleotides (RNA building blocks) to corresponding dNTPs. One would expect that such a central pathway for all living cells would be meticulously mapped by now. Yes—and no. Researchers have described several classes and subclasses of RNRs (see the figure) that appear to have the same evolutionary origin (2–5), but involve different chemical cofactors, and so enable cells to construct dNTPs under different environmental conditions. Whenever the field seems settled, however, fascinating new aspects appear (1, 2). On page 1526 of this issue, Boal *et al.* (3) report crystal structures of RNR complexes from the bacterium *Escherichia coli* that, together with earlier studies, confirm and neatly illuminate yet another way cells can construct dNTPs, this time with the help of manganese (Mn).

Early researchers initially identified two classes of RNR: class I, which is characterized by a nonheme diiron center and a protein-derived tyrosyl radical ( $\text{Fe}^{\text{III}}_2\text{-Tyr}^\bullet$ ); and class II, which involve the vitamin  $\text{B}_{12}$  coenzyme  $5'$ -deoxyadenosylcobalamin (AdoCbl). Both of these RNR classes operate when oxygen is present (aerobic conditions). Later, investigators identified an anaerobic class III RNR, which involves a glycyl radical cofactor (Gly $^\bullet$ ) generated by an iron-sulfur cluster that cleaves S-adenosylmethionine (AdoMet). Despite structural differences and the involvement of different cofactors (see the figure), all RNR classes have a common origin and generate a transient thiyl radical (Cys $^\bullet$ ) in the active site.

In 1988, investigators isolated a Mn-dependent RNR from *Corynebacterium ammoniagenes* (6). It was not recognized as its own class, however; gene sequencing classified it as part of RNR class Ib, a subclass of class I. In addition, the role of Mn was unclear, since the new RNR was active in vitro with an iron cofactor ( $\text{Fe}^{\text{III}}_2\text{-Tyr}^\bullet$ ) (7). Now, Boal *et al.*, together with Cox *et al.* (8), highlight the importance of the Mn form of the class Ib RNR in *C. ammoniagenes* and

Revealing another way cells make DNA building blocks, this time with manganese.

*E. coli*. The work also highlights the role of the protein NrdI, a flavodoxin that is a crucial player in the formation of Mn-RNR. NrdI is encoded in the same operon as NrdE and NrdF, the two components of the known class Ib RNR. NrdI is essential for the formation of  $\text{Tyr}^\bullet$  in Mn-NrdF (9).

The NrdIs are unusual flavodoxins. They are smaller than classical flavodoxins, with one notable variation in the loop that interacts with the flavin mononucleotide (FMN) (3, 10). Recent structures for NrdIs from *Bacillus anthracis* (10), *Bacillus cereus* (11), and *E. coli* (3) cover the three redox forms of FMN (oxidized, semiquinone, and hydroquinone). Whereas the two redox potentials of classical flavodoxin differ by more than 100 mV (12), *E. coli* NrdI maintains two almost identical redox potentials (9). The semiquinone form is thus transient in *E. coli* NrdI, which probably functions as a two-electron donor. Several NrdIs differ markedly from classical flavodoxin in their isoelectric points (pIs). Whereas flavodoxins have very similar pIs ( $4.5 \pm 0.6$ ), those of *E. coli* and *C. ammoniagenes* NrdIs are much higher, and *B. cereus* and *B. anthracis* NrdIs have pIs like those of flavodoxins (11). Both *B. cereus* and *B. anthracis* NrdIs

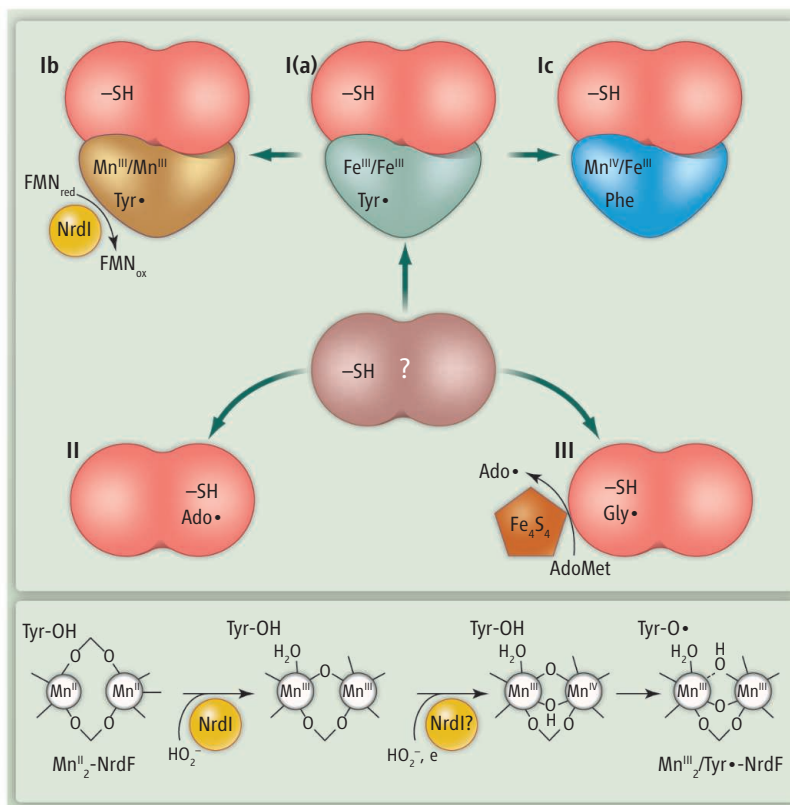
Department of Molecular Biology and Functional Genomics, Stockholm University, SE-10691 Stockholm, Sweden  
E-mail: britt-marie.sjoberg@molbio.su.se

have been crystallized in semiquinone form (10, 11) and may be one-electron donors.

The studies on class Ib Mn-RNRs from *E. coli* by Boal *et al.* (3) and from *C. ammoniagenes* by Cox *et al.* (8) fit together like hand in glove. The high-resolution structures of *E. coli* Mn-NrdF/NrdI complexes highlight a specific channel connecting the FMN cofactor in NrdI to the  $\text{Mn}^{\text{II}}_2$  site in NrdF. This perfect match between the two proteins is conceivably set up to transfer oxidant to the metal site during activation of NrdF. In previous studies, *C. ammoniagenes* class Ib RNR had been expressed in *E. coli*, but Cox *et al.* (8) chose the safe road and expressed high levels of *C. ammoniagenes* NrdF in its homologous background. The intrinsic NrdI probably works catalytically in this expression system and forms enzymatically active Mn-NrdF with Tyr•. Their high-resolution structure shows two Mn ions bridged by one oxo/hydroxo ligand and one carboxylate. Using advanced spectroscopic methods, the authors elegantly reason that the manganese site is  $\text{Mn}^{\text{III}}_2$  and observe, with electron paramagnetic resonance, a deprotonated weakly H-bonded Tyr• cofactor.

Just as there are acidic (*B. anthracis* and *B. cereus*) and basic (*E. coli* and *C. ammoniagenes*) NrdIs, the corresponding NrdFs group into different clades in a phylogenetic tree (13), with 67% identity between *E. coli* and *C. ammoniagenes* NrdFs and only ~40% identities between the *B. cereus* group NrdFs and the other two. In contrast to the  $\text{Mn}^{\text{III}}_2$  site in *C. ammoniagenes*, the  $\text{Mn}^{\text{II}}_2$  site in *E. coli* is bridged by three carboxylates (3). This metal ligation is unique to *E. coli* Mn-NrdF and differs from *C. ammoniagenes*  $\text{Mn}^{\text{II}}_2$ -NrdF with two bridging carboxylates (14).

Failure to oxidize isolated *E. coli*  $\text{Mn}^{\text{II}}_2$ -NrdF with small-molecule oxidants led investigators to propose that reduced NrdI reacts with  $\text{O}_2$  to produce peroxide ( $\text{HO}_2^-$  or  $\text{H}_2\text{O}_2$ ) (9). The channel in the  $\text{Mn}^{\text{II}}_2$ -NrdF/NrdI complex is wide enough to transfer a peroxide spe-



**A dimanganese RNR subclass.** Three major classes of RNR (I to III) have a common origin in the substrate-binding components (red) where the enzyme reaction occurs (top). Class Ib and Ic are subclasses of class I (often called class Ia). Canonical class I has a diiron/tyrosyl radical cofactor (green), subclass Ib has a dimanganese/tyrosyl radical cofactor (brown), and subclass Ic has a manganese/iron mixed-valent cofactor (blue). The flavodoxin NrdI (yellow) is essential for generation of the tyrosyl radical in dimanganese class Ib. In a simplified reaction mechanism for formation of the dimanganese/tyrosyl radical cofactor (bottom), the FMN in NrdI forms peroxide via reduction of dioxygen.

cies and is lined by hydrophilic residues and backbone atoms favoring the peroxide anion (3). Models suggest that density observed in one of the crystallized complexes is a peroxide species. Binding and heterolytic cleavage of the peroxide would generate a  $\mu$ -oxo-bridged  $\text{Mn}^{\text{III}}_2$  site (9). A second peroxide would generate  $\text{Mn}^{\text{III}}/\text{Mn}^{\text{IV}}$  mixed-valent NrdF with the potential to form the enzymatically active  $\text{Mn}^{\text{III}}_2$ -Tyr•. The figure shows a simplified reaction scheme for the *C. ammoniagenes* NrdF-NrdI couple (8).

Although the class Ib Mn-RNRs are now firmly established, several open questions remain. Are class Ib RNRs essential? *Streptococcus pyogenes* NrdI is essential for NrdEF function (15), *B. subtilis* class Ib RNR is essential both for aerobic and anaerobic growth (16), and the requirement of *C. ammoniagenes* and *C. glutamicum* for manganese is related to its class Ib RNR functionality (8). In contrast, *E. coli* uses class Ia RNR and not class Ib RNR for its aerobic growth, but oxidative stress and severe iron limitation may promote use of class Ib RNR and Mn-

dependent growth (9).

Are class Ib RNRs active with either metal (cambialistic)? *C. ammoniagenes* and *E. coli* NrdFs can be reactivated in vitro with ferrous iron and  $\text{O}_2$  to the classical  $\text{Fe}^{\text{III}}_2$ -Tyr• cofactor normally found in class Ia RNRs, and the Fe-NrdFs are enzymatically active. Are they cambialistic in vivo? The requirement of *C. ammoniagenes* for manganese argues against this idea, and it would be interesting to study how the NrdF-NrdI system may differentiate between Fe and Mn ions. In the presence of NrdI, Mn-NrdF has higher enzyme activity compared to Fe-NrdF (9).

Characterization of class Ib Mn-RNRs has been a long, meandering path spanning 30 years. It is now crowned by beautiful three-dimensional structures of a  $\text{Mn}^{\text{III}}_2$  form of NrdF (8), as well as complexes of  $\text{Mn}^{\text{II}}_2$ -NrdF/NrdI (3), and these results add up to much more than their sum.

## References

1. P. Reichard, *Biochem. Biophys. Res. Commun.* **396**, 19 (2010).
2. P. Nordlund, P. Reichard, *Annu. Rev. Biochem.* **75**, 681 (2006).
3. A. K. Boal, J. A. Cotruvo Jr., J. Stubbe, A. C. Rosenzweig, *Science* **329**, 1526 (2010); published online 5 August 2010 (10.1126/science.1190187).
4. D. T. Logan, J. Andersson, B.-M. Sjöberg, P. Nordlund, *Science* **283**, 1499 (1999).
5. M. D. Sintchak, G. Arjara, B. A. Kellogg, J. Stubbe, C. L. Drennan, *Nat. Struct. Biol.* **9**, 293 (2002).
6. A. Willing, H. Follmann, G. Auling, *Eur. J. Biochem.* **170**, 603 (1988).
7. F. Fieschi *et al.*, *J. Biol. Chem.* **273**, 4329 (1998).
8. N. Cox *et al.*, *J. Am. Chem. Soc.* **132**, 11197 (2010).
9. J. A. Cotruvo Jr., J. Stubbe, *Biochemistry* **49**, 1297 (2010).
10. R. Johansson *et al.*, *FEBS J.* **277**, (2010).
11. A. K. Röhr, H. P. Hersleth, K. K. Andersson, *Angew. Chem. Int. Ed. Engl.* **49**, 2324 (2010).
12. M. L. Ludwig *et al.*, *Biochemistry* **36**, 1259 (1997).
13. D. Lundin, E. Torrents, A. M. Poole, B. M. Sjöberg, *BMC Genomics* **10**, 589 (2009).
14. M. Högbom, Y. Huque, B.-M. Sjöberg, P. Nordlund, *Biochemistry* **41**, 1381 (2002).
15. I. Roca, E. Torrents, M. Sahlin, I. Gilbert, B.-M. Sjöberg, *J. Bacteriol.* **190**, 4849 (2008).
16. E. Härtig, A. Hartmann, M. Schätzle, A. M. Albertini, D. Jahn, *Appl. Environ. Microbiol.* **72**, 5260 (2006).

10.1126/science.1196347



## PHYSICS

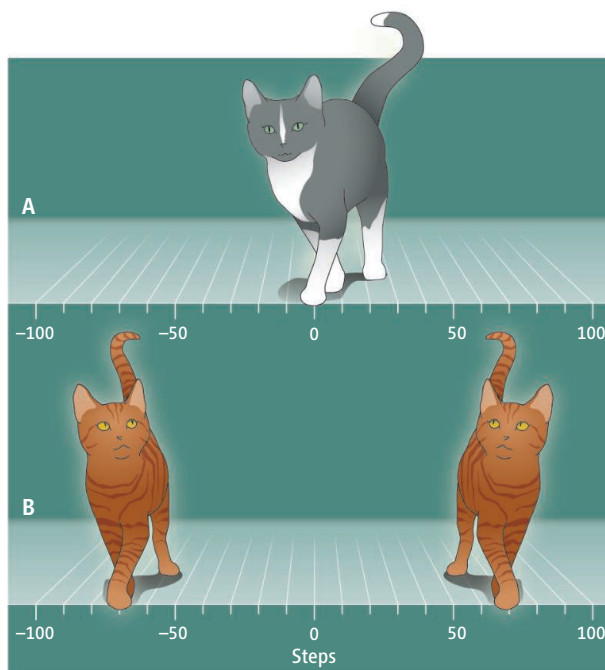
# Quantum Walks Through a Waveguide Maze

Mark Hillery

Two of the major goals of the field of quantum information are to build a quantum computer—one that processes bits of information according to quantum rather than classical rules—and to figure out what to do with one, once you have it. The field that encompasses the latter goal is quantum algorithms. It has not been easy to develop quantum algorithms, but within the past 10 years, a fruitful approach has arisen based on what are known as quantum walks, which in the classical world are the basis for a description of diffusion processes. On page 1500 of this issue, Peruzzo *et al.* (1) describe a device they have built that substantially improves our ability to perform quantum walks. They used it to follow two photons that are performing a quantum walk along a line.

It is best to approach quantum walks by comparing them with classical random walks. To perform the simplest random walk, begin by flipping a coin, and take one step to the right, when it comes up heads, and one step to the left, when it comes up tails. Repeat this process a number of times, and you will have experienced a random walk (see the figure, panel A). This surprisingly simple process can serve as a model for how the smell from a bottle of perfume diffuses throughout a room, or how a stock price moves up and down. It also serves as the basis for a number of random computer algorithms. Thus, the quantum version of a random walk, a quantum walk, could be used as a basis for quantum algorithms.

Random walks are performed by classical objects, but quantum walks are performed by quantum objects such as photons. Peruzzo *et al.* start a photon traveling down a channel (waveguide) in an optical medium. This medium has many parallel channels, and the photon can leak from one channel to another.



**Walk like a photon.** The difference between a classical random walk and a quantum walk is illustrated. (A) After starting at the origin and making a classical random walk of 100 steps, a classical cat is most likely to be found where it started (top). (B) A quantum object starting at the origin and making a quantum walk of 100 steps will most likely be found about 70 steps to the right or to the left of where it started. Here the object is represented by a cat, but in the study by Peruzzo *et al.*, the walkers are two photons. Quantum walks can help speed up search algorithms based on random walks.

These channels serve as the locations in the quantum walk. In other words, we are interested in which channel the photon is located after it has “walked” for a certain amount of time (see the figure, panel B).

The difference between the classical random walk and the quantum walk is a phenomenon known as interference. Quantum objects like photons experience it, whereas classical objects, including people, do not. Suppose the photon can get from one channel to another via two different paths. Each of these paths is assigned a complex number called an amplitude. According to the rules of quantum mechanics, the probability that the photon makes the transition from one channel to the other can be obtained by adding the amplitudes and then squaring the magnitude of this complex number. Thus, each individual path can give a nonzero probability for the photon to transfer channels, but there

Compared to classical objects, a quantum object such as a photon will randomly search through a maze in fewer steps.

are circumstances under which the two paths combine such that there is zero chance that this transition occurs. Interference makes the behavior of a quantum walk very different from that of a random walk.

Quantum walks come in two basic types—one in which the movement proceeds in discrete steps, and one in which the movement is continuous (2, 3). Peruzzo *et al.* examined a continuous quantum walk on a line. Theorists initially studied the behavior of a quantum walk on a line, but went on to look at walks on more complicated structures such as grids,  $n$ -dimensional cubes, and tree graphs (graphs with no closed paths). These structures are collectively called graphs, a graph being just a collection of vertices with edges between them.

The first application of quantum walks was to searches (4). One of the vertices in the graph, called the marked vertex, has different properties than the others, and we would like to find out which vertex it is. What typically happens is that after  $N^{1/2}$  steps, where  $N$  is the number of vertices, the particle making the walk becomes localized on the marked vertex, so we just look and see where the particle is, and that is the marked vertex. It is also possible to locate marked edges as well as subgraphs within a graph (5). Classically, it would be necessary to check each vertex to see if it is the marked one, which would require  $N$  steps, so quantum walks make the procedure more efficient.

Recently, two quantum algorithms based on quantum walks have been discovered. The first, developed by Ambainis, makes use of a black box that evaluates the output function,  $f(x)$ , for a given input  $x$  (6). The object is to find two different inputs that give the same output, or else reveal that each input gives a different output. Ambainis’s quantum algorithm is more efficient than any classical algorithm for the same task. The second, developed by Farhi, Goldstone, and Gutman, can evaluate certain kinds of Boolean formulas (logical statements) more efficiently than can be done on a classical computer (7).

Department of Physics and Astronomy, Hunter College of The City University of New York, 695 Park Avenue, New York, NY 10065, USA. E-mail: mhillery@hunter.cuny.edu

On the experimental side, quantum walks have been performed in a number of different systems, including trapped ions, atoms in optical lattices, and photons. A distinctive feature of the method described by Peruzzo *et al.* is their use of two walkers, i.e., two photons. They measured quantum correlations between the photons that are stronger than those that can be obtained with phase-averaged classical light. There have been only a few investigations of quantum walks with two walkers, and most of these have focused on the case in which the walkers can undergo statistical correlations, as in the study of Peruzzo *et al.*, but do not interact through forces (for example, as

charged particles might do). Recently, Gamble *et al.* (8) found that two interacting walkers are more successful at distinguishing non-isomorphic graphs (ones that connect vertices differently) than are noninteracting walkers.

There is still a great deal to be learned about quantum walks. For a single walker, walks on more complicated graphs or simple graphs with defects are possible areas of investigation. Walks with multiple walkers, both the noninteracting and interacting cases, are relatively unexplored. Finally, it is possible that more quantum algorithms will emerge from a better understanding of quantum walks that will enable new ways to

speed up computation.

## References

1. A. Peruzzo, *Science* **329**, 1500 (2010).
2. D. Aharonov, A. Ambainis, J. Kempe, U. Vazirani, in *Proceedings of the 33rd Annual ACM Symposium on Theory of Computing* (Association for Computing Machinery, New York, 2001), pp. 50–59.
3. E. Farhi, S. Gutman, *Phys. Rev. A* **58**, 915 (1998).
4. N. Shenvi, J. Kempe, K. B. Whaley, *Phys. Rev. A* **67**, 052307 (2003).
5. M. Hillery, D. Reitzner, V. Buzek, *Phys. Rev. A* **81**, 062324 (2010).
6. A. Ambainis, *SIAM J. Comput.* **37**, 210 (2007).
7. E. Farhi, J. Goldstone, S. Gutman, *Theory Comput.* **4**, 169 (2008).
8. J. K. Gamble, M. Friesen, D. Zhou, R. Joynt, S. N. Copper-smith, <http://arxiv.org/abs/1002.3003> (2010).

10.1126/science.1195446

## NEUROSCIENCE

# Should Confidence Be Trusted?

Hakwan Lau<sup>1,2</sup> and Brian Maniscalco<sup>1</sup>

Imagine two witnesses in a courtroom. One is absolutely sure of her testimony; the other gives opposing testimony, but is less confident. Who would you trust more? All else being equal, we would tend to trust the former, because we believe that judgments made with high confidence are more accurate. This correlation between confidence and accuracy, though often true, unfortunately is not infallible. On page 1541 in this issue, Fleming *et al.* (1) report a relationship between the brain scans of people obtained by magnetic resonance imaging (MRI) and how seriously we should take their expressed level of confidence.

When analyzing how confidence predicts accuracy, it is desirable to account for the effect of “response bias.” For instance, perhaps the witness’s high confidence is driven by a brash personality rather than a genuinely accurate memory. The problem of response bias is traditionally addressed by methods such as “signal detection theory,” which is an analytic tool that allows us to separate efficacy from bias (2). By applying such techniques (3), one can characterize how well the subject’s expressed level of confidence distinguishes between correct and incorrect responses, independent of response bias. This measure of the efficacy of confidence ratings has been called “type 2 performance” to distinguish it from “type 1 performance,” which measures how accurately a subject actually identifies a stimulus.

<sup>1</sup>Department of Psychology, Columbia University, New York, NY 10027, USA. <sup>2</sup>Donders Institute for Brain, Cognition and Behaviour, Radboud University Nijmegen, Netherlands. E-mail: hakwan@psych.columbia.edu



**Confidence ratings.** Why does a witness’s expressed level of confidence, when giving testimony, affect our judgement of its accuracy?

In other words, high type 2 performance indicates a close relationship between the confidence of the subjects and how accurately they identify the stimulus.

But there is another problem: Type 2 performance is influenced by type 1 performance (3). The intuition is simple: Suppose a subject has great difficulty making accurate judgments about stimuli (such as the orientation of a figure), making many incorrect judgments as well as “fluke” judgments that are correct only by chance. The subject cannot distinguish incorrect judgments from those that are correct only by chance; they all seem like guesses. Thus, some variation in type 2 performance may be attributable merely to the quality of “lower-level” stimulus processing in the brain (i.e., type 1 performance). To isolate this confounding factor, Fleming *et al.* controlled for type 1 performance by programming a computer to give harder

trials to the better observers, and easier trials to the poorer observers. The authors still found substantial variability in type 2 performance across 32 observers. Also, structural MRI brain scans revealed that those observers with a high type 2 performance had higher gray matter signal intensity (which implies greater volume or density) in the frontal lobe than the low type 2 performers. The difference was most prominent in the frontal polar areas, but also was apparent in the dorsal lateral prefrontal cortex and anterior cingulate cortex. Furthermore, neuronal fibers connecting these regions showed higher signal intensity in the MRI scans.

The results speak to the debated issue (4) of whether type 2 performance reflects genuine metacognition (5)—that is, cognition about another cognitive process, rather than about an external stimulus. For instance, one may argue that confidence ratings in a perceptual task may be made by tracking the strength of the external stimulus, rather than by introspection of the efficacy of the perceptual process (metacognition). However, metacognition is one plausible way in which such confidence ratings can be made, as has been demonstrated by computational modeling (6). The correlation of type 2 performance with structures in the frontal polar region of the brain seems to support the metacognitive account, because this area is at the top of the



information-processing hierarchy, receiving input from other cognitive regions rather than early sensory areas (7).

Metacognition is perhaps particularly controversial in nonhuman animals, such as dolphins and monkeys (4, 8). Such animals can make responses that seem to reflect confidence. For instance, when given the option to abort a trial quickly instead of trying for an answer, they took the option when their accuracy was low, as if they were expressing “uncertainty,” i.e., a lack of confidence (4). Do the same brain structures identified by Fleming *et al.* govern the “uncertain responses” in these animals? There is considerable behavioral evidence in favor of the metacognitive account of uncertainty judgments for these animals (4). Or do they use non-metacognitive mechanisms to generate “uncertain responses,” thus recruiting different brain structures? It would be interesting to determine whether lesions to the prefrontal cortex would affect these responses.

One might expect type 2 performance of nonhuman animals to be considerably poorer than that of humans, because their prefrontal cortices are not as developed. One difficulty in testing this possibility is that we cannot easily control for observers’ type 1 performance across studies and species. How-

ever, the mathematical relationship between type 1 and type 2 performance has recently been mapped out (3), and a method is now available (9, 10) to estimate type 2 performance even when we cannot control for type 1 performance. Future studies can use this method to test the hypothesis that across species, or across different developmental stages in humans, type 2 performance may be correlated with structural development in prefrontal regions.

Fleming *et al.* were cautious in interpreting their results in relation to sensory awareness. Nonetheless, the close conceptual relationship between confidence and sensory awareness has been discussed for at least a century (11). Given that type 1 performance can be shown to dissociate from sensory awareness in some cases (9, 12, 13), perhaps we should not equate the two, as is commonly done (14). Rather, perhaps awareness arises when the observer’s brain introspectively “recognizes” that the perceptual signal was actually strong rather than weak, regardless of the underlying type 1 performance (6, 14, 15). Although this does not mean that sensory awareness is the same as type 2 (metacognitive) performance, both may depend on shared neural mechanisms that support the same kind of introspective monitoring of perceptual certainty.

Indeed, although the sensory signal itself may be represented by activity in posterior brain regions, visual awareness may depend on prefrontal regions similar to those reported by Fleming *et al.* (9, 12, 13, 16).

#### References and Notes

1. S. M. Fleming, R. S. Weil, Z. Nagy, R. J. Dolan, G. Rees, *Science* **329**, 1541 (2010).
2. N. A. Macmillan, C. D. Creelman, *Detection Theory: A User’s Guide* (Erlbaum, Hillsdale, NJ, 2005).
3. S. J. Galvin, J. V. Podd, V. Drga, J. Whitmore, *Psych. B. Rev.* **10**, 843 (2003).
4. J. D. Smith, *Trends Cogn. Sci.* **13**, 389 (2009).
5. J. Metcalfe, A. P. Shimamura, *Metacognition: Knowing about Knowing* (MIT Press, Cambridge, MA, 1996).
6. A. Cleeremans, B. Timmermans, A. Pasquali, *Neural Netw.* **20**, 1032 (2007).
7. N. Ramnani, A. M. Owen, *Nat. Rev. Neurosci.* **5**, 184 (2004).
8. N. Kornell, L. K. Son, H. S. Terrace, *Psychol. Sci.* **18**, 64 (2007).
9. E. Rounis, B. Maniscalco, J. C. Rothwell, R. E. Passingham, H. Lau, *Cognit. Neurosci.* **1**, 165 (2010).
10. For freely shared code online, see [www.columbia.edu/~bsm2105/type2sdt/](http://www.columbia.edu/~bsm2105/type2sdt/).
11. C. S. Peirce, J. Jastrow, *Mem. Natl. Acad. Sci.* **3**, 73 (1884).
12. H. C. Lau, R. E. Passingham, *Proc. Natl. Acad. Sci. U.S.A.* **103**, 18763 (2006).
13. L. Weiskrantz, *Consciousness Lost and Found* (Oxford Univ. Press, New York, NY, 1997).
14. H. Lau, *WIREs Cognit. Sci.* **10.1002/wcs.93** (2010).
15. H. C. Lau, *Prog. Brain Res.* **168**, 35 (2007).
16. A. Del Cul, S. Dehaene, P. Reyes, E. Bravo, A. Slachetky, *Brain* **132**, 2531 (2009).

10.1126/science.1195983

## GEOPHYSICS

# Seismic Images of the Biggest Crash on Earth

Rainer Kind and Xiaohui Yuan

In plate tectonics, the upper layer of Earth (the lithosphere) consists of rigid plates that shift over geological time scales. Data from global positioning surveys have estimated that the entire Indian subcontinent has moved over the past 50 years about 2 m to the north, diving slowly underneath Tibet. This giant collision has been ongoing for 50 million years and has thrown up the highest mountains as well as the largest and highest plateau on Earth. Not only is the world climate strongly influenced by this massive plateau (average elevation of 5000 m), but the collision also causes catastrophic earthquakes in southern, central, and eastern Asia.

There is an ongoing international effort to record seismic waves in Tibet and use them to study the deeper structure beneath Tibet. The Sino-American experiment Hi-CLIMB (Himalayan-Tibetan Continental Lithosphere during Mountain Building) (1–6), the multinational experiment INDEPTH (International Deep Profiling of Tibet and the Himalayas) (7–10), and others (11) have covered the main part of the plateau. Different seismic techniques have been combined in these studies: (i) Seismic tomography, which is sensitive to smooth variations of material properties, can locate the lithosphere and asthenosphere by their higher and lower seismic velocities, respectively (2, 12, 13); (ii) the analyses of converted waves (where the propagating seismic waves change from shear to compressional waves, or vice versa, also called receiver functions) (1,

Several large seismic experiments are providing a large-scale and detailed picture of the Indian tectonic plate diving underneath Tibet.

5–8, 10, 11) or of internally reflected waves (3), which are sensitive to sharp boundaries, can locate the crust-mantle boundary (Moho) and the lithosphere-asthenosphere boundary (LAB) with high resolution; and (iii) seismic anisotropy studies can provide an indication of mantle deformation (4, 9, 11). These new seismic studies cover the entire lithosphere, especially the LAB, whereas earlier studies focused on the more accessible crust.

The main results of the various seismic field campaigns in Tibet can be summarized graphically (see the figure). Different tomography results (2, 12, 13) indicate a broad Indian lithosphere of 100 to 200 km thickness reaching farther north than the northern boundary of the stable Indian plate at the surface (see the figure, top panel). A clear boundary between the Indian and Asian

Deutsches GeoForschungsZentrum, Telegrafenberg, 14473 Potsdam, Germany. E-mail: kind@gfz-potsdam.de

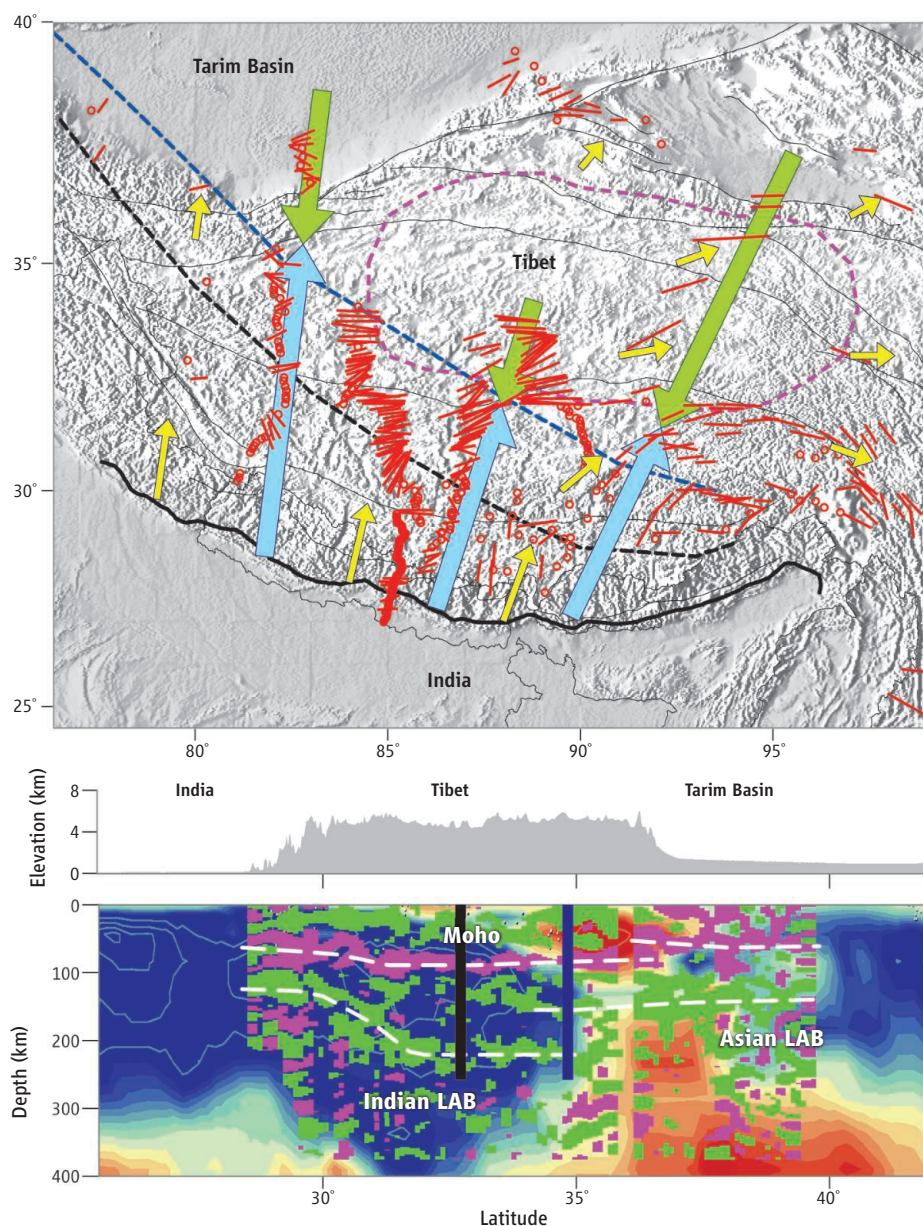
plates is seen at depth by receiver functions (11), as marked in the top panel; of the figure by the clashing arrows.

A comparison has been made between tomographic observations of the lithosphere

(13) and converted-wave observations (11) along the westernmost profile (see the figure, bottom panel). Taking into account that the lateral resolution of seismic tomography is much better than the vertical resolution,

the northern end of the Indian lithosphere agrees very well in both data sets. There is a clear step in the LAB where the two lithospheres meet. It jumps up from about 200 km depth at the Indian side to about 150 km depth at the Asian side. Seismic anisotropy (red lines in the figure, top panel) is very small in south Tibet and is much stronger in central and eastern Tibet (4, 9, 11). Its direction changes from northeast in central Tibet to east and southeast in eastern Tibet. This is considered a result of squeezing hot mantle material from the direct lithospheric collision into easterly and southeasterly directions (14). Global Positioning System (GPS) data indicate similar surface displacements in central and eastern Tibet (15). A relatively soft, warm, and mobile zone in central and eastern Tibet (16) is marked in the figure. The observed large depth of the Moho means the Indian crust is not participating in the subduction; instead, it is being peeled off and remains at the surface. Indian lower crust is observed below the Asian crust in a large region in central Tibet (5, 7, 8).

The large international seismic experiments in Tibet have generated quality data in large quantities and have led to a much improved understanding of the collision of two continental plates and their resulting deformations. Continuing comparable efforts at the northern and eastern boundaries of Tibet are promising because there are indications that the mode of lithospheric collision might be very different there.



**What lies beneath. (Top)** Topographic map of Tibet with results of seismic studies. The northern boundary of the Indian plate at the surface is marked by the continuous black line. This boundary at 200 km depth is marked by the black and blue dashed lines [from two tomography studies (12, 13)]. Observations of the bottom of the Asian and Indian plates at depths of about 150 to 200 km are marked by the green and blue arrows [applying receiver function technique (10, 11)]. Directions of material flow in the mantle below Tibet are marked by red lines [from seismic anisotropy measurements (4, 9, 11)]. Surface displacements obtained from GPS measurements are marked by yellow arrows [modified from (15)]. Dashed magenta line marks observations of a hot and mobile region in central Tibet (16). The push of India far to the north beneath Tibet is causing escape flow in central Tibet in easterly direction [e.g., (14)]. **(Bottom)** Seismic profile from India to the Tarim Basin (along the westernmost blue and green arrows in the top panel) obtained with two seismic techniques, tomography (13) and receiver functions (11). The background colors mark tomography results (blue/red means cold/hot regions). Foreground colors are results of receiver function studies (green/magenta means decreasing/increasing velocity jump downward). LAB and Moho are marked with white dashed lines. Northern limits of the Indian plate from the top panel (black and blue dashed lines) are marked by black and blue vertical lines.

#### References and Notes

1. R. Nowack, W.-P. Chen, T.-L. Tseng, *Bull. Seismol. Soc. Am.* **100**, 1743 (2010).
2. S.-H. Hung, W.-P. Chen, L.-Y. Chiao, T.-L. Tseng, *Geophys. Res. Lett.* **37**, L06304 (2010).
3. T.-L. Tseng, W.-P. Chen, R. L. Nowack, *Geophys. Res. Lett.* **36**, L24304 (2009).
4. W.-P. Chen *et al.*, *Earth Planet. Sci. Lett.* **295**, 297 (2010).
5. J. Nábelek *et al.*, *Science* **325**, 1371 (2009).
6. Q. Xu, J. M. Zhao, Z. X. Cui, S. P. Pei, H. B. Liu, *Chin. Sci. Bull.* **55**, 607 (2010).
7. R. Kind *et al.*, *Science* **298**, 1219 (2002).
8. X. Yuan, J. Ni, R. Kind, J. Mechie, E. Sandvol, *J. Geophys. Res.* **102**, 27491 (1997).
9. W.-C. Huang *et al.*, *J. Geophys. Res.* **105**, 27979 (2000).
10. P. Kumar, X. Yuan, R. Kind, J. Ni, *J. Geophys. Res.* **111**, B06308 (2006).
11. J. Zhao *et al.*, *Proc. Natl. Acad. Sci. U.S.A.* **107**, 11229 (2010).
12. C. Li, R. van der Hilst, A. Meltzer, E. Engdahl, *Earth Planet. Sci. Lett.* **274**, 157 (2008).
13. H. Bijwaard, W. Spakman, *Geophys. J. Int.* **141**, 71 (2000).
14. L. H. Royden, B. C. Burchfiel, R. D. van der Hilst, *Science* **321**, 1054 (2008).
15. W. Gan *et al.*, *J. Geophys. Res.* **112**, B08416 (2007).
16. M. Barazangi, J. Ni, *Geology* **10**, 179 (1982).
17. Tomography results in the bottom panel were provided by W. Spakman.

10.1126/science.1191620



# Tyrannosaur Paleobiology: New Research on Ancient Exemplar Organisms

Stephen L. Brusatte,<sup>1,2\*</sup> Mark A. Norell,<sup>1</sup> Thomas D. Carr,<sup>3</sup> Gregory M. Erickson,<sup>1,4</sup> John R. Hutchinson,<sup>5</sup> Amy M. Balanoff,<sup>1,2†</sup> Gabe S. Bever,<sup>6†</sup> Jonah N. Choiniere,<sup>1,7†</sup> Peter J. Makovicky,<sup>8†</sup> Xing Xu<sup>9†</sup>

Tyrannosaurs, the group of dinosaurian carnivores that includes *Tyrannosaurus rex* and its closest relatives, are icons of prehistory. They are also the most intensively studied extinct dinosaurs, and thanks to large sample sizes and an influx of new discoveries, have become ancient exemplar organisms used to study many themes in vertebrate paleontology. A phylogeny that includes recently described species shows that tyrannosaurs originated by the Middle Jurassic but remained mostly small and ecologically marginal until the latest Cretaceous. Anatomical, biomechanical, and histological studies of *T. rex* and other derived tyrannosaurs show that large tyrannosaurs could not run rapidly, were capable of crushing bite forces, had accelerated growth rates and keen senses, and underwent pronounced changes during ontogeny. The biology and evolutionary history of tyrannosaurs provide a foundation for comparison with other dinosaurs and living organisms.

**T**yrannosaurs, the group of carnivores that includes *Tyrannosaurus rex* and its closest relatives, are archetypal dinosaurs (1) (Fig. 1 and table S1). They are pop culture icons, but also valuable research subjects, and have become an exemplar group used to study many themes in vertebrate paleontology. Research on tyrannosaurs is undergoing a renaissance, as new discoveries and technological approaches are helping to elucidate the biology and evolution of these animals in unprecedented detail.

*Tyrannosaurus rex* was initially described 105 years ago (2), and for most of the 20th century tyrannosaurs were known almost solely from fossils of *T. rex* and four closely related species of large, multi-ton Late Cretaceous predators (3). Within the last decade, however, the diversity of tyrannosaurs has more than doubled, and during the past year alone, six new species were described, some of which are 100 million years older and 1/100 the size of *T. rex* (4, 5) (Fig. 1). These discoveries have fostered an increased understand-

ing of tyrannosaur anatomy (6, 7), growth dynamics (8, 9), population structure (10), feeding (11), locomotion (12), biogeography (13), and soft tissue morphology (14–16). This breadth of information, and of research activity, on a restricted group of organisms is unparalleled in contemporary dinosaur paleontology.

Here we assess the current state of tyrannosaur research, with a focus on the phylogenetic relationships and large-scale evolutionary patterns exhibited by the group, the biology of tyrannosaurs as living organisms, and information revealed from the newest discoveries.

## Phylogenetic Relationships and Evolution of Tyrannosaurs

Tyrannosaurs, which formally comprise the clade Tyrannosauroidae, are a relatively derived group of theropod dinosaurs, more closely related to birds than to other large theropods such as allosauroids and spinosaurids (1, 17). Approximately 20 tyrannosauroid genera are currently known, 5 of which were described during the past year. To assess their interrelationships, we conducted a phylogenetic analysis, which includes all

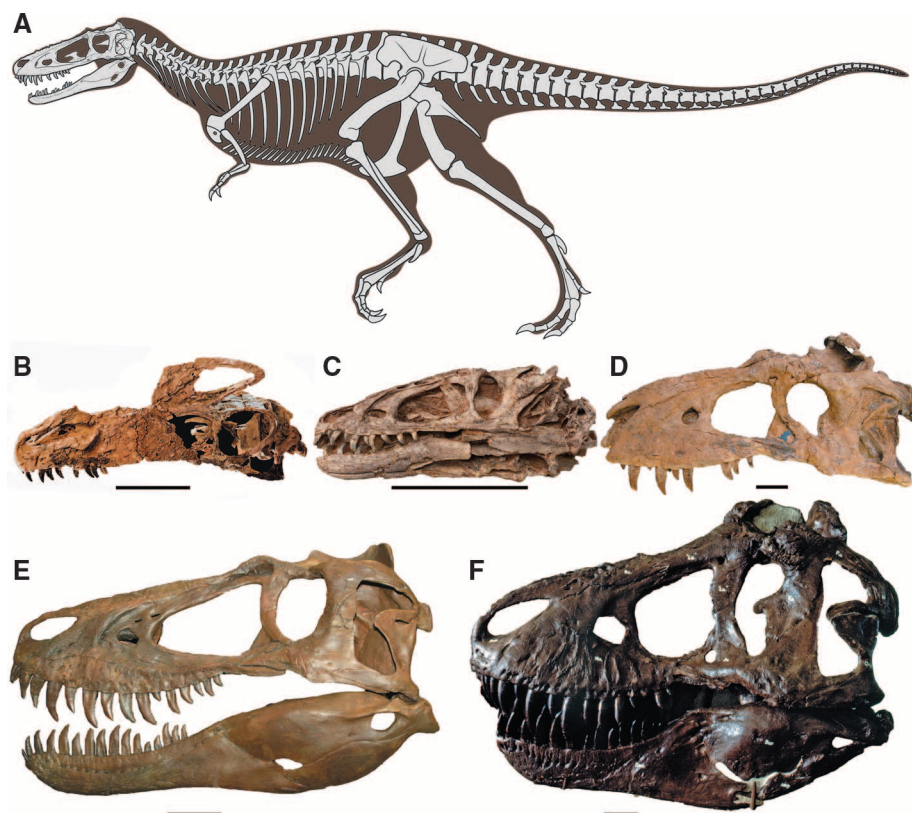


**Fig. 1.** The anatomy of tyrannosaurs, showing the variety of skeletal and cranial morphology in the group. (A) A skeletal reconstruction of *Alioramus*, a gracile and long-snouted tyrannosaurid, which exhibits many features of the generalized tyrannosaurid body plan (large skull, small arms, long hindlimbs, long tail). (B to D) Skulls of the basal tyrannosauroids *Guanlong* (B), *Dilong* (C), and *Bistahieversor* (D). (E and F) Skulls of juvenile (E) and adult (F) *Tyrannosaurus* scaled to the same length, illustrating the transition from a longer to a deeper skull during ontogeny. All scale bars equal 10 cm. Credits: F. Ippolito, American Museum of Natural History (AMNH) (A); I. Block, National Geographic Stock (B); M. Ellison, AMNH (C); D. Baccadutre, New Mexico Museum of Natural History and Science (D); S. Williams, Burpee Museum of Natural History (E); AMNH Photo Archives (#2752, *Tyrannosaurus* skull as mounted in the old hall) (F).

<sup>1</sup>Division of Paleontology, American Museum of Natural History, Central Park West at 79th Street, New York, NY 10024, USA.

<sup>2</sup>Department of Earth and Environmental Sciences, Columbia University, New York, NY 10964, USA. <sup>3</sup>Department of Biology, Carthage College, Kenosha, WI 53140, USA. <sup>4</sup>Department of Biological Science, Florida State University, Tallahassee, FL 32306, USA. <sup>5</sup>Department of Veterinary Basic Sciences, The Royal Veterinary College, Hatfield, Herts AL9 7TA, UK. <sup>6</sup>Department of Geology and Geophysics, Yale University, New Haven, CT 06520, USA. <sup>7</sup>Department of Biological Sciences, The George Washington University, Washington, DC 20052, USA. <sup>8</sup>Department of Geology, The Field Museum of Natural History, Chicago, IL 60605, USA.

<sup>9</sup>Institute of Vertebrate Paleontology and Paleoanthropology, Chinese Academy of Sciences, Beijing 100044, People's Republic of China.

\*To whom correspondence should be addressed. E-mail: sbrusatte@amnh.org

†These authors contributed equally to this work.

well-known genera scored for 307 morphological characters (18). The data set is based on personal observation of specimens and includes 123 novel characters (40% of total) based on recently discovered tyrannosaur taxa (4, 19–21).

Tyrannosaurs are a long-lived group that originated by the Middle Jurassic, ~165 million years ago (5) (Fig. 2). The oldest and most basal tyrannosaurs comprise a speciose subclade, Proceratosauridae, which includes mostly small-bodied animals no larger than a human, many of which possessed elaborate cranial crests (22). Progressively more derived tyrannosaurs form a pectinate series on the line toward Tyrannosauridae, the subclade of multi-ton, deep-skulled behemoths from the terminal Cretaceous (Campanian–Maastrichtian), including *Tyrannosaurus*, *Tarbosaurus*, *Albertosaurus*, and close relatives (1). Taxa phylogenetically intermediate between proceratosaurids and tyrannosaurids include a range of genera from the Late Jurassic–early Late Cretaceous of Asia, North America, and Europe, most of which have been recently discovered (4, 14, 20, 21, 23, 24). These taxa run the gamut from small to medium size (~1.4 to 9.0 m in length), and few were likely apex predators in their ecosystems (21).

Until recently, the prevailing notion was that tyrannosaur body size gradually, and progressively, increased over time, in concert with the piecemeal accumulation of signature tyrannosaur skeletal features (14, 21). However, new discoveries have led to a reassessment. The Early Cretaceous proceratosaurid *Sinotyrannus* may have approached 10 m in body length, demonstrating that tyrannosaurs could attain a large size early in their history (25). More striking, the close tyrannosaurid outgroup *Raptorex* is only 2 to 3 m in length, suggesting that there was great size variability among close tyrannosaurid relatives and perhaps that the immediate ancestors of tyrannosaurids were small animals (4). Truly enormous size, however, is restricted to the latest Cretaceous tyrannosaurids, some of which grew to lengths of 13 m and masses of 5 to 8 tons (8). Therefore, for the first 80 million years of their history tyrannosaurs were mostly small- to mid-sized animals that lived in the shadow of other giant predators (e.g., allosauroids, megalosauroids), and only during the final 20 million years of the Mesozoic did they develop into some of the largest terrestrial carnivores to ever live (26). The dominance of tyrannosaurs as megapredators was purely a latest Cretaceous phenomenon.

### Tyrannosaur Anatomy

The spate of new discoveries has prompted a renewed focus on tyrannosaur anatomy, including external, internal, and soft-tissue morphology (Fig. 3). All tyrannosaurs are bipedal predators and possess several unique features, including a small premaxilla with D-shaped “incisor”-like teeth, fused nasals, extreme pneumaticity in the skull roof and lower jaws, a pronounced muscle attachment ridge on the ilium, and an elevated femoral head (6, 27, 28).

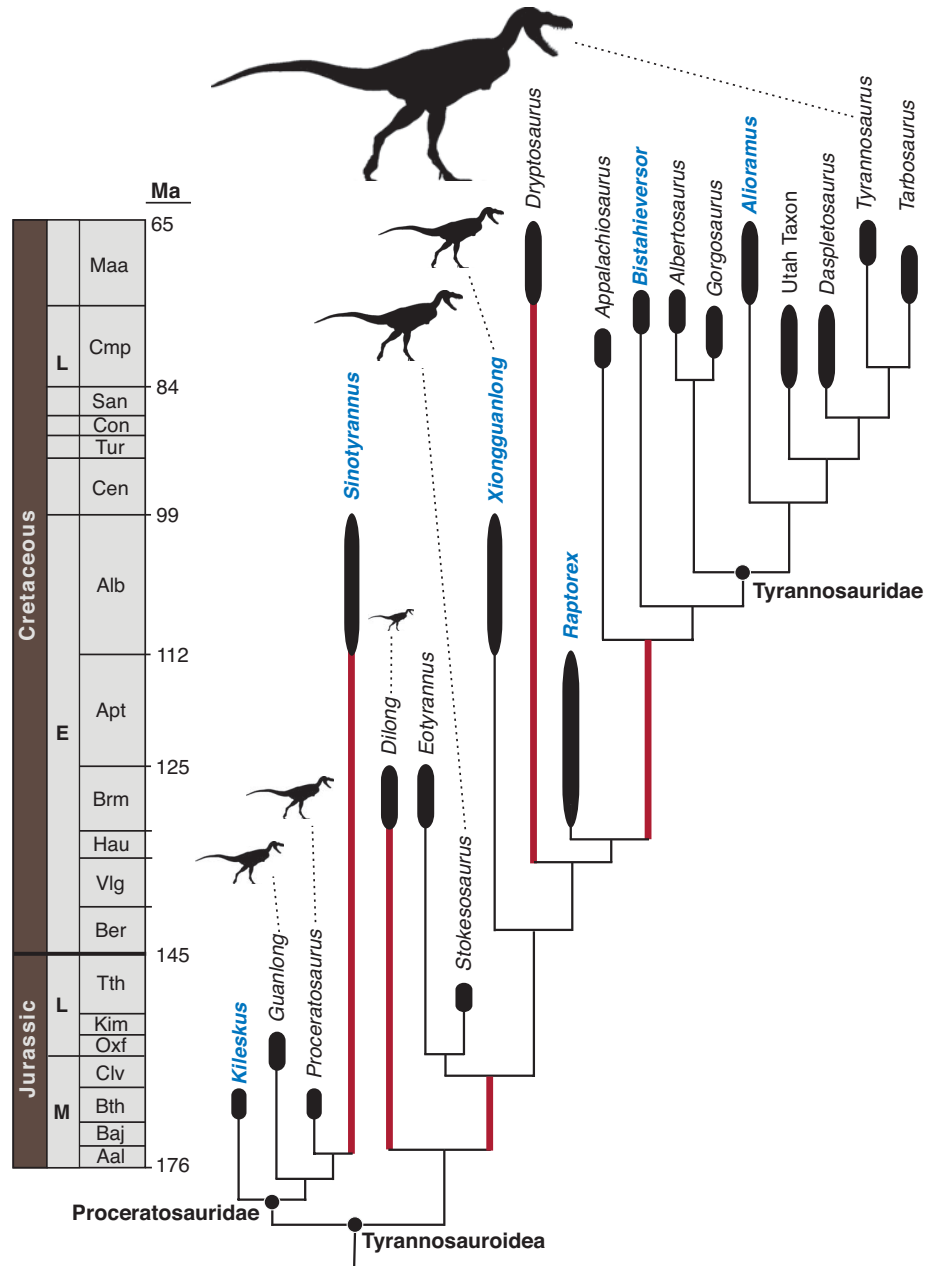


**Fig. 2.** Phylogenetic relationships of tyrannosauroid theropods, assessed by a cladistic analysis (18). Single most parsimonious tree, showing the relationships of 19 tyrannosaurs, scaled to the geologic time scale (in millions of years ago, Ma). Taxa in blue are those that have been described during the past year. Silhouettes indicate relative body size (based on femur length as a proxy). Thick red bars indicate major ghost lineages. Thick black bars represent the finest age resolution for each taxon, not actual duration.

A number of derived specializations characterize the giant tyrannosaurids: a large and deep skull with powerful jaw muscles, robust teeth, reinforced sutures between skull bones, and tiny forelimbs (6, 29), features often considered adaptations for a hypercarnivore to function at large size (4). Basal tyrannosauroids, in contrast, have smaller skulls and longer arms and generally resemble sleek, bird-like theropods more than their enormous tyrannosaurid cousins (14, 22). New discoveries have shown, however, that the hallmark tyrannosaurid body plan (large and deep skull, robust teeth, etc.) does not uniquely

or uniformly characterize the tyrannosaurid clade. Most of these features are now known to be present in *Raptorex*, the man-sized tyrannosaurid outgroup that lived 40 million years before tyrannosaurids originated (4). Furthermore, the gracile and long-snouted *Aloramus*, a tyrannosaurid that is about half the size of close relatives such as *Tarbosaurus* and *Tyrannosaurus*, lacks a deep and muscular skull and thick teeth (19). Thus, characteristic tyrannosaurid features did not evolve as a consequence of large body size, but likely originated in small animals, and not even all derived, Late Cretaceous tyranno-



saurids are united by a characteristic morphotype (4, 19).

Much is also known about the internal anatomy of the tyrannosaur skull, thanks to the discovery of exceptionally preserved fossils and the application of digital techniques such as computerized tomography (CT) scanning (7, 30, 31). Tyrannosaurs possessed the required neuroanatomy to lead the active, predatory life-style expected of derived theropods (7, 30). Their encephalization quotient—an estimate of relative brain size—varies between 2.0 and 2.4, larger than in basal theropods but lower than that of birds and their closest relatives (19). Large olfactory lobes indicate a strong sense of smell (7, 31). Elongate cochlear and semicircular canals apparently support elevated sensitivity to low-frequency sound and highly coordinated head and eye movements (7).

Several tyrannosaurid specimens have been reported to preserve integumentary structures and other soft tissues, which rarely fossilize in dinosaurs. Although impressions of scaly skin have been described for large tyrannosaurids (32), simple filamentous integument, interpreted as homologous to feathers, is clearly preserved in a specimen of the basal tyrannosaurid *Dilong* (14). These branched filaments appear to have extensively covered the body, as they are observed near the skull and tail. A recent study suggests that much larger tyrannosaurids were covered with elongate, broader integumentary structures (33), which were likely used for display (34). Several easily degraded soft tissues, such as cells, blood vessels, and collagen, have been reported from a specimen of *Tyrannosaurus* (15, 35). Some of these findings have been met with skepticism (36), and they remain to be validated by other research groups. However, if correct, they promise to give radical new insight into the process of fossilization and may allow for molecular phylogenetic analysis of these extinct taxa (37).

### Tyrannosaur Growth

Arguably we know more about tyrannosaur biology than that of any other dinosaurs (Figs. 3 and 4). Much of this knowledge has been gained over the past 20 years, through the collection of skeletons of both adults and juveniles, bones of their prey with bite marks, coprolites (fossil feces), stomach contents, and pathological specimens (38).

Much attention has focused on how tyrannosaurs grew, especially on how giants such as *T. rex* achieved such massive size and how their skeletons changed during the transition from embryo to multi-ton adult. Comparative growth curves for

several species, which plot body mass (calculated from femur size) against age in years (calculated from counting growth lines in histological section) (8) (Fig. 4B), show that large tyrannosaurids reached somatic maturity around 20 years old, though most rarely lived for more than 25 years. *T. rex* evidently attained its large size via acceleration of growth rates relative to closely related species, not by extending its life span. Its maximum growth rate may have exceeded 767 kg per year, equivalent to adding a remarkable 2 kg per day (8).

Tyrannosaur skeletons changed substantially as individuals matured. Although less is known about the growth of small, basal tyrannosaurs, tyrannosaurids and their closest large-bodied relatives are united by a conservative pattern of

ences between juvenile and adult tyrannosaurids are so great that different growth stages have often been mistaken for different species (3, 9).

### Tyrannosaur Behavior

A variety of studies have used biomechanical modeling, which incorporates mathematics, physics, and computer programming (41), to infer tyrannosaur behavior. Tyrannosaurs, especially the large, derived forms, have often been used as exemplars to demonstrate the utility of such computer models.

Most studies have suggested that although large tyrannosaurids might have been able to run at slow to moderate speeds at best (top speeds between 5 and 11 ms<sup>-1</sup>), they could not run nearly as fast as large athletic animals today, such as

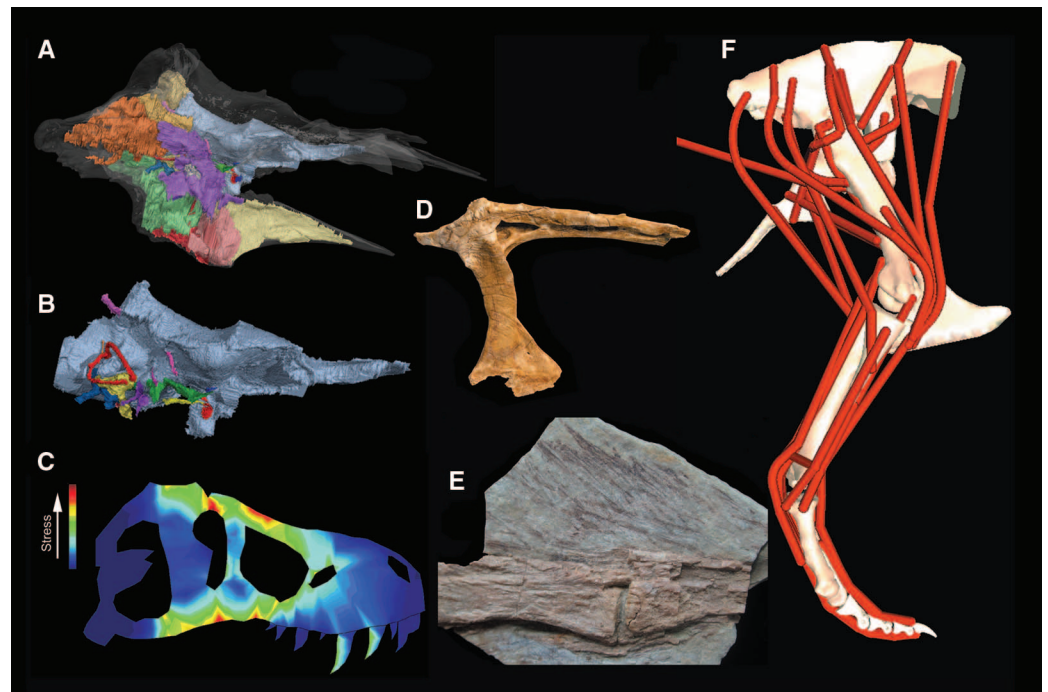


**Fig. 3.** Tyrannosaur soft tissues, feeding, and locomotion. (A) CT imagery of internal pneumatic sinuses of the braincase of *Alioramus altai* (19). (B) Endocast of brain, cranial nerves, and semicircular canals of *A. altai* (19). (C) Finite element analysis of a skull of *T. rex* (11, 47), showing high stresses (red colors) in the nasal and cheek regions (courtesy of E. Rayfield). (D) Lacrimal of *A. altai* (reversed), showing pneumatic spaces that housed air sacs (credit: M. Ellison). (E) Feathery integument along the tail of *Dilong paradoxus*. (F) Three-dimensional biomechanical model based on muscle reconstruction of the right hindlimb of *T. rex* (16), used to assess running mechanics.

growth in which the skulls of juveniles were entirely reshaped during ontogeny (9, 20, 39). This sequence has been reconstructed by cladistic analysis, based on the principle that ontogeny, like phylogeny, involves a hierarchically nested series of character changes (19, 39). During the growth of an individual species, the skull and jaws deepened, pneumatic bones inflated, ornamented structures enlarged and coarsened, sutural surfaces deepened and became more rugose, and the teeth became larger and thicker (9, 40) (Fig. 1). Changes have also been documented in the postcranial skeleton. Most notably, the forearm shortened and the long shin and foot of juveniles became shorter and stockier in adults (40). The differ-

ence between juveniles and adults was so great that even though large tyrannosaurids were not restricted to a pillar-like columnar limb posture to maximize mechanical advantage, they were still far from having very crouched, more birdlike postures (12, 41, 42). Aspects of tyrannosaurid anatomy, such as the long legs and large pelvic limb muscles, which intuitively seem to indicate fast running capacity, were inherited from small, presumably fast-running ancestors. Modeling studies have incorporated these features and shown that they did not make large tyrannosaurids extremely fast. However, it is worth noting that these studies rely on estimates of muscle size and attachment points, a somewhat conjectural

exercise, albeit constrained by the anatomy of extant relatives (12, 16), that plagues all such functional analyses.

Both trace fossils (bite marks, coprolites) and quantitative techniques have helped to reveal what tyrannosaurs ate and how they fed. Tyrannosaurid bite marks have been found on the bones of a wide diversity of species, including various other tyrannosaurs, demonstrating that they were ecological generalists (43). Bite mark patterns show that tyrannosaurids characteristically bit deeply into carcasses, often through bones, and then pulled back, creating long cuts [puncture-pull feeding sensu (44)]. Some *T. rex* bite marks (44) and coprolites with bone chunks (45) indicate that bone was fractured, ingested, and used for sustenance, a mammal-like attribute not seen in extant reptiles. The bite forces needed to crunch through bone would have been enormous. Biomechanical experiments have replicated the size and depth of fossilized bite marks and suggest that *T. rex* generated bite forces of at least 13,400 N. Maximal bite forces were probably greater (46).

Such large bite forces would have exerted tremendous stress on the skull. Tyrannosaurid skull shape and its relation to bite-induced stress have been extensively studied by finite element analysis. The results indicate that large tyrannosaurids had skulls optimized to endure strong bites, as various sutures absorbed stress and the fused nasals strengthened the snout (11, 47, 48). Similar biomechanical techniques have also been used to examine the role of the tyrannosaur neck in feeding, showing that it was important for generating pulling forces on food items and in inertial feeding (49), and the function of the unusual “pinched metatarsus” of the foot in turning, indicating that it was structured to resist shearing and twisting forces (50).

Little is known about the ecological community structure for most extinct animals, but large sample sizes permit some understanding of tyrannosaur ecology. Late Cretaceous tyrannosaurids were the first dinosaurs for which population dynamics—the balance between deaths and births that create a population’s age structure—could be assessed (10) (Fig. 4C). Like large birds and mammals, but unlike living reptiles, tyrannosaurids probably experienced extremely high neonate mortality, followed by few deaths after 2 years of age (presumably a release from predation), and then increased mortality at mid-life (probably from the rigors of reproduction), so that few individuals had a long reproductive life span. Furthermore, a number of fossil sites have preserved multiple individuals, suggesting that tyrannosaurs were at least occasionally gregarious (51). Bite marks indicate that individuals of the same species bit each other in the face during encounters (52), and many older individuals with gout, bacterial legions, and bone fractures have been reported, showing that disease and injury were common (53).

Multiple lines of evidence indicate that tyrannosaur ecological habits changed during ontogeny.

In Late Cretaceous tyrannosaurids, the difference in form between the lightly built, fleet juveniles and the larger, bulkier adults suggests that foraging behavior and targeted prey size changed as tyrannosaurs grew. The deep and muscular adult skull, with reinforced sutures and robust teeth, is well suited for sustaining high bite forces, whereas juveniles had none of these features (9, 39). Furthermore, the longer and more gracile hind limbs of juveniles indicate that they were relatively faster than adults (40), which has been corroborated by biomechanical analysis (12). These differences could have promoted major size-related shifts in ecology and behavior. It is plausible that adults preferentially attacked larger, but less mobile, prey than their younger counterparts. Such an ontogenetic shift is not seen in many familiar predators today (e.g., lions), but is present in extant crocodylians (54). As most basal tyrannosauroids are similar in skull and body proportions to juvenile Late Cretaceous tyrannosaurids, it is likely that they behaved and fed in a similar manner. However, detailed biomechanical analyses have yet to be carried out for most non-tyrannosaurid tyrannosauroids.

Whether *T. rex* and other large tyrannosaurs were scavengers or predators has generated much speculation and dispute. Bite marks from mass death assemblages of herbivorous dinosaurs show that tyrannosaurs scavenged on occasion (38). However, multiple reports of healed tyrannosaur bite marks on prey bones (55, 56) and tyrannosaur stomach contents containing remains of young dinosaurs (57) indicate that tyrannosaurs were capable of active predation. Like most carnivores, tyrannosaurs probably both scavenged and hunted.

One of the largest voids in our understanding of dinosaur biology is the sex of individual specimens. It has been suggested that female tyrannosaurs required a larger pelvic outlet for the passage of eggs, reflected by a greater span between the ischial bones and a smaller or more posteriorly located first tail chevron, but these indices find little neontological support in living archosaurs (58, 59). More recently, medullary bone, a calcium phosphate deposit for the use of shelling in eggs, was reported in one *T. rex* specimen (60). This provides a surefire identification of sex in dino-

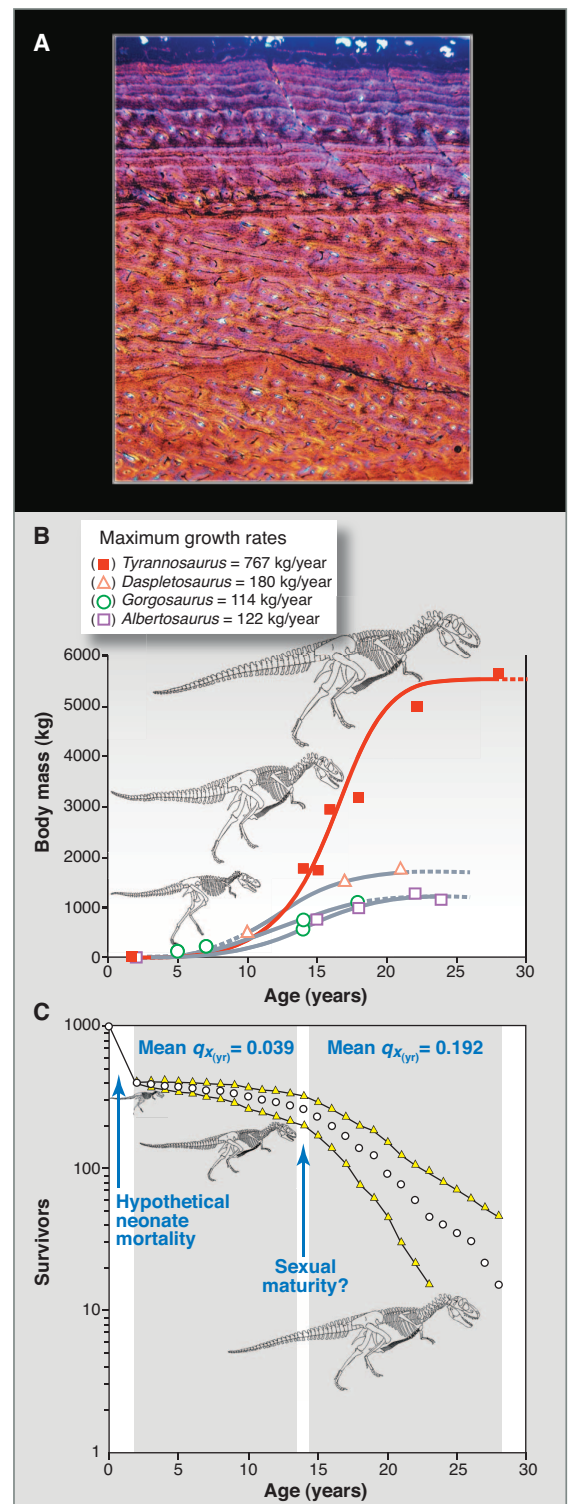


**Fig. 4.** Tyrannosaur growth and ecology. **(A)** Histological section of a *T. rex* dorsal rib, showing growth lines whose counts are used to reveal age and longevity. **(B)** Growth curves for North American tyrannosaurids derived from growth line counts and body size estimations for individuals showing how size changes with age. No sampled tyrannosaurid adults were more than 30 years old, and accelerated rather than prolonged development was the key to the great size of *T. rex* (8). **(C)** Survivorship curve for *Albertosaurus sarcophagus*. This tyrannosaur exhibited high neonate mortality, then few deaths after age two, and then increased mortality at mid-life (8).



saur, and holds much promise for future studies of dinosaur sex and ecology.

### Tyrannosaur Biogeography

Until recently, all tyrannosaur fossils were limited to Asia and North America, but the discovery and recognition of basal tyrannosauroids over the last decade reveals a more cosmopolitan distribution during their early evolution (5, 22–24, 61). Members of the Middle–Late Jurassic proceratosaurid radiation are known from Europe and Asia (5), whereas the Late Jurassic genus *Stokesosaurus* is known from both Europe and North America (24). However, all well-known tyrannosaurs more derived than *Eotyrannus* and *Stokesosaurus* exhibit a purely Asian or North American distribution. Faunal interchange between these continents is characteristic of most Campanian–Maastrichtian dinosaur clades and reflects an increasing Laurasian–Gondwanan provincialism during the final stages of the Age of Dinosaurs (62). Tyrannosaurs, because of their rich fossil record and well-studied phylogenetic relationships, are one of the primary sources of evidence for this long-established biogeographic hypothesis.

Emerging evidence, however, indicates that tyrannosaurs were likely present on the southern continents during their early evolutionary history. An isolated pubis from the Early Cretaceous of Australia was recently identified as belonging to a derived tyrannosaur (13). As contemporary Early–mid Cretaceous dinosaurs mostly belong to globally distributed clades (26), the absence of Gondwanan tyrannosaurs during this time had been a puzzling anomaly. Even with this discovery, if it is from a tyrannosaur, tyrannosaurs are absent in the well-sampled mid–Late Cretaceous units of South America, Africa, and Madagascar (63). It is possible that tyrannosaurs were rare on the southern continents during the Early–mid Cretaceous, and it is likely that Gondwanan forms did not persist into the latest Cretaceous, at least as common and ecologically dominant carnivores.

Most tyrannosaurs are known from mesic (moderate moisture) or seasonally mesic paleoenvironments, and their fossils are notably absent from xeric (dry) facies, even those that interfinger with tyrannosaur-bearing mesic sediments within the same sedimentary rock basins in Asia (64). This likely indicates that tyrannosaurs preferred wetter habitats, although it may still reflect a sampling bias. Wherever they were present during the Late Cretaceous in North America and Asia, tyrannosaurs were the sole apex predators in their environments. Multiple large tyrannosaurids co-occurred during some intervals in North America and Asia (19, 27), but the Maastrichtian of western North America was solely dominated by *T. rex* (39). In contrast, most nontyrannosaurid tyrannosauroids are found alongside larger non-

tyrannosaur predators, demonstrating that tyrannosaurs did not exclusively dominate the apex predator niche, regardless of where they lived, until the final 20 million years of the Cretaceous.

### Conclusion

*Tyrannosaurus rex* and its close relatives are the most intensely studied dinosaurs. Derived tyrannosaurs such as *Albertosaurus*, *Tarbosaurus*, and *Tyrannosaurus* are known from more fossils than are most other dinosaurs, and these specimens span the spectrum from juvenile to adult. Many modern analytical approaches have been pioneered with the use of *Tyrannosaurus* and close kin, and the results of these studies are allowing for quantitative comparisons between the biology of extinct dinosaurs and living species.

### References and Notes

- We use the vernacular “tyrannosaur” to refer to members of the clade Tyrannosauroidae, defined as the most inclusive clade containing *Tyrannosaurus rex* but not *Ornithomimus edmontonicus*, *Troodon formosus*, or *Velociraptor mongoliensis*. The more derived Tyrannosauridae is defined as the least inclusive clade containing *T. rex*, *Gorgosaurus libratus*, and *Albertosaurus sarcophagus* (4).
- H. F. Osborn, *Bull. Am. Mus. Nat. Hist.* **21**, 259 (1905).
- D. A. Russell, *Nat. Mus. Nat. Sci. Pub. Paleontol.* **1**, 1 (1970).
- P. C. Sereno *et al.*, *Science* **326**, 418 (2009).
- O. W. M. Rauhut, A. C. Milner, S. Moore-Fay, *Zool. J. Linn. Soc.* **158**, 155 (2010).
- C. A. Brochu, *Soc. Vert. Paleontol. Mem.* **7**, 1 (2003).
- L. M. Witmer, R. C. Ridgely, *Anat. Rec.* **292**, 1266 (2009).
- G. M. Erickson *et al.*, *Nature* **430**, 772 (2004).
- T. D. Carr, *J. Vertebr. Paleontol.* **19**, 497 (1999).
- G. M. Erickson, P. J. Currie, B. D. Inouye, A. A. Winn, *Science* **313**, 213 (2006).
- E. J. Rayfield, *Proc. Biol. Sci.* **271**, 1451 (2004).
- J. R. Hutchinson, M. Garcia, *Nature* **415**, 1018 (2002).
- R. B. J. Benson, P. M. Barrett, T. H. Rich, P. Vickers-Rich, *Science* **327**, 1613 (2010).
- X. Xu *et al.*, *Nature* **431**, 680 (2004).
- M. H. Schweitzer, J. L. Wittmeyer, J. R. Horner, J. K. Toporski, *Science* **307**, 1952 (2005).
- M. T. Carrano, J. R. Hutchinson, *J. Morphol.* **253**, 207 (2002).
- T. R. Holtz, in *The Dinosauria*, D. B. Weishampel, P. Dodson, H. Osmólska, Eds. (Univ. of California Press, Berkeley, ed. 2, 2004), pp. 111–136.
- Supporting material is available on Science Online.
- S. L. Brusatte, T. D. Carr, G. M. Erickson, G. S. Bever, M. A. Norell, *Proc. Natl. Acad. Sci. U.S.A.* **106**, 17261 (2009).
- T. D. Carr, T. E. Williamson, *J. Vertebr. Paleontol.* **30**, 1 (2010).
- D. Li, M. A. Norell, K. Q. Gao, N. D. Smith, P. J. Makovicky, *Proc. Biol. Sci.* **277**, 183 (2010).
- X. Xu *et al.*, *Nature* **439**, 715 (2006).
- S. Hutt, D. W. Naish, D. M. Martill, M. J. Barker, P. Newberry, *Cretac. Res.* **22**, 227 (2001).
- R. B. J. Benson, *J. Vertebr. Paleontol.* **28**, 732 (2008).
- Q. Ji, S.-A. Ji, L.-J. Zhang, *Geol. Bull. China* **28**, 1369 (2009).
- S. L. Brusatte *et al.*, *Naturwissenschaften* **96**, 1051 (2009).
- P. J. Currie, *Acta Palaeontol. Pol.* **48**, 191 (2003).
- J. H. Hurum, K. Sabath, *Acta Palaeontol. Pol.* **48**, 161 (2003).
- R. E. Molnar, *Palaeont. A* **217**, 137 (1991).
- C. A. Brochu, *J. Vertebr. Paleontol.* **20**, 1 (2000).
- D. K. Zelenitsky, F. Therrien, Y. Kobayashi, *Proc. Biol. Sci.* **276**, 667 (2009).
- P. J. Currie, D. Badamgarav, E. B. Koppelhus, *Ichnos* **10**, 1 (2003).
- X. Xu, X. T. Zheng, H. L. You, *Nature* **464**, 1338 (2010).
- X. Xu, X. T. Zheng, H. L. You, *Proc. Natl. Acad. Sci. U.S.A.* **106**, 832 (2009).
- M. H. Schweitzer *et al.*, *Science* **316**, 277 (2007).
- T. G. Kaye, G. Gaugler, Z. Sawlowicz, A. Stepanova, *PLoS ONE* **3**, e2808 (2008).
- C. L. Organ *et al.*, *Science* **320**, 499 (2008).
- G. M. Erickson, *Sci. Am.* **9**, 32 (1999).
- T. D. Carr, T. E. Williamson, *Zool. J. Linn. Soc.* **142**, 479 (2004).
- P. J. Currie, *Can. J. Earth Sci.* **40**, 651 (2003).
- S. M. Gatesy, M. Bäker, J. R. Hutchinson, *J. Vertebr. Paleontol.* **29**, 535 (2009).
- W. I. Sellers, P. L. Manning, *Proc. Biol. Sci.* **274**, 2711 (2007).
- A. R. Jacobsen, *Hist. Biol.* **13**, 17 (1998).
- G. M. Erickson, K. H. Olson, *J. Vertebr. Paleontol.* **16**, 175 (1996).
- K. Chin, T. T. Tokaryk, G. M. Erickson, L. C. Calk, *Nature* **393**, 680 (1998).
- G. M. Erickson *et al.*, *Nature* **382**, 706 (1996).
- E. J. Rayfield, *Zool. J. Linn. Soc.* **144**, 309 (2005).
- E. Snively, D. M. Henderson, D. S. Phillips, *Acta Palaeontol. Pol.* **51**, 435 (2006).
- E. Snively, A. P. Russell, *Paleobiology* **33**, 610 (2007).
- E. Snively, A. P. Russell, *J. Morphol.* **255**, 215 (2003).
- P. J. Currie, *Gaia* **15**, 271 (2000).
- D. H. Tanke, P. J. Currie, *Gaia* **15**, 168 (2000).
- D. H. Tanke, B. M. Rothschild, *New Mex. Mus. Nat. Hist. Sci. Bull.* **20**, 1 (2001).
- P. Dodson, *J. Zool.* **175**, 315 (1975).
- K. Carpenter, *Gaia* **15**, 135 (2000).
- J. Happ, in *Tyrannosaurus rex: The Tyrant King*, P. Larson, K. Carpenter, Eds. (Indiana Univ. Press, Bloomington, 2008), pp. 354–368.
- D. J. Varricchio, *J. Paleontol.* **75**, 401 (2001).
- G. M. Erickson, A. K. Lappin, P. Larson, *Zool* **108**, 277 (2005).
- A. Prieto-Marquez, P. M. Gignac, S. Joshi, *J. Vertebr. Paleontol.* **27**, 603 (2007).
- M. H. Schweitzer, J. L. Wittmeyer, J. R. Horner, *Science* **308**, 1456 (2005).
- A. O. Averianov, S. A. Krasnolutskii, S. V. Ivantsov, *Proc. Zool. Inst. RAS* **314**, 42 (2010).
- P. Upchurch, C. A. Hunn, D. B. Norman, *Proc. Biol. Sci.* **269**, 613 (2002).
- D. B. Weishampel *et al.*, in *The Dinosauria*, D. B. Weishampel, P. Dodson, H. Osmólska, Eds. (Univ. of California Press, Berkeley, ed. 2, 2004), pp. 517–606.
- P. J. Makovicky *et al.*, *Proc. Biol. Sci.* **277**, 191 (2010).
- Funded by NSF Graduate Research Fellowship (S.L.B.), American Museum of Natural History (S.L.B., M.A.N.), NSF (M.A.N., G.M.E., J.R.H., P.J.M.), Natural Environment Research Council (J.R.H.), and National Natural Science Foundation of China and Special Funds For Major State Basic Research Projects of China (X.X.).

### Supporting Online Material

www.sciencemag.org/cgi/content/full/329/5998/1481/DC1  
Materials and Methods  
SOM Text  
Fig. S1  
Table S1  
References  
10.1126/science.1193304

# Island Biogeography Reveals the Deep History of SIV

Michael Worobey,<sup>1</sup> Paul Telfer,<sup>2,3</sup> Sandrine Souquière,<sup>3</sup> Meredith Hunter,<sup>2</sup> Clint A. Coleman,<sup>2</sup> Michael J. Metzger,<sup>2</sup> Patricia Reed,<sup>2,3</sup> Maria Makuwa,<sup>3</sup> Gail Hearn,<sup>4</sup> Shaya Honarvar,<sup>4</sup> Pierre Roques,<sup>3</sup> Cristian Apetrei,<sup>2</sup> Mirdad Kazanji,<sup>3</sup> Preston A. Marx<sup>2\*</sup>

The ubiquity of simian immunodeficiency virus (SIV) in African nonhuman primates and the discovery of ancient endogenous lentiviruses (1) suggest that SIV is very old. Conversely, molecular clock methods calibrated by using modern sequences indicate a time scale of just centuries (2, 3). To resolve this conundrum, we sampled monkeys on Bioko Island, Equatorial Guinea, which was isolated from Africa as sea levels rose 10,000 to 12,000 years before the present (yr B.P.) (fig. S1) (4). Bushmeat specimens were screened by SIV serological tests and reverse transcription polymerase chain reaction (RT-PCR) and sequencing of conserved viral *pol* gene fragments [472 to 633 base pairs (bp)], followed by phylogenetic analyses.

Of 79 individuals from six species, we detected 22 sequence-confirmed SIV positives in four species, with a prevalence of 22 to 33% (table S1). Phylogenetic analyses (Fig. 1 and figs. S2 and S3) revealed previously uncharacterized species-specific SIV lineages in *Cercopithecus erythrotis erythrotis* (SIVreg-Bioko), *Colobus satanas satanas* (SIVble-Bioko), and *Cercopithecus preussi insularis* (SIVprg-Bioko). The fourth, the Bioko drill, *Mandrillus leucophaeus poensis*, is infected with SIVdrl-Bioko and has a mainland conspecific

counterpart, *Mandrillus leucophaeus leucophaeus*, infected with SIVdrl (fig. S1). These viruses form a monophyletic group with SIVmnd-2 from the mandrill, the closest relative of the drill (Fig. 1).

Each Bioko SIV lineage shares ancestry with a mainland virus found in a monkey of the same genus (Fig. 1). Barring the possibility that humans introduced multiple species-specific SIV lineages to the wild monkey populations of Bioko, the mainland and island SIVdrl variants must have been evolving independently since Bioko became isolated ~10,000 yr B.P., and perhaps longer given the high levels of genetic diversity seen within local SIV populations. We used the SIVdrl/SIVdrl-Bioko ancestor dated ~10,000 yr B.P. to calibrate our molecular clock phylogenetic analysis. From amino acid sequences, the mean estimate of the time of the most recent common ancestor (TMRCA) of SIV was 76,794 yr B.P. (95% highest probability density from 32,821 to 132,780). This is older than TMRCA estimates from nucleotides [using all three codon positions, 49,129 (29,078 to 71,268); with third positions only, 28,077 (19,184 to 37,305)]. This pattern suggests that the more rapidly evolving the character, the more biased the dating estimate becomes toward the present. Perhaps both the nu-

cleotide and the amino acid analyses run up against stringent evolutionary constraints and saturation problems (fig. S4), which makes correcting for repeated substitutions at the same site difficult.

The four Bioko SIV lineages are genetically diverse and phylogenetically connected with those found across continental Africa, which leaves little doubt that the age of SIV is much greater than previously inferred (3). Molecular clock analyses of RNA viruses produce plausible, often unassailable, inferences over the short term, but our results raise the possibility of fundamental problems at deeper times scales for SIV and perhaps other viruses. Although we accept current estimates of HIV-1 and HIV-2 TMRCA of <100 yr B.P., implying short-term evolutionary rates ~125 times faster than our (conservative) Bioko-calibrated SIV estimate, the possibility of a deeper-than-assumed history for HIV may be worth investigating.

SIVs have been present in African primates for more than 32,000 years, which suggests that humans may have had sporadic encounters with these viruses for millennia. Changes in human behavior or ecology were likely necessary before nascent HIVs could become established (5, 6). Although evidence of codivergence between SIV and its natural hosts is still lacking, our results are suggestive that generally low pathogenicity of SIV is likely a consequence of long-term host-virus coevolution. A similar accommodation between HIV and humans should therefore not be expected to arise soon.

## References and Notes

1. R. J. Gifford et al., *Proc. Natl. Acad. Sci. U.S.A.* **105**, 20362 (2008).
2. P. M. Sharp et al., *Biochem. Soc. Trans.* **28**, 275 (2000).
3. J. O. Wertheim, M. Worobey, A. J. Drummond, *PLoS Comput. Biol.* **5**, e1000377 (2009).
4. P. J. Jones, *Biodivers. Conserv.* **3**, 772 (1994).
5. E. Drucker, P. G. Alcades, P. A. Marx, *Lancet* **358**, 1989 (2001).
6. J. D. de Sousa, V. Müller, P. Lemey, A. M. Vandamme, *PLoS One* **5**, e9936 (2010).
7. We thank T. M. Butynski, J. M. Esara Echube, A. Lackner, and M. Sanderson for assistance and comments and acknowledge support from NIH grants 1R01AI27698 and 1R01AI44596, a Tulane Phase II Enhancement Grant, the ExxonMobil Foundation, and the David and Lucile Packard Foundation. Newly reported SIV sequences have been deposited in GenBank under accession numbers HM363406 to HM363427. P. Reed and P.T. are at the Wildlife Conservation Society, Bronx, NY, USA. P. Roques is at Commissariat à l'Energie Atomique-Life Science Division, Fontenay-aux-Roses, France. C.A. is at University of Pittsburgh, PA. M.J.M. is at University of Washington, Seattle, WA. M.K. is at Institut de Bangui, Bangui, Central African Republic.

## Supporting Online Material

www.sciencemag.org/cgi/content/full/329/5998/1487/DC1

Materials and Methods

Figs. S1 to S6

Table S1

References

14 April 2010; accepted 23 July 2010

10.1126/science.1193550

<sup>1</sup>University of Arizona, Tucson, AZ 85721, USA. <sup>2</sup>Tulane National Primate Research Center, Covington, LA 70433, USA.

<sup>3</sup>Center for International Medical Research, Franceville, Gabon.

<sup>4</sup>Drexel University, Philadelphia, PA 19104, USA.

\*To whom correspondence should be addressed. E-mail: pmarx@tulane.edu

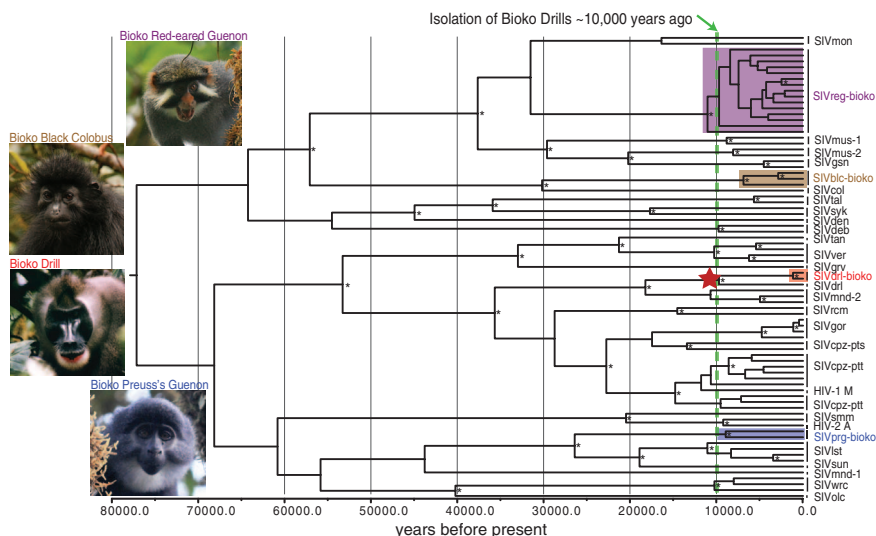


**Fig. 1.** The biogeographical calibration point: the isolation of Bioko ~10,000 years ago. The dashed green line indicates the most recent time the current mainland and Bioko drill viruses could have shared a common ancestor (red star). This is a maximum clade credibility tree from amino acid sequences, with node heights (yr B.P.) representing the mean value of the posterior sample of the Bayesian analysis. Well-supported nodes (0.95 or greater posterior probability) are marked with asterisks. Viruses from Bioko species are highlighted with colored rectangles. See fig. S3 for species-specific SIV abbreviations and probability distributions of the TMRCA for each node. [Photo credits: for red-eared guenon and black colobus, T. Laman; drill, C. Santiestevan; Preuss's guenon, R. Berg]



# Hemispheric Aerosol Vertical Profiles: Anthropogenic Impacts on Optical Depth and Cloud Nuclei

Antony Clarke\* and Vladimir Kapustin

Understanding the effect of anthropogenic combustion upon aerosol optical depth (AOD), clouds, and their radiative forcing requires regionally representative aerosol profiles. In this work, we examine more than 1000 vertical profiles from 11 major airborne campaigns in the Pacific hemisphere and confirm that regional enhancements in aerosol light scattering, mass, and number are associated with carbon monoxide from combustion and can exceed values in unperturbed regions by more than one order of magnitude. Related regional increases in a proxy for cloud condensation nuclei (CCN) and AOD imply that direct and indirect aerosol radiative effects are coupled issues linked globally to aged combustion. These profiles constrain the influence of combustion on regional AOD and CCN suitable for challenging climate model performance and informing satellite retrievals.

Natural and anthropogenic combustion emissions, including biomass burning, are major sources of CO, CO<sub>2</sub>, and aerosol particles. Aerosols influence Earth's radiation balance through direct interaction with solar radiation (1–3) and by modifying cloud droplet number and radiative effects (4). Long-range aerosol transport affects regions more than 10,000 km downwind of sources (5, 6), but sources, vertical mixing, lifetime, and removal processes are highly variable and uncertain. Constraining uncertainties in global assessments requires vertical profiles of regionally representative aerosol data to evaluate column radiative effects, refine satellite products (7), and challenge chemical transport models (3, 8). Such factors motivated the NSF and NASA to initiate aircraft experiments in the 1990s to measure in situ gas and aerosol properties over diverse regions. Initial missions (Fig. 1 and Table 1)—including the Aerosol Characterization Experiment (ACE)–1 over the Southern Ocean and the Pacific Exploratory Mission Tropics (PEMT A and B) over the South Pacific—focused on “background” environments. In the next decade, similar experiments addressed increasingly polluted regions downwind of Asia, North America and, most recently, the megacity of Mexico City, Mexico. Satellite and model capabilities have increased dramatically during this time, making it essential to harmonize them with in situ observations for validated assessments of aerosol direct and indirect effects and climate influences (3, 8).

In this work, we compare consistent measurements for regions ranging from cleanest to most polluted (Fig. 1) and for ~1000 vertical profiles employing the same instrumentation (9). We focus on aerosol light scattering ( $\sigma_{sc}$ ), fundamental to assessing column aerosol optical depth (AOD), aerosol radiative effects, and aerosol

forcing (3), total aerosol number (condensation nuclei at ambient temperature, hereafter referred to as CN<sub>cold</sub>, diameter  $\sim 10$  nm), and nonvolatile CN (CN<sub>hot</sub>, diameter  $> 10$  nm, remaining at 300°C after a residence time of  $\sim 1$  to 2 s). All are shown at standard temperature and pressure to allow direct comparison of concentrations at various altitudes and their relation to CO mixing ratios. Because continuous profiles were infrequent, we show regional 1-min data for all altitudes. The effective profiles are indicated by the number of passes through 1- and 4-km altitudes (Table 1).

The difference between the total number (CN<sub>cold</sub>) and CN<sub>hot</sub> is defined as volatile CN. In the remote free troposphere (FT), these smaller volatile aerosols are frequently nucleated in cloud outflow and associated with elevated sulfuric acid (10). Their concentrations increase with altitude over the tropical Pacific and Southern Oceans (11), as predicted by theory (12), and they are typically smaller than the aged primary aerosol linked to continental combustion sources that often dominate  $\sigma_{sc}$  and CN<sub>hot</sub> (10, 13). Their smaller size makes them less effective as cloud condensation nuclei (CCN) and at scattering light or contributing to AOD. Because CN<sub>hot</sub> are typically larger internal mixtures with a major soluble-mass component (10), they commonly dominate CCN at low supersaturations near 0.2%, a value commonly associated with low clouds in the marine boundary layer (MBL) (14). The intermode minimum in MBL size distributions often found near 60 to 100 nm is a result of activation and cloud processing of CCN larger than this size, whereas the smaller sizes are not effective CCN in such clouds (15). Downwind of source regions we find a strong relation between CN<sub>hot</sub> and a measured particle number larger than  $\sim 80$  to 100 nm, prompting our referring to the latter as a proxy for CCN (CCN<sub>proxy</sub>) (16). This is shown in Fig. 2, A and B, for the Intercontinental Chemical Transport Experiment (INTEX-B), in which we encountered both very clean and polluted air. CN<sub>cold</sub> clearly exceed CCN<sub>proxy</sub> for all locations, whereas CN<sub>hot</sub> shows a better correspondence. In INTEX-B air with low CO (blue) and CCN<sub>proxy</sub> below

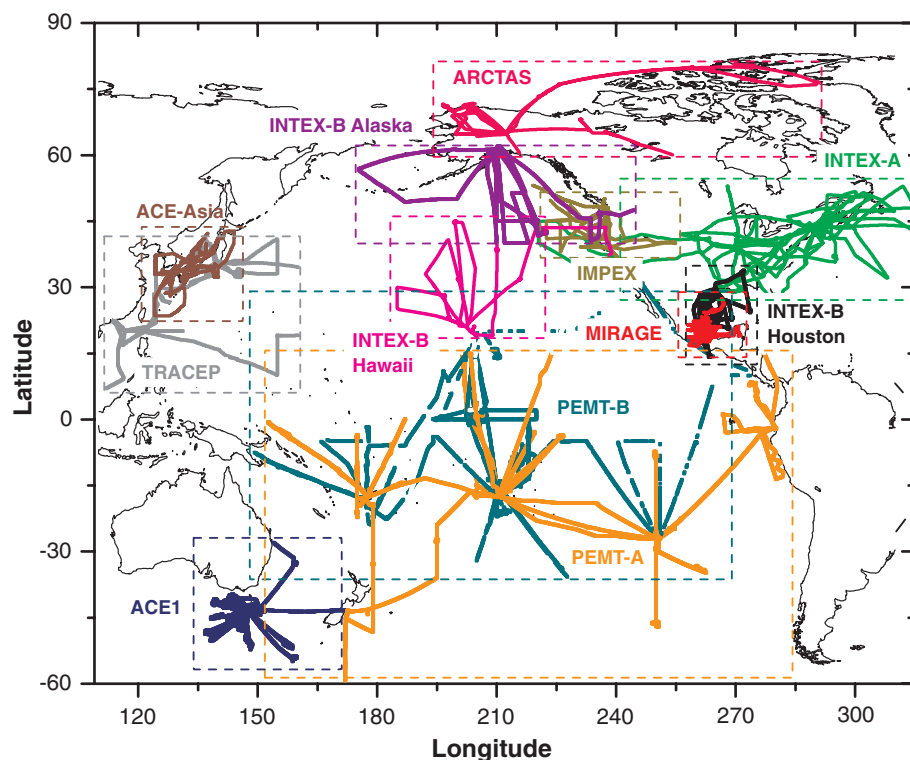


**Fig. 1.** Flight tracks for all experiments, as identified in Table 1 and included in the SOM (40).

School of Ocean and Earth Science and Technology (SOEST), University of Hawaii, Honolulu, HI 96822, USA.

\*To whom correspondence should be addressed. E-mail: tclarke@soest.hawaii.edu

$\sim 50 \text{ cm}^{-3}$ , the CNhot overestimates the integrated CCNproxy, but it can also underestimate the proxy. These cases are generally a small fraction of those in the MBL or those in which  $\sigma_{\text{sc}}$  contributes substantially to AOD (Fig. 3). In cases such as ACE-1 (A1) and PEMT-B (PB), we use data from other instruments to establish regional mean CCN and AOD.

Aerosol light scattering,  $\sigma_{\text{sc}}$ , measured at 450, 550, and 700 nm, yields the angstrom exponent,  $\alpha$ , a nondimensional measure of its wavelength dependence (17).  $\alpha$  varies with size distribution and ranges from  $\sim 2$  for submicrometer accumulation-mode particles down to near zero for coarse particles such as dust or sea salt (13). We use an  $\alpha$  of  $> 1.3$  to stratify data dominated by smaller sizes, characteristic of combustion sources, from values influenced by coarse dust or sea salt (red). Dust generally dominates coarse sizes, except for near-surface maritime altitudes influenced by sea salt, as in clean marine settings such as A1, PB, and International Transport Experiment-B Hawaii, INTEX-B Hawaii (IBH). The integral of ambient  $\sigma_{\text{sc}}$  over altitude approximates column AOD, a quantity commonly determined from satellites and used to model aerosol optical effects (18).

Here, we emphasize the relation of aerosol to CO because more than 70% of atmospheric CO is attributed to fossil fuel or biomass burning (19), and much of the latter is anthropogenic. CO lifetimes range from a few weeks near the equator to a few months nearer the poles (19). This implies changes of less than 15% for transport times of about 1 week for springtime Pacific aerosol data discussed here. Figure 2B shows that highest CNhot occur in regions of highest CO, but their greater change in concentration relative to CO reflects more rapid removal via precipitation scavenging.

Figure 3 shows vertical profiles CNcold, CNhot, and dry  $\sigma_{\text{sc}}$  for all regions indicated in Fig. 1. Data points are colored with CO concentrations to reveal their association with combustion. Because combustion aerosol is dominated by submicrometer sizes, we use  $\alpha$  as a multiplier to scale the size of points plotted for  $\sigma_{\text{sc}}$ . This approach visually highlights contributions from smaller aerosol sizes (larger  $\alpha$ ) while visually suppressing those dominated by coarse dust and sea salt associated with  $\alpha$  approaching zero. Because most coarse aerosols are not directly associated with CO but can contribute substantially to  $\sigma_{\text{sc}}$  and AOD, their influence is separately revealed in the adjacent histograms. An  $\alpha > 1.3$  separates histograms of scattering values dominated by submicrometer combustion sources (blue) from those influenced by a substantial amount of coarse dust or sea salt (red).

**Regional characteristics.** The top two rows are the least polluted regions with the lowest CO values: ACE-1 (A1) near Tasmania and PB in the equatorial Pacific in March and April, the season of low biomass burning in the Southern Hemisphere. Both exhibit increasing CN but decreasing  $\sigma_{\text{sc}}$  with altitude and low CNhot fraction, indicative of numerous small volatile particles. These natural volatile aerosols, nucleated homogeneously in cloud outflow (20), age during subsidence before being entrained into the boundary layer (10–12). Although they can grow to CCN sizes in the MBL by the addition of mass,  $\sigma_{\text{sc}}$  in marine regions is often dominated by coarse sea salt. Point sizes are small (suppressed) for coarse sea salt on profile plots, but the histograms reveal where it dominates extinction in clean oceanic regions (21). Because CNhot can underestimate CCNproxy due to larger volatile aerosols in the cleanest environments, we include the campaign mean profile of CCN measured during A1 at 0.2% S (14). CCN

concentrations exceed CNhot below 4 km but are similar at higher altitudes where more aged polluted aerosol was evident (22, 23).

Data from PEM-Tropics A (PA) are from a region similar to PB (Fig. 1) but are taken during the biomass burning period and include regions along coastal South America. We later separate these data into the more remote (PA1) west of  $260^\circ\text{W}$  versus the data nearer South America dominated by the higher CO values (PA2, orange). PA2 data with CO values exceeding  $\sim 100$  parts per billion (ppb) were encountered near 3 km altitude off Peru and Ecuador (Fig. 1) and linked to biomass burning in South America, but values approaching 100 ppb at 3 to 4 km in the central Pacific and associated with excursions in scattering and CNhot (24, 25) originated from the western Pacific. Between 1 and 5 km, the relative increase in  $\sigma_{\text{sc}}$  associated with elevated CO is clearly greater than the relative increase in number, indicating that aerosol mean size also increases.

In contrast to clean marine cases, conditions over the North Pacific during spring, when Asian pollution and dust transport is most active (5, 26), are represented in rows [Aerosol Characterization Experiment-Asia, ACE-Asia (AA); Transport and Chemical Evolution over the Pacific, TRACE-P (TP); IBH, Intercontinental and Megacity Pollution Experiment, IMPEX (IP); Intercontinental Chemical Transport Experiment-A (IA); Arctic Research of the Composition of the Troposphere from Aircraft and Satellite, ARCTAS (AS)]. Aerosol near-source regions are dominated by anthropogenic combustion along with dust for AA (27) and biomass burning for TP (26), and near-surface CO often exceeds 200 parts per billion by volume (ppbv) for both. CN below 1-km range between 1000 and  $10,000 \text{ cm}^{-3}$  with  $\sigma_{\text{sc}}$  centered near  $100 \text{ Mm}^{-1}$ . The AA histograms show the broad range of  $\sigma_{\text{sc}}$  for both pollution- and dust-dominated cases ( $\alpha < 1.3$ ). Below 2 km, high  $\sigma_{\text{sc}}$  values for AA are due to both enhanced pollution and dust. Both CN and  $\sigma_{\text{sc}}$  have minima near 3.5 km, whereas above 4 km, both are influenced by long-range transport from European (27) and other sources to the west. The similar concentrations for CN and CNhot aloft confirm the absence of smaller volatile aerosols, but the relative increase in  $\sigma_{\text{sc}}$  reveals their larger size. Unlike AA, the CN concentrations and  $\sigma_{\text{sc}}$  during TP differ from unperturbed regions (e.g., A1, PB), mostly at lower altitudes. Between 2 and 4 km, CN and  $\sigma_{\text{sc}}$  range down to background, except for events associated with biomass burning (28, 29), also captured in models (30). These differences aloft between AA and TP reflect the Hadley circulation that favors the FT transport of volatile nuclei formed in air scavenged by equatorial convection to latitudes near  $30^\circ\text{N}$  (10, 11).

The last three rows in Fig. 3 are regional data off the east coast of North America (IA), in the vicinity of Mexico City [Megacities Impacts on Regional and Global Environments, MIRAGE (MI)], and over Mexico [INTEX-B Mexico (IBM)]. IA concentrations below 2 km appear similar to

**Table 1.** Experiment identifiers (Project), number of profiles through 1 and 4 km, dates, number of 1-min measurements, mean column effective CO in excess of a “background” of 50 parts per billion by volume (CO-50), and mean dry differential AOD from  $\sigma_{\text{sc}}$  over flight altitude for  $\alpha > 1.3$ . The latter stratification for  $\alpha > 1.3$  also selects for optically effective submicrometer sizes that increase with pollution and include the greatest number active as CCN at 0.2 to 0.4% S.

Project	Number of profiles		Project, aircraft, and dates	Number of measurements (<2 km, 2 to 4 km, >4 km)	CO-50 (column) ( $\alpha > 1.3$ )	AOD
	1 km	4 km				
A1	138	104	ACE-1, C130, 10 Nov to 15 Dec 1995	2373, 957, 1587	20	0.006
PB	104	73	PEMT-B, P3B/DC8, Mar to Apr 1999	1537, 596, 1566	16	0.012
PA	96	77	PEMT-A, P3B/DC8, Aug to Sept 1996	1509, 755, 1404	47	0.033
AA	292	134	Ace-Asia, C130, 30 Mar to 2 May 2001	2665, 933, 1253	146	0.209
TP	129	101	TRACE-P, P3B, 24 Feb to 10 Apr 2001	1592, 1337, 1681	129	0.121
IBH	28	34	INTEX-B, DC8, Hawaii, 23 to 28 Apr 2006	267, 224, 651	78	0.020
IP	101	136	IMPEX, C130, 17 Apr to 15 May 2006	1103, 1256, 2007	93	0.094
IBA	32	36	INTEX-B, DC8, Alaska, 4 to 15 May 2006	265, 292, 1034	103	0.056
AS	45	46	ARCTAS, P3B, 25 Mar to 9 Apr 2008	639, 508, 1484	126	0.144
IA	185	185	INTEX-A, DC8, 1 Jul to 14 Aug 2004	1813, 928, 2178	72	0.117
MI	34	101	MIRAGE, C130, 4 to 29 Mar 2006	106, 854, 1085	98	0.281
IBM	52	50	INTEX-B, DC8, Houston, TX, 4 to 19 Mar 2006	693, 671, 818	78	0.232



those of AA and TP, but with somewhat lower CO, possibly because IA occurred in summer. Above 2 km, IA also has lower CO concentration than AA, but higher number and volatility. MI and IBM flights are largely in the subtropics over Mexico. As Mexico City is located above 2 km, emissions can be transported long distances in the FT before removal. IBM data from regional Mexico exhibit typical elevated  $\sigma_{sc}$  and CO near the surface. Like TP, values aloft on IBM and at times on MI are very similar to the cleanest regions (A1, PB), indicating the influence of the Hadley circulation bringing nuclei northward from equatorial convection.

**Implications of regionally representative profiles.** The color coding on these Pacific regional springtime altitude profiles reveals the long-range influences of CO from combustion sources on hemispheric  $\sigma_{sc}$ , CNcold, and CNhot. The contribution of smaller submicrometer aerosols to regional AOD<sub>1.3</sub> ( $\alpha > 1.3$ ) (Table 1) calculated from dry  $\sigma_{sc}$  scales approximately with aerosol submicrometer mass. Ambient total AOD will exceed values calculated from dry  $\sigma_{sc}$  profiles by ~30% due to water uptake at ambient humidity (31, 32) and ~0.02 contributed from aerosol above peak aircraft altitudes (21, 33). These profiles also reveal the influence of deep convection (A1, PB, PA) in scavenging aerosol mass, evident as lower  $\sigma_{sc}$  aloft, but increasing concentrations of volatile nuclei in “clean” aged air with low CO concentration < 70 ppbv. These features, present in all regions south of 30°N (A1, PB, PA, IBH, and IBM), demonstrate the

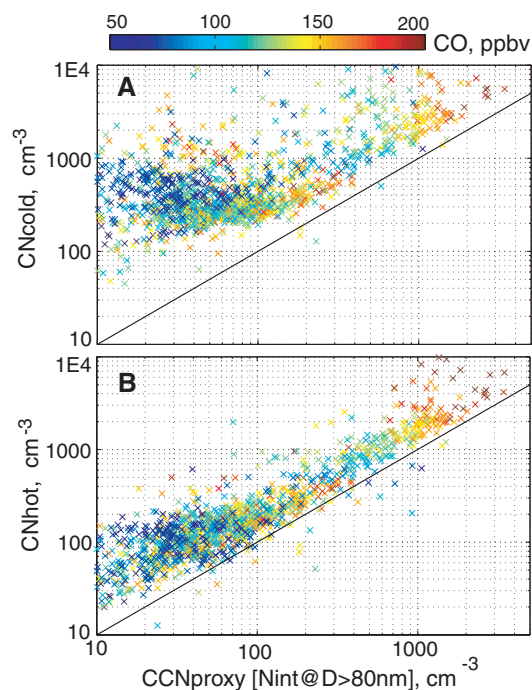
importance of the Inter-Tropical Convergence Zone for both aerosol removal and new particle generation, as well as its coupling to the Hadley cell circulation and hemispheric aerosol cycling. North of 30°N, enhanced CO,  $\sigma_{sc}$ , and CNhot indicate dominant contributions from lofted continental combustion aerosols to the west. When present, their larger surface area will suppress the formation and the aging of smaller “natural” aerosols up to CCN sizes due to their preferential uptake of precursor gases and/or increasing the loss of smaller sizes through coagulation. Such combustion-derived aerosols (16, 34) include larger sizes effective as CCN that can influence cloud properties far downwind of sources when they subside into the MBL (5).

The clean marine cases in the Southern Ocean and equatorial Pacific (A1, PB) reveal low CO, low accumulation-mode aerosol, low associated CNhot, and a resulting low differential AOD<sub>1.3</sub> near 0.02 (due primarily to natural sulfate). AOD<sub>1.3</sub> values for PA1 during the biomass burning season exceeded those for PB and are linked to changes in CO profiles. Near major source regions (AA, TP, IA, MI, PA2), elevated CO is clearly linked to dry accumulation-mode aerosol with large increases in AOD<sub>1.3</sub> (Table 1). Total AOD is also increased by sea salt in marine areas (A1, PA, PB, IBH) or dust (AA, TP, MI, IP) in a continental air mass. Because dust leaving Asia is often mixed with pollution aerosol (29), the latter can also substantially affect  $\sigma_{sc}$  and AOD for  $\alpha < 1.3$  (e.g., AA), as revealed in the histograms of  $\sigma_{sc}$  for the different regions and altitudes. This illustrates the advan-

tage of using  $\alpha$  to scale point sizes and to stratify the histograms (Fig. 3) to focus on the smaller combustion-related sizes.

Although INTEx-B Alaska (IBA), IP, IBH, and AS profiles occurred downwind of Asia 5 to 7 years after the AA and TP experiments, it is unlikely that possible changes in near-surface mean emissions will alter their general features discussed here. IBA and IP over the Pacific have lower near-surface numbers and scattering relative to CO compared with either source regions, suggestive of removal in the boundary layer during transport. CNhot profiles for IBA indicate that about half of the measurements are volatile, much more than the near-surface data for AA, TP, or AS. As values of  $\sigma_{sc}$  are much higher than in regions that favor nucleation, this suggests diverse encounters with polluted air and cleaner air with high volatile-particle concentrations, similar to the TP data above 5 km. CNhot for IBA and IP profiles track with the scattering, indicative of their relation to larger sizes. Their concentrations of 400 to 800 cm<sup>-3</sup> aloft exceed those in the MBL, implying that they provide enough nuclei to influence CCN in the MBL after subsidence and entrainment (5).

Enhanced  $\sigma_{sc}$  between 2 and 4 km over the North Pacific for IP and 3 and 5 km for IBA is consistent with frontal lifting of Asian pollution over a potential temperature surface sloping to the north (5). Observations and models indicate that Asian plumes can often subside and entrain into the MBL (5), and the Harvard University chemical transport model, GEOS-Chem, suggests



**A1 profile.** A similar relative range is assumed for PB (no measured CCN). The height of the boxes is the associated range in column AOD, after excluding coarse sea salt (21), that contributed an additional 0.037 (A1) and 0.022 (PB). CCN sizes activated between 60 and 100 nm are associated with variations of ~0.2 to 0.4 in supersaturation (14). The apparent AS outlier is because most aerosol (and AOD) is located above 2 km (Fig. 3) where CNhot is about three times greater than it is below 2 km. A factor of 3 in CCNproxy would shift this AS point to the right and onto the Andreae line.

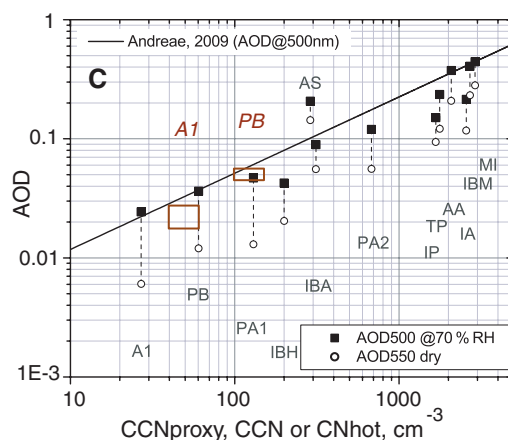


**Fig. 2. (A and B)** CCNproxy, defined here as the aerosol integral number larger than 80 nm (Nint) (16), averaged over the lowest 2 km (Nint). CNcold (A) and CNhot (B) versus CCNproxy for INTEx-B demonstrates that CNhot is better related to aerosol sizes effective as CCN than CNcold. D, diameter. (C) AOD (500 nm) versus CCN at 0.4% S (solid line), taken from (38) as determined from Aeronet AOD (500 nm), and nearby surface measurements/estimates of CCN at 0.4% S in locations assumed to be dust free. See (38) for approaches, caveats, and uncertainties. Column AOD<sub>1.3</sub> is plotted versus CNhot, calculated from measured dry  $\sigma_{sc}$  (open circles) and adjusted (dashed lines) to 500 nm (a factor of 1.2 based on  $\alpha = 2$ ) and to ambient  $\sigma_{sc}$  in the lowest 2 km (solid squares). The latter assumes a factor of 1.7, as measured for Asian pollution at ~70% relative humidity (RH) (32); this would increase to 2.4 at 80% RH, reflecting the sensitivity of AOD to regional RH. AOD contributions from aerosols above aircraft altitude, estimated at  $0.015 \pm 0.005$  (21, 33), are also included. In the cleanest regions, the A1 and PB values are supplemented with published mission averaged data (orange boxes), where the left sides of the boxes are CCNproxy (calculated for diameters larger than 100 nm) (21), and the right sides are measured CCN at 0.2% S (23), as shown in the Fig. 3

measured dry  $\sigma_{sc}$  (open circles) and adjusted (dashed lines) to 500 nm (a factor of 1.2 based on  $\alpha = 2$ ) and to ambient  $\sigma_{sc}$  in the lowest 2 km (solid squares). The latter assumes a factor of 1.7, as measured for Asian pollution at ~70% relative humidity (RH) (32); this would increase to 2.4 at 80% RH, reflecting the sensitivity of AOD to regional RH. AOD contributions from aerosols above aircraft altitude, estimated at  $0.015 \pm 0.005$  (21, 33), are also included. In the cleanest regions, the A1 and PB values are supplemented with published mission averaged data (orange boxes), where the left sides of the boxes are CCNproxy (calculated for diameters larger than 100 nm) (21), and the right sides are measured CCN at 0.2% S (23), as shown in the Fig. 3

that European contributions to CO can be 50% of Asian sources approaching North America (35). However, CO values coming from Europe on AA above 4 km (Fig. 3) are near 200 ppbv but associated with  $\sigma_{sc}$  below 20  $Mm^{-1}$ , indicating earlier scavenging of accumulation-mode aerosols and a small European impact column AOD. In contrast, the increase in CNhot near 3 km on TP is associated with high  $\sigma_{sc}$  linked to biomass burning over Southeast Asia. Aerosols from AA and TP sources tend to be transported east over the North Pacific (36), and both can descend later in the region of the North Pacific high (5).

The color gradient (CO) evident in high  $\sigma_{sc}$  for major near-surface source regions (AA, TP, IA, MI) reveals the strong coupling between CO emissions and combustion aerosol prior to scavenging.

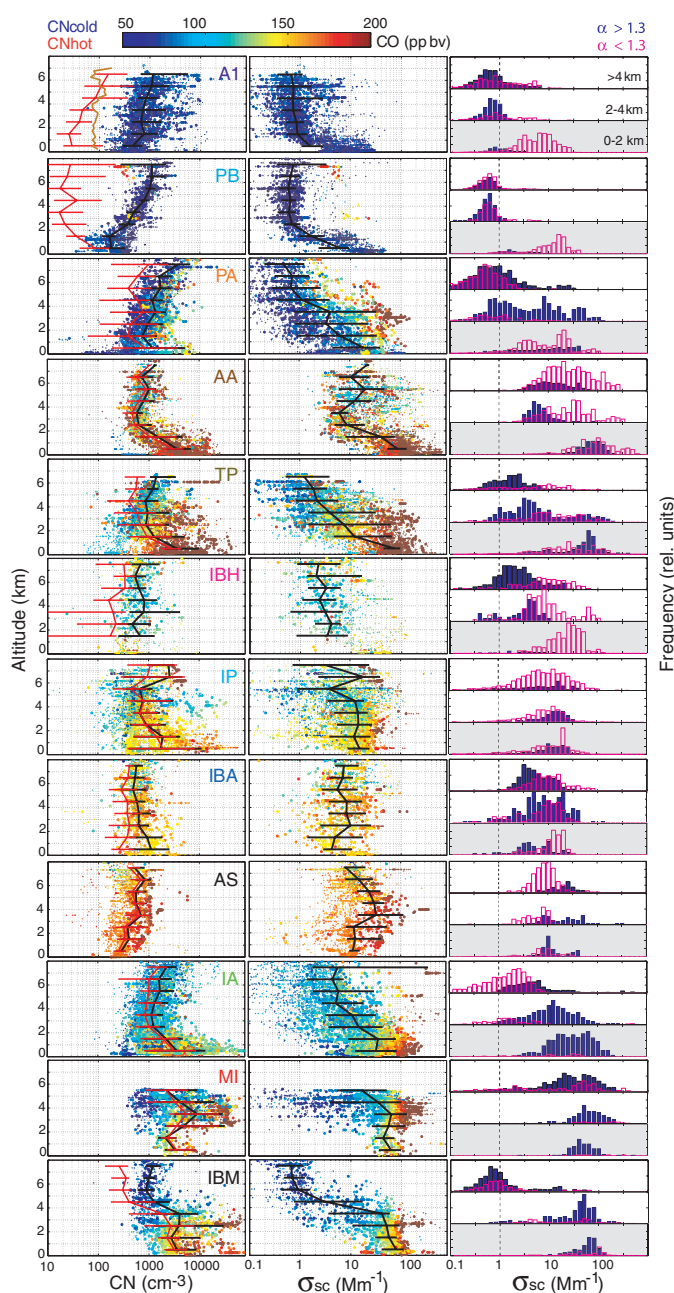
Histograms in Fig. 3 show that scattering values on profiles near 100  $Mm^{-1}$  are associated with CO near 200 ppbv. Hence, data revealing a relative decrease in  $\sigma_{sc}$  downwind of sources relative to CO values (e.g., AS, IP) indicate scavenging of aerosol relative to CO during transport over the Pacific. Flights over the western Arctic region (AS) consistently found CO concentrations of more than 150 ppbv, and almost all CN are nonvolatile (Fig. 3). This is consistent with AA and TP as source regions. However, highest-number concentrations and  $\sigma_{sc}$  are found above 2 km, consistent with warmer southerly flows being lifted over colder Arctic air with lower potential temperatures. AS histograms of  $\sigma_{sc}$  between 2 and 4 km appear bimodal around 10 and 40  $Mm^{-1}$ . Aerosol chemistry and trace gases indicate that the

larger values were dominated by biomass burning combustion aerosol. Histograms above 4 km indicate that Arctic  $\sigma_{sc}$  values trend lower and are often influenced by dust aerosol. Unlike all other regions, the lowest values are below 2 km and suggest scavenging to the surface where deposition of black carbon associated with CO emissions can reduce snow albedo (37).

These data capture the influence of aerosol associated with combustion-derived CO on both AOD (Table 1) and CCN in diverse regions and over global scales. As discussed for Fig. 2, we use CNhot as a proxy for CCN at supersaturations of  $\sim 0.2$  to 0.4, characteristic of low MBL clouds. In Fig. 2C, we plot regional mean values of dry (open circles) and ambient (closed squares) AOD<sub>1.3</sub> at 550 nm from Table 1 against this CCNproxy in the lowest 2 km. The magnitude, variability, and slope for these regional-mean hemispheric data are remarkably consistent with the related observations of Andreae and his best-fit regression line (38). This line lies somewhat above our points, probably because (i) some of his AOD is contributed by coarse aerosol, and (ii) our CNhot can include smaller sizes that are not CCN at 0.2 to 0.4% S. Even so, the variations in campaign average values demonstrate that mean perturbations to CCN by combustion sources, relative to unperturbed environments, are regionally evident over global scales and linked directly to changes in optical depth due to submicrometer combustion aerosol. This plot also supports the generality of the dependency found by Andreae, as well as our claim that CNhot is a useful proxy for CCN.

**Conclusions.** These vertically resolved measurements of aerosol and CO over the Pacific hemisphere highlight the importance of combustion and biomass burning commonly linked to anthropogenic activities. The cleaner regions (A1, PB) have natural sources of volatile CN that contribute  $\sim 50$  to  $100\text{ cm}^{-3}$  CCN in the MBL (14, 21). However, the small differences in mean CNhot and CNcold for most regional profiles influenced by CO suggest that these natural volatile CCN have been suppressed and far exceeded by the larger nonvolatile aerosols associated with combustion. Comparisons of AOD<sub>1.3</sub>, CNhot (and CCN), and CO (Fig. 2A) with unperturbed regions reveal their large concurrent springtime enhancement over the remote Pacific associated with combustion, in addition to any recognized contributions from dust or sea salt. The data also confirm that combustion aerosols contribute to direct and indirect forcing ( $\alpha > 1.3$ ) over similar size ranges (39) and over global scales, thereby requiring that both effects be considered as a coupled issue. These diverse regional data sets also provide essential constraints (3) for challenging vertically resolved model results and interpreting retrievals of CO and AOD from remote sensing; they also constitute valuable reference data needed to inform policy-makers. Summary statistics of the regional profile data discussed here are provided for this purpose as supporting online material (SOM).

**Fig. 3.** The first column shows CNcold and CNhot with medians and standard deviations over each kilometer (black and red lines, respectively). Profiles of  $\sigma_{sc}$  (550 nm) have symbol size scaled by  $\alpha$  to visually emphasize combustion aerosols and suppress coarse non-combustion aerosols (dust and sea salt).  $\sigma_{sc}$  values for small natural aerosols will also be emphasized, but these are typically low and associated with low CO concentrations. Data points are colored by measured CO, with minimum values near 50 ppbv (blue) and high CO (red) associated with increased aerosol number and elevated  $\sigma_{sc}$ . Adjacent histograms of  $\sigma_{sc}$  for 0 to 2 km, 2 to 4 km, and above 4 km include all measured values stratified by  $\alpha > 1.3$  (smaller sizes, e.g., combustion) or  $\alpha < 1.3$  (larger sizes, e.g., dust or sea salt). The upper left A1 panel includes the published profile of CCN at  $\%S = 0.2$  ( $\pm 20\text{ cm}^{-3}$ ) (23) in brown.





## References and Notes

- V. Ramanathan, P. J. Crutzen, J. T. Kiehl, D. Rosenfeld, *Science* **294**, 2119 (2001).
- M. L. Ryder, J. Langner, H. Rodhe, *Nature* **348**, 22 (1990).
- M. Chin *et al.*, *Climate Change Science Program Synthesis and Assessment Product 2.3*, U.S. Climate Change Science Program, Ed. (Global Change Research Information Office, Washington, DC, 2009).
- S. Twomey, R. Gall, M. Leuthold, *Boundary-Layer Meteorol.* **41**, 335 (1987).
- A. D. Clarke *et al.*, *J. Geophys. Res. Atmos.* **106**, 32555 (2001).
- A. Stohl, *J. Geophys. Res. Atmos.* **111**, 1 (2006).
- L. Remer *et al.*, *J. Geophys. Res. Atmos.* **113**, D14S07 (2008).
- J. E. Penner *et al.*, *Atmos. Chem. Phys.* **6**, 3391 (2006).
- Measurements of CNcold were initially made on AA and PA using a TSI model 3760 (detection limit ~12 to 14 nm) and a TSI model 3010 (detection limit ~8 to 12 nm) on other experiments. Consequently, the low values of CNhot for AA and PA may not include the smallest nonvolatile residual sizes between 8 and 14 nm detected on other experiments. CNhot particles typically include soot, dust, sea salt, and/or some organic aerosol stable at 300°C. Residence times in the heater for experiments were typically 1 to 2 s, and, even if 99% of the mass is volatilized, some larger sizes >100-nm diameter may not fully vaporize. A 100-nm particle with only 0.1% mass remaining at 350°C will still be 10 nm. However, most smaller volatile sizes will shrink below the detection limit such that CNhot commonly selects for larger sizes likely to be CCN.
- A. D. Clarke *et al.*, *J. Geophys. Res. Atmos.* **104**, 5735 (1999).
- A. D. Clarke, V. N. Kapustin, *J. Atmos. Sci.* **59**, 363 (2002).
- F. Raes, *J. Geophys. Res. Atmos.* **100**, 2893 (1995).
- A. D. Clarke *et al.*, *J. Geophys. Res. Atmos.* **112**, D12S18 (2007).
- J. G. Hudson, *Geophys. Res. Lett.* **34**, L08801 (2007).
- W. A. Hoppel, G. M. Frick, J. W. Fitzgerald, R. E. Larson, *J. Geophys. Res. Atmos.* **99**, 14443 (1994).
- V. N. Kapustin *et al.*, *J. Geophys. Res. Oceans* **111**, 1 (2006).
- T. L. Anderson *et al.*, *J. Geophys. Res.* **108**, ACE 15 (2003).
- J. E. Penner *et al.*, *J. Atmos. Sci.* **59**, 441 (2002).
- A. C. Staudt *et al.*, *J. Geophys. Res. Atmos.* **106**, 32571 (2001).
- A. D. Clarke *et al.*, *J. Geophys. Res. Atmos.* **103**, 16397 (1998).
- Y. Shinozuka, A. D. Clarke, S. G. Howell, V. N. Kapustin, B. J. Huebert, *J. Geophys. Res. Atmos.* **109**, D24201 (2004).
- A. D. Clarke *et al.*, *J. Geophys. Res.* **103**, 16397 (1998).
- J. G. Hudson, Y. Xie, S. S. Yum, *J. Geophys. Res. Atmos.* **103**, 16609 (1998).
- E. V. Browell *et al.*, *J. Geophys. Res. Atmos.* **106**, 32481 (2001).
- K. G. Moore, A. D. Clarke, V. N. Kapustin, S. G. Howell, *J. Geophys. Res.* **108**, 8236 (2003).
- D. J. Jacob *et al.*, *J. Geophys. Res.* **108**, GTE 2-1 (2003).
- B. J. Huebert *et al.*, *J. Geophys. Res.* **108**, ACE 1-1 (2003).
- Y. Ma *et al.*, *J. Geophys. Res.* **108**, GTE 37-1 (2003).
- A. D. Clarke *et al.*, *J. Geophys. Res.* **109**, D15S09 (2004).
- M. Chin *et al.*, *J. Geophys. Res.* **108**, ACE 22-1 (2003).
- Y. Shinozuka *et al.*, *J. Geophys. Res. Atmos.* **112**, D12S20 (2007).
- C. M. Carrico, P. Kus, M. J. Rood, P. K. Quinn, T. S. Bates, *J. Geophys. Res.* **108**, ACE 18-1 (2003).
- R. Halthore, P. F. Caffrey, *J. Geophys. Res.* **33**, L14819 (2006).
- C. S. McNaughton *et al.*, *J. Geophys. Res. Atmos.* **109**, D19S06 (2004).
- L. Jaegle *et al.*, *J. Geophys. Res.* **108**, GTE 23-1 (2003).
- C. L. Heald *et al.*, *J. Geophys. Res.* **108**, 4804 (2003).
- A. D. Clarke, K. J. Noone, *Atmos. Environ.* **19**, 2045 (1985).
- M. O. Andreae, *Atmos. Chem. Phys.* **9**, 543 (2009).
- D. A. Hegg, H. Jonsson, *J. Geophys. Res. Atmos.* **105**, 1987 (2000).
- The SOM includes altitude-resolved mean data for key parameters related to this paper. Additional higher-resolution data for most experiments discussed here can be found at the following links: for PEMT-A, PEMT-B, and TRACE-P, <http://www-gte.larc.nasa.gov/FM.html>; for ACE-Asia, [http://data.eol.ucar.edu/master\\_list?project=ACE-ASIA](http://data.eol.ucar.edu/master_list?project=ACE-ASIA); for INTEX-A, <http://www-air.larc.nasa.gov/cgi-bin/arcstat>; for INTEX-B (IBM, IBH, IBA), IMPEX, and MIRAGE, <http://www-air.larc.nasa.gov/cgi-bin/arcstat-b>; and for ARCTAS, <http://www-air.larc.nasa.gov/cgi-bin/arcstat-c>.
- We thank the NSF Atmospheric Chemistry Program, the NASA Global Tropospheric Experiment, and NASA Earth Science Project Office for the many years of support represented here. We also thank G. Sachse, G. Kok, T. Campos, and J. Podolske for their associated CO measurements and our colleagues S. Howell, C. McNaughton, Y. Shinozuka, J. Zhou, J. Porter, B. Lieneart, M. Litchy, K. Moore, and M. Pinkerton for their dedicated efforts in obtaining these data. This retrospective synthesis is supported under grants NASA 657001 and 652485 and NSF ATM05-11521. This is SOEST contribution number 7948.

## Supporting Online Material

[www.sciencemag.org/cgi/content/full/329/5998/1488/DC1](http://www.sciencemag.org/cgi/content/full/329/5998/1488/DC1)  
Tables S1 to S14

26 February 2010; accepted 29 July 2010  
10.1126/science.1188838

# Evidence for an Alternative Glycolytic Pathway in Rapidly Proliferating Cells

Matthew G. Vander Heiden,<sup>1,2,3\*</sup> Jason W. Locasale,<sup>2,3</sup> Kenneth D. Swanson,<sup>2</sup> Hadar Sharfi,<sup>2</sup> Greg J. Heffron,<sup>4</sup> Daniel Amador-Noguez,<sup>5</sup> Heather R. Christofk,<sup>2</sup> Gerhard Wagner,<sup>4</sup> Joshua D. Rabinowitz,<sup>5</sup> John M. Asara,<sup>2</sup> Lewis C. Cantley<sup>2,3†</sup>

Proliferating cells, including cancer cells, require altered metabolism to efficiently incorporate nutrients such as glucose into biomass. The M2 isoform of pyruvate kinase (PKM2) promotes the metabolism of glucose by aerobic glycolysis and contributes to anabolic metabolism. Paradoxically, decreased pyruvate kinase enzyme activity accompanies the expression of PKM2 in rapidly dividing cancer cells and tissues. We demonstrate that phosphoenolpyruvate (PEP), the substrate for pyruvate kinase in cells, can act as a phosphate donor in mammalian cells because PEP participates in the phosphorylation of the glycolytic enzyme phosphoglycerate mutase (PGAM1) in PKM2-expressing cells. We used mass spectrometry to show that the phosphate from PEP is transferred to the catalytic histidine (His<sup>11</sup>) on human PGAM1. This reaction occurred at physiological concentrations of PEP and produced pyruvate in the absence of PKM2 activity. The presence of histidine-phosphorylated PGAM1 correlated with the expression of PKM2 in cancer cell lines and tumor tissues. Thus, decreased pyruvate kinase activity in PKM2-expressing cells allows PEP-dependent histidine phosphorylation of PGAM1 and may provide an alternate glycolytic pathway that decouples adenosine triphosphate production from PEP-mediated phosphotransfer, allowing for the high rate of glycolysis to support the anabolic metabolism observed in many proliferating cells.

One of the major differences observed between cancer cells and normal cells is in how they metabolize glucose; most cancer cells primarily metabolize glucose by glycolysis, whereas most normal cells completely catabolize glucose by oxidative phosphorylation (1). This shift to aerobic glycolysis with lactate production (also known as the Warburg effect), coupled with

increased glucose uptake, is likely used by proliferating cells to promote the efficient conversion of glucose into the macromolecules needed to construct a new cell (2). The glycolytic enzyme pyruvate kinase is alternatively spliced to produce either the M1 (PKM1) or M2 (PKM2) isoforms (3). The splice isoform of pyruvate kinase expressed in cells influences the extent to which

glucose is metabolized by either aerobic glycolysis or oxidative phosphorylation. Cells expressing PKM2 produce more lactate and consume less oxygen than cells expressing PKM1 (4). Consistent with this metabolic phenotype, all cancer cells studied to date exclusively express PKM2, whereas cells in many normal differentiated tissues express PKM1. PKM2 differs from PKM1 in that its activity can be negatively regulated in response to growth factor signaling by binding to tyrosine-phosphorylated proteins (5, 6). Paradoxically, it is this ability to interact with tyrosine-phosphorylated proteins, and to decrease pyruvate kinase activity, that appears to be important for cell proliferation (5). This selection for the decreased activity of a rate-limiting glycolytic enzyme appears inconsistent with the increased glucose use that is characteristic of cancer cells. However, complete catabolism of pyruvate to CO<sub>2</sub> may be counterproductive in a dividing cell because it may limit the availability

<sup>1</sup>Dana Farber Cancer Institute, Harvard Medical School, Boston, MA 02115, USA. <sup>2</sup>Beth Israel Deaconess Medical Center, Division of Signal Transduction and Department of Medicine, Harvard Medical School, Boston, MA 02115, USA. <sup>3</sup>Department of Systems Biology, Harvard Medical School, Boston, MA 02115, USA. <sup>4</sup>Department of Biological Chemistry and Molecular Pharmacology, Harvard Medical School, Boston, MA 02115, USA. <sup>5</sup>Lewis-Sigler Institute for Integrative Genomics and Department of Chemistry, Princeton University, Princeton, NJ 08544, USA.

\*Present address: Koch Institute for Integrative Cancer Research at Massachusetts Institute of Technology, Cambridge, MA 02139, USA.

†To whom correspondence should be addressed. E-mail: lewis\_cantley@hms.harvard.edu

of precursors and reducing potential necessary to produce biomass.

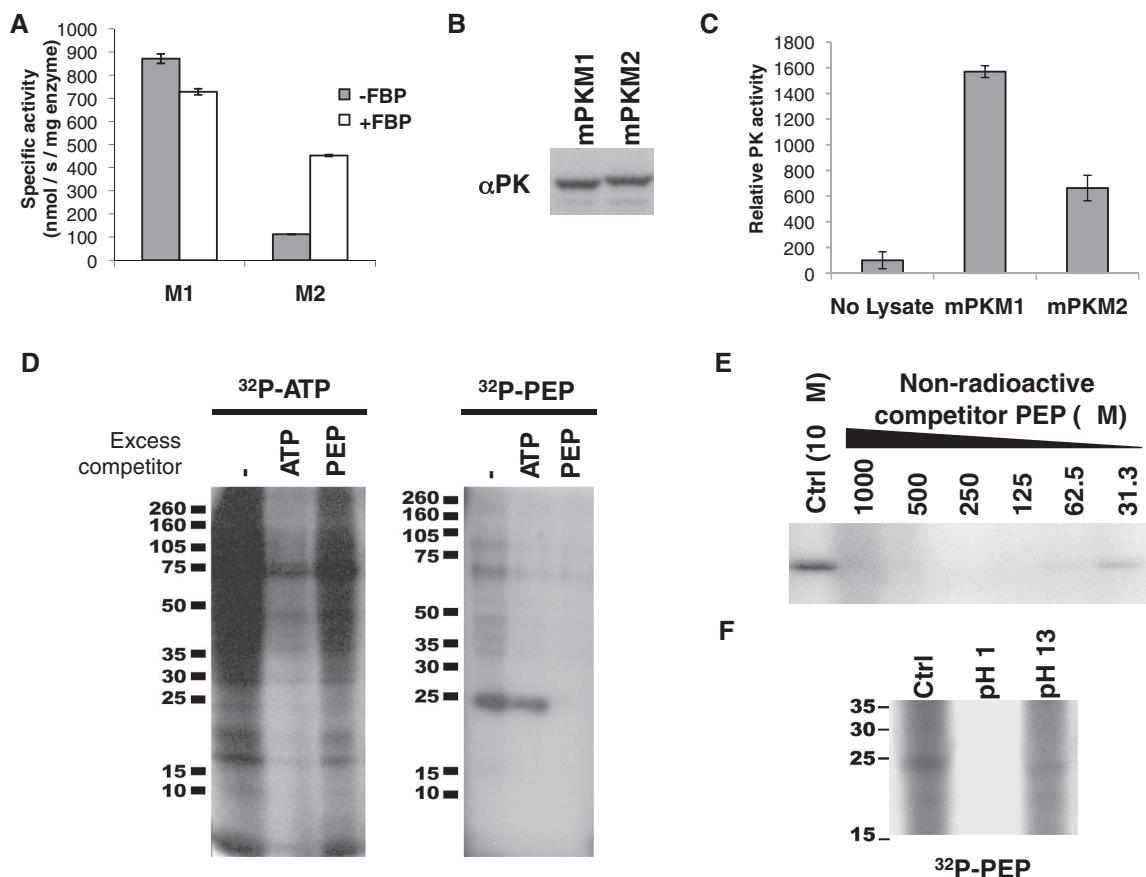
**PKM2 is less active than PKM1 in vitro and in cells.** We directly compared the specific activity of PKM1 and PKM2 both in vitro and in cell lysates (7). Recombinant PKM1 enzyme had a high specific activity that was independent of the PKM2-specific allosteric activator FBP (Fig. 1A) (8). The specific activity of PKM2 that is fully activated by FBP is about half that of PKM1. The property of PKM2 that appears to promote cell proliferation in vivo is its interaction with tyrosine-phosphorylated proteins and consequent release of FBP. In the absence of FBP, PKM2 had less than one-quarter of the activity of PKM1 (Fig. 1A). To determine whether the differences in activity observed with recombinant enzymes are also seen in cells, we measured pyruvate kinase activity in lysates from cells engineered to express equivalent amounts of either PKM1 or PKM2 in the absence of the other isoform (Fig. 1B). Under these identical conditions, PKM2 expression provides a selective advantage for growth in vivo (4). Lysates from PKM2-expressing cells exhibited less than half the pyruvate kinase

activity of lysates from cells expressing the equivalent amount of PKM1 (Fig. 1C). Thus, the selection for PKM2 expression in proliferating cells is accompanied by a decrease in total cellular pyruvate kinase activity.

**Donation of phosphate from phosphoenolpyruvate to a cytosolic protein of about 25-kD.** It is possible that the relative decrease in PKM2 activity allows an upstream metabolite in glycolysis to signal energy status or to be shunted to an undiscovered, or underappreciated, metabolic pathway required for cell division. The substrate for pyruvate kinase in cells is phosphoenolpyruvate (PEP). Bacteria use PEP as the initial phosphate donor for protein phosphorylation in a signaling cascade that regulates carbohydrate metabolism in response to nutrient availability (9, 10). In addition, transfer of the PEP phosphate to a protein occurs as an enzymatic intermediate within the Calvin cycle of C4 plants (11, 12). This prompted us to explore the possibility that PEP might transfer its phosphate to a protein in mammalian cells. We generated [ $^{32}$ P]PEP (fig. S1) and tested hypotonic lysates from human embryonic kidney (HEK) cells for the presence of

such a PEP-dependent protein phosphorylation activity. Incubation of extracts with [ $\gamma$ - $^{32}$ P]adenosine triphosphate (ATP) resulted in numerous  $^{32}$ P-labeled proteins, and the  $^{32}$ P-labeling of these proteins was abolished after addition of a 100-fold excess amount of nonradioactive ATP (Fig. 1D). No decrease in incorporation of phosphate from [ $\gamma$ - $^{32}$ P]ATP was observed in the presence of excess nonradioactive PEP. However, incubation of cell extracts with [ $^{32}$ P]PEP resulted in the incorporation of  $^{32}$ P into several proteins, the most prominent of which resolved at a relative molecular size of about 25-kD by SDS-polyacrylamide gel electrophoresis (PAGE). The  $^{32}$ P-labeling of this protein was eliminated after addition of excess amounts of nonradioactive PEP but not by excess nonradioactive ATP, consistent with PEP acting as the phosphate donor (Fig. 1D). Other purine nucleotides, including guanine triphosphate (GTP), did not compete with  $^{32}$ P-labeled PEP to phosphorylate the 25-kD protein, and phosphorylation of a 25-kD protein was observed in extracts from multiple cell lines incubated with [ $^{32}$ P]PEP (fig. S2). Cytoplasmic concentrations of PEP are less than 30  $\mu$ M in eukaryotic cells (13, 14). To determine whether

**Fig. 1.** Evidence of PEP-dependent phosphorylation of a 25-kD protein in PKM2-expressing cells with less pyruvate kinase activity. (A) 6 $\times$ His-tagged human PKM1 and PKM2 were expressed in *Escherichia coli* and purified by Ni affinity chromatography. The specific activity of each enzyme was determined in the presence of saturating amounts of PEP and adenosine diphosphate (ADP). The activity of PKM1 and PKM2 in the presence and absence of FBP is shown. Error bars indicate SEM in all figures. (B) H1299 cells were engineered to express equivalent amount of PKM1 or PKM2 protein as described previously (4). Equivalent expression of PKM1 and PKM2 was confirmed by Western blot using an antibody ( $\alpha$ PK) that recognizes an epitope shared by PKM1 and PKM2. (C) As in (A), pyruvate kinase activity was determined by using saturating amounts of PEP and ADP. The relative pyruvate kinase activity observed in the PKM1- or PKM2-expressing cells described in (B), relative to lysis buffer alone, is shown. (D) HEK293 cells were hypotonically lysed and incubated with [ $^{32}$ P]ATP or [ $^{32}$ P]PEP before analysis by SDS-PAGE and autoradiography. The lysates were incubated with [ $^{32}$ P]ATP or [ $^{32}$ P]PEP in the presence of 10  $\mu$ M ATP or PEP, respectively (–), or with the addition of 1 mM nonradio-



active competitor ATP or PEP. (E) Cell lysate was incubated with [ $^{32}$ P]PEP in the presence of the indicated concentration of nonradioactive competitor PEP before analysis by SDS-PAGE and autoradiography. (F) Cell lysate was incubated with  $^{32}$ P-labeled PEP as above, and the pH of the reaction was changed to pH 1 or pH 13. Reactions were incubated for 2 hours at 65°C before analysis by SDS-PAGE and autoradiography.



phosphorylation of this protein is possible at low  $\mu\text{M}$  concentrations of PEP, we added increasing concentrations of nonradioactive PEP to estimate the Michaelis constant ( $K_m$ ) for PEP in the reaction (Fig. 1E). Increasing the amount of unlabeled PEP above 10  $\mu\text{M}$  resulted in decreased  $^{32}\text{P}$ -labeling of the 25-kD protein, suggesting that the  $K_m$  for PEP involved in this reaction is in a range where this reaction could occur at concentrations of PEP present in cells.

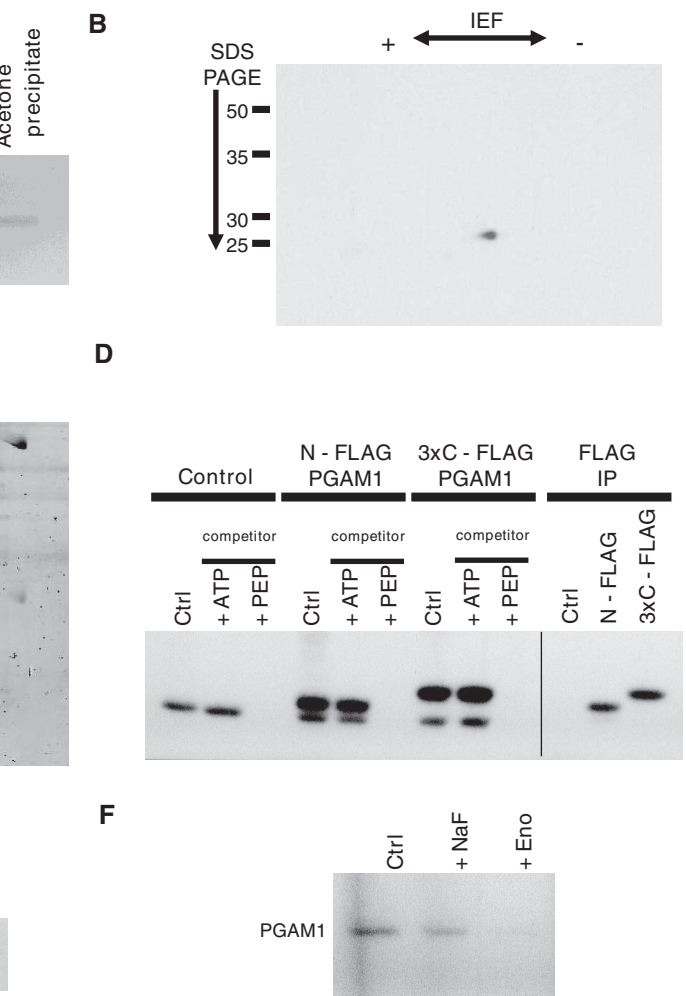
**PEP-dependent phosphorylation of the 25-kD protein on histidine.** The phosphorylation reaction involving PEP in bacterial two-component signaling and the analogous PEP-dependent protein phosphorylation as an enzymatic intermediate in C4 plants both involve transfer of the

PEP phosphate to a histidine residue. O-linked protein phosphates such as those seen upon phosphorylation of serine, threonine, or tyrosine residues are stable under acidic conditions (15, 16). In contrast, N-linked protein phosphates such as phospholysine or phosphohistidine are labile at low pH but stable under basic conditions. Therefore, we exposed protein extracts that had been incubated with  $^{32}\text{P}$ PEP to acidic or basic conditions before analysis by SDS-PAGE and autoradiography. The  $^{32}\text{P}$  signal was lost after incubation at pH 1 but retained at pH 13 (Fig. 1F), which is consistent with an N-linked phosphate resulting from PEP-dependent phosphorylation of the 25-kD protein. Incubation of  $^{32}\text{P}$ ATP-labeled lysates at pH 1 resulted in no loss of protein phosphorylation, indicat-

ing that loss of signal from the PEP-phosphorylated protein at low pH was not the result of nonspecific acid hydrolysis. Consistent with a N-linked phosphorylation, in “standard” phosphoaminoacid analysis involving acid hydrolysis of the 25-kD PEP-phosphorylated protein all of the resulting radioactivity migrated as inorganic phosphate ( $\text{P}_i$ ) on thin-layer electrophoresis (fig. S3A). During reverse-phase thin-layer chromatography after base hydrolysis, the  $^{32}\text{P}$  migrated with phosphohistidine, consistent with histidine as the target of PEP-dependent phosphotransfer (fig. S3B).

**Identification of the 25-kD PEP-phosphorylated protein as phosphoglycerate mutase.** The PEP-utilizing phosphorylating activity and the 25-kD target of phosphorylation were present in the

**Fig. 2. PGAM1 as the target of PEP-dependent phosphorylation through an enolase-independent reaction. (A)** The S100 fraction from a HEK293 cell lysates was passed sequentially through a custom column and a strong cation exchange column before incubating with  $^{32}\text{P}$ PEP (S FT). This reaction was then applied to a hydroxyapatite (HAP) column and eluted with 50 mM  $\text{NaH}_2\text{PO}_4$ . The salt elution (E) containing the  $^{32}\text{P}$ -labeled species was diluted to  $<25$  mM  $\text{NaH}_2\text{PO}_4$  and applied to a weak anion exchange (DEAE) column. Elution from the DEAE column was performed with 100 mM and 200 mM NaCl. The 200-mM salt fraction containing the  $^{32}\text{P}$ -labeled species was diluted to 50 mM NaCl and applied to a strong anion exchange (Q) column and eluted sequentially with 100 mM and 350 mM NaCl. The 350-mM salt fraction containing the  $^{32}\text{P}$ -labeled species was acetone-precipitated for analysis by 2D-IEF and SDS-PAGE. An aliquot of each fraction was analyzed by SDS-PAGE and autoradiography. Flow-through fractions are indicated as FT. **(B)** The acetone-precipitated 350 mM salt fraction described in (A) was separated by 2D-IEF and SDS-PAGE, and the  $^{32}\text{P}$ -labeled species was identified by autoradiography. **(C)** The acetone-precipitated 350-mM salt fraction prepared as described in (A) was separated by 2D-IEF and SDS-PAGE, and proteins were identified by Coomassie stain. The species corresponding to the  $^{32}\text{P}$ -labeled species is indicated with an arrow. **(D)** HEK293 cells were transiently transfected with control plasmid (Control), a N-terminally FLAG-tagged PGAM1 complementary DNA (cDNA) (N-FLAG PGAM1), or a C-terminal triple FLAG-tagged PGAM1 cDNA (3xC-FLAG PGAM1). Hypotonic lysates from these cells were incubated with  $^{32}\text{P}$ PEP alone (Ctrl) or in the presence of 1 mM cold com-



petitor ATP or PEP. The products of these reactions were separated by SDS-PAGE and analyzed by autoradiography. Protein immunoprecipitated with an antibody to FLAG from the reactions without nonradioactive competitor were also analyzed by SDS-PAGE and autoradiography. **(E)** Recombinant 6xHis-tagged PGAM1 (rPGAM1) was produced in *E. coli* and purified by Ni affinity chromatography. Increasing quantities of rPGAM1 were incubated with 10  $\mu\text{g}$  of HEK293 cell lysate and  $^{32}\text{P}$ PEP. The phosphorylation of both the endogenous PGAM1 present in the cell lysate and rPGAM1 was determined by SDS-PAGE and autoradiography. **(F)** Cell lysates were incubated with  $^{32}\text{P}$ PEP in the absence (Ctrl) or presence of NaF or exogenously added rabbit muscle enolase enzyme (Eno). The labeling of PGAM1 was determined by SDS-PAGE and autoradiography.

S100 cytosolic fraction of HEK293 cells and were retained in the flow-through fractions of both a strong cation exchange column and a C11NP column, which contained a resin we synthesized as a possible PEP affinity column. We fractionated the previously phosphorylated 25-kD target by both anion exchange and hydroxyapatite chromatography using salt elution but were unable to detect phosphorylation activity within any of the fractions from these columns upon their incubation with [ $^{32}$ P]PEP. This is consistent with the presence of an enzymatic transfer of phosphate from PEP to a protein and a separation of the 25-kD target protein from an activity required for the observed phosphorylation. We purified the target protein by collecting the flow through fractions from an S100 protein extract passed sequentially through a C11NP column and a strong cation exchange (S) column. The [ $^{32}$ P] PEP was added to this partially fractionated lysate to label the 25-kD protein, and the resulting  $^{32}$ P-labeled protein was then sequentially fractionated over three columns to effect the maximal recovery of the target protein (Fig. 2A). The proteins in the fraction from the strong anion exchange (Q) column containing the  $^{32}$ P-labeled 25-kD protein were precipitated with acetone and subjected to two-dimensional (2D) electrophoresis (Fig. 2, A and B, and fig. S4). Analysis of the 2D sequential isoelectric focusing (IEF) and SDS-PAGE gel by autoradiography identified a single radioactive isoelectric species ( $pI \sim 6.2$ ) at 25-kD (Fig. 2B). The  $^{32}$ P-labeled spot corresponded to the most acidic Coomassie-stained spot in a series of several adjacent isoelectric species at 25-kD on a Coomassie-stained gel (Fig. 2C). In-gel trypsin digestion followed by microcapillary liquid chromatography–tandem mass spectrometry (LC/MS/MS) with protein database searching identified the  $^{32}$ P-labeled species as well as the adjacent species to be different isoelectric forms of the glycolytic enzyme phosphoglycerate mutase 1 (PGAM1) (table S1).

To confirm that PGAM1 was indeed the target of PEP phosphorylation, we transiently transfected FLAG-tagged PGAM1 constructs into HEK293 cells and incubated lysates from these cells with [ $^{32}$ P]PEP. When the proteins in these reactions were analyzed by SDS-PAGE and autoradiography, a second  $^{32}$ P-labeled species of greater molecular weight corresponding to the size of the epitope-tagged PGAM1 was observed (Fig. 2D and fig. S5A). The larger species was removed and recovered by immunoprecipitation with an antibody to FLAG, and its labeling with  $^{32}$ P was blocked with excess nonradioactive PEP but not with excess nonradioactive ATP (Fig. 2D). Thus, the  $^{32}$ P from [ $^{32}$ P]PEP can be transferred to PGAM1. To confirm that the 25-kD protein labeled from [ $^{32}$ P]PEP is also PGAM1, we incubated lysates from control- and epitope-tagged PGAM1-transfected cells with [ $^{32}$ P]PEP and subjected them to limited proteolysis. When analyzed by SDS-PAGE, both the control lysates and those containing FLAG-tagged PGAM1 produced identical patterns of

$^{32}$ P-labeled peptides after limited proteolysis (fig. S5B). Lastly, recombinant PGAM1 added with [ $^{32}$ P]PEP to a fixed amount of cell lysate could compete for phosphorylation of endogenous PGAM1 (Fig. 2E). These data demonstrate that PGAM1 can be phosphorylated by PEP.

**PGAM1 phosphorylation is independent of enolase activity.** Although recombinant PGAM1 can be phosphorylated by [ $^{32}$ P]PEP in cell lysates, purified recombinant PGAM1 is not a direct substrate (fig. S5C), indicating that an enzymatic activity in cell lysates is required to catalyze PGAM1 phosphorylation by PEP. PGAM1 acts as an enzyme in glycolysis to interconvert 3-phosphoglycerate (3PG) and 2-phosphoglycerate (2PG) through a phosphohistidine intermediate (17). Because PEP can be converted by the glycolytic enzyme enolase into 2PG, it seemed possible that the PEP-dependent phosphorylation of PGAM1 that we observed in cell lysates involved conversion of [ $^{32}$ P]PEP into [ $^{32}$ P]2PG by enolase, followed by transfer of the [ $^{32}$ P]phosphate from 2PG to the catalytic histidine of PGAM1. We therefore increased enolase activity by addition of exogenous enolase enzyme or decreased it by addition of the enolase inhibitor NaF (18) to cell lysates (fig. S6). The inhibition of enolase activity with NaF had minimal effect on the transfer of  $^{32}$ P from PEP to PGAM1 (Fig. 2F). Furthermore, the addition of exogenous enolase prevented the transfer of  $^{32}$ P from PEP to PGAM1 presumably by converting [ $^{32}$ P]PEP to 2PG. These data indicate that conversion of PEP to 2PG by enolase is not involved in the observed phosphotransfer from PEP to PGAM1.

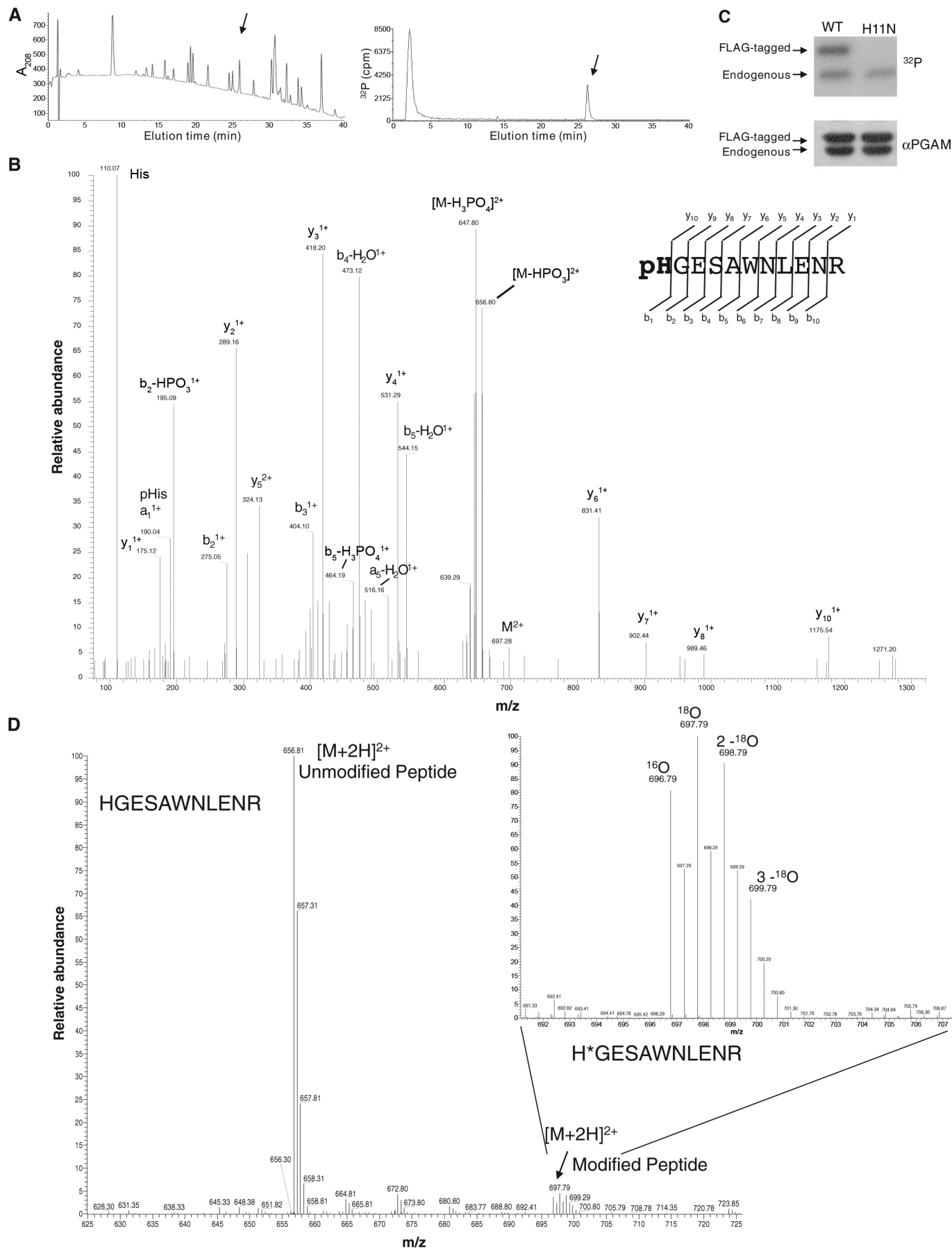
**Phosphorylation of PGAM1 on the catalytic histidine (His<sup>11</sup>) by the phosphate from PEP.** To determine whether the phosphate from PEP was transferred to one or more sites on PGAM1, we labeled PGAM1 with  $^{32}$ P from PEP, digested the protein with trypsin, and analyzed the resulting peptides by 2D thin-layer chromatography and thin-layer electrophoresis followed by autoradiography (fig. S7A). This revealed a single  $^{32}$ P-labeled species, indicating that only a single site is phosphorylated on PGAM1 in the reaction with PEP.

Phosphoaminoacid analysis indicated that PGAM1 was phosphorylated on a histidine residue (fig. S3). To determine which histidine residue was phosphorylated, we incubated recombinant PGAM1 with [ $^{32}$ P]PEP and HEK293 cell lysate and recovered the [ $^{32}$ P]PGAM1 through association with Ni-agarose beads (fig. S7B). This [ $^{32}$ P]PGAM1 was then digested with trypsin, and the resulting peptides were separated by high-performance liquid chromatography (HPLC) (Fig. 3A). A single  $^{32}$ P-labeled peptide was observed. HPLC fractions were collected to confirm which peak contained the  $^{32}$ P-labeled peptide (fig. S7, C and D), and the fraction containing the  $^{32}$ P-labeled peptide was sequenced by LC/MS/MS using a hybrid linear ion trap–orbitrap mass spectrometer with use of the higher energy collision dissociation cell (HCD) (19). HCD was required to clearly resolve the low mass fragment ions to show that

the site of phosphorylation in the peptide sequence was localized to His<sup>11</sup> (H11) of PGAM1 (Fig. 3B and fig. S8). Detection of histidine phosphorylation using mass spectrometry is challenging but has previously been reported (20–23). The pHis site was confirmed by using two different commercially available database search algorithms [Mascot (24) and Sequest (25)] with statistically significant scores. Consistent with H11 being the residue phosphorylated, mutation of H11 to Asp<sup>11</sup> abolished transfer of  $^{32}$ P from PEP to PGAM1 (Fig. 3C). To confirm that the phosphate at H11 is from exogenously added PEP rather than a phosphate that was present before cell lysis, we incubated recombinant PGAM1 with [ $^{18}$ O]phosphate-labeled PEP (fig. S9) in the presence of 1 mM normal isotopic ATP and HEK293 cell lysate and then isolated PGAM1 with Ni-agarose beads, digested it with trypsin, and separated the peptides by HPLC. The peptide fraction containing H11 was analyzed by orbitrap mass spectrometry in Fourier transform mass spectrometry (FT-MS) mode, and several isotopic species were identified that corresponded to the H11-phosphorylated peptide (Fig. 3D). The heavy isotopic forms were consistent with  $^{18}$ O labeling of the phosphate that was transferred to the peptide from the [ $^{18}$ O]PEP rather than from the normal isotopic [ $^{16}$ O]ATP. These data demonstrate that the phosphate group from PEP is transferred to H11 of PGAM1.

**Association of PGAM1 phosphorylation with pyruvate generation from PEP in the absence of pyruvate kinase.** Because the [ $^{32}$ P]phosphate (and [ $^{18}$ O]phosphate) from PEP is transferred to the catalytic histidine of PGAM1, we wondered whether we were observing a net increase in H11 phosphorylation of PGAM1 or merely observing an exchange of phosphate already present on PGAM1 with phosphate from PEP (as can occur during the interconversion of 2PG and 3PG). To address this issue, we added recombinant PGAM1 to a cell extract in the presence or absence of PEP. These extracts were then subjected to 2D gel electrophoresis and analyzed by Western blot with an antibody to PGAM. Consistent with PEP phosphorylation of H11, a new, more acidic isoelectric species of both endogenous and recombinant PGAM1 was detected in the PEP-containing lysate (Fig. 4A). No change in the isoelectric forms of PGAM1 was observed when lysates were incubated with ATP instead of PEP (fig. S10A). To confirm that this species did indeed represent the H11-phosphorylated form of PGAM1, we added PEP to a cell lysate to phosphorylate PGAM1 and then incubated the reaction either at neutral pH or at pH 2 to chemically disrupt H11 phosphorylation. Analysis of 2D Western blots with an antibody to PGAM1 showed that incubation at pH 2 resulted in loss of the most acidic PGAM1 species (fig. S10B). Therefore, we concluded that 2D Western blots could be used to assess H11 phosphorylation status in cells. These data also demonstrate that PEP can cause a net increase in H11-phosphorylated PGAM1 and that the phosphorylation of PGAM we observe cannot be ac-





counted for by exchange of the PEP phosphate with a previously phosphorylated H11.

To determine whether H11-phosphorylated PGAM1 is catalytically competent for enzymatic activity, we assayed the ability of PEP-phosphorylated PGAM1 to convert 3PG to 2,3-bisphosphoglycerate (2,3-BPG), the intermediate in 3PG to 2PG conversion (26). Recombinant His-tagged PGAM1 was incubated with PEP and cell extract to allow phosphorylation on H11, and the protein was recovered through association with Ni-agarose beads. Addition of 3PG to the recovered PGAM1 resulted in 2,3-BPG production as determined by selected reaction monitoring (SRM) using hybrid quadrupole linear ion trap mass spectrometry (fig. S11). Thus, phosphorylation of PGAM1 by PEP leads to an enzyme species that is active to carry out the known enzymatic function of PGAM1.

We fractionated a cell lysate over a weak anion exchange column and isolated the PEP-dependent PGAM1-phosphorylating activity in a fraction that was separate from the enolase-containing fraction as determined by both enzyme activity assays and Western blot (Fig. 4, B and C, and fig. S12A). The fraction containing the PGAM1-phosphorylating activity was also separated from pyruvate kinase, as determined by both enzyme activity assay and Western blot. In support of this finding that pyruvate kinase is not involved in the transfer of phosphate to PGAM1, we found that short hairpin RNA knockdown of pyruvate kinase resulted in the enhanced ability of a cell lysate to transfer  $^{32}\text{P}$  from  $^{32}\text{P}$ -labeled PEP to PGAM1 with no change in the level of PGAM1 protein (fig. S12, B to D). It has been reported that a complex containing the nucleoside diphosphate kinase nm23 and glyceraldehyde-3-phosphate dehydrogenase (GAPDH) can phosphorylate PGAM1 (27). However, neither GAPDH nor nm23 copurify in substantial quantities with the PEP-dependent PGAM1-phosphorylating activity (fig. S12E), suggesting that these proteins are not involved in the activity we observe.

We further investigated the consequences of metabolizing PEP through phosphotransfer to PGAM1. To test whether PEP is converted to pyruvate during the phosphotransfer reaction,

we incubated the anion exchange fraction containing the PGAM1-phosphorylating activity (D500 fraction) with [ $^{13}\text{C}$ ]PEP and recombinant PGAM1. Similar reactions with a whole-cell lysate served as a positive control, and a [ $^{13}\text{C}$ ]PEP sample that contained no cellular material served as a negative control. We then extracted metabolites from the resulting reactions to study the products derived from the labeled PEP by [ $^1\text{H}$ ,  $^{13}\text{C}$ ] heteronuclear single-quantum coherence (HSQC) nuclear magnetic resonance (NMR) (28). We detected [ $^{13}\text{C}$ ]pyruvate in the whole-cell lysate as determined by an isolated peak corresponding to a  $^{13}\text{C}$ -labeled methyl group of pyruvate (29). No pyruvate was observed in the mock-treated control, indicating that PEP did not undergo spontaneous dephosphorylation and tautomerization to pyruvate under the reaction conditions. Incubation with the anion exchange fraction containing the PGAM1-phosphorylating activity also caused generation of pyruvate. The amount of [ $^{13}\text{C}$ ]pyruvate produced by the D500 fraction was about 50% of the amount produced by a whole-cell lysate (Fig. 4D). Thus, one or more factors in the partially purified fraction from cell lysates lacking pyruvate kinase mediates PEP-dependent phosphorylation of PGAM1 and conversion of PEP to pyruvate.

The [ $^{13}\text{C}$ ]pyruvate was produced from PEP in the D500 fraction at a rate of about 30 to 60  $\mu\text{M}/\text{min}$ . Given that the number of PGAM1 molecules in this fraction is small relative to the number of PEP molecules consumed, this fraction must also contain the ability to release  $\text{P}_i$ . To determine whether  $\text{P}_i$  production from PEP also occurred in this fraction, we incubated the D500 fraction with [ $^{32}\text{P}$ ]PEP and recombinant PGAM1 and assessed the release of  $^{32}\text{P}_i$  over time (fig. S13A). We also tested whether the rate of  $\text{P}_i$  production was enhanced by PGAM1. Addition of PGAM1 should have no impact on (or should decrease) the rate of  $\text{P}_i$  production from PEP if this reaction is independent of PEP-mediated PGAM1 phosphorylation. However, PGAM1 addition stimulated  $\text{P}_i$  production in the fraction lacking pyruvate kinase (fig. S13B), suggesting a link between PEP-dependent PGAM1 phosphorylation and PEP-to-pyruvate conversion with  $\text{P}_i$  release. These results

suggest that release of  $\text{P}_i$  from either phosphorylated PGAM1, PEP, or both occurs in this fraction and accounts for how PEP to pyruvate conversion can occur at a rate that is super-stoichiometric to the amount of PGAM1 present.

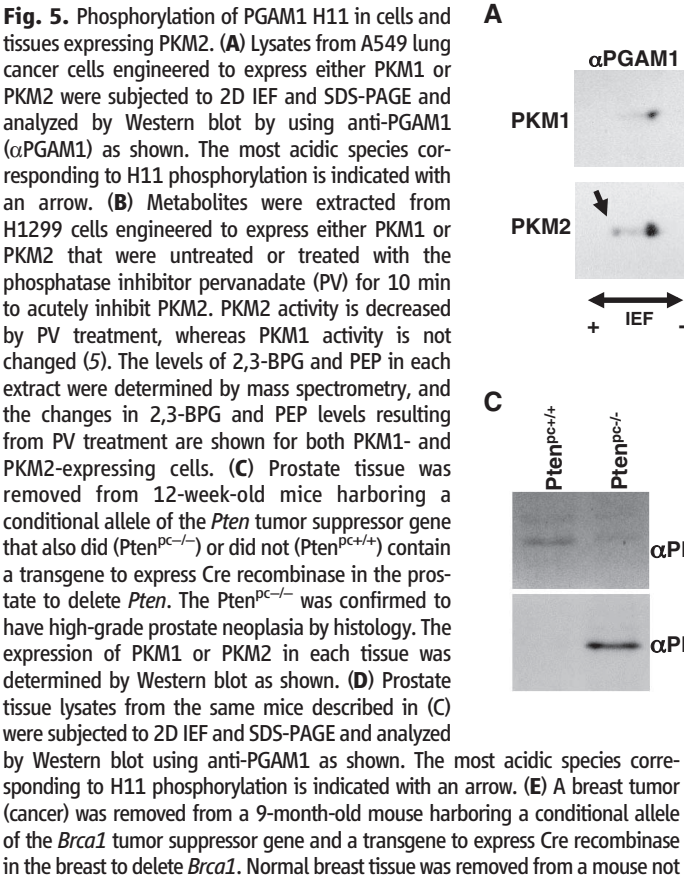
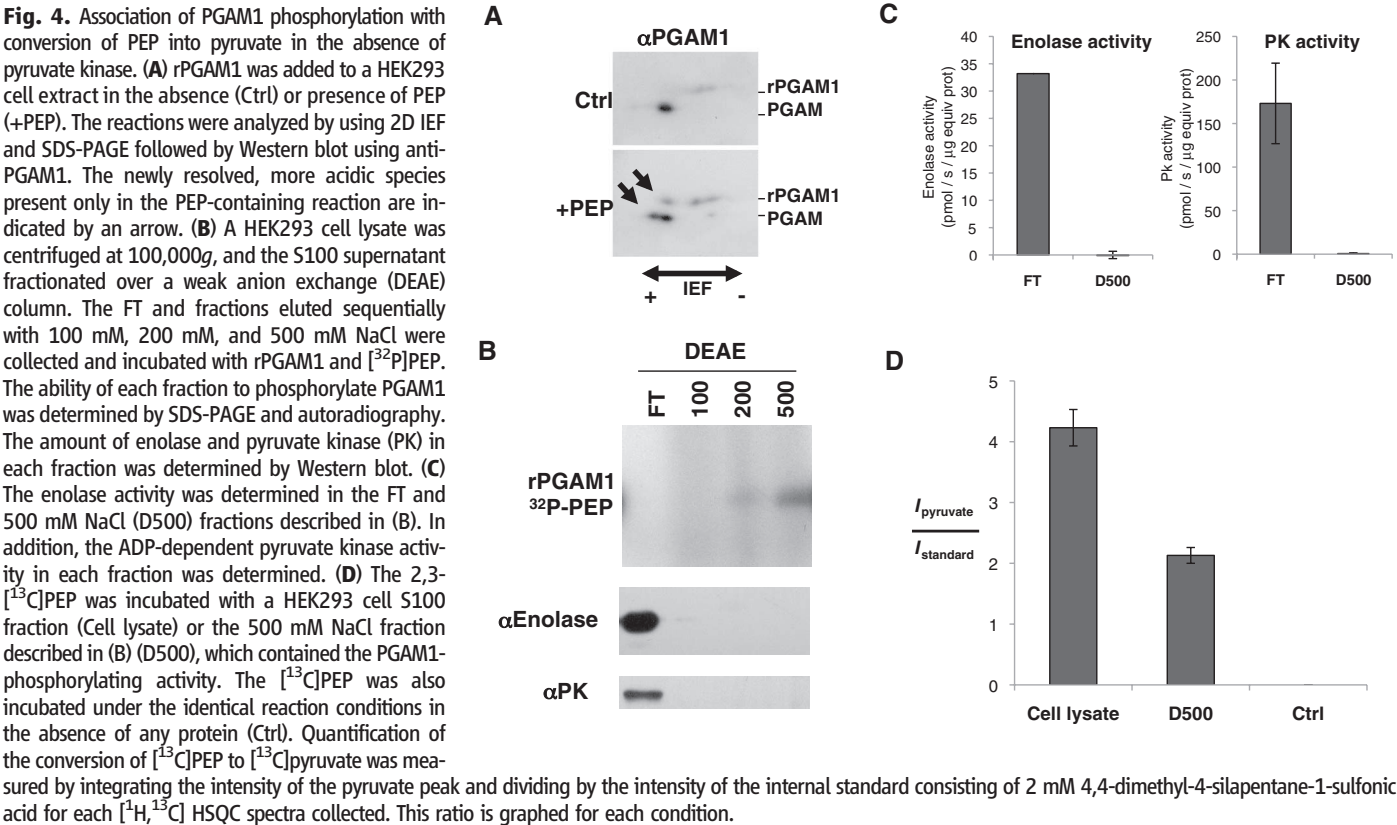
**Selective detection of PGAM1 H11 phosphorylation and altered glycolytic regulation in PKM2-expressing cells and tumor tissues.** To test whether increased H11 phosphorylation of PGAM1 might be characteristic of PKM2-expressing cells as a consequence of their lower pyruvate kinase activity, we engineered H1299 and A549 lung cancer cells to express either PKM1 or PKM2 (4). PGAM1 expression was similar regardless of which pyruvate kinase isoform was present (fig. S14A). However, when the isoelectric forms of PGAM1 were assessed by 2D Western blot, only lysates prepared from PKM2-expressing cells had detectable amounts of the most acidic species that correspond to H11-phosphorylated PGAM1 (Fig. 5A and fig. S14B). Thus, switching cells from PKM2 to PKM1 expression reduced the amount of H11 phosphorylated PGAM1.

Accumulation of PEP in cells should enhance PGAM1 phosphorylation. Because the PGAM1 mutase reaction involves a 2,3-BPG intermediate (24), this in turn should drive conversion of 3PG to 2,3-BPG (fig. S15). Accordingly, acute inhibition of pyruvate kinase in cells with PEP-dependent PGAM1 phosphorylation activity should increase 2,3-BPG levels. To test this hypothesis, we acutely inhibited PKM2 activity in cells by addition of pervanadate to increase protein tyrosine phosphorylation (5). Pervanadate has no effect on PKM1 activity (5); thus, comparing the response of PKM2-expressing cells to PKM1-expressing cells separates the effects of acute PKM2 inhibition from other effects of pervanadate on metabolism. Acute inhibition of PKM2 leads to about a twofold increase in PEP and a yet larger increase in 2,3-BPG (Fig. 5B), suggesting that glycolysis involving PGAM1 phosphorylation by PEP occurs in PKM2-expressing cells and that relative flux through this alternative pathway is increased when PKM2 is inactivated by interaction with tyrosine phosphorylated proteins.

**Fig. 3.** Transfer of the phosphate of PEP to H11 of PGAM1. **(A)** Recombinant 6 $\times$ His-tagged PGAM1 (rPGAM1) was phosphorylated by [ $^{32}\text{P}$ ]PEP in a cell extract and recovered by binding to Ni-agarose beads. The [ $^{32}\text{P}$ ]rPGAM was then digested with trypsin, and the peptides were separated by using HPLC. A chromatograph identifying peptide peaks by absorbance at 208 nm and the presence of  $^{32}\text{P}$  determined by in-line scintillation counting is shown. The peptide peak eluting at ~26 min containing  $^{32}\text{P}$  is delineated with an arrow. **(B)** The HCD MS/MS spectrum for the phosphorylated histidine-containing peptide pHGESAWNLENR (A, Ala; E, Glu; G, Gly; L, Leu; N, Asn; R, Arg; S, Ser; W, Trp) acquired by using a hybrid LTQ linear ion trap—Orbitrap XL mass spectrometer (Thermo Fisher Scientific, San Jose, CA). The  $a_1/\text{pHIS}$  immonium ion along with the b- and y-series fragment ions are all consistent with the site of phosphorylation localized to the His1 position of the peptide (H11 in PGAM1). Phosphate losses observed are typical of His phosphorylation (21). The His $^{41}$  phosphorylation site was confirmed by using both Sequest (www.thermofisher.com/global/en/products/home.asp) and Mascot (www.matrixscience.com) database search engines with a statistically significant expectation value of

0.078. **(C)** Extracts were prepared from HEK293 cells transiently transfected with N-terminally FLAG-tagged PGAM1 (Ctrl) or N-terminally FLAG-tagged PGAM1 where H11 was mutated to N (H11N). Expression of both FLAG-tagged proteins in relation to endogenous PGAM1 was determined by Western blot using anti-PGAM1. The same extracts were incubated with [ $^{32}\text{P}$ ]PEP, and phosphorylation of PGAM1 determined by SDS-PAGE and autoradiography. **(D)** rPGAM1 was incubated with a cell extract containing [ $^{18}\text{O}$ ]phosphate-labeled PEP and normal isotopic ( $^{16}\text{O}$ ]phosphate) ATP before recovery of the H11-containing tryptic peptide by HPLC as described in (A). This peptide was analyzed by microcapillary LC/MS using the high mass accuracy of the FT-MS—only scan in a LTQ Orbitrap-XL mass spectrometer at 30,000 resolution obtaining sub-2-parts-per-million mass accuracy. The peaks at mass/charge ( $m/z$ ) = 697.79, 698.79, and 699.79 represent the doubly charged phosphorylated peptide pHGESAWNLENR that is heavy by two, four, and six mass units corresponding to the incorporation of one, two, and three  $^{18}\text{O}$ -labeled oxygen atoms, respectively. The peak at  $m/z$  = 696.79 represents the phosphorylated peptide containing unlabeled oxygen atoms.





expressing Cre and hence where *Brca1* was not deleted in the breast. Normal breast expresses PKM1; breast tumors express PKM2 (4) (fig. S14C). Lysates from the normal breast tissue and the breast tumor were subjected to 2D IEF and SDS-PAGE and analyzed by Western blot using anti-PGAM1 as shown. The most acidic species corresponding to H11 phosphorylation is indicated with an arrow.

Tumors express PKM2, whereas PKM1 is expressed in many normal tissues (3, 4). To determine whether a correlation between PGAM1 H11 phosphorylation status and PKM2 expression could also be observed for cancers in vivo, we analyzed tissues from animals by 2D Western blot with an antibody to PGAM. PKM1 was expressed in normal prostate tissue, whereas neoplastic prostate tissue expressed PKM2 (Fig. 5C). Analysis of these same cell lysates by 2D Western blot with an antibody against PGAM1 (anti-PGAM1) revealed that the isoelectric species corresponding to H11-phosphorylated PGAM1 was only detectable in the neoplastic prostate tissue (Fig. 5D). In a mouse with breast-specific deletion of the *Brcal* tumor suppressor gene, breast tumor tissue had an even more dramatic shift in isoelectric migration of PGAM1 associated with the H11-phosphorylated species (Fig. 5E), and this correlated with expression of PKM2 (fig. S14C). Thus, PEP-dependent phosphorylation of H11 on PGAM1 likely occurs in tumors as well as in cell lines expressing PKM2.

**Discussion.** We have shown that the high-energy phosphate of PEP can be transferred to the catalytic histidine (H11) of PGAM1 by an enzymatic process that does not require enolase-dependent conversion to 2PG. Phosphorylation of H11 is known to be required for PGAM1 catalytic function, and 2,3-BPG has been characterized as the cofactor required for PGAM1 activation (17). Our results reveal that PGAM1 can also be activated by PEP. The activity that catalyzes phosphate transfer from PEP to PGAM1 is separable from the well-known PEP-metabolizing enzymes, pyruvate kinase and enolase, and the by-product of the reaction appears to be pyruvate. Importantly, we find that, in cells expressing PKM2, a significant fraction of PGAM1 migrates at an isoelectric point consistent with the phospho-H11 species and that replacing PKM2 with the more active PKM1 isoform results in disappearance of this species. These results are consistent with a model where PKM2-expressing cells use a greater fraction of PEP for charging PGAM1 and less for the synthesis of ATP.

Despite the fact that PGAM1 has not been considered a rate-limiting enzyme in glycolysis, the differential H11 phosphorylation of PGAM1 we observed in PKM2- versus PKM1-expressing cells and tissues suggests that this enzyme may have a previously unappreciated regulatory function in controlling glycolysis in proliferating cells. PGAM1 is unique among the glycolytic enzymes in that its transcription is regulated by the tumor suppressor p53 (30), and increased expression of PGAM1 has been reported to immortalize primary cells through an unknown mechanism (31). PGAM1 was also identified as the target of a compound from a chemical genomics screen for molecules that inhibit breast cancer cell growth (32). Thus, one important consequence of down-regulating PKM2 activity by tyrosine kinases may be to increase H11-phosphorylated PGAM1. Phosphorylation of H11 on PGAM1 increases the mutase

function of the enzyme. This generates a positive feedback loop such that production of PEP increases the enzymatic activity of PGAM1. One possibility is that this feedback loop may promote the redistribution of metabolites upstream of PGAM1 into biosynthetic pathways that branch from glycolysis.

We propose that, in addition to pyruvate kinase, another activity to convert PEP into pyruvate may be active in cells (fig. S15). The existence of such an alternate glycolytic pathway may explain how cancer cells with less pyruvate kinase activity continue to display a high rate of glycolysis. The rate of PEP to pyruvate conversion observed in the absence of pyruvate kinase is comparable to the maximum enzyme velocity ( $V_{\max}$ ) of pyruvate kinase [65  $\mu\text{M}/\text{min}$  (33)], suggesting that this activity could account for a significant amount of the pyruvate produced from glucose in cells with a less active form of pyruvate kinase. When catalyzed by pyruvate kinase, the conversion of PEP into pyruvate is coupled to ATP generation (34). Phosphorylation of PGAM1 by PEP does not directly generate ATP but generates pyruvate. In order for a significant amount of pyruvate to be generated by this alternative pathway, the phosphohistidine of PGAM1 must turn over. Although conversion of 3PG to 2PG does not result in net loss of phosphohistidine, spontaneous hydrolysis of phosphohistidine on PGAM1 does occur (17). Also, 2,3-BPG can be produced by addition of 3PG or 2PG to phosphorylated-PGAM1 (reversal of the 2,3-BPG charging reaction), and the resulting 2,3-BPG can be hydrolyzed to 2PG and  $\text{P}_i$  (35). Lastly, it is possible that the activity responsible for PGAM1 phosphorylation can also act as a PEP phosphatase. Each of these possibilities results in the net conversion of PEP to pyruvate and  $\text{P}_i$  with no ATP synthesis. This lack of ATP synthesis may allow cells to metabolize glucose by a modified glycolysis that does not generate ATP and provides an advantage to proliferating cells. Historically, efforts to understand aerobic glycolysis stressed the importance of ATP consumption to allow the high rate of glucose metabolism observed in tumor cells (36). Cells must avoid ATP production in excess of demand to avoid allosteric inhibition of phosphofructokinase and other rate-limiting steps in glycolysis that are inhibited by a high ATP/adenosine monophosphate ratio (34). Thus, inhibition of PKM2 by cell growth signals may serve to uncouple the ability of cells to assimilate nutrients into biosynthetic pathways from the production of ATP and account for why PKM2 activity is decreased in rapidly dividing cells.

#### References and Notes

1. R. G. Jones, C. B. Thompson, *Genes Dev.* **23**, 537 (2009).
2. M. G. Vander Heiden, L. C. Cantley, C. B. Thompson, *Science* **324**, 1029 (2009).
3. S. Mazurek, C. B. Boschek, F. Hugo, E. Eigenbrodt, *Semin. Cancer Biol.* **15**, 300 (2005).
4. H. R. Christofk *et al.*, *Nature* **452**, 230 (2008).

5. H. R. Christofk, M. G. Vander Heiden, N. Wu, J. M. Asara, L. C. Cantley, *Nature* **452**, 181 (2008).
6. T. Hitosugi *et al.*, *Sci. Signal.* **2**, ra73 (2009).
7. Materials and methods are available as supporting material on Science Online.
8. J. D. Dombrackas, B. D. Santarsiero, A. D. Mesecar, *Biochemistry* **44**, 9417 (2005).
9. M. H. Saier Jr., J. Reizer, *Mol. Microbiol.* **13**, 755 (1994).
10. J. Deutscher, C. Francke, P. W. Postma, *Microbiol. Mol. Biol. Rev.* **70**, 939 (2006).
11. J. N. Burnell, M. D. Hatch, *Arch. Biochem. Biophys.* **231**, 175 (1984).
12. J. N. Burnell, M. D. Hatch, *Arch. Biochem. Biophys.* **245**, 297 (1986).
13. S. Minakami, H. Yoshikawa, *Biochem. Biophys. Res. Commun.* **18**, 345 (1965).
14. R. Lagunas, C. Gancedo, *Eur. J. Biochem.* **137**, 479 (1983).
15. S. Klump, J. Krieglstein, *Eur. J. Biochem.* **269**, 1067 (2002).
16. P. G. Besant, P. V. Attwood, *Biochim. Biophys. Acta* **1754**, 281 (2005).
17. L. A. Fothergill-Gilmore, H. C. Watson, *Adv. Enzymol. Relat. Areas Mol. Biol.* **62**, 227 (1989).
18. M. E. Lee, T. Nowak, *Biochemistry* **31**, 2172 (1992).
19. J. V. Olsen *et al.*, *Nat. Methods* **4**, 709 (2007).
20. K. F. Medzihradsky, N. J. Philipps, L. Senderowicz, P. Wang, C. W. Turck, *Protein Sci.* **6**, 1405 (1997).
21. A. J. Kleijnijenhuis, F. Kjeldsen, B. Kallipolitis, K. F. Haselmann, O. N. Jensen, *Anal. Chem.* **79**, 7450 (2007).
22. U. M. Hohenester, K. Ludwig, J. Krieglstein, S. König, *Anal. Bioanal. Chem.* **397**, 3209 (2010).
23. X. L. Zu, P. G. Besant, A. Imhof, P. V. Attwood, *Amino Acids* **32**, 347 (2007).
24. D. N. Perkins, D. J. Pappin, D. M. Creasy, J. S. Cottrell, *Electrophoresis* **20**, 3551 (1999).
25. J. K. Eng, A. L. McCormack, J. R. Yates III, *J. Am. Soc. Mass Spectrom.* **5**, 976 (1994).
26. W. A. Blättler, J. R. Knowles, *Biochemistry* **19**, 738 (1980).
27. M. Engel, S. Mazurek, E. Eigenbrodt, C. Welter, *J. Biol. Chem.* **279**, 35803 (2004).
28. L. E. Kay, P. Keifer, T. Saarinen, *J. Am. Chem. Soc.* **114**, 10663 (1992).
29. D. S. Wishart *et al.*, *Nucleic Acids Res.* **35**, D521 (2007).
30. E. C. Cheung, K. H. Vousden, *Curr. Opin. Cell Biol.*, in press; published online 8 January 2010.
31. H. Kondoh *et al.*, *Cancer Res.* **65**, 177 (2005).
32. M. J. Evans, A. Saghatelian, E. J. Sorensen, B. F. Cravatt, *Nat. Biotechnol.* **23**, 1303 (2005).
33. S. Ainsworth, N. MacFarlane, *Biochem. J.* **131**, 223 (1973).
34. A. L. Lehninger, D. L. Nelson, M. M. Cox, *Principles of Biochemistry* (Worth, New York, ed. 2, 1993).
35. J. Cho, J. S. King, X. Qian, A. J. Harwood, S. B. Shears, *Proc. Natl. Acad. Sci. U.S.A.* **105**, 5998 (2008).
36. E. Racker, *J. Cell. Physiol.* **89**, 697 (1976).
37. We thank A. Carrecedo and P. P. Pandolfi for normal and neoplastic prostate tissue; L. Burga and G. Wulf for normal breast and breast tumor; G. Bellinger for assistance with mouse dissection; M. Sasaki for help generating constructs; V. Vyas, A. Subtelny, L. Freimark, X. Yang, L. Schmidt, and M. Balastik for technical assistance; M. Bayro and S. Hyberts for help with processing the NMR spectra; and A. Shaywitz, J. Hutter, C. Benes, D. Anastasiou, A. Couvillion, and A. Saci for helpful discussions. This work was partially supported by the Damon Runyon Cancer Research Foundation (M.V.H.), the Burroughs Wellcome Fund (M.V.H.), the American Cancer Society (J.W.L.), Dana-Farber/Harvard Cancer Center (J.M.A. and J.W.L.), and by grants from the NIH (1K08CA136983 to M.V.H., 5P30CA006516-43 to J.M.A., 5 T32 CA009361-28 to J.W.L., R21/R33 DK070299 and P01GM047467 to G.W., R01 AI078063 and R21 CA128620 to J.D.R., R01-GM56302 and P01CA089021 to L.C.C., and 1P01CA120964-01A to J.M.A. and L.C.C.).

#### Supporting Online Material

www.sciencemag.org/cgi/content/full/329/5998/1492/DC1  
Materials and Methods  
Figs. S1 to S15  
Table S1  
References

5 February 2010; accepted 27 July 2010  
10.1126/science.1188015



# Quantum Walks of Correlated Photons

Alberto Peruzzo,<sup>1</sup> Mirko Lobino,<sup>1</sup> Jonathan C. F. Matthews,<sup>1</sup> Nobuyuki Matsuda,<sup>2</sup> Alberto Politi,<sup>1</sup> Konstantinos Poulkos,<sup>1</sup> Xiao-Qi Zhou,<sup>1</sup> Yoav Lahini,<sup>3</sup> Nur Ismail,<sup>4</sup> Kerstin Wörhoff,<sup>4</sup> Yaron Bromberg,<sup>3</sup> Yaron Silberberg,<sup>3</sup> Mark G. Thompson,<sup>1</sup> Jeremy L. O'Brien<sup>1\*</sup>

Quantum walks of correlated particles offer the possibility of studying large-scale quantum interference; simulating biological, chemical, and physical systems; and providing a route to universal quantum computation. We have demonstrated quantum walks of two identical photons in an array of 21 continuously evanescently coupled waveguides in a SiO<sub>x</sub>N<sub>y</sub> chip. We observed quantum correlations, violating a classical limit by 76 standard deviations, and found that the correlations depended critically on the input state of the quantum walk. These results present a powerful approach to achieving quantum walks with correlated particles to encode information in an exponentially larger state space.

Random walks are a powerful tool used in a broad range of fields, from genetics to economics. The quantum mechanical analog—quantum walks (1, 2)—generates a large coherent superposition state that allows massive parallelism in exploring multiple trajectories through a given connected graph (Fig. 1). A quantum walk can be implemented via a constant tunneling of quantum particles [including photons (3)] into several possible sites, realizing what is termed a “continuous-time quantum walk.” The mathematical model of continuous-time quantum walks such as the ones implemented here have been shown to be the limit of the discrete-time quantum walks (4). For continuous-time quantum walks, no quantum coin is required to generate superposition; this evolves continuously through tunneling between neighboring sites. Classical Markov chain theory dictates that the distribution of classical random walks converges toward a stationary distribution independent of the initial state (5). This is in contrast to the reversible (unitary) evolution of quantum walks, which do not in general converge to a steady state (5) but spread ballistically (Fig. 2C) when evolving in a low-noise (decoherence) environment. These features are at the heart of new algorithms for database search (6), random graph navigation, universal quantum computation (7), and quantum simulation (8, 9).

Quantum walks have been demonstrated with nuclear magnetic resonance (10), trapped ions (11, 12) and trapped neutral atoms (13), the frequency space of an optical resonator (14), single photons in bulk (15) and fiber (16) optics,

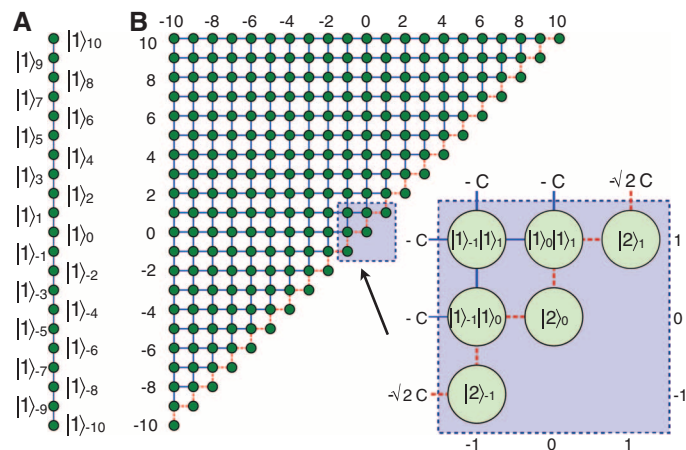
and the scattering of light in coupled waveguide arrays (17). However, these realizations have been limited to single-particle quantum walks, which have an exact mapping to classical wave phenomena (18), and therefore cannot provide any advantage (computational or otherwise) as a result of uniquely quantum mechanical behavior [in (12), two trapped ions were used to realize a three-sided coin in a quantum walk of the center-of-mass mode of the two ions]. Indeed, single-particle quantum walks have been observed with classical light (17). In contrast, for quantum walks of more than one indistinguishable particle, classical theory no longer provides a sufficient description—quantum theory predicts that probability amplitudes interfere, leading to distinctly nonclassical correlations (19). This quantum behavior gives rise to a computational advantage in quantum walks of two identical particles, which can be used to solve the graph isomorphism problem (determining whether there is a one-to-one mapping between two graphs), for example (20). The continuous-time model has been shown to

offer an exponential speed-up for particular computations (21). The major challenge associated with realizing quantum walks of correlated particles is the need for a low-decoherence system that preserves their nonclassical features.

The intrinsically low-decoherence properties and easy manipulation of single photons make them ideal for observing quantum mechanical behavior and for quantum technologies (22), and the effectiveness of arrays of continuously coupled waveguides for bright classical light has been demonstrated (17). However, quantum walks with correlated photons in such structures require a means to measure two-photon correlations across the waveguide array. The spacing between waveguides in an array required for evanescent coupling (on the order of several micrometers) is smaller than the minimum spacing of optical fiber arrays (127 μm) typically used to couple to single-photon detectors. Previous quantum optical waveguide circuits in a silica-on-silicon architecture promise to avoid decoherence effects present in other experimental realizations—interferometric stability and near-perfect mode overlap (22–25)—which is problematic in large-scale bulk optical realizations [an arbitrary  $N$  mode multipoint would require a network of  $O(N^2)$  beams splitters (26)]. However, the low refractive index contrast [ $\Delta = (n_{\text{core}}^2 - n_{\text{cladding}}^2)/2n_{\text{core}}^2 \approx 0.5\%$ ] in this architecture results in a large minimum bend radius (<0.1 dB loss at 800 nm) of  $\approx 15$  mm, making it unsuitable for coupling into and out of large-array quantum walk devices.

We fabricated waveguide arrays in SiO<sub>x</sub>N<sub>y</sub> (silicon oxynitride), a material that enables a much higher refractive index contrast than silica-on-silicon (the refractive index is determined by  $x$  and  $y$ ), resulting in more compact devices (Fig. 2A) and a practical means to realize large coupled waveguide arrays that can be coupled to optical fibers. The device shown in Fig. 2A is a 5-mm-

**Fig. 1. Quantum walks with one and two indistinguishable photons described by a Hamiltonian of coupled harmonic oscillators (Eq. 1). (A)** The linear array of vertices representing the state space of one photon populating  $N = 21$  waveguides in a coupled one-dimensional array. Site potentials for each vertex are  $-\beta$ , and hopping amplitudes between nearest neighbors are all equal to  $-C$ . **(B)** The two-dimensional lattice of vertices that represent the state space of two photons populating  $N = 21$  waveguides in a coupled one-dimensional waveguide array. (Inset) Enlarged portion of the lattice displays the vertex representation of the two photon basis states. Site potentials are all equal to  $-2\beta$ , and hopping amplitudes between adjacent vertices are either  $-C$  or  $-\sqrt{2}C$  as labeled.



<sup>1</sup>Centre for Quantum Photonics, H. H. Wills Physics Laboratory and Department of Electrical and Electronic Engineering, University of Bristol, Merchant Venturers Building, Woodland Road, Bristol BS8 1UB, UK. <sup>2</sup>Research Institute of Electrical Communication, Tohoku University, Sendai, Miyagi 980-8577, Japan. <sup>3</sup>Department of Physics of Complex Systems, The Weizmann Institute of Science, Rehovot, Israel. <sup>4</sup>Integrated Optical Microsystems Group, MESA+ Institute for Nanotechnology, University of Twente, Enschede, Netherlands.

\*To whom correspondence should be addressed. E-mail: jeremy.obrien@bristol.ac.uk

long silicon chip with  $\text{SiO}_x\text{N}_y$  waveguides with high refractive index contrast  $\Delta = 4.4\%$ . The minimum bend radius for this index contrast is  $600\text{ }\mu\text{m}$ , which enables much more rapid spreading of the waveguides from the evanescent coupling region where waveguides are pitched at  $2.8\text{ }\mu\text{m}$  to a pitch suitable for optical fiber [ $250\text{ }\mu\text{m}$  and  $125\text{ }\mu\text{m}$  for photon injection and photon collection, respectively (27)].

Photon pairs were generated in a frequency-entangled but spatial mode-separable state via type I spontaneous parametric downconversion in a 2-mm-thick  $\chi_2$  nonlinear bismuth borate  $\text{BiB}_3\text{O}_6$  (BiBO) crystal, pumped with 40 mW of 402-nm light from a continuous-wave diode laser. With an opening angle of  $3^\circ$ , pairs of degenerate photons of wavelength  $\lambda = 804\text{ nm}$  were filtered by 2-nm interference filters and focused onto two inputs of an array of polarization-maintaining fibers, which were butt-coupled to the waveguide chip. At the output of the chip, an array of multimode fibers guides the photons to 12 single-photon-counting modules. The detectors were connected to photon-counting logic based on three FPGA (field programmable gate array) boards used to postselect all possible two-photon coincidences between different outputs of the array in order to reconstruct the correlation matrices (Figs. 3 and 4). Quantum interference (degree of indistinguishability) was controlled by relative temporal delay between the pair of photons, using an

automated linear actuator, and characterized with a standard Hong-Ou-Mandel experiment. The pitch of the waveguide outputs is half that of the collecting fiber arrays, allowing 121 of the 231 possible two-photon correlations to be measured at the output.

Photons propagating through the coupled waveguide array (Fig. 2A) are modeled assuming nearest-neighbor coupling with the Hamiltonian for coupled oscillators (28), setting  $\hbar = 1$ :

$$\hat{H} = \sum_{j=1}^N \left[ \beta_j a_j^\dagger a_j + C_{j,j-1} a_{j-1}^\dagger a_j + C_{j,j+1} a_{j+1}^\dagger a_j \right] \quad (1)$$

where the creation and annihilation operators  $a_j^\dagger$  and  $a_j$  obey Bose-Einstein statistics and act on waveguide  $j$ . In our devices, the waveguide propagation constant  $\beta_j = \beta$  and coupling constant between adjacent waveguides  $C_{j,j+1} = C$  are designed to be uniform for all  $j$ . Through choice of operator  $\hat{A}$ , the Heisenberg equation of motion  $i d\hat{A}/dz = [\hat{A}, \hat{H}]$  models the dynamics of photons propagating along distance  $z$  of the array. For example, the propagation of a single photon initially injected into waveguide  $k$  is described by  $\hat{A} = a_k^\dagger$ , yielding (29)

$$i \frac{da_k^\dagger}{dz} = -\beta a_k^\dagger - C a_{k-1}^\dagger - C a_{k+1}^\dagger \quad (2)$$

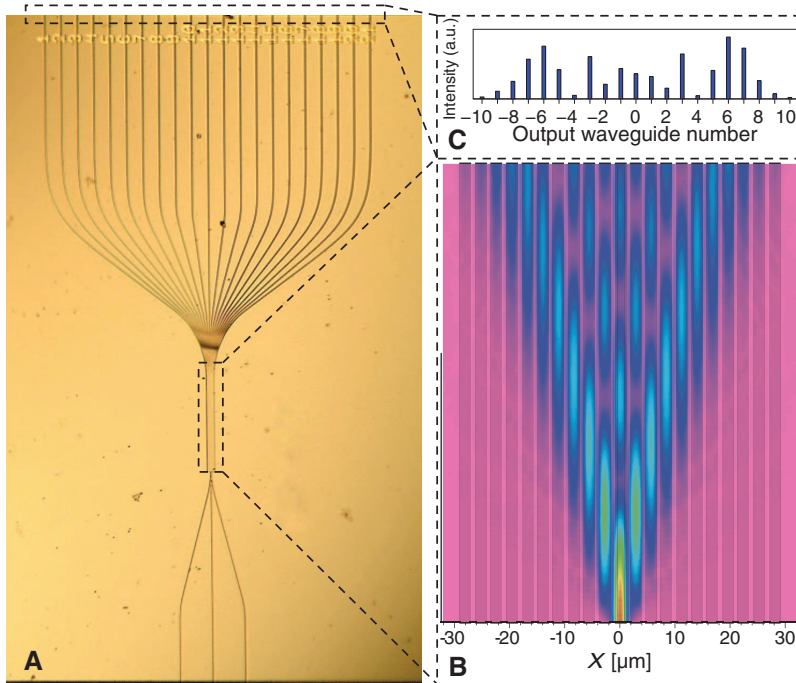


**Fig. 2.** A continuously coupled waveguide array for realizing correlated photon quantum walks. **(A)** An optical micrograph of a 21-waveguide array showing the three input waveguides, initially separated by  $250\text{ }\mu\text{m}$ , bending into the  $700\text{-}\mu\text{m}$ -long coupling region. All 21 outputs bend out to  $125\text{-}\mu\text{m}$  spacing. **(B)** Simulation of the intensity of laser light propagating in the array performed with commercial beam propagation software (this is equivalent to  $\langle a^\dagger a \rangle$  in the case of a single photon). **(C)** Output pattern of 810-nm laser light propagating through the waveguide array.

Evolving the vacuum state  $|0\rangle$  according to Eq. 2 and inspecting in the Schrödinger picture  $i d|\psi_1\rangle/dz = H^{(1)}|\psi_1\rangle$ , yields the effective Hamiltonian in the one-photon subspace  $H^{(1)}$ . From this Hamiltonian, an adjacency matrix  $M_{j,k}^{(1)} = {}_j\langle 1|H^{(1)}|1\rangle_k$  of the graph in Fig. 1A is constructed with the single-photon Fock basis  $\{|1\rangle_j\rangle$  for representation. A quantum walk on this graph evolves over length  $z$  according to the unitary transform  $U^{(1)} = \exp[-iH^{(1)}z]$  (2, 29), the exact dynamics of which can be observed by injecting bright light into the waveguide array (17). We used this approach to calibrate our device and the coupling efficiencies by launching horizontally polarized 810-nm laser light into the input of the central waveguide, waveguide 0. We measured the interference pattern shown in Fig. 2C, which corresponds to the probability distribution for single photons detected at the 21 output waveguides (numbered  $-10$  on the left, through 0, to 10 on the right). Before the waveguides reach their minimum separation at the central coupling region, they are coupled in the spreading regions on both sides. This coupling provides an effective coupling length of  $82\text{ }\mu\text{m}$ . We determined this length by comparing the output interference pattern for an array of length  $350\text{ }\mu\text{m}$  (fig. S1). From these data, the coupling constant  $C = 5\text{ mm}^{-1}$  was determined by running the simulation and minimizing the square of the errors (27).

The propagation of two indistinguishable photons initially injected into waveguide  $j$  and  $k$  is modeled with the operator  $\hat{A} = a_j^\dagger a_k^\dagger$  yielding

$$i \frac{da_j^\dagger a_k^\dagger}{dz} = -2\beta a_j^\dagger a_k^\dagger - C \left[ a_j^\dagger a_{k-1}^\dagger + a_j^\dagger a_{k+1}^\dagger + a_{k-1}^\dagger a_j^\dagger + a_{k+1}^\dagger a_j^\dagger \right] \quad (3)$$

From Eq. 3, the effective Hamiltonian  $H^{(2)}$  acting on the two-photon Fock space is extracted as a matrix represented in the two-photon Fock basis  $\{|1\rangle_j|1\rangle_k, |2\rangle_l\rangle$  which is equal to the adjacency matrix for the graph given in Fig. 1B. Evolution of the two-photon state through the device therefore simulates a single-particle quantum walk on the graph in Fig. 1B with  $O(N^2)$  vertices and unitary transform  $U^{(2)} = \exp[-iH^{(2)}z]$ . In general, a linear increase in the number of photons input into the coupled array results in exponential growth of the Hilbert space and of the corresponding graph. Emulating this with a single photon (or bright laser beam) would require an exponentially large number of waveguides. However, only when indistinguishable photons are injected in the device can the output state be nonseparable, exhibiting nonclassical correlated behavior (27). The two-photon unitary evolution can also be computed from the product of single-photon mode transformations (29).

The measured correlation matrices  $\Gamma_{q,r}$  (defined as the probability of detecting a two-photon coincidence across waveguides  $q,r$ ) (29, 30) for injecting two single photons into the central neighboring waveguides 0 and 1 (i.e.,  $a_0^\dagger a_1^\dagger|0\rangle$ ) are



**Fig. 3.** Measured and simulated correlations in waveguide arrays when two photons are coupled to waveguides 0 and 1:  $a_0^\dagger a_1^\dagger |0\rangle$  (A and B) for input photons separated with temporal delay longer than their coherence length and (C and D) for photons arriving simultaneously in the array. All resulting measurements are corrected for coupling fluctuations using simultaneously detected single-photon signal as well as relative detector efficiency; the integration time was 1 hour. The outcome of two photons populating one waveguide was detected using nondeterministic photon number resolving detection with an optical fiber splitter.

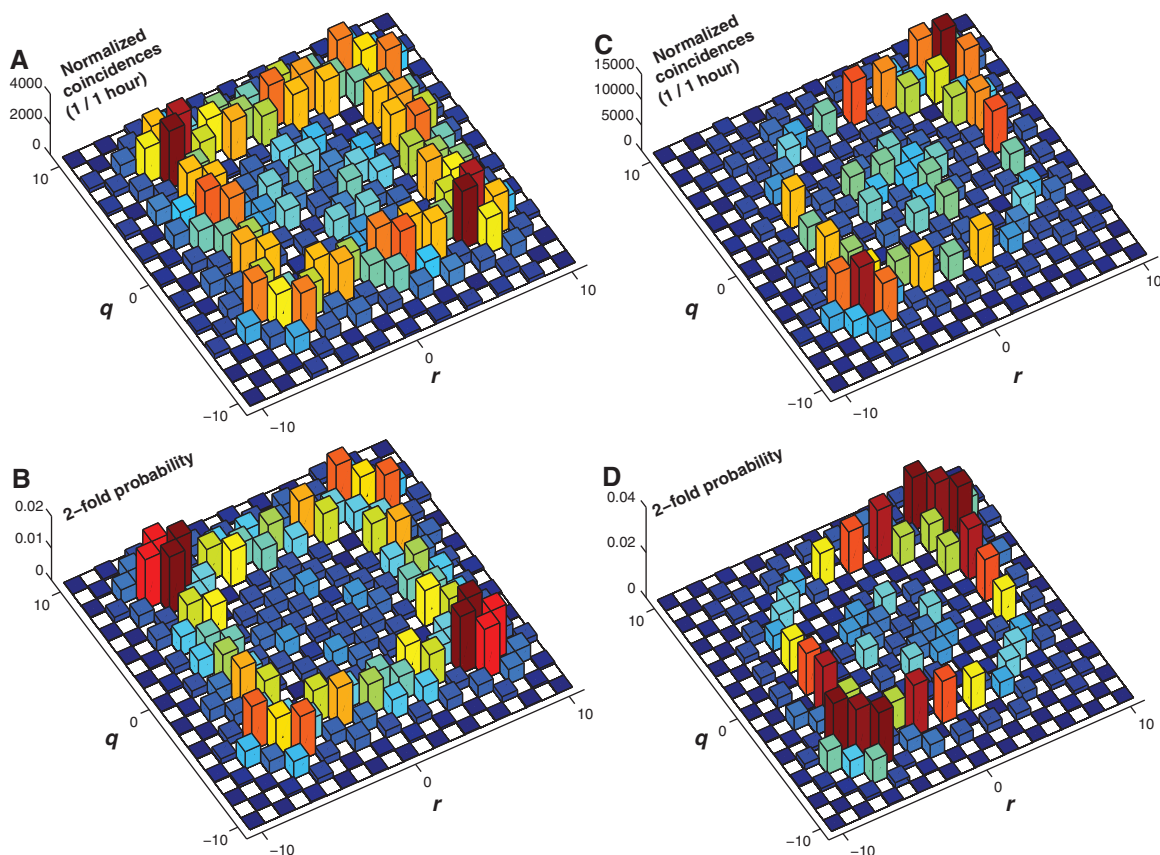
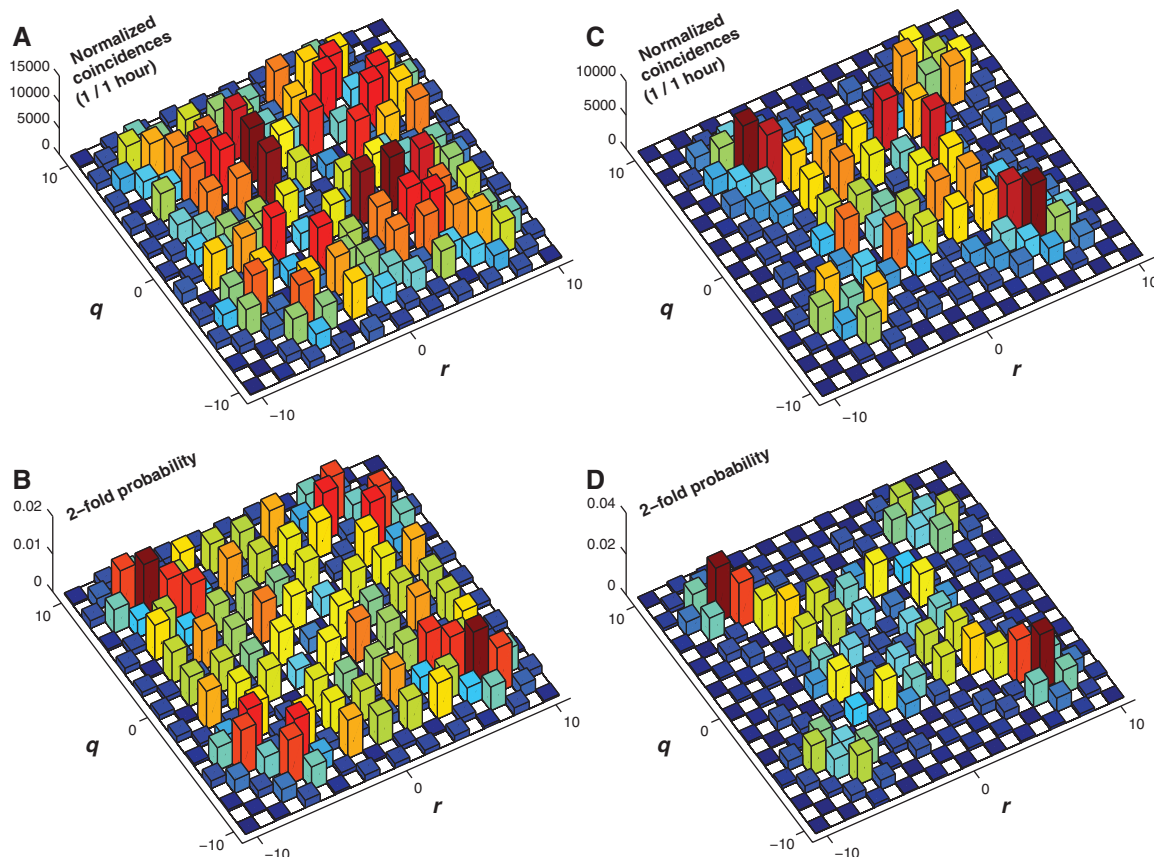


**Fig. 4.** Measured and simulated correlations in waveguide arrays when two photons are coupled to waveguides  $-1$  and  $1$ :  $a_{-1}^\dagger a_1^\dagger |0\rangle$  (A and B) for input photons separated with temporal delay longer than their coherence length and (C and D) for the photons arriving simultaneously in the array. All measurements are corrected for coupling fluctuations using the simultaneously detected single-photon count rate and relative detector efficiency; the integration time was 1 hour. The outcome of two photons populating one waveguide was detected using nondeterministic photon number resolving detection with an optical fiber splitter.



plotted in Fig. 3A for photons made distinguishable using temporal delay (not overlapped) and in Fig. 3C for pairs of indistinguishable (overlapped) photons. The overlap of these measured distributions with ideal simulations (plotted in Fig. 3, B and D) are  $S = 0.980 \pm 0.001$  and  $S = 0.934 \pm 0.001$ , respectively, where  $S$  is the similarity between two probability distributions  $\Gamma$  and  $\Gamma'$  defined by

$$S = \left( \sum_{i,j} \sqrt{\Gamma_{i,j} \Gamma'_{i,j}} \right)^2 / \sum_{i,j} \Gamma_{i,j} \sum_{i,j} \Gamma'_{i,j},$$

which is a generalization of the average fidelity based on the (classical) fidelity between probability distributions. The lower  $S$  in the overlapped case is attributed to imperfect quantum interference. These results display a generalized bunching behavior (tending to both travel to one side of the array or the other) characteristic of quantum interference: The vanishing of the two off-diagonal lobes is a result of destructive interference of quantum amplitudes resulting from repeated  $\pi/2$  phase shifts in the photon tunneling between neighboring waveguides.

Distinctly different behavior is observed on injecting two photons in two waveguides with one waveguide separating them. The measured correlation matrices for injecting photons into waveguides  $-1$  and  $1$ , and the vacuum in waveguide  $0$  (i.e.,  $a_{-1}^\dagger a_1^\dagger |0\rangle$ ) in the center of the array are plotted in Fig. 4. The similarities with the ideal simulation are  $S = 0.970 \pm 0.002$  and  $S = 0.903 \pm 0.002$  for the delayed and overlapped photons, respectively. In this case, instead of bunching, when the two photons are indistinguishable they generate a pattern in which the main feature is the vanishing of the probability of simultaneously detecting one photon in the center of the array and one at the limit of ballistic propagation (for example, in waveguides  $0$  and  $7$  in Fig. 4, C and D).

Detecting twofold coincidences of two indistinguishable photons leads to nonclassical correlations across pairs of waveguides in the array (29). The correlation function after length  $z$  for two photons populating waveguides  $q$  and  $r$  is given (29, 30) by

$$\Gamma_{q,r}(z) = \frac{1}{1 + \delta_{q,r}} \left| U_{q,q}^{(1)} U_{r,r}^{(1)} + U_{q,r}^{(1)} U_{r,q}^{(1)} \right|^2 \quad (4)$$

For classical light, including random phase fluctuations that mimic certain properties of quantum light, diagonal correlations  $\Gamma_{q,q}$  are related to correlations in the off-diagonal lobes  $\Gamma_{q,r}$ ,  $q \neq r$  according to the inequality (29)

$$V_{q,r} = \frac{2}{3} \sqrt{\Gamma_{q,q}^{(C)} \Gamma_{r,r}^{(C)}} - \Gamma_{q,r}^{(C)} < 0 \quad (5)$$

Inequality Eq. 5 is violated when two indistinguishable photons are injected into the device. Measured violations from injecting photons into  $0$ ,  $1$ , and  $-1, +1$  are plotted in fig. S2, with

white data points representing no violation, and colored data points representing the extent of violating Eq. 5 for each pair of waveguides. This is quantified as a function of standard deviations  $\sigma$  (computed from propagation of error from two-photon coincidence detection, assuming Poissonian statistics), with the maximum violation reaching 76 standard deviations. Inequality Eq. 5 is not violated when the photons of the input pairs are distinguishable.

These demonstrations show uniquely nonclassical behavior of two identical particles, tunneling through arrayed potential wells; two photons initially prepared in a separable product state interfere in a generalization of the Hong-Ou-Mandel effect, yielding nonclassical spatial correlations. Increasing the photon number  $n$  will emulate quantum walks on hypercubic graphs exponentially large in  $n$ , and exploiting quantum interference in three-dimensional directly written waveguides (31) allows a further increase in graph size (32). Enlarging the guided mode or decreasing the waveguide separation provides another increase in graph complexity. This requires a model beyond nearest-neighbor coupling, tending toward a multimode interference slab waveguide when the channel separation goes to zero.

Here, we have modeled and used arrays of waveguide with fixed propagation and coupling coefficients  $\beta_k = \beta$  and  $C_{k+1} = C$ , but varying these parameters independently for each  $k$  provides a means to engineer the quantum walk's precise graph structure. For example, varying these parameters randomly and independently allows one to investigate correlated quantum walks in disordered systems and to verify the effects of Anderson localization, known to affect propagation of quantum information (33, 34). Reconfigurable waveguide circuits (22, 24) will allow real-time control of the input state and the graph structure itself, enabling, for example, phase control over entangled "NOON" input states, such as  $|20\rangle + e^{i\phi} |02\rangle$ , to yield methods for simulating symmetric and antisymmetric particles undergoing a quantum walk (29). The waveguide architecture is intrinsically scalable—networks of hundreds of waveguides are routinely implemented in photonics applications (switches, modulators, etc.)—and single-particle quantum walks with classical light have been implemented in such devices (17). Homogeneity of the coupling constant for quantum walk devices with hundreds of waveguides is set by the tolerance of waveguide fabrication and will be comparable to that observed here (indicated by the symmetry in Fig. 2C). For future application, computational data rates will be defined by high-efficiency and high-repetition rate single-photon sources and detectors (22).

## References and Notes

1. Y. Aharonov, L. Davidovich, N. Zagury, *Phys. Rev. A* **48**, 1687 (1993).
2. E. Farhi, S. Gutmann, *Phys. Rev. A* **58**, 915 (1998).

3. B. J. Smith, M. G. Raymer, *Phys. Rev. A* **74**, 062104 (2006).
4. A. M. Childs, *Commun. Math. Phys.* **294**, 581 (2010).
5. J. Kempe, *Contemp. Phys.* **44**, 307 (2003).
6. A. M. Childs, J. Goldstone, *Phys. Rev. A* **70**, 022314 (2004).
7. A. M. Childs, *Phys. Rev. Lett.* **102**, 180501 (2009).
8. M. Mohseni, P. Rebentrost, S. Lloyd, A. Aspuru-Guzik, *J. Chem. Phys.* **129**, 174106 (2008).
9. M. B. Plenio, S. F. Huelga, *N. J. Phys.* **10**, 113019 (2008).
10. C. A. Ryan, M. Laforest, J. C. Boileau, R. Laflamme, *Phys. Rev. A* **72**, 062317 (2005).
11. H. Schmitz *et al.*, *Phys. Rev. Lett.* **103**, 090504 (2009).
12. F. Zähringer *et al.*, *Phys. Rev. Lett.* **104**, 100503 (2010).
13. M. Karski *et al.*, *Science* **325**, 174 (2009).
14. D. Bouwmeester, I. Marzoli, W. Karman, *Phys. Rev. A* **61**, 013410 (1999).
15. B. Do *et al.*, *J. Opt. Soc. Am. B* **22**, 499 (2005).
16. A. Schreiber *et al.*, *Phys. Rev. Lett.* **104**, 050502 (2010).
17. H. B. Perets *et al.*, *Phys. Rev. Lett.* **100**, 170506 (2008).
18. P. L. Knight, E. Roldán, J. E. Sipe, *Phys. Rev. A* **68**, 020301 (2003).
19. Y. Omar, *Phys. Rev. A* **74**, 042304 (2006).
20. J. K. Gamble *et al.*, *Phys. Rev. A* **81**, 052313 (2010).
21. A. M. Childs *et al.*, in *STOC '03: Proceedings of the Thirty-Fifth Annual ACM Symposium on Theory of Computing* (Association for Computing Machinery, New York, 2003), pp. 59–68.
22. J. L. O'Brien *et al.*, *Nat. Photonics* **3**, 687 (2009).
23. A. Politi *et al.*, *Science* **320**, 646 (2008).
24. J. C. F. Matthews *et al.*, *Nat. Photonics* **3**, 346 (2009).
25. A. Politi *et al.*, *Science* **325**, 1221 (2009).
26. M. Reck, A. Zeilinger, H. J. Bernsten, P. Bertani, *Phys. Rev. Lett.* **73**, 58 (1994).
27. Materials and methods are available as supporting material on Science Online.
28. L. E. Estes, T. H. Keil, L. M. Narducci, *Phys. Rev.* **175**, 286 (1968).
29. Y. Bromberg, Y. Lahini, R. Morandotti, Y. Silberberg, *Phys. Rev. Lett.* **102**, 253904 (2009).
30. K. Mattle *et al.*, *Appl. Phys. B* **60**, S111 (1995).
31. G. D. Marshall *et al.*, *Opt. Express* **17**, 12546 (2009).
32. T. D. Mackay *et al.*, *J. Phys. Math. Gen.* **35**, 2745 (2002).
33. J. P. Keating, N. Linden, J. C. F. Matthews, A. Winter, *Phys. Rev. A* **76**, 012315 (2007).
34. Y. Lahini *et al.*, *Phys. Rev. Lett.* **100**, 013906 (2008).
35. We thank N. Brunner, A. Laing, T. Rudolph, and J. Twamley for helpful discussions. This work was supported by Engineering and Physical Sciences Research Council, European Research Council, EU-FP7 project "Quantum Integrated Photonics", Quantum Information Processing Interdisciplinary Research, Intelligence Advanced Research Projects Activity, the Leverhulme Trust, Centre for Nanoscience and Quantum Information, and the Japan Society for the Promotion of Science. J.L.O.B. acknowledges a Royal Society Wolfson Merit Award.

## Supporting Online Material

www.sciencemag.org/cgi/content/full/329/5998/1500/DC1  
Methods  
Figs. S1 to S3  
References

9 June 2010; accepted 28 July 2010  
10.1126/science.1193515



# Global Distribution of Large Lunar Craters: Implications for Resurfacing and Impactor Populations

James W. Head III,<sup>1\*</sup> Caleb I. Fassett,<sup>1</sup> Seth J. Kadish,<sup>1</sup> David E. Smith,<sup>2,3</sup> Maria T. Zuber,<sup>2,3</sup> Gregory A. Neumann,<sup>3</sup> Erwan Mazarico<sup>2,3</sup>

By using high-resolution altimetric measurements of the Moon, we produced a catalog of all impact craters  $\geq 20$  kilometers in diameter on the lunar surface and analyzed their distribution and population characteristics. The most-densely cratered portion of the highlands reached a state of saturation equilibrium. Large impact events, such as Orientale Basin, locally modified the prebasin crater population to  $\sim 2$  basin radii from the basin center. Basins such as Imbrium, Orientale, and Nectaris, which are important stratigraphic markers in lunar history, are temporally distinguishable on the basis of crater statistics. The characteristics of pre- and postmare crater populations support the hypothesis that there were two populations of impactors in early solar system history and that the transition occurred near the time of the Orientale Basin event.

The record of impact craters on the surface of the Moon, particularly the size-frequency distribution (SFD) and spatial density of craters, has long been used to infer information about the age of surfaces and the sequence of geological events (1). Unfortunately, uneven areal coverage, different image resolutions, and

a wide range of solar illumination geometries from previous spacecraft mission data have precluded the compilation of a consistent global data set of the impact crater population. In the past year, the Lunar Orbiter Laser Altimeter (LOLA) (2), an instrument on board the Lunar Reconnaissance Orbiter (LRO) spacecraft, has acquired globally

distributed, high-precision measurements of the topography of the Moon, which enable the creation of a 64-pixels-per-degree digital terrain model (DTM) and a shaded relief model of the surface (3). These data provide a view of the global distribution of impact craters without the observational uncertainties that arose from measurement of craters on images of heterogeneous illumination condition and uneven coverage and quality. We used this data set to produce a global compilation of the distribution of impact craters  $\geq 20$  km in diameter.

We mapped craters on the Moon by overlaying a 20-km reference grid on the topography and hillshade and by systematically measuring across the lunar surface (4) with the CraterTools extension to ArcMap (5) to make diameter measurements of craters. All craters with a measurable rim and central depression were cataloged, regardless of their degradation states or whether they were embayed or buried by younger surface

<sup>1</sup>Department of Geological Sciences, Brown University, Providence, RI 02912, USA. <sup>2</sup>Department of Earth, Atmospheric and Planetary Sciences, Massachusetts Institute of Technology, Cambridge, MA 02129, USA. <sup>3</sup>Solar System Exploration Division, NASA Goddard Space Flight Center, Greenbelt, MD 20771, USA.

\*To whom correspondence should be addressed. E-mail: james\_head@brown.edu

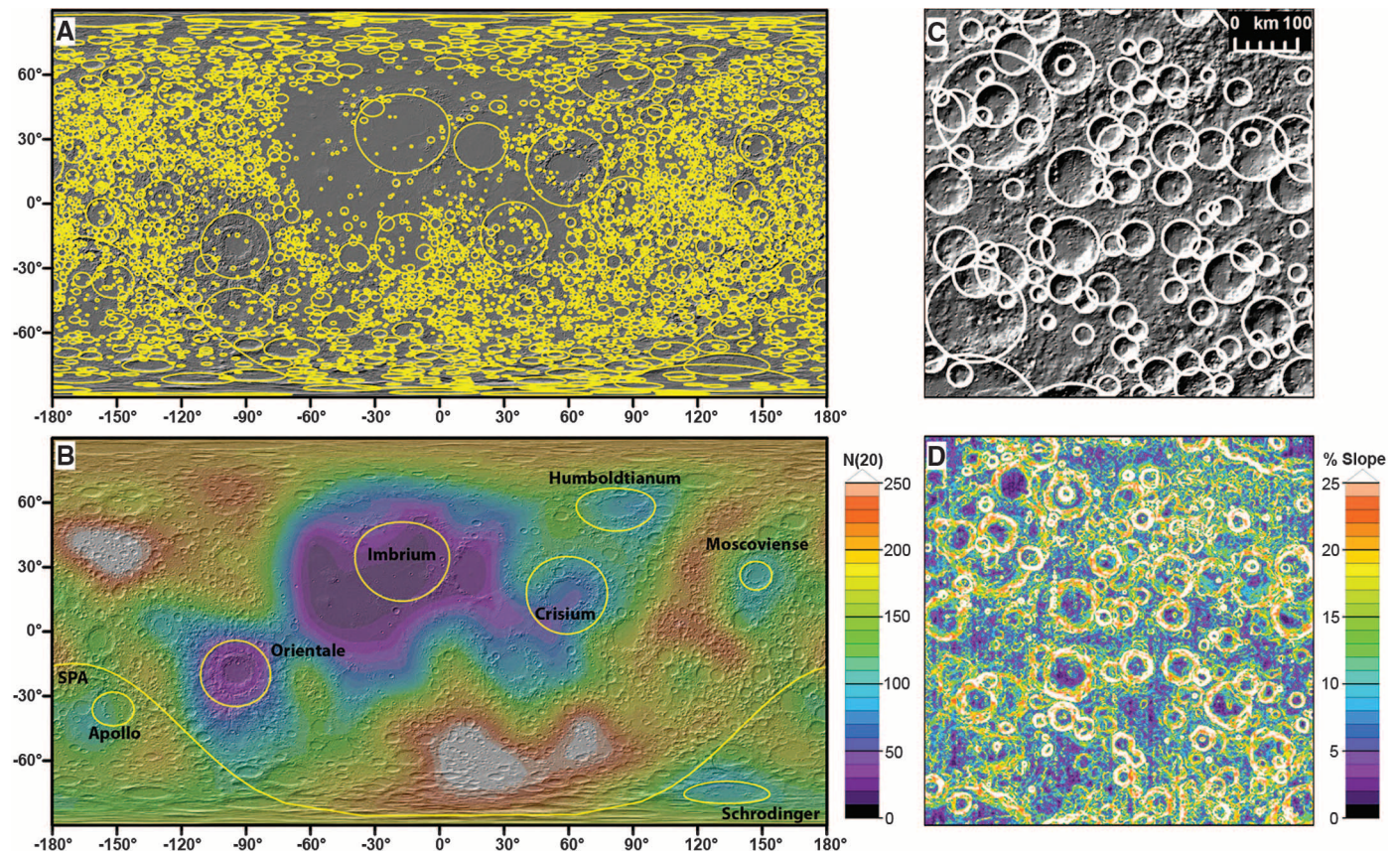


**Fig. 1.** (A) An outline of the craters mapped on the surface of the Moon from LOLA data superposed on a hillshade rendering of LOLA topography (2, 3). (B) Crater densities on the Moon for craters  $\geq 20$  km in diameter, calculated in neighborhoods of radius 500 km. (C and D) Central far-side highlands

(centered at  $-7^\circ\text{N}$ ,  $130^\circ\text{E}$ ), one of the most densely cratered areas of the Moon. (C) Craters superposed on a LOLA hillshade base map. (D) Slope map of area in (C) showing the lack of smooth intercrater plains such as those found on Mercury (11).



units; identified craters were also examined in an underlying ArcMap layer containing the best available images. In total, we mapped 5185 craters with diameters  $\geq 20$  km on the lunar surface, a factor of  $\sim 2$  increase in the number of craters of this size from Wilhelms *et al.* (6), whose analysis examined 82% of the lunar surface.

By using the craters mapped in our data set (Fig. 1A), we determined the areal density of craters on the Moon by calculating the number of craters in a moving neighborhood of 500 km in radius (Fig. 1B). The scale of this moving neighborhood sets the minimum area that is effectively sampled,  $\sim 8 \times 10^5$  km<sup>2</sup>. The resulting crater densities reflect first-order variations in the crater retention age (for 20-km craters and larger) across the surface. We report densities here as  $N(20)$  values, which represent the number of craters per

unit area with diameter  $\geq 20$  km, normalized to  $10^6$  km<sup>2</sup>. The most prominent features in Fig. 1B are (i) the densely cratered highlands, particularly on the southern nearside and north-central far side of the Moon, (ii) the interior and surroundings of stratigraphically young impact basins, especially Orientale, and (iii) mare regions, which have the lowest crater densities on the Moon.

Impact crater SFD analyses for units in the maria have been used successfully to develop stratigraphic sequences for individual areas (7) and combined with radiometric dates from samples returned from the lunar maria to establish a volcanic flux for the Moon as a whole (8). These SFD techniques can thus link specific mare crustal units to relative and absolute ages. For the highlands, on the other hand, crater densities are in the

range  $N(20) = 100$  to 280. These extremely high densities in the highlands are important because they fall in a range of  $\sim 3$  to 10% of geometric saturation (9), consistent with empirical saturation equilibrium (10), a condition where, on average, every new crater erases a preexisting crater of comparable size. Because nearly all of the lunar highlands are in this range, our data further demonstrate that impact crater SFDs, unlike those in the younger maria, do not directly reflect differences in the actual age of the underlying crustal rocks. Examples of the most densely cratered surfaces on the Moon (Fig. 1C) illustrate this well: Crater densities in the north-central far side are so high that addition of new craters over most of the size range does not measurably change the SFD (and thus the age), despite the fact that the crustal rocks themselves are likely to date from

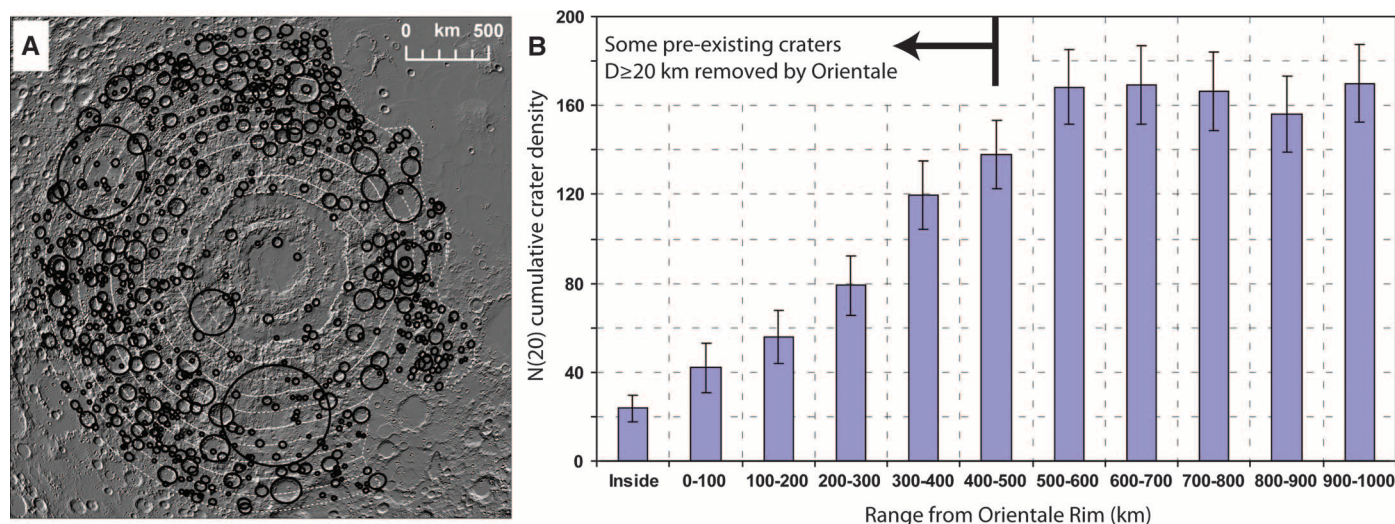


**Fig. 2.** Orientale Basin and radial distribution of craters. (A) Distribution of craters in the surroundings of Orientale on LOLA hillshade base map. (B)  $N(20)$  cumulative crater density as a function of increasing radial range from the Orientale basin center. Error bars in all figures are  $\sigma \pm \sqrt{N/A}$ , where  $A$  is the count area.

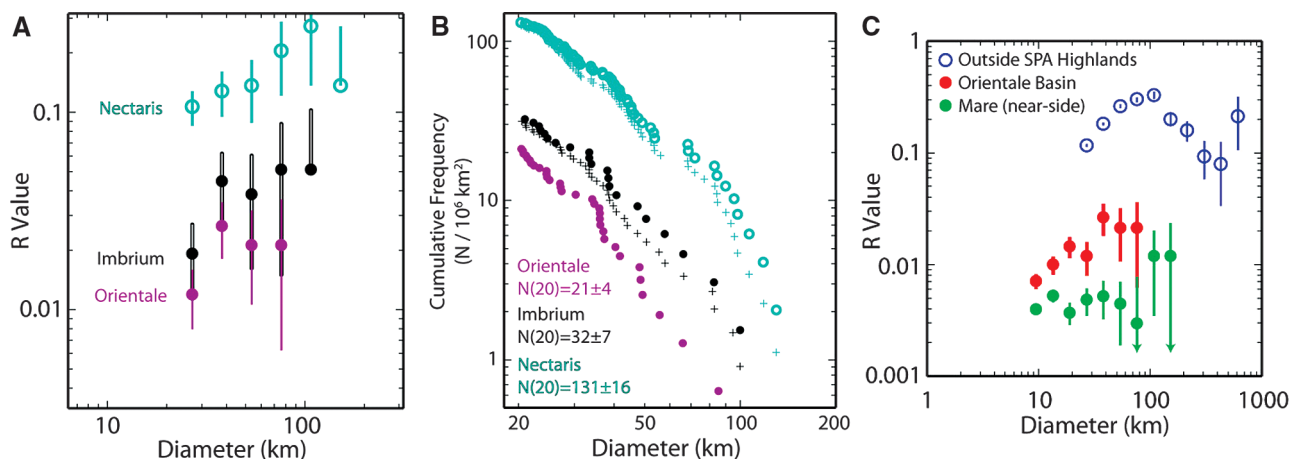


**Fig. 3.** Crater size-frequency distributions. (A)  $R$  plot (21) and (B) cumulative plot of craters superposed on three important basin stratigraphic markers on the Moon, which are clearly separable in crater density. On the cumulative plot, for mare-filled basins Imbrium and Nectaris, relevant counts areas are computed in two ways that give a similar qualitative results: a traditional rim-area method [circles, also the data in (B)] and

with a buffered crater counting correction (16) that allows inclusion of craters on the margin of the mare that superpose the basin (hatches). (C)  $R$  plot (areal density) (21) of craters superposed on lunar nearside mare, Orientale, and representative highlands crust (outside South Pole-Aitken Basin), which illustrates the difference in density and SFD slope on these terrains (18).



the most ancient period of lunar crustal genesis, a few hundred million years after lunar formation. Furthermore, slope maps of this area (Fig. 1D) show no evidence for extensive smooth areas such as intercrater plains, the type of volcanic resurfacing thought to have accompanied the early crustal history of Mercury (11). Such early volcanism could have occurred on the Moon (12) but is not now detectable by using SFD data because of crater saturation equilibrium. Conversely, these observations demonstrate that extrusive volcanism in early lunar history, if it occurred, was characterized by a flux low enough that it did not influence the crater population in a detectable manner.

Examination of the highlands impact crater density distribution (Fig. 1, A and B) does show regional variations, however. The interior and surroundings of stratigraphically young impact basins, especially Orientale, show  $N(20)$  numbers intermediate between the most heavily cratered highlands [ $N(20) = 150$  to  $250$ ] and the lunar maria [ $N(20) = 25$  to  $50$ ]. These data show that the proximity of a given region to young craters and basins was a key factor in establishing the local variations in crater density that is observed. This phenomenon results from the obliteration of craters below the impact basin itself, the burial of craters near the basin rim [in a process described as proximity weathering or degradation (13)], and their modification further away, by the dynamic emplacement of the basin ejecta. This process, proximity age resetting, results in selective loss of craters of different diameters as a function of the basin size and increasing radial range. For example, the formation of the 930-km-diameter Orientale Basin (Figs. 1B and 2A) resulted in the complete obliteration of craters below the basin (an area of  $6.8 \times 10^5 \text{ km}^2$ ), and the demonstrable loss of craters  $\geq 20$  km diameter out to about 500-km radius from the basin rim crest (Fig. 2B). Within 100 km of the basin rim crest, the  $N(20)$  number decreased by  $\sim 74\%$  compared with the regional background population, between 100 and 300 km by  $\sim 60\%$  and between 300 to 500 km by  $\sim 19\%$ , before returning to the regional average of  $\sim N(20) = 160$  at radial distances greater than  $\sim 500$  km from the rim crest (Fig. 2B). Thus, detailed examination of the Orientale crater population (Figs. 1 and 2) shows that this single basin-forming event significantly altered the preexisting crater population, causing proximity age resetting out to a radial range of  $\sim 965$  km from the basin center, an area comprising  $\sim 8\%$  of the total lunar surface. Furthermore, analysis of Fig. 1B in the vicinity of Orientale Basin shows low-density lobes extending to the south over Mendel-Rydberg Basin and to the northwest toward Hertzprung Basin, both of which predate Orientale but are relatively young stratigraphically.

In addition to obliterating craters, impact basin events also create large secondary craters at radial distances in excess of about one basin radius from the rim crest. These craters are predicted to be  $\sim 4\%$  of the size of the primary (14) and known to

range up to diameter ( $D$ )  $\sim 25$  km for Orientale Basin (1). Thus, basins larger than Orientale could have produced even larger secondary craters and crater clusters. Indeed, basin secondary craters up to 20 to 40 km in diameter have been hypothesized to be an important part of the highland crater population, potentially polluting the primary impactor population and skewing surfaces to artificially older ages (15). To test this hypothesis, we performed an analysis similar to that shown in Fig. 2 for Orientale ( $D = 930$  km), Imbrium ( $D = \sim 1160$  km) and South Pole–Aitken ( $D \sim 2500$  km) basins, centering the count areas on each basin and extending the annular analysis out to one basin diameter from the rim crest, an area known to contain radial ejecta and secondary crater chains and fields (1). As can be seen in the Orientale example (Fig. 2), the  $N(20)$  values for the range between 500 and 1000 km from the rim crest are similar to the  $N(20)$  values for typical, but not the most densely cratered, highlands (Fig. 1B). Similar relationships are seen for Imbrium and South Pole–Aitken basins. No annular zones of statistically significant increased crater density are observed, nor do secondaries traceable to these basins appear to contribute a significant number of craters  $\geq 20$  km to the crater population of surrounding regions.

We used the global crater database to revisit the SFD of important basins (Orientale, Imbrium, and Nectaris) that represent important markers within the lunar stratigraphy (1) and determined the superposed crater populations on these three basins (Fig. 3, A and B). Not surprisingly, the SFD plots (both  $R$  and cumulative) show a clear, separable distinction between these three basins, with Orientale and Imbrium being closer together in crater frequency than Imbrium and Nectaris. Our global data set, however, permits the use of buffered crater-counting techniques (16), and this results in a more robust SFD to be determined for these three important stratigraphic markers (see crosses in Fig. 3B). This enables a reanalysis of the sequence of basins proposed by Wilhelms (1) to lie between, and before, these key events. Further, should absolute age dates of key basin events be firmly established, these data will permit a more robust determination of the flux in early lunar history, and a test of the late heavy bombardment hypothesis (17).

Controversy has long existed concerning the nature of the impactor population bombarding inner planetary body surfaces throughout solar system history. Some hypothesize that the impactor population has been essentially similar in source and makeup throughout history, differing only in flux (18). Others have suggested that there is a clear difference in the populations with time and that this difference is reflected in the shape of the SFD of older and younger crater populations seen on planetary surfaces (6, 19). The global data set permits the assessment and testing of these hypotheses. For Orientale and the nearside mare, both of which are geologically young, we have extended our crater database to a

minimum diameter of  $D = 8$  km and examined stratigraphic relationships to ensure that measured craters are superposed on (postdate) these features.

Our data show a distinct difference between the shape of the SFD of the older highland and younger mare crater populations (Fig. 3C). The highlands have a greater density of large craters ( $D \sim 50$  to  $100$  km) compared with small craters (e.g.,  $D \sim 20$  to  $30$  km) than the mare surfaces. This is consistent with a less-steep production function at this size range. We applied the two-sample Kolmogorov-Smirnov test to assess the formal significance of this apparent difference in the shape of crater SFD on these units and found a very low probability that these SFD are the same distribution ( $P \sim 1.5 \times 10^{-9}$ ). This difference is evident in our data both in the highlands as a whole, as well as in “pure” subregions of the highlands (20), which have been suggested as examples of the least modified cratered regions of the lunar crust. The SFD distribution of craters superposed on Orientale may be intermediate in nature, although it is statistically not distinguishable from the mare. These global observations show a change in the lunar SFD, consistent with observations on less comprehensive lunar data sets (6, 19). This supports the conclusions of Strom *et al.* (19), who hypothesized the existence of an early and a later impactor population inside the asteroid belt. Furthermore, it places the transition between these two populations at about the time of Orientale Basin, the last large multi-ringed basin thought to have formed  $\sim 3.8$  billion years ago (1).

## References and Notes

1. D. E. Wilhelms, *The Geologic History of the Moon* (U.S. Geological Survey Professional Paper no. 1348, Washington, DC, 1987).
2. D. E. Smith *et al.*, *Space Sci. Rev.* **150**, 209 (2010).
3. D. E. Smith *et al.*, *Geophys. Res. Lett.*, in press; available online at [www.agu.org/journals/pip/gl/2010GL043751-pip.pdf](http://www.agu.org/journals/pip/gl/2010GL043751-pip.pdf).
4. Crater diameter measurements using the CraterTools extension (3) are defined on the basis of a best-fit circle, fit to the crater rim based on three points selected along the rim or, alternatively, based on drawing a rim-to-rim diameter. CraterTools corrects measurements to a local map projection. Regions poleward of  $70^\circ$  latitude are examined separately in polar projections, and these data are then merged with the mid- and low-latitude data to produce the global data set. This survey method is repeated at multiple scales to ensure that all craters were detected, from the basins to 20-km-scale craters.
5. T. Kneissl *et al.*, *Planet. Space Sci.*, in press; published online 24 March 2010 (10.1016/j.pss.2010.03.015).
6. D. E. Wilhelms *et al.*, *Proc. Lunar Sci. Conf.* **IX**, 3735 (1978).
7. H. Hiesinger, R. Jaumann, G. Neukum, J. W. Head III, *J. Geophys. Res.* **105**, 29,239 (2000).
8. H. Hiesinger *et al.*, *J. Geophys. Res.* **108**, 5065 (2003).
9. D. E. Gault, *Radio Sci.* **5**, 273 (1970).
10. J. E. Richardson, *Icarus* **204**, 697 (2009).
11. R. G. Strom, N. J. Trask, J. E. Guest, *J. Geophys. Res.* **80**, 2478 (1975).
12. J. W. Head III, L. Wilson, *Geochim. Cosmochim. Acta* **56**, 2155 (1992).
13. J. W. Head, *Moon* **12**, 299 (1975).
14. H. J. Melosh, *Impact Cratering* (Oxford, New York, 1989).
15. D. E. Wilhelms, *Proc. Lunar Sci. Conf.* **VII**, 2883 (1976).

16. C. I. Fassett, J. W. Head III, *Icarus* **195**, 61 (2008).
17. B. A. Cohen, T. D. Swindle, D. A. Kring, *Science* **290**, 1754 (2000).
18. G. Neukum, B. A. Ivanov, W. K. Hartmann, *Space Sci. Rev.* **96**, 55 (2001).
19. R. G. Strom, R. Malhotra, T. Ito, F. Yoshida, D. A. Kring, *Science* **309**, 1847 (2005).
20. W. K. Hartmann, *Meteoritics* **30**, 451 (1995).
21. *R* plots are constructed by dividing the differential SFD by a power law  $dN/dD \sim D^{-3}$ , where  $N$  is the number of craters within a given increment of crater diameter in a given area (18).
22. We thank the LRO and LOLA mission teams for their efforts, which made the observations

in this study possible, and T. Kneissl for developing the CraterTools extension to ArcMap. Funding was provided by NASA grant NNX09AM54G for LOLA.

13 July 2010; accepted 25 August 2010  
10.1126/science.1195050

# Global Silicate Mineralogy of the Moon from the Diviner Lunar Radiometer

Benjamin T. Greenhagen,<sup>1\*</sup> Paul G. Lucey,<sup>2</sup> Michael B. Wyatt,<sup>3</sup> Timothy D. Glotch,<sup>4</sup> Carlton C. Allen,<sup>5</sup> Jessica A. Arnold,<sup>4</sup> Joshua L. Bandfield,<sup>6</sup> Neil E. Bowles,<sup>7</sup> Kerri L. Donaldson Hanna,<sup>3</sup> Paul O. Hayne,<sup>8</sup> Eugenie Song,<sup>6</sup> Ian R. Thomas,<sup>7</sup> David A. Paige<sup>8</sup>

We obtained direct global measurements of the lunar surface using multispectral thermal emission mapping with the Lunar Reconnaissance Orbiter Diviner Lunar Radiometer Experiment. Most lunar terrains have spectral signatures that are consistent with known lunar anorthosite and basalt compositions. However, the data have also revealed the presence of highly evolved, silica-rich lunar soils in kilometer-scale and larger exposures, expanded the compositional range of the anorthosites that dominate the lunar crust, and shown that pristine lunar mantle is not exposed at the lunar surface at the kilometer scale. Together, these observations provide compelling evidence that the Moon is a complex body that has experienced a diverse set of igneous processes.

Remote characterization of mineralogy through thermal emission spectroscopy has a long history in planetary science that recently has been highlighted by global maps of martian mineralogy obtained from orbit and measurements from the martian surface (1, 2). Although infrared emission spectroscopy is sensitive to the bulk composition and can readily identify important lunar silicates such as feldspar, pyroxene, olivine, and quartz (3), earlier lunar observations (4, 5) lacked sufficient spatial resolution or coverage to identify areas that may have escaped extensive physical mixing and retain unusual lithologies. High-resolution lunar mapping has thus far been limited to visible and near-infrared spectroscopy and multispectral imaging, which have been used to identify diverse compositions over large areas of the lunar surface (6–9). However, these techniques are relatively insensitive to nominally iron-free minerals such as quartz and feldspar and can only unambiguously detect the important lunar rock-type anorthosite in exposures that contain almost no mafic minerals, such as pyroxene or olivine (9). Multispectral thermal emission data from the Diviner lunar radiometer have high spatial

resolution, near global coverage, and sensitivity to important iron-poor mineralogy.

Launched onboard the Lunar Reconnaissance Orbiter (LRO) in June 2009, Diviner is a nine-channel pushbroom mapping radiometer that measures emitted thermal radiation (seven channels) and reflected solar radiation (two channels) between 0.3 and 400  $\mu\text{m}$  at a spatial resolution of approximately 200 m (10). The Diviner compositional investigation relies primarily on the three shortest wavelength thermal infrared channels near 8  $\mu\text{m}$ : 7.55 to 8.05  $\mu\text{m}$ , 8.10 to 8.40  $\mu\text{m}$ ,

and 8.38 to 8.68  $\mu\text{m}$ . Pioneering lunar mid-infrared spectroscopic studies, including airborne (4), ground-based (5), and laboratory (11–13) measurements, have shown this region is key to identifying common lunar silicate minerals, and the Diviner compositional investigation was designed by using the results of those studies (14).

We chose Diviner's 8- $\mu\text{m}$ -region channels to characterize a well-studied compositional indicator of silicate mineralogy called the Christiansen feature (CF) (14, 15). The wavelength position of CF is strongly dependent on the degree of polymerization of minerals, with framework silicate minerals such as feldspars exhibiting CFs at shorter wavelengths than less polymerized pyroxene and olivine (3, 16, 17). Common lunar minerals thus exhibit widely separated CF positions. The CF position of soils is close to the weighted average of the constituent minerals, which enables determination of major lunar lithologies (18). The presence of strong thermal gradients in the lunar environment causes systematic shifts in CF position and an enhancement of CF spectral contrast relative to other mid-infrared features, such as Reststrahlen bands (3, 19, 20). Therefore, lunar thermal emission observations are only directly comparable with laboratory emission measurements in a simulated lunar environment (21, 22).

We used  $\sim 10^8$  three-point 8- $\mu\text{m}$ -region spectra collected between 5 August 2009 and 24 November 2009, covering  $\sim 50\%$  of the lunar surface

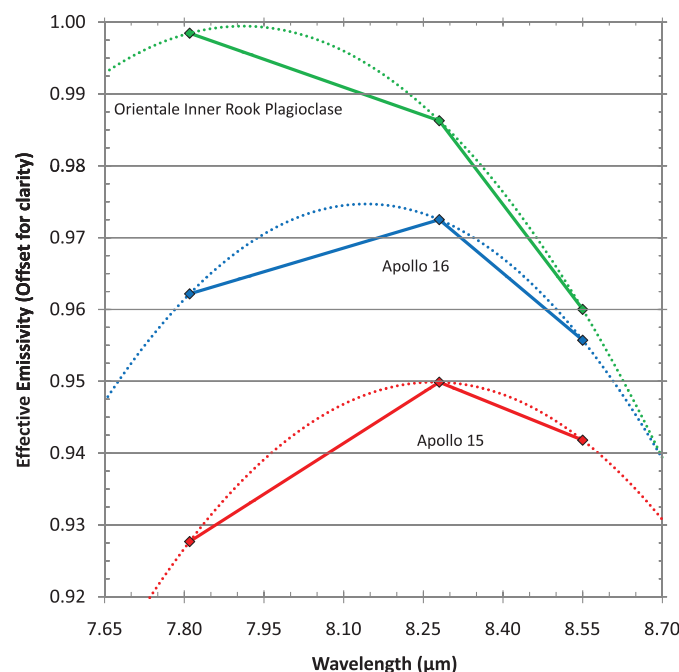


**Fig. 1.** Diviner 8- $\mu\text{m}$ -region channel three-point spectra representing typical spectral variability. The CF position was determined by using a parabolic fit to the three points (dotted traces).

<sup>1</sup>Jet Propulsion Laboratory, California Institute of Technology, Pasadena, CA 91109, USA. <sup>2</sup>Hawaii Institute of Geophysics and Planetology, University of Hawaii, Honolulu, HI 96822, USA. <sup>3</sup>Department of Geological Sciences, Brown University, Providence, RI 02912, USA. <sup>4</sup>Department of Geosciences, Stony Brook University, Stony Brook, NY 11794, USA. <sup>5</sup>NASA Johnson Space Center, Houston, TX 77058, USA. <sup>6</sup>Department of Earth and Space Sciences, University of Washington, Seattle, WA 98195, USA. <sup>7</sup>Department of Atmospheric, Oceanic, and Planetary Physics, Oxford University, OX1 3PU Oxford, UK. <sup>8</sup>Department of Earth and Space Sciences, University of California, Los Angeles, Los Angeles, CA 90095, USA.

\*To whom correspondence should be addressed. E-mail: benjamin.t.greenhagen@jpl.nasa.gov



between 60°N and 60°S. The field of view of the instrument causes spatial gaps between orbit tracks as collected to date; however, Diviner has comprehensively sampled all major lunar terrains and continues to increase spatial coverage as the LRO mission proceeds. To characterize silicate mineralogy from Diviner spectra, we first binned and averaged calibrated radiance at 32 pixels per degree (~1 km per pixel at the equator), calculated an effective emissivity for each channel, and then estimated the position of the CF using a parabolic fit to the three channels (Fig. 1) (16). High-spectral-resolution laboratory experiments have shown that a parabola is a good approximation for the shape of the CF across this restricted wavelength range (11, 16, 21, 22).

We analyzed Diviner 8- $\mu$ m-region spectra to determine the maxima of parabolic fits ("CF values") and assembled the result into a comprehensive map of lunar silicate mineralogy (Fig. 2). The data were corrected to remove temperature effects, including anisothermality (topographically driven subpixel variations in temperature) (16). Over 90% of the CF values are between 8.04 and 8.36  $\mu$ m (Fig. 3). The known mineralogical differences between basaltic maria with abundant pyroxene and the feldspathic highlands, which are rich in plagioclase feldspar, are readily apparent. The observed variability in CF values is also influenced by space weathering, which is the re-action of the lunar surface to exposure to micrometeorites and solar wind sputtering (23). The space-weathering effect was not anticipated (18) and shifts CF values to longer wavelengths with increasing maturity (longer exposure time on the surface) relative to fresh "immature" surfaces (16).

Diviner observations are consistent with previous regional lunar surface observations (4) and are directly comparable with laboratory measurements of returned lunar soils in a simulated lunar environment (12, 13, 16). The mean CF values for highland-dominated areas are shorter than those for the mare-dominated areas, which are consistent with the mineralogical differences between the feldspar-rich lunar highlands of the Apollo 16 landing site and the feldspar-poor lunar maria of the Apollo 11, 12, 15, and 17 landing sites (Fig. 4) (24, 25). The Apollo 14 site, which is dominated by mafic basin ejecta, has an intermediate mean CF value. Although most Diviner observations fall within the range of typical highlands and maria, there are locations with unusual CF positions, 8- $\mu$ m-region spectral signatures, or both.

In restricted regions that have previously been shown to exhibit unusually high abundances of the incompatible element thorium (26), there is evidence of highly silicic material: quartz, silica glass of similar composition, or sodium- or potassium-rich (or both) varieties of feldspar. These minerals are indicators of extremely differentiated lunar rocks, including granites. Diviner data associated with these kilometer-scale or larger exposures, and laboratory measurements of similar materials in simulated lunar environment, exhibit distinct spectral characteristics owing to CF positions well

shortward of the 8- $\mu$ m-region channels' wavelength range (21, 22). Prior work had highlighted some of these locations (lunar red spots) because of their unusual morphologies and anomalous ultraviolet ratios and because of their unusually high thorium values (27–30). However, a definitive compositional diagnosis required direct detection of the indicator minerals. Glotch *et al.* (22) have used Diviner data to perform a comprehensive survey of the lunar red spots and identify Hansteen Alpha, Lassell Massif, the Gruithuisen Domes, and Aristarchus Crater as high-silica features. Because the volume of silicic rock relative to a basaltic precursor is small, simple extreme differentiation of a basaltic magma raises issues of storage and heat supply to such large magma bodies. This suggests that basaltic intrusive magmatism may have remelted and subsequently differentiated a previously more silica-rich precursor, such as anorthositic crust (22). Alternatively, it is possible that the thorium-rich, high-silica features may represent direct ex-

trusive examples of the incompatible element-rich residual liquids from the lunar magma ocean.

The silica-rich red spots are confined to a large region on the lunar nearside called the Procellarum KREEP (for potassium, rare earth elements, and phosphorous) Terrane (PKT), where most of the surface thorium on the Moon is found, and the presence of high concentrations of heat-producing elements is invoked to account for the extensive basaltic volcanism on the lunar nearside (31). This regionally concentrated heat source plausibly enabled the differentiation that gave rise to the silicic anomalies. However, we also detected high amounts of silica outside the PKT in the Compton Belkovich thorium anomaly on the lunar far side. Recent Lunar Reconnaissance Orbiter Camera images show that this location is a low dome, with unusual morphologies revealed at the 10-m scale (32). Therefore, whatever process gave rise to these silicic features either did not require the special thermal conditions of the PKT (such

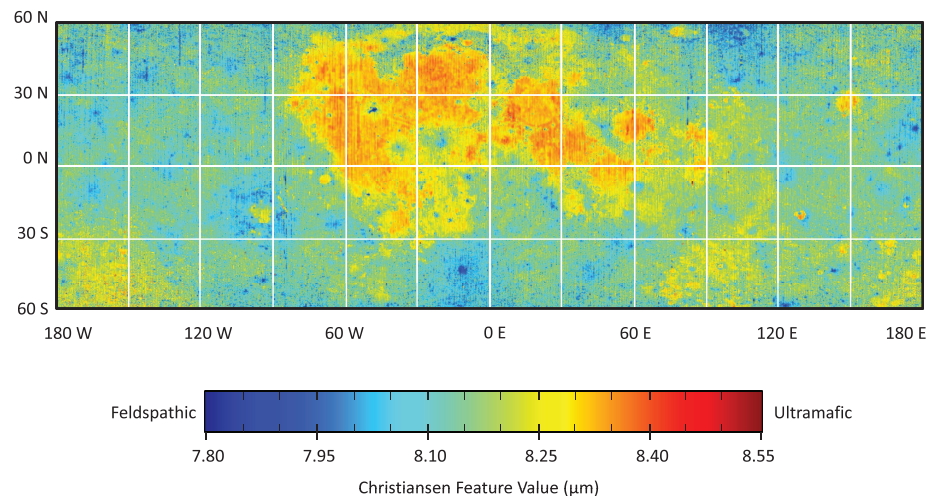


**Fig. 2.** CF value map of silicate mineralogy. The color map was chosen to highlight compositional variability of common lunar terrains and saturate blue or red for unusual compositions (Fig. 3). This map uses a pyramidal spatial resolution structure between 8 and 0.5 pixels per degree.

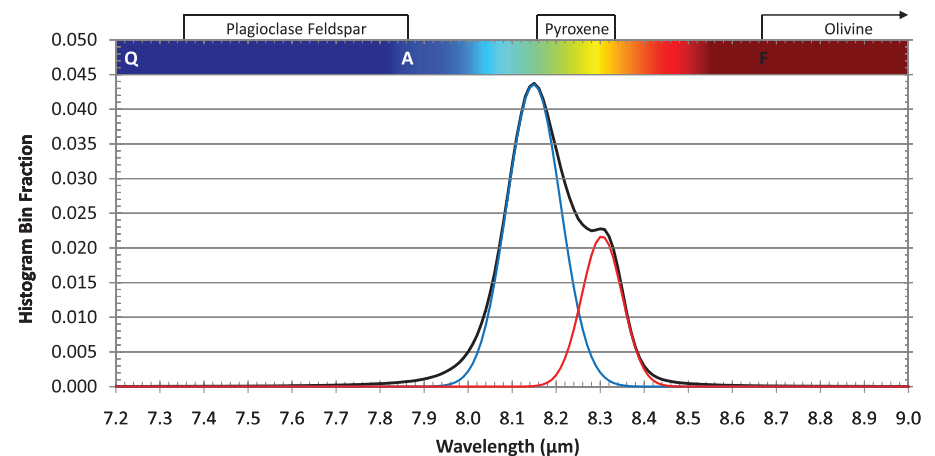


**Fig. 3.** Histogram of Diviner CF values between 30°N and 30°S. Diviner CF values (black trace) have a bimodal distribution with modal means for highland (blue trace) and mare (red trace) compositions of 8.15 and 8.30  $\mu$ m, respectively. CF positions were measured in simulated lunar conditions for relevant minerals (A, anorthite; F, forsterite; and Q, quartz), and ranges for mineral types are included.

as whether it is a direct magma ocean product), or the PKT is much more extensive but its thorium is sequestered at depth, which is in contrast to prior interpretations that suggested the far-side thorium had been depleted (26).

We have also identified a class of anomalous kilometer-scale exposures with CF values between those of the high silica features and those of the extraordinarily calcium-rich anorthite that is well known from anorthosites in the lunar sample collection. This class of feature (“intermediate composition plagioclase”) is consistent with plagioclase compositions such as bytownite or labradorite, which are somewhat more sodium-rich than the crust-forming ferroan anorthosites (Fig. 3) (14). Unlike the high-silica features, these plagioclase features have CF positions near the 8- $\mu$ m-region channels (thus enabling the determination of a CF value) and are not correlated with thorium anomalies. The CF value difference between the intermediate plagioclase composition features (for example, Guthnick crater in the southern highlands has a mean CF value of 7.68  $\mu$ m) and immature crystalline anorthite measured in a simulated lunar environment (7.84  $\mu$ m for An90) is large and is of similar magnitude to the difference in modal CF values of highlands and maria (16, 21, 22).

The intermediate composition plagioclase features occur in a wide range of lunar terrains. We found that 15 of the areas previously shown to be pure plagioclase feldspar on the basis of near-infrared spectroscopy (9) show evidence for intermediate composition plagioclase and that an additional 19 of the areas have either extremely immature pure anorthite or are mature or mixed intermediate composition plagioclase, or both (16). The detection of widespread intermediate composition plagioclase indicates that the lunar crust may have localized variations in plagioclase composition. Anorthosites with approximately these compositions are known in the sample collection (such as the alkali anorthosites), but all of these are rich in incompatible elements and may not be related to the thorium-poor locations we have identified (33). The intermediate composition plagioclase may thus reflect geochemical heterogeneities

and variable cooling within the lunar magma ocean or secondary processing of an early lunar crust.

There is no evidence of olivine-rich ultramafic lithologies, including any that might indicate the presence of kilometer-scale exposures of lunar mantle at the surface. Using the same methodology we used to directly detect high-silica features (extreme mean CF values and distinct character owing to CF positions well outside the 8- $\mu$ m-region channels’ wavelength range), we failed to detect any contiguous regions with very long wavelength CF positions. Most of the proposed lunar mantle compositions contain little or no feldspar, being dominated by pyroxene, olivine, or both (34), and such ultramafics would be readily identified by Diviner (16). Given our current constraints in latitude, spatial coverage, and spatial resolution, we found no exposures that have CF values longer than typical lunar maria, which contain tens of percent plagioclase feldspar. Rare individual 1/32-degree pixels are detected with these characteristics, but in the absence of other evidence we attribute these occurrences to processing errors caused by shadows, topographic relief, or both (16). A recent inspection of full-resolution Diviner data for central peaks and other locations that have been previously suggested to reveal uplifted ultramafic compositions on the basis of multispectral near-infrared data (7) also revealed no evidence of surfaces dominated by olivine-rich ultramafic lithologies (35).

Our study includes the interior of the vast South Pole Aitken basin, which is large enough to have penetrated through the crust and into the mantle (36). If the basin did excavate mantle material, the upper surface is extensively mixed with more feldspathic crustal rocks from the many basins and lesser impacts into the ancient South Pole Aitken basin, and no pristine exposures are found at the kilometer scale. Recently, Yamamoto *et al.* (37) have reported possible mantle outcrops in several regions on the Moon. Although we have not compared their reported locations directly, our coverage includes all of their study areas. Our results suggest that if the Yamamoto *et al.* (37) detections include mantle material, it must be

mixed with feldspathic material to have eluded detection by Diviner. The search for lunar mantle is a prime example of the complementary nature of near infrared and thermal infrared spectroscopy with respective sensitivities to iron-rich and iron-poor mineralogy.

## References and Notes

1. J. L. Bandfield *et al.*, *Science* **287**, 1626 (2000).
2. P. R. Christensen *et al.*, *Science* **306**, 1733 (2004).
3. J. W. Salisbury, L. S. Walter, *J. Geophys. Res.* **94**, (B7), 9192 (1989).
4. F. H. Murray, D. G. Murray, W. J. Williams, *J. Geophys. Res.* **75**, 2662 (1970).
5. A. L. Sprague *et al.*, *Icarus* **115**, 181 (1992).
6. C. M. Pieters, *Rev. Geophys.* **24**, 557 (1986).
7. S. Tompkins, C. M. Pieters, *Meteorit. Planet. Sci.* **34**, 25 (1999).
8. P. G. Lucey, *Geophys. Res. Lett.* **31**, L08701 (2004).
9. M. Ohtake *et al.*, *Nature* **461**, 236 (2009).
10. D. A. Paige *et al.*, *Space Sci. Rev.* **150**, 125 (2010).
11. L. M. Logan, G. R. Hunt, J. W. Salisbury, S. R. Balsamo, *J. Geophys. Res.* **78**, 4983 (1973).
12. J. W. Salisbury *et al.*, *Proc. Lunar Planet. Sci. Conf.* **4**, 3191 (1973).
13. L. M. Logan *et al.*, in *Infrared and Raman Spectroscopy of Lunar and Terrestrial Minerals*, C. Karr, Ed. (Academic Press, New York, 1975), pp. 117–142.
14. B. T. Greenhagen, *Ph.D. Dissertation*, UCLA (2009).
15. J. E. Conel, *J. Geophys. Res.* **74**, 1614 (1969).
16. Materials and methods are available as supporting material on Science Online.
17. W. B. White, in *Infrared and Raman Spectroscopy of Lunar and Terrestrial Minerals*, C. Karr, Ed. (Academic Press, New York, 1975), pp. 325–358.
18. D. B. Nash, J. W. Salisbury, J. E. Conel, P. G. Lucey, P. R. Christensen, *J. Geophys. Res.* **98**, 23535 (1993).
19. L. M. Logan *et al.*, *Proc. Lunar Planet. Sci. Conf.* **3**, 3191 (1972).
20. B. G. Henderson, P. G. Lucey, B. M. Jakosky, *J. Geophys. Res.* **101**, 14969 (1996).
21. I. R. Thomas *et al.*, *Proc. Lunar Planet. Sci. Conf.* **41**, 1364 (2010).
22. T. D. Glotch *et al.*, *Science* **329**, 1510 (2010).
23. B. Hapke, *J. Geophys. Res.* **106**, 10039 (2001).
24. L. A. Taylor, C. M. Pieters, L. P. Keller, R. V. Morris, D. S. McKay, *J. Geophys. Res.* **106**, 27985 (2001).
25. L. A. Taylor *et al.*, *J. Geophys. Res.* **115**, E00E15 (2010).
26. D. J. Lawrence *et al.*, *J. Geophys. Res.* **108**, 5102 (2003).
27. E. A. Whitaker, *Moon* **4**, 348 (1972).
28. J. W. Head 3rd, T. B. McCord, *Science* **199**, 1433 (1978).
29. B. C. Bruno *et al.*, *Proc. Lunar Planet. Sci. Conf.* **21**, 405 (1991).
30. J. J. Hagerty *et al.*, *J. Geophys. Res.* **111**, E06002 (2006).
31. M. A. Wiczkorek, R. J. Phillips, *J. Geophys. Res.* **105**, 20417 (2000).
32. B. L. Jolliffe *et al.*, *Proc. Lunar Planet. Sci. Conf.* **41**, 2412 (2010).
33. J. W. Shervais, J. J. McGee, *Am. Mineral.* **84**, 806 (1999).
34. C. K. Shearer, J. J. Papike, *Am. Mineral.* **84**, 1469 (1999).
35. E. Song *et al.*, *Proc. Lunar Planet. Sci. Conf.* **41**, 2578 (2010).
36. P. G. Lucey, G. J. Taylor, B. R. Hawke, P. D. Spudis, *J. Geophys. Res.* **103**, 3701 (1998).
37. S. Yamamoto *et al.*, *Nat. Geosci.* **3**, 533 (2010).
38. This research was carried out in part at the Jet Propulsion Laboratory, California Institute of Technology, under a contract with NASA. This work was funded by the Diviner science budget and the NASA LRO Participating Scientist program.

## Supporting Online Material

[www.sciencemag.org/cgi/content/full/329/5998/1507/DC1](http://www.sciencemag.org/cgi/content/full/329/5998/1507/DC1)

Materials and Methods

SOM Text

Figs. S1 to S3

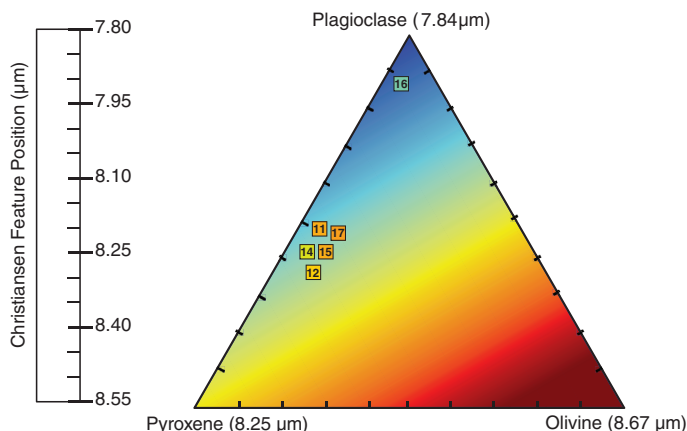
Table S1

References

12 May 2010; accepted 1 September 2010

10.1126/science.1192196

**Fig. 4.** Silicate ternary with CF values. This ternary was constructed by using CF positions for crystalline immature plagioclase (anorthite endmember), pyroxene (intermediate composition), and olivine (forsterite endmember) measured in simulated lunar conditions and assuming a linear mixing behavior for the CF position (18). The ternary location for a representative soil sample and mean CF value from each Apollo site are superimposed.





# Highly Silicic Compositions on the Moon

Timothy D. Glotch,<sup>1\*</sup> Paul G. Lucey,<sup>2</sup> Joshua L. Bandfield,<sup>3</sup> Benjamin T. Greenhagen,<sup>4</sup> Ian R. Thomas,<sup>5</sup> Richard C. Elphic,<sup>6</sup> Neil Bowles,<sup>5</sup> Michael B. Wyatt,<sup>7</sup> Carlton C. Allen,<sup>8</sup> Kerri Donaldson Hanna,<sup>6</sup> David A. Paige<sup>9</sup>

Using data from the Diviner Lunar Radiometer Experiment, we show that four regions of the Moon previously described as “red spots” exhibit mid-infrared spectra best explained by quartz, silica-rich glass, or alkali feldspar. These lithologies are consistent with evolved rocks similar to lunar granites in the Apollo samples. The spectral character of these spots is distinct from surrounding mare and highlands material and from regions composed of pure plagioclase feldspar. The variety of landforms associated with the silicic spectral character suggests that both extrusive and intrusive silicic magmatism occurred on the Moon. Basaltic underplating is the preferred mechanism for silicic magma generation, leading to the formation of extrusive landforms. This mechanism or silicate liquid immiscibility could lead to the formation of intrusive bodies.

**S**pectroscopically unique features that occur on the nearside of the Moon within the Procellarum KREEP Terrane (PKT) (Fig. 1) have been investigated for more than three decades (1–4). Remote sensing data from these localities, known as red spots, are generally characterized by deep ultraviolet (UV) absorptions with respect to the near-infrared (NIR) as well as low FeO and TiO<sub>2</sub> concentrations. The unusual spectral characteristics of the Gruithuisen Dome red spots, which also have steep slopes (15° to 30°) and rough surface textures suggest that they formed from feldspathic magmas with high silica contents, similar to terrestrial rhyolite domes (3, 5, 6). Recent analyses suggest that four red spots—Hansteen Alpha, the Gruithuisen Domes, the Lassell Massif, and Aristarchus Crater—have elevated Th and low FeO abundances, suggesting derivation from evolved magmas (7, 8). None of the previously applied techniques, including UV/visible/NIR (UV/VIS/NIR) spectroscopy and gamma-ray spectroscopy (GRS), are directly sensitive to the key indicators of silicic volcanism (quartz, silica-rich glass, and alkali and ternary feldspars). Therefore, unambiguous identification of the composition of these features has not previously been possible.

The Diviner Lunar Radiometer Experiment on the Lunar Reconnaissance Orbiter is a multi-spectral radiometer that is well suited to detecting the mineral indicators of silicic volcanism. Diviner has three narrow spectral bandpass filters centered at 7.8, 8.25, and 8.55  $\mu\text{m}$  (channels 3 to 5). These three “8- $\mu\text{m}$ ” channels were specifically designed to characterize the position of the Christiansen

Feature (CF) (9, 10), which is directly sensitive to silicate mineralogy and the bulk SiO<sub>2</sub> content of a material (11–15).

We have compared the mid-IR spectral shapes of lunar red spots to those of the surrounding mare and highlands, which are regions suggested to be pure plagioclase feldspar, based on SELENE Multiband Imager data (16); and the laboratory emissivity spectra of minerals and rocks acquired in a simulated lunar environment (15). The available data cover portions of Hansteen Alpha, the Lassell Massif region, the Gruithuisen Gamma and Northwest Domes, Aristarchus Crater, Southern Montes Rhipaeus, and Helmet red spots.

Silicic minerals and lithologies exhibit short-wavelength position CFs. The response of the Diviner 8- $\mu\text{m}$  channels to this characteristic is to show a strong positive slope in three-point spectra toward short wavelengths with a weak curvature. Convolved to the Diviner bandpasses, quartz and silica-rich materials such as obsidian glass and alkali feldspar have three-point spectra that are strongly concave upward. Moderate-composition feldspars such as labradorite are weakly concave upward, whereas anorthite and more typical lunar materials that are mafic to ultramafic (anorthite,

pyroxene, olivine, and mixtures thereof) show strongly concave-downward spectra (Fig. 2). The combination of spectral slope and concavity in the Diviner 8- $\mu\text{m}$  channels are strongly tied to the silica content of a material and can be used to identify Si-rich compositions.

To map variations in silicate mineralogy, we defined two spectral parameters to describe the Diviner three-point spectra. The first spectral index,  $I$ , measures the slope between channels 3 and 4 in the form  $I = \epsilon_3 - \epsilon_4$ , where  $\epsilon_3$  and  $\epsilon_4$  are the emissivities in channels 3 and 4, respectively. A second spectral index,  $c$ , determines the direction of concavity between channels 3 and 5 (17). A positive value of this index is indicative of a concave-up shape, whereas a negative index value is indicative of a concave-down shape.

Hansteen Alpha, the Lassell Massif region, the Gruithuisen Domes, and the southern rim and ejecta blanket of Aristarchus each have  $I$  parameter values that are substantially higher than those of the surrounding highlands material in each region. Portions of each of these features also display positive  $c$  (concave-up) index values (Fig. 3 and Table 1).

Comparison to laboratory spectra acquired under simulated lunar conditions and convolved with the Diviner bandpasses indicates that anorthite and all minerals more silicic than it have positive  $I$  parameter values. Only the most-silicic materials, containing substantial amounts of Si-rich glass, quartz, and/or alkali feldspars, display strongly concave-up spectral character, although labradorite is also weakly concave-up (Fig. 2). The CF positions of these materials occur at wavelengths well short of the Diviner 8- $\mu\text{m}$  channels. Other regions in each of these red spots have negative concavity index values but positive  $I$  parameter values. The average calculated CF position for these concave-down spectral shapes, modeled in the manner of (10), is 7.87  $\mu\text{m}$  (1271  $\text{cm}^{-1}$ ), which is consistent with a mixture of the silicic composition with more mafic components.

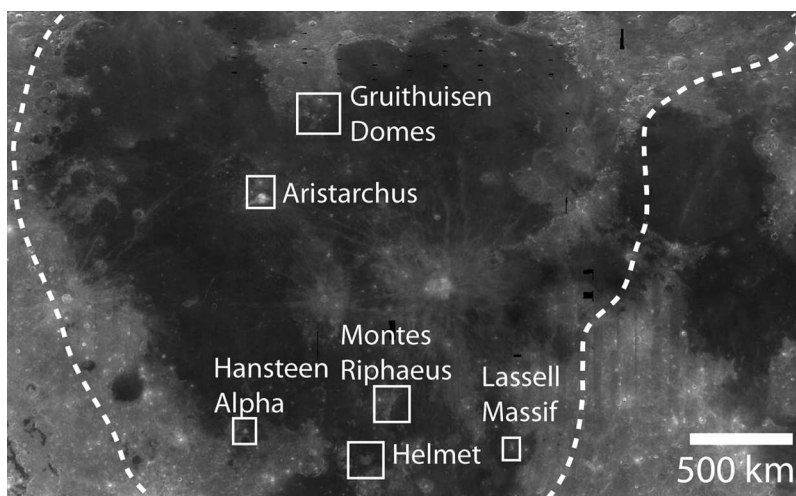


**Fig. 1.** Clementine 750-nm mosaic showing the locations of the features discussed in the text. The outline marks the boundary of the PKT as defined by (32).

<sup>1</sup>Department of Geosciences, Stony Brook University, Stony Brook, NY, USA. <sup>2</sup>Hawaii Institute of Geophysics and Planetary Science, University of Hawaii, Hawaii, HI, USA. <sup>3</sup>Department of Earth and Space Sciences, University of Washington, Seattle, WA, USA. <sup>4</sup>Jet Propulsion Laboratory, California Institute of Technology, 4800 Oak Grove Drive, Pasadena, CA 91109–8099, USA. <sup>5</sup>Department of Physics, University of Oxford, Oxford, UK. <sup>6</sup>NASA Ames Research Center, Moffett Field, CA 94035–1000, USA. <sup>7</sup>Department of Geological Sciences, Brown University, Providence, RI, USA. <sup>8</sup>NASA Johnson Space Center, Houston, TX 77058, USA. <sup>9</sup>Department of Earth and Space Sciences, University of California, Los Angeles, Los Angeles, CA, USA.

\*To whom correspondence should be addressed. E-mail: tglootch@notes.cc.sunysb.edu

Three-point spectra of each of the red spots are distinct from those of the surrounding terrain. Both mare and highlands materials in each region have spectral shapes with negative concavity and slope index values. The average CF positions of local mare and highlands material in

each region are 8.33 and 8.19  $\mu\text{m}$ , respectively, which compare well with those derived from the global data set (10).

The regions previously interpreted to be the most silicic on the Moon have been classified as nearly pure anorthite, based on VIS/NIR spectral

observations (16, 18). The spectral properties of these areas are key to our interpretation of the presence of even more-silicic minerals, indicating evolved lithologies. Diviner spectra of pure plagioclase from the inner ring of the Orientale multi-ring impact basin are concave-down with a positive slope index (Fig. 4), and the modeled CF position is 7.89  $\mu\text{m}$ , which is similar to that derived for the red-spot mixed lithologies. Of all the feldspars, anorthite has the longest-wavelength CF position, and this comparison indicates that red spots with CF positions shorter than those of areas interpreted to be pure anorthite, along with positive  $I$  parameter and  $c$  index values, are largely composed of quartz, Si-rich glass, and alkali feldspars, or mixtures thereof.

The concave-upward shapes and positive slope indices in the spectra of Hansteen Alpha, Lassell Massif, the Gruithuisen Domes, and the southern rim and ejecta of Aristarchus Crater indicate the presence of highly silicic evolved lithologies. Evolved compositions are also consistent with strong positive anomalies of Th, an incompatible large-ion lithophile element (7, 8). Red spots that lack high Th anomalies also lack the concave-up spectral character in Diviner data, confirming a lack of silicic indicator minerals. These include the Helmet Feature, Darney Chi, Darney Tau, Montes Rhipaeus, and Mons La Hire. Spectra of the Helmet Feature and Montes Rhipaeus display concave-down shapes and have negative slope parameters (Fig. 4) and are generally indistinguishable from the surrounding highlands in the Diviner data (Fig. 3) (19). The distribution of high-Si compositions is spatially correlated with the Th anomalies in Lunar Prospector Gamma-Ray Spectrometer (GRS) data (8, 9) and low FeO abundance derived from Clementine UV/VIS/NIR imagery (20, 21). Red spots lacking a silicic composition have typical Th and FeO abundances.

The four silicic features described here have variable geologic settings that probably represent both extrusive and intrusive igneous processes. The Gruithuisen Domes and Hansteen Alpha have previously been proposed to be silicic volcanic constructs (3, 5, 6, 22). The compositions as determined by Diviner are consistent with previous interpretations of these features resulting from silicic extrusive volcanic processes. The Aristarchus and Lassell regions appear to be sampling silicic lithologies emplaced at depth. The Si-rich materials at Aristarchus are confined to the southern rim and ejecta of Aristarchus Crater, whereas the thick blanket of  $\text{TiO}_2$ -poor pyroclastic materials that covers much of the Aristarchus Plateau (23, 24) does not have a silicic spectral signature in Diviner data. This suggests that Aristarchus Crater exposed an intrusive silicic lithology. Alternatively, the Aristarchus cratering event could have exposed an extrusive lithology that was subsequently buried by mare lavas and the pyroclastic deposits of the Aristarchus Plateau. The silicic materials in the Lassell region (Fig. 3e) are associated with an  $\sim 50 \times 20$ -km patch of highlands material (the

**Fig. 2.** Full-resolution ( $2\text{ cm}^{-1}$  spectral sampling) laboratory spectra of major rock-forming minerals and those spectra convolved to the Diviner channel-3 to -5 bandpasses. Arrows mark the position of the silicate CF. Microcline does not display a strong CF.

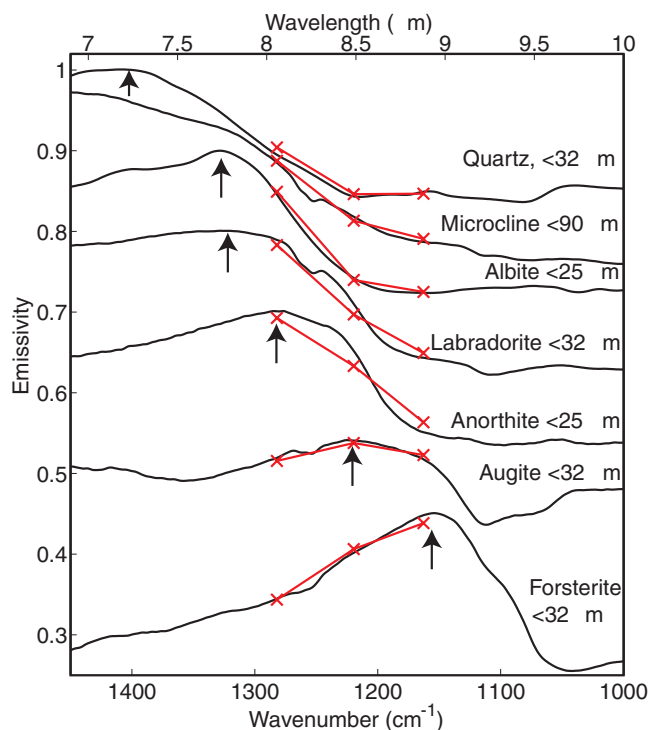
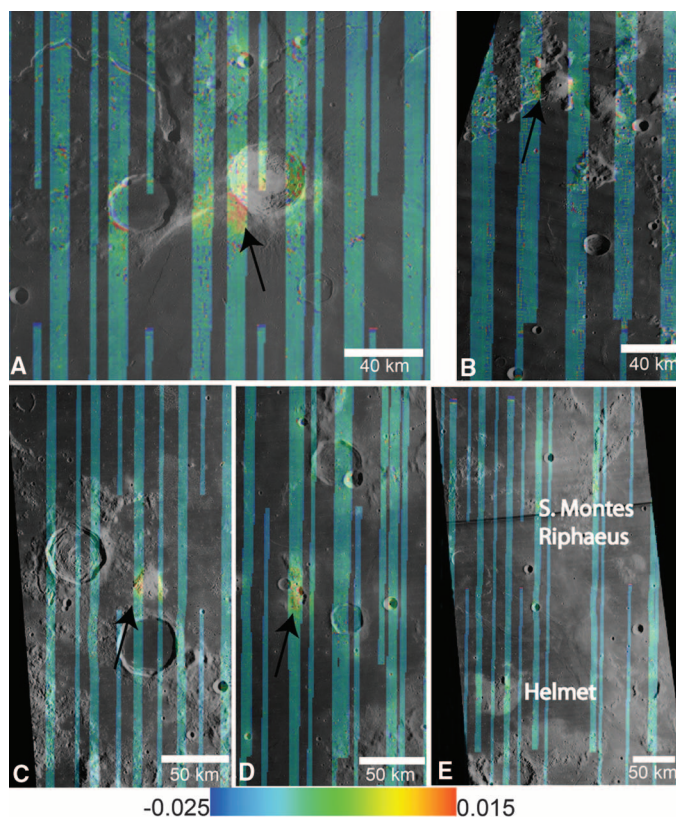


**Fig. 3.** Concavity index maps overlaid on digitized Lunar Orbiter IV images. High values of the index (red) indicate increasingly silicic compositions. (A) Aristarchus Crater. (B) Gruithuisen Domes. (C) Hansteen Alpha. (D) Lassell. (E) Helmet and Southern Montes Rhipaeus.





Lassell Massif) and the small impact craters Lassell K, G, and C (25). The direct association of the silicic signature with the impact craters at the Lassell site suggests that it is due to the exposure of plutonic material or a thick sequence of buried extrusive lavas sampled at depth.

Silicic lithologies on the Moon probably occur as both intrusive plutons and extrusive lavas. Extrusive silicic volcanism, which is likely to have formed Hansteen Alpha and the Gruithuisen Domes, occurred in the Late Imbrian epoch be-

fore most mare volcanism occurred (22, 25, 26). Mare lavas embay these likely volcanic edifices, indicating that they were once more extensive. The mechanisms for forming highly evolved lithologies are a subject for debate. Small fragments of lunar granite/felsite are present in Apollo soil samples, and age dating gives crystallization ages that span a range of 500 million years (27), indicating that magmatic processes capable of producing highly evolved compositions occurred over an extended period of time. Two basic mod-

els have been proposed to account for the presence of highly evolved compositions on the Moon. Silicate liquid immiscibility is a mechanism that has been proposed to be responsible for the origin of the Apollo granite/felsite grains (28). It requires that a basaltic magma undergo nearly complete fractional crystallization before the single residual melt separates into two immiscible melts: one that is SiO<sub>2</sub>-poor and FeO rich, and one that is rich in SiO<sub>2</sub> and alkalis. It is unlikely that the silicic lavas produced from the small amount of residual melt produced by this process could form large volcanic structures such as the Gruithuisen Domes or Hansteen Alpha (7). It is possible, however, that large granitic plutons could have been produced within the lunar crust as a result of the slow crystallization of late-stage magma ocean residual melt (29, 30). This slow cooling method would preclude the formation of large volumes of extrusive lavas (7), but it is a reasonable scenario for the formation of large granitic bodies that could be exposed by impact craters.

A second mechanism that could produce large volumes of silicic melt is basaltic underplating, in which a hot basaltic magma intrudes into the lunar crust, causing melting of the anorthositic crust and the generation of silicic magmas (7). This process can produce large volumes of buoyant silicic magmas that rise to the surface as rhyolite plumes (31). As previously suggested, the thin crust, high abundance of heat-producing elements, and large-scale basaltic magmatism in the PKT all favor the basaltic underplating hypothesis (7). Because all four silicic regions discussed in this work occur within the PKT, this mechanism for silicic melt production should be strongly considered.

These four silicic regions have distinctly different geologic settings. The Gruithuisen Domes and Hansteen Alpha are probably the result of extrusive silicic volcanism (5, 6, 22). Silicic materials have also been exposed by impact craters in the Aristarchus and Lassell regions, perhaps indicating the formation of silicic plutons at depth. Taken together with the proposed magmatic processes, Diviner data point to multiple igneous processes occurring over a sustained period of time, resulting in the formation of silica and rare earth element-enriched compositions on the Moon.

**Table 1.** Characteristics of features discussed in the text. Dashes indicate that no CF position was calculated.

Feature	Modeled CF*	c	I	Surface temperature	Th (ppm)†
Hansteen Alpha (c > 0)	—	0.00514	0.0217	381.4	6
Hansteen Alpha (c < 0)	7.98	−0.00535	0.0041	381.9	6
Hansteen Mare	8.36	−0.01471	−0.0275	386.4	5
Hansteen Highlands	8.29	−0.01300	−0.0202	379.2	3
Lassell (c > 0)	—	0.00651	0.0256	375.3	11
Lassell (c < 0)	7.69	−0.00564	0.0076	372.9	11
Lassell Highlands	8.12	−0.01184	−0.0124	374.0	4
Lassell Mare	8.31	−0.01324	−0.0225	379.9	7
Gruithuisen Gamma (c > 0)	—	0.00448	0.0139	356.0	10
Gruithuisen Gamma (c < 0)	7.93	−0.01048	0.0019	358.5	10
Gruithuisen NW (c > 0)	—	0.02935	0.0462	360.4	10
Gruithuisen Mare	8.29	−0.01462	−0.0224	345.3	7
Gruithuisen Highlands	8.15	−0.01111	−0.0091	330.7	13
Aristarchus Crater (c > 0)	—	0.00797	0.0339	371.8	14
Aristarchus Crater (c < 0)	7.72	−0.00459	0.0112	377.4	14
Aristarchus Plateau	8.25	−0.01344	−0.0208	375.5	11
Helmet	8.20	−0.01010	−0.0113	379.1	4
Helmet Mare	8.36	−0.01443	−0.0286	382.0	4
Southern Montes Rhiphaeus	8.09	−0.00634	−0.0028	377.2	5

\*CF positions for spectra with positive concavity index values cannot be calculated in the manner of (10). †Small-region Th values [in parts per million (ppm)] are based on the deconvolved abundances determined by (33).

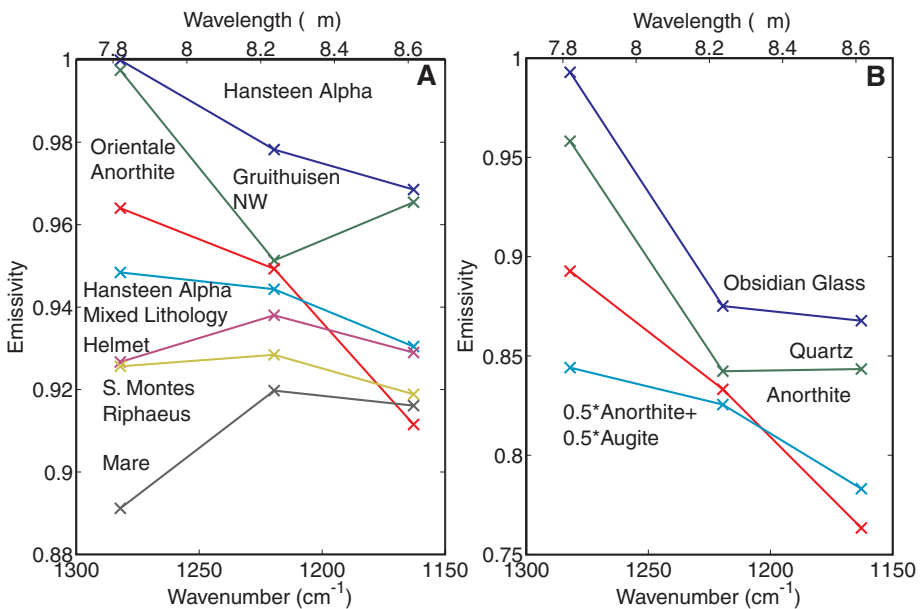


**Fig. 4.** Diviner and laboratory three-point spectra. (A) Spectra from select regions discussed in the text. (B) Laboratory spectra convolved to Diviner spectral resolution.

**References and Notes**

1. E. A. Whitaker, *Moon* **4**, 348 (1972).
2. M. Malin, *Earth Planet. Sci. Lett.* **21**, 331 (1974).
3. J. W. Head 3rd, T. B. McCord, *Science* **199**, 1433 (1978).
4. B. C. Bruno *et al.*, *Proc. Lunar Planet. Sci. Conf.* **21**, 405 (1991).
5. J. W. Head *et al.*, *Lunar Planet. Sci.* **IX**, 488 (abstract) (1978).
6. S. D. Chevrel, P. C. Pinet, J. W. Head, *J. Geophys. Res.* **104**, 16,515 (1999).
7. J. J. Hagerty *et al.*, *J. Geophys. Res.* **111**, E06002 (2006).
8. J. J. Hagerty *et al.*, *J. Geophys. Res.* **114**, (2009).
9. D. A. Paige *et al.*, *Space Sci. Rev.* **150**, 125 (2009).
10. B. T. Greenhagen *et al.*, *Science* **329**, 1507 (2010).
11. J. E. Conel, *J. Geophys. Res.* **74**, 1614 (1969).
12. L. M. Logan, G. R. Hunt, J. W. Salisbury, S. R. Balsamo, *J. Geophys. Res.* **78**, 4983 (1973).
13. J. W. Salisbury, L. S. Walter, *J. Geophys. Res.* **94**, 9192 (1989).

14. The CF occurs in the portion of the mid-IR spectrum where the real part of the complex refractive index is changing rapidly and approaching that of the surrounding medium, resulting in minimal scattering and an emissivity maximum.
15. Materials and methods are available as supporting material on Science Online.
16. P. D. Spudis, B. R. Hawke, P. Lucey, *J. Geophys. Res.* **89**, C197 (1984).
17. We defined a line using channels 3 and 5 and interpolated the value of the channel 4 emissivity on this line. We then subtracted the true channel-4 emissivity from this value.
18. M. Ohtake *et al.*, *Nature* **461**, 236 (2009).
19. Diviner data meeting our analysis criteria have not been acquired over Mons La Hire, Darney Chi, or Darney Tau.
20. P. G. Lucey, G. J. Taylor, E. Malaret, *Science* **268**, 1150 (1995).
21. P. G. Lucey, D. T. Blewett, B. R. Hawke, *J. Geophys. Res.* **103**, 3679 (1998).
22. B. R. Hawke *et al.*, *J. Geophys. Res.* **108**, 5069 (2003).
23. P. G. Lucey, B. R. Hawke, C. M. Pieters, J. W. Head, T. B. McCord, *J. Geophys. Res.* **91** (suppl.), D344 (1986).
24. B. B. Wilcox, P. G. Lucey, B. R. Hawke, *J. Geophys. Res.* **111**, E09001 (2006).
25. C. A. Wood, J. W. Head, *Conference on the Origin of Mare Basalts* (Lunar Science Institute, Houston, TX, 1975).
26. R. Wagner *et al.*, *Lunar Planet. Sci.* **XXVII**, 1367 (abstract) (1996).
27. L. E. Nyquist, C. Y. Shih, *Geochim. Cosmochim. Acta* **56**, 2213 (1992).
28. B. L. Jolliff *et al.*, *Am. Mineral.* **84**, 821 (1999).
29. C. R. Neal, L. A. Taylor, *Geochim. Cosmochim. Acta* **53**, 529 (1989).
30. B. L. Jolliff, *Int. Geol. Rev.* **40**, 916 (1998).
31. S. Maaløe, A. R. McBirney, *J. Volcanol. Geotherm. Res.* **76**, 111 (1997).
32. B. L. Jolliff, J. J. Gillis, L. A. Haskin, R. L. Korotev, M. A. Wicczorek, *J. Geophys. Res.* **105**, 4197 (2000).
33. D. J. Lawrence *et al.*, *J. Geophys. Res.* **105**, 20307 (2000).
34. This work was funded in part by the Diviner science budget. T.D.G., J.L.B., M.B.W., and R.C.E. were supported by the NASA Lunar Reconnaissance Orbiter Participating Scientist program.

#### Supporting Online Material

www.sciencemag.org/cgi/content/full/329/5998/1510/DC1

Materials and Methods

Figs. S1 and S2

References

11 May 2010; accepted 1 September 2010

10.1126/science.1192148

# Rainforest Aerosols as Biogenic Nuclei of Clouds and Precipitation in the Amazon

U. Pöschl,<sup>1\*</sup> S. T. Martin,<sup>2\*</sup> B. Sinha,<sup>1</sup> Q. Chen,<sup>2</sup> S. S. Gunthe,<sup>1</sup> J. A. Huffman,<sup>1</sup> S. Borrmann,<sup>1</sup> D. K. Farmer,<sup>3</sup> R. M. Garland,<sup>1</sup> G. Helas,<sup>1</sup> J. L. Jimenez,<sup>3</sup> S. M. King,<sup>2</sup> A. Manzi,<sup>4</sup> E. Mikhailov,<sup>1,5</sup> T. Pauliquevis,<sup>6,7</sup> M. D. Petters,<sup>8,9</sup> A. J. Prenni,<sup>8</sup> P. Roldin,<sup>10</sup> D. Rose,<sup>1</sup> J. Schneider,<sup>1</sup> H. Su,<sup>1</sup> S. R. Zorn,<sup>1,2</sup> P. Artaxo,<sup>6</sup> M. O. Andreae<sup>1</sup>

The Amazon is one of the few continental regions where atmospheric aerosol particles and their effects on climate are not dominated by anthropogenic sources. During the wet season, the ambient conditions approach those of the pristine pre-industrial era. We show that the fine submicrometer particles accounting for most cloud condensation nuclei are predominantly composed of secondary organic material formed by oxidation of gaseous biogenic precursors. Supermicrometer particles, which are relevant as ice nuclei, consist mostly of primary biological material directly released from rainforest biota. The Amazon Basin appears to be a biogeochemical reactor, in which the biosphere and atmospheric photochemistry produce nuclei for clouds and precipitation sustaining the hydrological cycle. The prevailing regime of aerosol-cloud interactions in this natural environment is distinctly different from polluted regions.

Atmospheric aerosols are key elements of the climate system. Depending on composition and abundance, aerosols can influence Earth's energy budget by scattering or absorbing radiation and can modify the characteristics of clouds and enhance or suppress precipitation. The direct and indirect aerosol effects on climate are among the largest uncertainties in the current understanding of regional and global environmental change. A crucial challenge is devel-

oping a quantitative understanding of the sources and properties of aerosol particles, including primary emission from the Earth's surface, secondary formation in the atmosphere, chemical composition and mixing state, and the ability to nucleate cloud droplets and ice crystals—all as influenced by human activities as compared with natural conditions (1–4).

During the wet season, the Amazon Basin is one of the few continental regions where aerosols can be studied under near-natural conditions (5–7). The Amazonian Aerosol Characterization Experiment 2008 (AMAZE-08) was conducted in the middle of the wet season at a remote site north of Manaus, Brazil (February to March 2008), and the investigated air masses came with the trade wind circulation from the northeast over some 1600 km of pristine tropical rainforest (8). Here, we focus on measurements performed in the period of 3 to 13 March 2008, when the influence of long-range transport from the Atlantic Ocean, Africa, or regional anthropogenic sources of pollution was particularly low and the aerosol properties were dominated by particles emitted or formed within the rainforest ecosystem (6, 7, 9, 10). The

measurement techniques applied include scanning electron microscopy (SEM) with energy-dispersive x-ray spectroscopy (EDX), atomic force microscopy (AFM), secondary ion mass spectrometry (NanoSIMS), aerosol mass spectrometry (AMS), differential mobility particle sizing (DMPS), ultra-violet aerodynamic particle sizing (UV-APS), and counting of cloud condensation nuclei (CCN) and ice nuclei (IN) (8). To our knowledge, this study provides the first comprehensive, detailed, and size-resolved account of the chemical composition, mixing state, CCN activity, and IN activity of particles in pristine rainforest air approximating pre-industrial conditions (5–7).

SEM images of characteristic particle types are shown in Fig. 1. Nearly all detected particles could be attributed to one of the following five categories: (i) secondary organic aerosol (SOA) droplets that were formed by atmospheric oxidation and gas-to-particle conversion of biogenic volatile organic compounds (9) and in which no other chemical components were detectable; (ii) SOA-inorganic particles composed of secondary organic material mixed with sulfates and/or chlorides from regional or marine sources (6); (iii) primary biological aerosol (PBA) particles, such as plant fragments or fungal spores (6, 11, 12); (iv) mineral dust particles consisting mostly of clay minerals from the Sahara desert (6, 13); or (v) pyrogenic carbon particles that exhibited characteristic agglomerate structures and originated from regional or African sources of biomass burning or fossil fuel combustion (6). In mixed SOA-inorganic particles, the organic fraction was typically larger than the inorganic fraction. The primary biological, mineral dust, and pyrogenic carbon particles were also partially coated with organic material [supporting online material (SOM) text].

The average number and mass size distribution, composition, and mixing state of particles as detected with microscopy and complementary online measurements are shown in Fig. 2. The online instruments measure different types of equivalent diameters, which can vary depending on the shape and the density of the particles. Nevertheless, the size distribution patterns obtained with the different techniques are in overall agreement with each other. SEM is the one method that cov-

<sup>1</sup>Max Planck Institute for Chemistry, 55128 Mainz, Germany.

<sup>2</sup>School of Engineering and Applied Sciences and Department of Earth and Planetary Sciences, Harvard University, Cambridge, MA 02138, USA. <sup>3</sup>Department of Chemistry and Biochemistry and Cooperative Institute for Research in Environmental Science, University of Colorado, Boulder, CO 80309, USA. <sup>4</sup>National Institute of Amazonian Research, 69060 Manaus, Brazil. <sup>5</sup>Atmospheric Physics Department, Institute of Physics, St. Petersburg State University, 198904 St. Petersburg, Russia. <sup>6</sup>Institute of Physics, University of São Paulo, 05508 São Paulo, Brazil. <sup>7</sup>Federal University of São Paulo, 04023 Diadema, Brazil. <sup>8</sup>Department of Atmospheric Science, Colorado State University, Fort Collins, CO 80523, USA. <sup>9</sup>Marine Earth and Atmospheric Science, North Carolina State University, Raleigh, NC 27695, USA. <sup>10</sup>Department of Physics, Lund University, 22100 Lund, Sweden.

\*To whom correspondence should be addressed. E-mail: u.poschl@mpic.de (U.P.); scot\_martin@harvard.edu (S.T.M.)



ers the full particle size range and provides detailed information about composition and mixing state. The online measurement techniques, however, are more reliable for the absolute concentration values because of their better sampling and counting statistics. The integral particle number and mass concentrations as well as the relative proportions of different types of particles corresponding to the displayed size distributions are summarized in tables S1 and S2. The observed particle number and mass size distributions can be separated into two characteristic fractions with a dividing diameter of 1  $\mu\text{m}$ . The submicrometer fraction dominated the total particle number concentration (>99% of  $\sim 200\text{ cm}^{-3}$ ) (Fig. 2A and table S1), whereas the supermicrometer fraction accounted for most of the total particle mass concentration ( $\sim 70\%$  of  $\sim 2\text{ }\mu\text{g m}^{-3}$ ) (Fig. 2C and table S2).

The submicrometer fraction exhibited three characteristic modes as indicated by local maxima in the number size distribution (Fig. 2B): a nucleation mode ( $<0.03\text{ }\mu\text{m}$ ), an Aitken mode ( $0.03$  to  $0.1\text{ }\mu\text{m}$ ), and an accumulation mode ( $0.1$  to  $1\text{ }\mu\text{m}$ ). According to single particle analysis (SEM, AFM, and NanoSIMS), pure SOA droplets dominated the nucleation and Aitken modes (number fraction >99%) (Fig. 2A). The accumulation mode consisted of pure SOA droplets, mixed SOA-inorganic particles, and pyrogenic carbon particles. Overall, the pure SOA droplets represented  $\sim 85\%$  of the number concentration of submicrometer particles and potential CCN, and the mixed SOA-inorganic particles accounted for another  $\sim 10\%$  (table S1).

The microscopy results were consistent with the accompanying online measurements. Specifically, the proportion of organic matter measured by AMS was >90% in the Aitken range and >80% in the accumulation range, in which the proportion of sulfate increased (Fig. 2D). The submicrometer organic mass concentrations determined by means of AMS were higher than the corresponding SEM results, which is probably due to partial evaporation (14). The average oxygen-to-carbon ratio of 0.44 and the mass spectra observed during AMAZE-08 for the submicrometer organic matter are in good agreement with laboratory studies of biogenic SOA from isoprene and terpene oxidation (9, 15). PBA compounds detectable with AMS, such as proteins, amino acids, and carbohydrates, contributed less than 5% to the submicrometer particulate matter (9).

The predominance of SOA is further reflected in the effective hygroscopicity parameter  $\kappa$  determined through size-resolved CCN measurements (10). This parameter describes the influence of chemical composition on the ability of particles to absorb water vapor and form cloud droplets. Throughout the campaign, the  $\kappa$  values in the Aitken range were nearly constant at  $\kappa \approx 0.1$ , which is in agreement with laboratory investigations of biogenic SOA from isoprene and terpene oxidation (4, 16) and much lower than the  $\kappa$  values of ammonium sulfate, sodium chloride, and other inorganic salts commonly observed in

aerosols (0.6 to 1.3) (17). In the accumulation mode size range ( $0.1$  to  $1\text{ }\mu\text{m}$ ),  $\kappa$  increased to  $\sim 0.15$  as the proportion of sulfate increased to  $\sim 10\%$  (Fig. 2D). Nevertheless, the effective hygroscopicity remained lower by a factor of approximately two than the approximate global continental average value of  $\kappa \approx 0.3$  (10, 18).

The supermicrometer fraction with a local maximum (coarse mode) around 2 to 3  $\mu\text{m}$  consisted mostly of PBA particles with a number fraction of  $\sim 80\%$  (mass fraction 85%) plus some mineral dust and mixed SOA-inorganic particles with number fractions of 10 and 6%, respectively (Fig. 2, A and C, and tables S1 and S2). The SEM results were consistent with online measurements of fluorescent biological aerosol (FBA) particles, which can be regarded as a lower-limit proxy for PBA particles (19, 20). The number and mass fractions of supermicrometer FBA particles were 40 and 64%, respectively (Fig. 2, B and D, and tables S1 and S2).

Measurements and modeling of IN concentrations during AMAZE-08 suggest that ice formation in Amazon clouds at temperatures warmer than  $-25^\circ\text{C}$  is dominated by PBA particles (20). Although the number concentration of such efficient biological IN is low (about 1 to 2  $\text{L}^{-1}$ ), they are nevertheless the first to initiate ice formation and can have a strong influence on the evolution of clouds and precipitation (21–23). At temperatures colder than  $-25^\circ\text{C}$ , both locally emitted PBA and mineral dust particles imported from the Sahara desert can act as IN and induce cold rain formation. The IN activity of mineral dust may in fact also be influenced by biological materials, as suggested in earlier studies that include aircraft observations of ice cloud residuals (21, 24). In any case, PBA particles appear to be the most efficient IN and, outside of Saharan dust episodes, also the most abundant IN in the Amazon Basin. Moreover, the supermicrometer particles can also act as “giant” CCN, generating

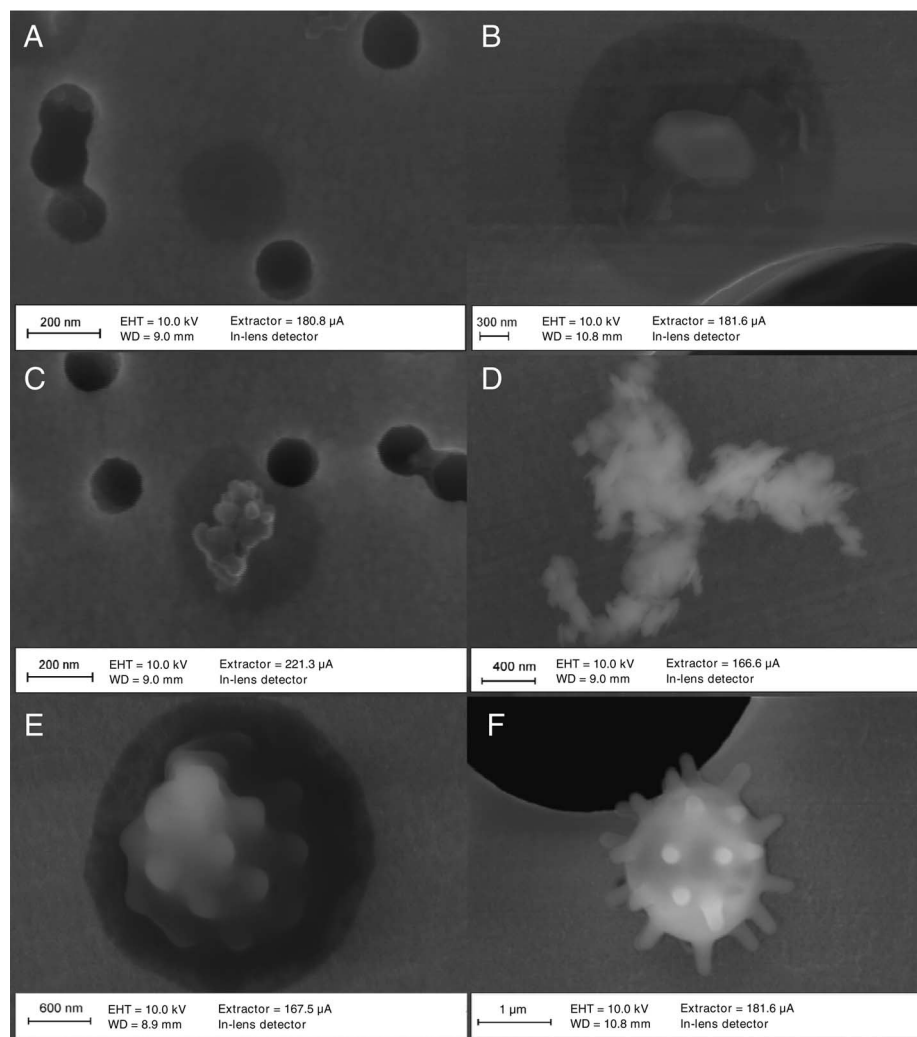


**Fig. 1.** Characteristic particle types observed by means of SEM of filter samples collected during AMAZE-08 (3 to 13 March 2008). **(A)** SOA droplet. **(B)** Mixed SOA-inorganic particle. **(C)** Pyrogenic carbon particle with organic coating. **(D)** Mineral dust particle without coating. **(E)** and **(F)** PBA particles **(E)** with and **(F)** without organic coating. SOA droplets and organic coatings appear dark gray, filter pores appear black, and filter material appears light gray (8).

large droplets and inducing warm rain without ice formation (2, 21).

The low aerosol concentrations and the high proportions of secondary organic and primary biological matter suggest that the climate system interactions between aerosols, clouds, and precipitation over pristine rainforest regions may substantially differ from both pristine marine regions ("green ocean" versus "blue ocean") as well as from polluted environments (2, 25). Model calculations using the aerosol size distributions and the hygroscopicity parameters determined in AMAZE-08 suggest that the activation of CCN in convective clouds over the pristine Amazonian rainforest is aerosol-limited, which means that

the number of cloud droplets is directly proportional to the number of aerosol particles (fig. S1) (26). In contrast, the formation of cloud droplets in polluted environments (including parts of the Amazon Basin influenced by intense biomass burning during the dry season), tends to be updraft-limited, which means that the number of cloud droplets depends primarily on the updraft velocity (26). In these environments, the abundance of CCN is usually dominated by anthropogenic particles from sources related to combustion processes (18).

Over the pristine Amazonian rainforest, convective clouds for which biogenic SOA particles serve as CCN may in turn promote the formation

**Fig. 2.** Prevalence of different aerosol types in the (A and B) number size distribution ( $dN/d\log D$ ) and (C and D) mass size distribution ( $dM/d\log D$ ) plotted against particle diameter ( $D$ ) as observed during AMAZE-08 (3 to 13 March 2008). Single particle analysis of filter samples was performed by means of SEM, and on-line measurements were made by means of differential mobility particle sizing (DMPS,  $<1\ \mu\text{m}$ ), aerosol mass spectrometry (AMS,  $<1\ \mu\text{m}$ ), and ultraviolet aerodynamic particle sizing (UV-APS,  $>1\ \mu\text{m}$ ). Relative uncertainties are in the range of  $\sim 10$  to 50% (8). There is a change of scales at  $D = 1\ \mu\text{m}$  (left versus right ordinate).

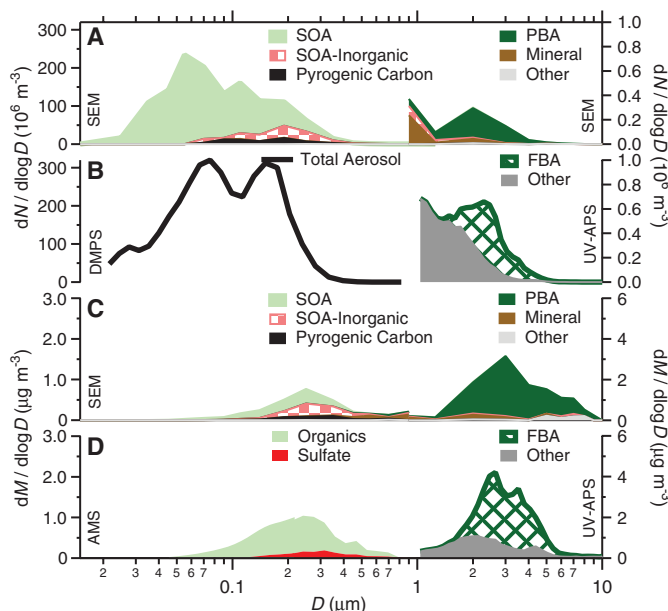
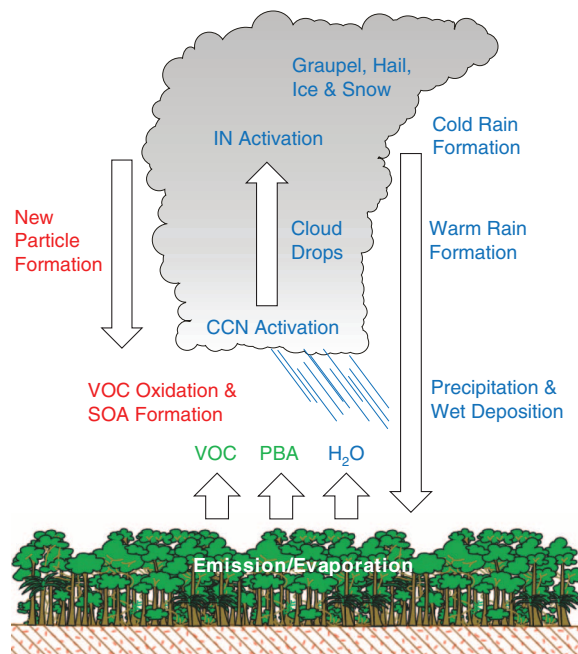


**Fig. 3.** Aerosol and water cycling over the pristine rainforest. SOA formed by photo-oxidation of volatile organic compounds (VOC) and PBA emitted from biota in the rainforest (plants and microorganisms) serve as biogenic nuclei for CCN and IN, which induce warm or cold rain formation, precipitation, and wet deposition of gases and particles.



of new SOA particles. During AMAZE-08, no new particle formation events were observed, which is consistent with earlier Amazonian aerosol studies (6, 7) but unlike most other continental regions of the world (27, 28). The low abundance of nucleation mode particles ( $<30\ \text{nm}$ ) (Fig. 2B, DMPS) and the relatively high abundance of SOA particles in the Aitken mode suggest, by inference, that new particle formation occurred in the free troposphere, possibly in the outflow of convective clouds, and that the newly formed particles were transported from aloft into the boundary layer, possibly in the downdraft of convective clouds (6, 7, 29, 30). Similarly, precipitation induced by PBA particles acting as IN or giant CCN sustains the reproduction of plants and microorganisms in the ecosystem from which both the SOA precursors and the PBA particles are emitted (such as bacteria, fungi, pollen, and plant debris) (6, 11). Accordingly, the Amazon Basin can be pictured as a biogeochemical reactor using the feedstock of plant and microbial emissions in combination with high water vapor, solar radiation, and photo-oxidant levels to produce SOA and PBA particles (31, 32). The biogenic aerosol particles serve as nuclei for clouds and precipitation, sustaining the hydrological cycle and biological reproduction in the ecosystem (Fig. 3). The feedback mechanisms involved may be important for stabilizing the Amazonian rainforest ecosystem and may also be generally relevant for the evolution of ecosystems and climate on global scales and in the Earth's history. To test this hypothesis, we suggest further studies and long-term observations of aerosol properties and aerosol-cloud-precipitation interactions under pristine conditions in other regions and climatic zones with high biological activity, including tropical, temperate, and boreal forests.

## References and Notes

- S. Solomon et al., *IPCC 4th Assessment Report* (Cambridge Univ. Press, Cambridge, 2007).
- D. Rosenfeld et al., *Science* **321**, 1309 (2008).
- B. Stevens, G. Feingold, *Nature* **461**, 607 (2009).
- J. L. Jimenez et al., *Science* **326**, 1525 (2009).
- M. O. Andreae, *Science* **315**, 50 (2007).
- S. T. Martin et al., *Rev. Geophys.* **48**, RG2002 (2010).
- S. T. Martin et al., *Atmos. Chem. Phys. Discuss.* **10**, 18139 (2010).
- Materials and methods are available as supporting material on Science Online.
- Q. Chen et al., *Geophys. Res. Lett.* **36**, L20806 (2009).
- S. S. Gunthe et al., *Atmos. Chem. Phys.* **9**, 7551 (2009).
- W. Elbert, P. E. Taylor, M. O. Andreae, U. Pöschl, *Atmos. Chem. Phys.* **7**, 4569 (2007).
- J. Fröhlich-Nowoisky, D. A. Pickersgill, V. R. Després, U. Pöschl, *Proc. Natl. Acad. Sci. U.S.A.* **106**, 12814 (2009).
- I. Koren et al., *Environ. Res. Lett.* **1**, 014005 (2006).
- K. S. Johnson et al., *Environ. Sci. Technol.* **42**, 6619 (2008).
- M. Hallquist et al., *Atmos. Chem. Phys.* **9**, 5155 (2009).
- S. M. King et al., *Atmos. Chem. Phys.* **10**, 3953 (2010).
- M. D. Petters, S. M. Kreidenweis, *Atmos. Chem. Phys.* **7**, 1961 (2007).
- M. O. Andreae, D. Rosenfeld, *Earth Sci. Rev.* **89**, 13 (2008).
- J. A. Huffman, B. Treutlein, U. Pöschl, *Atmos. Chem. Phys.* **10**, 3215 (2010).
- A. J. Prenni et al., *Nat. Geosci.* **2**, 402 (2009).



21. O. Möhler, P. J. DeMott, G. Vali, Z. Levin, *Biogeosciences* **4**, 1059 (2007).
22. B. C. Christner, C. E. Morris, C. M. Foreman, R. M. Cai, D. C. Sands, *Science* **319**, 1214 (2008).
23. R. M. Bowers *et al.*, *Appl. Environ. Microbiol.* **75**, 5121 (2009).
24. K. A. Pratt *et al.*, *Nat. Geosci.* **2**, 398 (2009).
25. M. O. Andreae *et al.*, *Science* **303**, 1337 (2004).
26. P. Reutter *et al.*, *Atmos. Chem. Phys.* **9**, 7067 (2009).
27. M. Kulmala *et al.*, *J. Aerosol Sci.* **35**, 143 (2004).
28. J. Merikanto, D. V. Spracklen, G. W. Mann, S. J. Pickering, K. S. Carslaw, *Atmos. Chem. Phys.* **9**, 8601 (2009).
29. R. Krejci *et al.*, *Atmos. Chem. Phys.* **5**, 1527 (2005).
30. A. M. L. Ekman *et al.*, *Geophys. Res. Lett.* **35**, L17810 (2008).
31. U. Kuhn *et al.*, *Atmos. Chem. Phys.* **7**, 2855 (2007).
32. J. Lelieveld *et al.*, *Nature* **452**, 737 (2008).
33. Support from a large number of colleagues, agencies, and institutions is gratefully acknowledged as detailed in the supporting online material.

## Supporting Online Material

www.sciencemag.org/cgi/content/full/329/5998/1513/DC1

Materials and Methods

SOM Text

Fig. S1

Tables S1 to S6

References and Notes

19 April 2010; accepted 28 June 2010

10.1126/science.1191056

# Melting of Peridotite to 140 Gigapascals

G. Fiquet,<sup>1\*</sup> A. L. Auzende,<sup>1</sup> J. Siebert,<sup>1</sup> A. Corgne,<sup>2,3</sup> H. Bureau,<sup>1</sup> H. Ozawa,<sup>1,4</sup> G. Garbarino<sup>5</sup>

Interrogating physical processes that occur within the lowermost mantle is a key to understanding Earth's evolution and present-day inner composition. Among such processes, partial melting has been proposed to explain mantle regions with ultralow seismic velocities near the core-mantle boundary, but experimental validation at the appropriate temperature and pressure regimes remains challenging. Using laser-heated diamond anvil cells, we constructed the solidus curve of a natural fertile peridotite between 36 and 140 gigapascals. Melting at core-mantle boundary pressures occurs at  $4180 \pm 150$  kelvin, which is a value that matches estimated mantle geotherms. Molten regions may therefore exist at the base of the present-day mantle. Melting phase relations and element partitioning data also show that these liquids could host many incompatible elements at the base of the mantle.

Geophysical and geochemical observations favor the presence of chemical heterogeneities in the lowermost mantle. These are thought to be either primitive mantle residues (1), dense subducted slab components (2), products of chemical interactions between the core and mantle (3, 4), or dense melts perhaps as old as the Earth itself (5). The core-mantle boundary is a complex region that has been the focus of numerous geophysical studies. Seismologic studies suggest the presence of two large low-shear velocity provinces (LLSVPs) under the African continent and in the Pacific basin (6, 7). The consensus view is that these slow regions (which are possibly up to 1000 km thick) exhibit an anomalously low shear velocity and increased bulk modulus but are not usually thought to be partially molten (8). Additionally, extensively documented ultralow-velocity zones (ULVZs) correspond to localized features at the core-mantle boundary (CMB), with strong reductions in seismic velocities (in the range of 10 to 30%) for both P and S waves (9, 10); the interpretation

is that these zones may be partially molten (5). Recent high-resolution waveform studies also find evidence that the ULVZ material is denser than the surrounding mantle (11). These partially molten regions have not been detected to be laterally continuous and have a thickness ranging from a few kilometers up to about 50 km.

It is attractive to link these observations with an episode of extensive melting that probably affected the primitive Earth, leading to the formation of a deep magma ocean. If the evolution of a terrestrial magma ocean resulted in the formation of a layer of melt at the base of the mantle early in Earth history, its survival depends on whether it was (and maybe still is) gravitationally and chemically stable (12). If this is the case, such a layer would be an ideal candidate for an unsampled geochemical reservoir hosting a variety of incompatible species, notably the planet's missing budget of heat-producing elements (13). The presence of high-pressure melts would also have consequences for chemical reactions between the mantle and core, the dynamics of the lowermost mantle, and the heat flow across the CMB.

To constrain the existence of melt at the base of the mantle, we performed melting experiments on a fertile peridotite composition over a range of lower-mantle pressures between 36 and 140 GPa using a laser-heated diamond-anvil cell (DAC) coupled with in situ synchrotron measurements (14). Our study thus extends the pressure range of previous measurements (15, 16) of the solidus and liquidus temperatures of a mantle-like composition to depths exceeding those of the CMB at 2900 km. The starting material used for the high-

pressure high-temperature melting experiments is a natural KLB-1 peridotite (14). To ensure chemical homogeneity at the smallest scale and Fe as mostly  $\text{Fe}^{2+}$ , a glass was prepared by using an aerodynamic levitation device coupled with  $\text{CO}_2$  laser heating under slightly reducing conditions of oxygen fugacity (17). At high temperature, pressures were measured from cell parameters of the magnesium perovskite ( $\text{Mg,FeSiO}_3$ ) by using a thermal equation of state recently reported for the same KLB-1 peridotitic starting material as

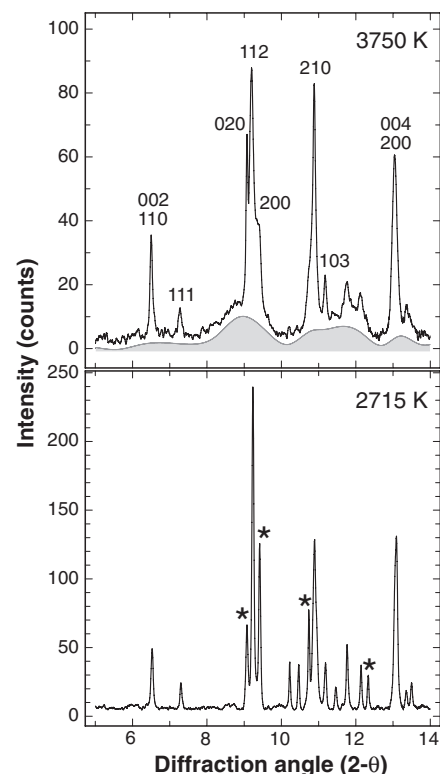


**Fig. 1.** Diffraction patterns collected at 61 GPa after normalized reference background subtraction: subsolidus at 2715 K (**bottom**) and above solidus at 3750 K (**top**). The diffuse scattering liquid contribution is outlined by the shaded area as a guide; it does not correspond to a physical structural model of the liquid. HKL indexes are given for remaining diffraction peaks that can be assigned to magnesium silicate perovskite, observed above the solidus temperature at this pressure (top). Stars denote diffraction peaks of Ca-perovskite and ferropericlase affected by partial melting at these conditions (bottom).

<sup>1</sup>Institut de Minéralogie et de Physique des Milieux Condensés, Institut de Physique du Globe de Paris, Université Pierre et Marie Curie, UMR CNRS 7590, Université Paris Diderot, 140 rue de Lourmel, 75015 Paris, France. <sup>2</sup>Institut de Physique du Globe de Paris, Equipe de Minéralogie à l'Institut de Minéralogie et de Physique des Milieux Condensés, 140 rue de Lourmel, 75015 Paris, France. <sup>3</sup>Observatoire Midi-Pyrénées, UMR CNRS 5562, 14 rue Edouard Belin, 31400 Toulouse, France. <sup>4</sup>Department of Earth and Planetary Sciences, Tokyo Institute of Technology 2-12-1 Ookayama, Meguro-ku, Tokyo 152-8551, Japan. <sup>5</sup>European Synchrotron Radiation Facility, BP220, 38043 Grenoble cedex, France.

\*To whom correspondence should be addressed. E-mail: guillaume.fiquet@impmc.upmc.fr

used in our study (18). We used in situ x-ray diffraction as primary criterion for melting (19) and to determine the order in which crystalline phases melt (Fig. 1).

At 36 GPa, melting begins at 2800 K, with Mg- and Ca-perovskite ( $\text{CaSiO}_3$ ) melting first. The produced melt is far more laser-absorbent; a sharp increase in temperature accompanies melting. This leads almost instantly to conditions above the liquidus, preventing an accurate characterization of a detailed melting sequence. Trans-

mission electron microscopy (TEM) examination of a focused ion beam section made across the laser-heated spot on the recovered sample (fig. S3) and the large temperature increase at melting may indicate that Mg-perovskite melts early in the sequence (fig. S4). At this pressure, the liquidus temperature is  $\sim 3850$  K, as determined during cooling from a fully molten state by a large temperature drop when the first phase crystallizes. At 61 GPa, melting of ferropericlase ( $\text{Mg,FeO}$ ) indicates the solidus temperature is  $\sim 3050$  K, closely

**Fig. 2.** Analytical TEM examination of a sample recovered after partial melting at 61 GPa: (left) bright field micrograph and (right) chemical maps. Some untransformed glassy material (GL) can be observed near the surface (panel 1), with chemical analysis yielding the average chemical composition of the starting material, thus showing the absence of reaction between sample and diamond during experimentation. A rim of ferropericlase (Fp) crystals appearing in red (iron-rich) exists at the edge of the laser-heated area. These crystals connect by veins to large patches of ferropericlase dispersed in the central area dominated by magnesium silicate perovskite (Mg-pv) in green (silicon-rich). Calcium silicate perovskite (Ca-pv) grains appear in blue (calcium-rich); most of them are located along ferropericlase-rich veins or at the edge of ferropericlase patches (panel 2). Some metallic iron precipitates exist in the iron-enriched ferropericlase regions (bright red spots). Melts probably formed after melting of ferropericlase and Ca-perovskite, which tend to percolate away from the heated area (probably as a result of thermal pressure) then crystallize on the edge in contact with the cold untransformed glassy material to form a rim surrounding the heated area.

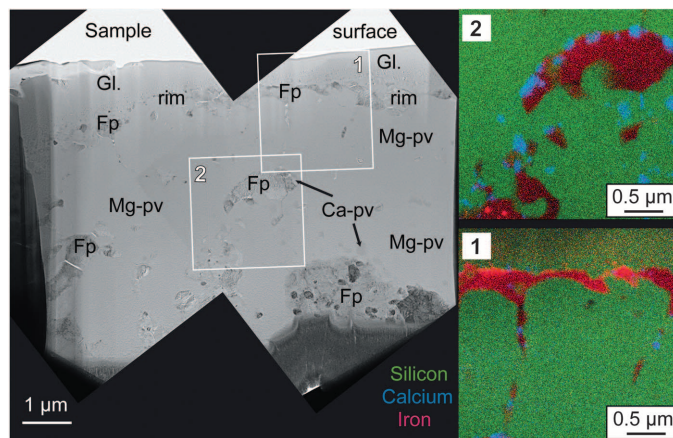
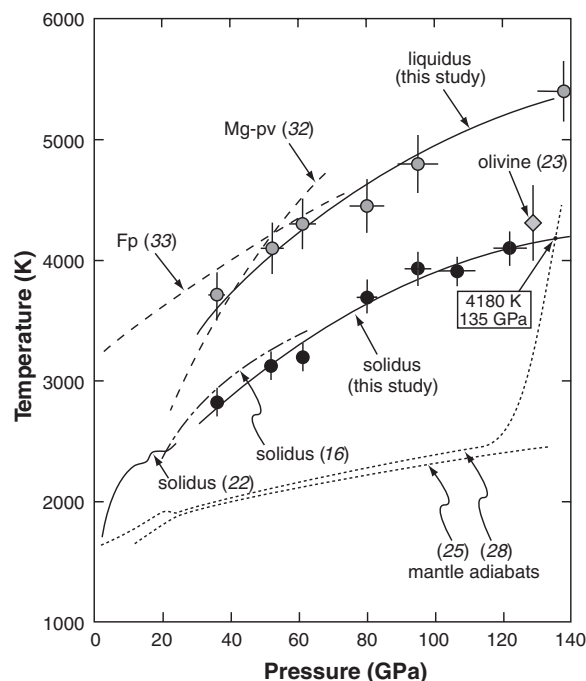


**Fig. 3.** Solidus (black solid circles) and liquidus (gray solid circles) of peridotite, along with melting curve data from the literature. Shown are the average estimate of the solidus for KLB-1 peridotite from previous multi-anvil work (22); the solid gray diamond indicates the shock melting point of olivine (23). Melting temperatures of the major lower mantle phases Mg-perovskite (32) and ferropericlase (33) are indicated by long-dashed lines. Melting data for a pyrolytic composition (dot-dashed line) are from (16). Temperature error bars represent temperature fluctuations during heating. Pressure error bars include the pressure variation in the sample chamber associated with temperature fluctuations as well as the uncertainty in the thermal equation of state of the magnesium silicate perovskite. Mantle geotherms are given for reference [adiabatic (25)] or estimated from perovskite to post-perovskite transition (28). Our solidus line, extrapolated to the CMB (solid line), intersects the geotherm at 135 GPa and 4180 K.



followed by melting of Ca-perovskite with increasing temperature. Mg-perovskite is the last stable phase below the liquidus, which is  $\sim 4200$  K. The observation of the recovered sample (Fig. 2) reveals the presence of connected veins of ferropericlase in a matrix made of Mg-perovskite. Ca-perovskite grains are found along these veins as well as within the Mg-perovskite matrix, suggesting that Ca-perovskite was partly mobilized by melting. Ferropericlase veins also collected small ( $<100$  nm) globules of metallic iron, which is consistent with the disproportionation of ferrous iron in the stability field of Mg-perovskite (20). At pressures above 61 GPa, it is more difficult to distinguish whether ferropericlase or Ca-perovskite melts first. It is clear, however, that Mg-perovskite is the last solid phase below the liquidus. We observed a smooth increase of melting temperatures with increasing pressures. At 112 GPa, the solidus is located at 3910 K. At CMB pressure and temperature conditions (136 GPa and temperatures above 4000 K) and above, the melting sequence remains the same: Ca-perovskite and ferropericlase melt first, followed by Mg-perovskite. Mg-perovskite is thus the liquidus phase between 60 GPa (perhaps less) and pressure conditions at the CMB (fig. S5).

Above 61 GPa, the observed liquidus phase deviates from previous observations made at 24 GPa in multi-anvil experiments, in which ferropericlase was shown to be the liquidus phase, followed by Mg-perovskite 50 K below the liquidus (located at 2600 K) and Ca-perovskite 150 K lower, near the solidus (21). However, our observations are in qualitative agreement with other multi-anvil experiments (15), which suggest that Mg-perovskite should replace ferropericlase as the liquidus phase at pressures above 30 GPa, whereas our measurements suggest that this should happen at pressures above 36 GPa.

Solidus and liquidus points determined in this study compare well with literature data (Fig. 3). Data from previous DAC work in the 40 to 60 GPa range (16) are reported as an average solidus curve derived from the last subsolidus measurements and the appearance of first melt described in this study. Our measurements are in agreement with this work, although a completely different melting criterion was used in the latter study. Extrapolation of our solidus curve to lower pressures is also consistent with a large-volume pressure measurement of the solidus for KLB-1 peridotite (22). Furthermore, our data are also in good agreement with the mantle solidus inferred at CMB conditions from a single shock experiment on  $(\text{Mg}_{0.9}\text{Fe}_{0.1})_2\text{SiO}_4$  (23) and from recent first principles molecular dynamics simulations (24). In the latter study, the predicted melting temperature of  $\text{MgSiO}_3$  perovskite at 136 GPa is  $5400 \pm 600$  K, and the authors estimate a mantle solidus temperature of 4100 K.

The solidus curve is about 1400 K above an average mantle adiabat (25) at mid-mantle pressures, but the difference shrinks rapidly above 120 GPa as we approach the CMB (Fig. 3). At



135 GPa, the peridotitic mantle solidus temperature extrapolated from our data set is at  $4180 \pm 150$  K. This value is within the range of proposed temperatures on the core side of the CMB, as calculated from an outer-core adiabat and melting experiments on iron alloys (26, 27) or as constrained by the reverse transition from the  $\text{CaIrO}_3$ -type to the perovskite phase at the base of the D'' layer (28). Partial melting in the deepest part of the mantle is therefore highly plausible. This process could therefore explain the presence of ULVZs. The close match between the average geotherm and mantle solidus at the CMB may also explain why ULVZs are not observed as a continuous layer in the deep mantle, with thicknesses of partially molten regions varying dramatically from cold to hot mantle areas.

Our results also provide insights in the way an early magma ocean could have crystallized. Partial melting of mantle material and related fractional crystallization will have important geochemical implications in terms of trace elements. This applies for both the inventory of incompatible elements and the isotopic evolution of the Earth. For instance, the semiquantitative analysis made on the sample recovered from 61 GPa shows a clear enrichment of the ferropicls in iron, and an ubiquitous iron depletion in Mg-perovskite (table S1), which is in agreement with observations made in earlier studies [(26) and references therein]. Partial melts enriched in Ca-perovskite and ferropicls components are thus expected to be denser than a solid residue of Fe-depleted Mg-perovskite. These liquids could have segregated downward and remained at least partly isolated in the lower mantle if mantle convection was not too vigorous [(29) and references therein]. Because Ca-perovskite is the major host mineral for many key trace elements, such as U, Th, and rare earth elements (30), these liquids could fractionate and host at present many incompatible elements at the core-mantle boundary, thus offering an explanation for primordial chemical signatures at the base of the mantle.

The estimated thickness of such a partially molten layer varies between 0 to 35 km from the intersection of the modern geotherm shown in Fig. 3 with the solidus of the mantle silicate material obtained in our study; however, this thickness could have been as large as 100 km in the Archean, assuming a secular cooling proceeding at a maximum rate of 100 K per billion years (31). These features depend on the estimates of the geotherm in the CMB region, which depends on the core thermal profile and temperature. The extension of such partially molten regions would also vary with lateral variations of the geotherm in the lowermost mantle, with the thickest portions occurring at the base of upwelling plumes and a thin layer elsewhere, which is compatible with seismic observations of ULVZs. Such a partially molten layer can alter several properties of the lowermost mantle that could, as proposed earlier (5), control the convection regime of the lowermost mantle and the heat transfer between

core and mantle and affect the stability of the thermal boundary layer at the CMB.

#### References and Notes

1. L. H. Kellogg, B. H. Hager, R. D. van der Hilst, *Science* **283**, 1881 (1999).
2. F. Albarede, R. D. van der Hilst, *Philos. Trans. R. Soc. London. A* **360**, 2569 (2002).
3. A. D. Brandon, R. J. Walker, J. W. Morgan, M. D. Norman, H. M. Prichard, *Science* **280**, 1570 (1998).
4. D. J. Frost *et al.*, *J. Geophys. Res.* **115**, B02202 (2010).
5. Q. Williams, E. J. Garnero, *Science* **273**, 1528 (1996).
6. D. Helmberger, T. Lay, S. Ni, M. Gurnis, *Proc. Natl. Acad. Sci. U.S.A.* **102**, 17257 (2005).
7. E. J. Garnero, A. K. McNamara, *Science* **320**, 626 (2008).
8. T. Lay, E. J. Garnero, Q. Williams, *Phys. Earth Planet. Inter.* **146**, 441 (2004).
9. L. X. Wen, D. V. Helmberger, *J. Geophys. Res. Solid Earth* **103** (B8), 17901 (1998).
10. E. J. Garnero, D. V. Helmberger, *J. Geophys. Res. Solid Earth* **103**, 12495 (1998).
11. S. Rost, E. J. Garnero, Q. Williams, *J. Geophys. Res. Solid Earth* **111** (B09310), 1 (2006).
12. S. Labrosse, J. W. Hernlund, N. Coltice, *Nature* **450**, 866 (2007).
13. M. Boyet, R. W. Carlson, *Science* **309**, 576 (2005).
14. Materials and methods are available as supporting material on Science Online.
15. E. Ito, A. Kubo, T. Katsura, M. J. Walter, *Phys. Earth Planet. Inter.* **143–144**, 397 (2004).
16. A. Zerr, A. Diegeler, R. Boehler, *Science* **281**, 243 (1998).
17. L. Hennet *et al.*, *Rev. Sci. Instrum.* **73**, 124 (2002).
18. A. Ricolléau *et al.*, *Geophys. Res. Lett.* **36**, L06302 (2009).
19. A. Dewaele, M. Mezouar, N. Guignot, P. Loubeyre, *Phys. Rev. B* **76**, 144106 (2007).
20. D. J. Frost *et al.*, *Nature* **428**, 409 (2004).
21. R. G. Trønnes, D. J. Frost, *Earth Planet. Sci. Lett.* **197**, 117 (2002).
22. J. Zhang, C. Herzberg, *J. Geophys. Res.* **99**, 17729 (1994).
23. K. G. Holland, T. J. Ahrens, *Science* **275**, 1623 (1997).
24. L. Stixrude, N. de Koker, N. Sun, M. Mookherjee, B. B. Karki, *Earth Planet. Sci. Lett.* **278**, 226 (2009).
25. J. M. Brown, T. S. Shankland, *J. R. Astron. Soc.* **66**, 579 (1981).
26. R. Boehler, *Rev. Geophys.* **38**, 221 (2000).
27. Q. Williams, R. Jeanloz, *J. Geophys. Res.* **95**, 19299 (1990).
28. S. Ono, A. Oganov, *Earth Planet. Sci. Lett.* **236**, 914 (2005).
29. C.-T. Lee *et al.*, *Nature* **463**, 930 (2010).
30. A. Corgne, C. Liebske, B. J. Wood, D. C. Rubie, D. J. Frost, *Geochim. Cosmochim. Acta* **69**, 485 (2005).
31. C. Michaut, C. Jaupart, *Earth Planet. Sci. Lett.* **257**, 83 (2007), and references therein.
32. A. Zerr, R. Boehler, *Science* **262**, 553 (1993).
33. A. Zerr, R. Boehler, *Nature* **371**, 506 (1994).
34. We thank L. Hennet and G. Ona Nguema for experimental assistance. X-ray diffraction plots were made using DATLAB software developed by K. Syassen. A.L.A. acknowledges support from Institut National des Sciences de l'Univers (INSU) program "PNP, theme SEDI-TPS," and A.C. acknowledges support from the European Research Council (ERC) under the European Community's Seventh Framework Programme (FP7/2007-2013)/ERC grant agreement 207467. The Focused Ion Beam (FIB) and Scanning Electron Microscope (SEM) facility of the Institut de Minéralogie et de Physique des Milieux Condensés is supported by Région Ile de France grant SESAME 2006 N°1-07-593/R, INSU-CNRS, Institut de Physique (INP)-CNRS, University Pierre et Marie Curie-Paris 6, and by the French National Research Agency (ANR) grant ANR-07-BLAN-0124-01.

#### Supporting Online Material

www.sciencemag.org/cgi/content/full/329/5998/1516/DC1  
Materials and Methods  
Figs. S1 to S5  
Table S1  
References

18 May 2010; accepted 2 August 2010  
10.1126/science.1192448

## A Test of the Snowball Theory for the Rate of Evolution of Hybrid Incompatibilities

Daniel R. Matute, Ian A. Butler, David A. Turissini, Jerry A. Coyne

Hybrids between species are often sterile or inviable because the long-diverged genomes of their parents cause developmental problems when they come together in a single individual. According to the Dobzhansky-Muller (DM) model, the number of genes involved in these "intrinsic postzygotic incompatibilities" should increase faster than linearly with the divergence time between species. This straightforward prediction of the DM model has remained contentious owing to a lack of explicit tests. Examining two pairs of *Drosophila* species, we show that the number of genes involved in postzygotic isolation increases at least as fast as the square of the number of substitutions (an index of divergence time) between species. This observation verifies a key prediction of the DM model.

**B**iological speciation involves the evolution of barriers to gene flow between two populations (1, 2). One of the most effective of those barriers, because it is considered irreversible, is "intrinsic postzygotic isolation,"

the developmentally based inviability or sterility of species hybrids. Dobzhansky (1) and Muller (3) proposed a simple two-locus model showing how this form of isolation can result from the accumulation of genes that function normally in a pure-species genome but produce epistatic interactions in hybrids.

The classic version of the Dobzhansky-Muller (DM) model, a population-genetics theory for the evolution of reproductive isolation (2), begins with

Department of Ecology and Evolution, The University of Chicago, 1101 East 57th Street, Chicago, IL 60637, USA.

\*To whom correspondence should be addressed. E-mail: dmatute@uchicago.edu

two loci in an ancestral species having genotype  $A_1A_1B_1B_1$  (the model can be expanded to more than two loci). The ancestral species then splits into two geographically isolated descendant species that eventually evolve genotypes  $A_1A_1B_2B_2$  and  $A_2A_2B_1B_1$  through natural selection, genetic conflict, or sexual selection—or (less likely) genetic drift—that fixes allele  $A_1$  in one species and  $B_1$  in the other. The DM model posits that postzygotic isolation arises as a collateral effect of this evolutionary divergence. In this case, although species having genotypes  $A_1A_1B_2B_2$  and  $A_2A_2B_1B_1$  at two loci are fit, in hybrids, where the  $B_2$  and  $A_2$  alleles first encounter each other, they interact abnormally, producing sterility or inviability (1–5).

Although several studies have identified genes causing hybrid incompatibilities (4–8), little is known about the evolutionary rate at which these incompatibilities arise (9, 10). Mathematical modeling has shown that the expected number of two-locus DM incompatibilities should increase as fast as the square of the number of substitutions between two species, the “snowball effect” (11, 12). (Three-way interactions should increase as fast as the cube of the number of substitutions between two species, and so on.) This is because DM interactions occur between two or more genes from different species, and if individual gene substitutions accumulate at a constant rate within each species, the number of negative epistatic interactions involving at least one gene from each species should grow at least with the square of time elapsed. Because this prediction requires counting genes causing hybrid incompatibilities in at least two different hybridizations between taxa of known divergence times, it cannot be tested in most groups of plants or animals (2, 13–15).

We took advantage of the fact that *Drosophila melanogaster* females (*mel*) produce hybrid females when crossed with *D. simulans* (*sim*) and *D. santomea* (*san*) males (6, 16–18) to test the snowball prediction of DM theory. We counted the number of incompatibilities that evolved since the divergence of each pair of species; the two pairs have divergence times differing by roughly 2.4 [*mel-sim*: 5.4 million years ago (Ma) and *mel-san*: 12.8 Ma (19)].

If we assume that DM interactions occur between pairs of loci, the snowball hypothesis leads us to expect at least six ( $\sim 2.4^2$ ) times as many incompatibilities between the older than between the younger species pair. We tested this prediction through fine-scale mapping and counting of the gene regions causing inviability in hybrid females (the only sex produced by both the *mel* × *sim* and *mel* × *san* crosses).

We crossed females from *D. melanogaster* stocks containing known genomic deletions, or “deficiencies” [Bloomington *Drosophila* Fly Stock Center (19)], maintained as heterozygotes against a balancer (*Bal*) chromosome carrying a dominant homozygous lethal mutation, to *san* and *sim* males. We determined the effect of each

hemizygous region (presumably expressing recessive alleles from *san* or *sim*) on the viability of hybrid female offspring from the two interspecific crosses (Fig. 1). If a *D. melanogaster* deficiency uncovered a recessive region of the other species’ genome producing hybrid lethality when hemizygous in hybrids with *D. santomea*, this cross would produce *Bal/san* but not *Df/san* hybrid females (or, in hybrids with *D. simulans*, *Bal/sim* but not *Df/sim*) (Fig. 1) (6, 16). We considered “inviability regions” to be those yielding relative viability (i.e., the ratio of hybrid progeny carrying the chromosome deficiency to the total number of offspring from that cross) significantly below 0.5 ( $\chi^2$  test;  $P < 0.05$ ). This approach detects epistatic interactions between a recessive allele of *D. santomea* (exposed when hemizygous) and a dominant factor in the *mel* genome. Although it is not clear whether we uncovered genes directly involved in speciation—for their divergence may have occurred after speciation was complete—they do represent an evolutionary accumulation of hybrid incompatibilities and thus constitute a test of the snowball effect.

The *mel/san* crosses tested about 92.0% of the *D. melanogaster* genome (calculated as the proportion of total chromosome bands covered in our deficiency screening); the *mel/sim* crosses tested about 79.4% of *D. melanogaster* genome. Finally, to establish whether the deficiencies had an effect on within-species viability when heterozygous in *D. melanogaster* females, we measured the relative viability of deficiency-carrying females in crosses between *D. melanogaster* *Df/Bal* (*mel Df/Bal*) females and *D. melanogaster* *ArkLa* males (a stock founded by females from wild populations collected in Arkansas and Louisiana).

The interspecific deficiency screening in *san/mel* hybrids shows 71 nonoverlapping chromosomal regions containing genes involved in DM incompatibilities (Fig. 2 and table S1). In contrast, in *sim/mel* hybrids, we found just 10 regions involved in DM incompatibilities (Fig. 2 and table S2). None of the deficiencies that

caused hybrid lethality showed reduced viability in intraspecific crosses, suggesting that the heterozygous-lethal effects are specific to hybrid backgrounds (table S3).

When possible, we used overlapping deficiencies to further localize inviability genes in each cross. This also ensured that the inviability observed with each lethal deficiency could be reproduced with an independent deficiency in the same chromosome region. Of the 71 regions that caused hybrid inviability in *mel/san* hybrids, 61 had overlapping deficiencies, and for each one of these 61 regions, at least one overlapping deficiency showed hybrid inviability. This shows that hybrid inviability is not an artifact of a stock’s genetic background and allowed us to further refine the mapping position of each inviability allele (Fig. 2 and tables S1 and S4).

We used Orr’s theoretical framework (4) to determine the existence of the snowball effect predicted by the DM model, that is, whether the number of genes causing inviability in these two pairs of crosses increased quadratically (or even faster) with their relative divergence times. Because there is no fossil record for these species, we estimated relative divergence times using a genetic proxy: the average number of synonymous substitutions per gene (*Ks*) between each of the two pairs across the whole genome (20). Under the assumption of an approximate molecular clock, *Ks* increases linearly with divergence time, and, unlike phylogeny-based estimates, the *Ks*-based estimates of divergence time need not be transformed with calibrations from fossils and make no assumptions about generation times (20).

We estimated *Ks* by counting the number of synonymous substitutions for the *sim-mel* (*Ks sim-mel*) and *san-mel* (*Ks san-mel*) species pairs for every sequenced gene shared by these species. These values were then averaged among genes to find the overall *Ks* (and its standard error, or SEM) for each pair of genomes (*Ks sim-mel* = 0.101, SEM =  $4.03 \times 10^{-4}$ ; and *Ks san-mel* =

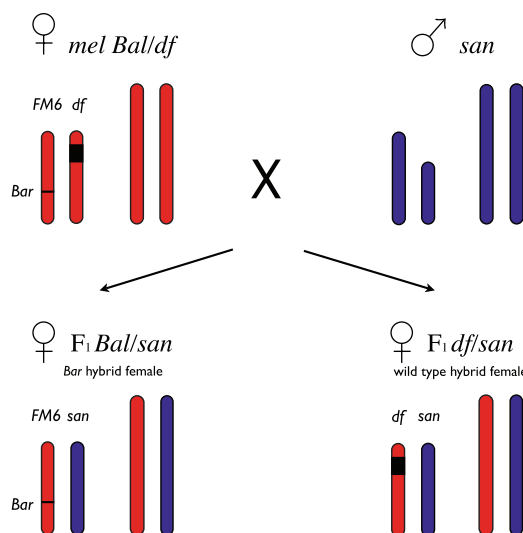


**Fig. 1.** Crossing scheme used to produce two classes of hybrid female offspring, one of which is hemizygous for a section of *D. santomea* genome uncovered by a deficiency from *D. melanogaster*. This example shows the cross of a *mel* female to a *san* male. If the deficiency does not uncover any lethal allele, half of the progeny will carry the *FM6* balancer paired with a *san* X chromosome; the other half will carry the deficiency paired with a *san* X chromosome. Lethality or semilethality results in a dearth of deficiency-carrying offspring.



0.242, SEM =  $8.17 \times 10^{-4}$ ). To establish whether the observed data fulfill theoretical expectations, we calculated the expected number of incompatibilities under two models: one in which incompatibilities accumulated linearly with the number of substitutions (i.e., absence of a snowball effect, which could reflect reproductive isolation caused by nonepistatic factors such as accumulated chromosomal rearrangements), and a model

in which the expected number of incompatibilities was proportional to the square of the total number of DNA substitutions (i.e., the presence of a snowball effect involving two-locus interactions). In these calculations we included viability data only for deficiency stocks tested in both sets of crosses (65 incompatibilities in the *mel* × *san* cross and 10 in the *mel* × *sim* cross). To determine which model was more likely to explain the data,

we used the AIC [Akaike Information Criterion (21)] scores of each model and calculated the evidence ratio of Akaike weights for the quadratic model over the linear model. These scores were then converted to the normalized probability that the quadratic model is preferred over the linear model (21).  
The *K<sub>s</sub>* values, the observed number of incompatibilities, the expected number of incom-

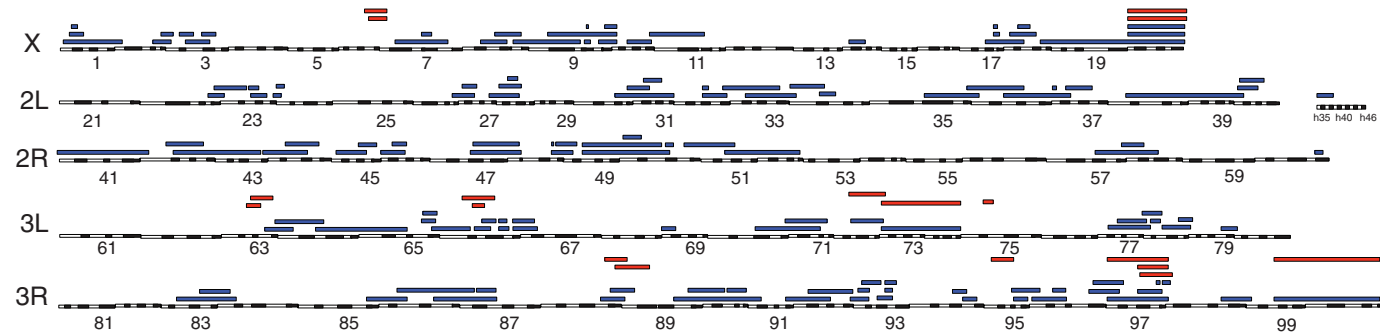


**Fig. 2.** Chromosomal locations of hybrid lethal regions (on a *D. melanogaster* cytological map) for *D. melanogaster* × *D. santomea* and *D. melanogaster* × *D. simulans* crosses. All lethal regions detected contain at least one gene involved in an epistatic interaction between a recessive

element in the *D. santomea* (or *D. simulans*) genome and one or more dominant or semidominant factors in the *D. melanogaster* genome. Regions reducing viability in *mel/san* hybrids are shown in blue; those in *mel/sim* hybrids in red.

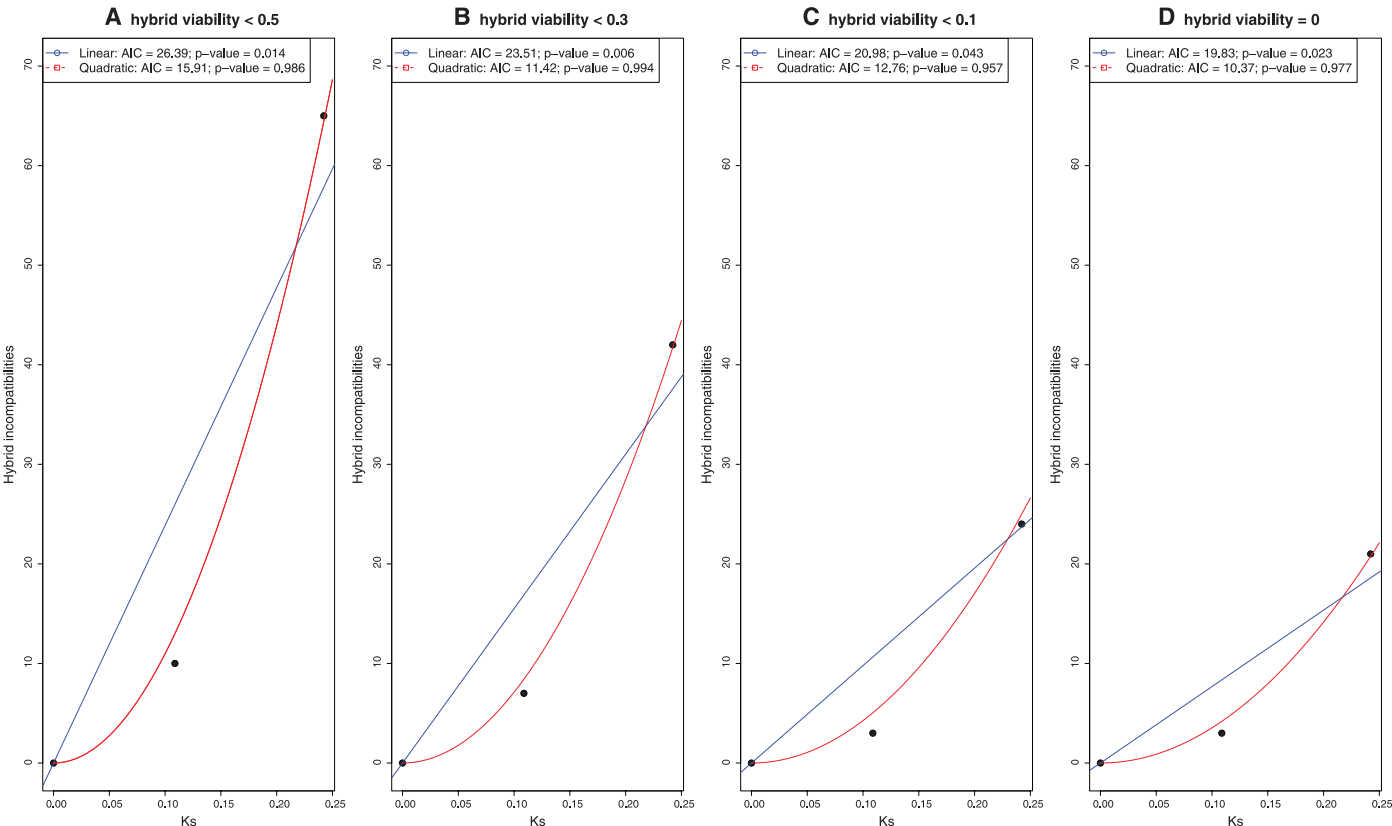


**Fig. 3.** Number of observed and expected hybrid incompatibilities in *san/mel* and *sim/mel* F<sub>1</sub> female hybrids. We fitted the linear and quadratic model that had lowest AIC values and forced the models through the origin (the assumption here is that at time zero, when there are no genetic substitutions between populations, there are no incompatibilities). *P* values are the normalized probability that each model is to be preferred over the other one (e.g., the quadratic

model is to be preferred over the linear model and vice versa) according to the evidence ratio of Akaike weights. Deviations are highly significant for the linear model but not for the quadratic model, regardless of how we quantify “viability”; and in all cases the quadratic model explains the data better than the linear model. Different panels represent the four different definitions of “inviability”: (A) Lower than 0.5; (B) lower than 0.3; (C) lower than 0.1; and (D) equal to 0.

patibilities, and the results for all the model comparisons are shown in Fig. 3. These data show that the number of incompatibilities does not accumulate linearly with divergence time and is more consistent with a quadratic increase, as expected if the evolution of those incompatibilities obeys the snowball effect. This result holds regardless of which estimate of divergence time we use (Fig. 1 and figs. S1 to S3). We thus conclude that hybrid incompatibilities between these species accumulate substantially faster than linearly with respect to their divergence time.

In addition to fitting the linear and quadratic models to regions that caused a relative viability lower than 0.5, we used more stringent criteria for inviability, fitting the two models to regions that showed relative viabilities lower than 0.3, 0.1, and 0. The results were similar in all cases (Fig. 1 and figs. S1 to S3) and revealed that, regardless of their size, deleterious epistatic interactions accumulate faster than linearly with divergence time.

Besides counting incompatibilities, our results can be used to identify and isolate genes causing reproductive isolation between species. Deletion mapping in *D. melanogaster*/*D. simulans* hybrids has identified two “hybrid inviability” genes with

function in nuclear transport and whose divergence occurred via natural selection (6, 8, 22).

By confirming a key prediction of the DM theory and showing a snowball effect of the accumulation of genetic incompatibilities causing reproductive isolation, we support the view that postzygotic reproductive isolation often results from deleterious interactions in hybrids between genes that behave normally within species.

#### References and Notes

1. T. Dobzhansky, *Genetics and the Origin of Species* (Columbia Univ. Press, New York, 1937).
2. J. A. Coyne, H. A. Orr, *Speciation* (Sinauer Associates, Sunderland, MA, 2004).
3. H. J. Muller, *Biol. Symp.* **6**, 71 (1942).
4. D. C. Presgraves, *Curr. Biol.* **17**, R125 (2007).
5. N. Phadnis, H. A. Orr, *Science* **323**, 376 (2009).
6. D. C. Presgraves, *Genetics* **163**, 955 (2003).
7. N. J. Brideau *et al.*, *Science* **314**, 1292 (2006).
8. S. Tang, D. C. Presgraves, *Science* **323**, 779 (2009).
9. S. Gourbière, J. Mallet, *Evolution* **64**, 1 (2010).
10. N. Johnson, in *Evolutionary Genetics: Concepts and Case Studies*, C. W. Fox and J. B. Wolf, Eds. (Oxford Univ. Press, New York, 2006), pp. 374–386.
11. H. A. Orr, *Genetics* **139**, 1805 (1995).
12. H. A. Orr, M. Turelli, *Evolution* **55**, 1085 (2001).
13. L. C. Moyle, T. Nakazato, *Genetics* **179**, 1437 (2008).
14. D. I. Bolnick, T. J. Near, *Evolution* **59**, 1754 (2005).
15. L. C. Moyle, B. A. Payseur, *Trends Ecol. Evol.* **24**, 591 (2009).
16. J. A. Coyne, S. Simeonidis, P. Rooney, *Genetics* **150**, 1091 (1998).
17. D. R. Matute, I. A. Butler, J. A. Coyne, *Cell* **139**, 1180 (2009).
18. Materials and methods are available as supporting materials on Science Online.
19. K. Tamura, S. Subramanian, S. Kumar, *Mol. Biol. Evol.* **21**, 36 (2004).
20. W. H. Li, *J. Mol. Evol.* **36**, 96 (1993).
21. K. P. Burnham, D. R. Anderson, *Model Selection and Multimodel Inference: A Practical Information-Theoretic Approach* (Springer, New York, 2002).
22. D. C. Presgraves, L. Balagopal, S. M. Abmayr, H. A. Orr, *Nature* **423**, 715 (2003).
23. We thank D. C. Presgraves, T. D. Price, R. Unckless, D. Kennedy, M. A. Sprigge, and M. Przeworski for discussions and reading of the manuscript; P. Andolfatto, T. Hu, and K. Thornton for sharing data; and A. Harris and J. Gladstone for technical help. Funded by NIH grant R01GM058260 (J.A.C.).

#### Supporting Online Material

www.sciencemag.org/cgi/content/full/329/5998/1518/DC1  
Materials and Methods

Figs. S1 to S3

Tables S1 to S4

References

8 June 2010; accepted 27 July 2010

10.1126/science.1193440

## Hybrid Incompatibility “Snowballs” Between *Solanum* Species

Leonie C. Moyle<sup>1</sup> and Takuya Nakazato<sup>1,2</sup>

Among the reproductive barriers that can isolate species, hybrid sterility is frequently due to dysfunctional interactions between loci that accumulate between differentiating lineages. Theory describing the evolution of these incompatibilities has generated the prediction, still empirically untested, that loci underlying hybrid incompatibility should accumulate faster than linearly with time—the “snowball effect.” We evaluated the accumulation of quantitative trait loci (QTL) between species in the plant group *Solanum* and found evidence for a faster-than-linear accumulation of hybrid seed sterility QTL, thus empirically evaluating and confirming this theoretical prediction. In comparison, loci underlying traits unrelated to hybrid sterility show no evidence for an accelerating rate of accumulation between species.

The Dobzhansky-Muller model of hybrid incompatibility [after (1, 2)] proposes that hybrid sterility and inviability are due to negative genetic interactions between two or more loci [commonly called “Dobzhansky-Muller incompatibilities” (DMIs)] that have accumulated substitutions in diverging lineages. When brought together in hybrids, alleles in each divergent lineage interact dysfunctionally, which results in reduced hybrid fitness (3). The action of DMIs is supported by empirical observation of the segregation of sterility in recombinant populations, and the molecular genetic

description of individual interacting loci underlying hybrid incompatibility phenotypes (4, 5). The Dobzhansky-Muller model (3, 6–9) has produced empirically testable predictions including the “snowball effect”—the number of DMIs accumulating between lineages is expected to “snowball” (increase faster than linearly) with increasing time since lineage divergence (3, 6). Formally, because DMIs are due to gene interactions (epistasis), the number of expected DMIs increases with the square of the number of substitutions differentiating two lineages, when DMIs are due to pairwise epistasis; DMIs due to interactions among more than two loci are expected to accumulate even faster (6). Previous attempts to detect the snowball effect by measuring the strength of reproductive isolation between lineages, rather than the number of genes involved, have failed to find a greater-than-linear

increase in sterility over time (10–12). However, testing this theoretical prediction requires information on the number of DMIs contributing to specific isolating barriers among multiple closely related species, rather than simply their phenotypic effects on hybrid sterility (3, 6).

To evaluate the expected snowball of DMIs, we used data from three quantitative trait loci (QTL) mapping experiments among species in the plant genus *Solanum* (13–15). Each QTL experiment used a unique library of hybrid introgression lines [near-isogenic lines (NILs)] in which all or most of the genome of a wild (undomesticated) *Solanum* species (*Solanum pennellii*, *Solanum habrochaites*, or *Solanum lycopersicoides*) was represented as short individual chromosomal regions serially introgressed into the genetic background of domesticated tomato (*Solanum lycopersicum*). These three experiments are comparable in the mean and distribution of hetero-specific introgression sizes and the generations of crossing used to create the lines, and they have similar statistical power for detecting pollen and seed sterility QTL (Table 1) (15). Each experiment identified the number, genomic location, and phenotypic effect-size of chromosomal regions associated with two separate postzygotic sterility phenotypes (pollen sterility and seed sterility) acting between two species (15). In each population, we also analyzed morphological traits unrelated to hybrid sterility (fruit shape and size of fertile seeds) as an internal control. As a proxy for time since lineage splitting, we estimated pairwise species molecular divergence as the number of synonymous substitutions per synonymous site ( $K_s$ ) at six unlinked loci distributed throughout the genome (15).

<sup>1</sup>Department of Biology, Indiana University, Bloomington, IN 47405, USA. <sup>2</sup>University of Memphis, Memphis, TN 38152, USA.

\*To whom correspondence should be addressed. E-mail: lmoyle@indiana.edu



0.242, SEM =  $8.17 \times 10^{-4}$ ). To establish whether the observed data fulfill theoretical expectations, we calculated the expected number of incompatibilities under two models: one in which incompatibilities accumulated linearly with the number of substitutions (i.e., absence of a snowball effect, which could reflect reproductive isolation caused by nonepistatic factors such as accumulated chromosomal rearrangements), and a model

in which the expected number of incompatibilities was proportional to the square of the total number of DNA substitutions (i.e., the presence of a snowball effect involving two-locus interactions). In these calculations we included viability data only for deficiency stocks tested in both sets of crosses (65 incompatibilities in the *mel* × *san* cross and 10 in the *mel* × *sim* cross). To determine which model was more likely to explain the data,

we used the AIC [Akaike Information Criterion (21)] scores of each model and calculated the evidence ratio of Akaike weights for the quadratic model over the linear model. These scores were then converted to the normalized probability that the quadratic model is preferred over the linear model (21).  
The *Ks* values, the observed number of incompatibilities, the expected number of incom-

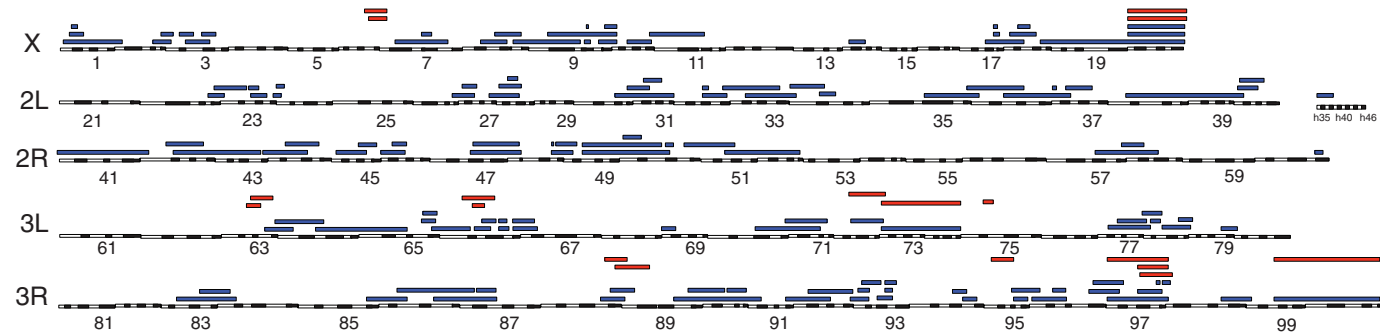


**Fig. 2.** Chromosomal locations of hybrid lethal regions (on a *D. melanogaster* cytological map) for *D. melanogaster* × *D. santomea* and *D. melanogaster* × *D. simulans* crosses. All lethal regions detected contain at least one gene involved in an epistatic interaction between a recessive

element in the *D. santomea* (or *D. simulans*) genome and one or more dominant or semidominant factors in the *D. melanogaster* genome. Regions reducing viability in *mel/san* hybrids are shown in blue; those in *mel/sim* hybrids in red.

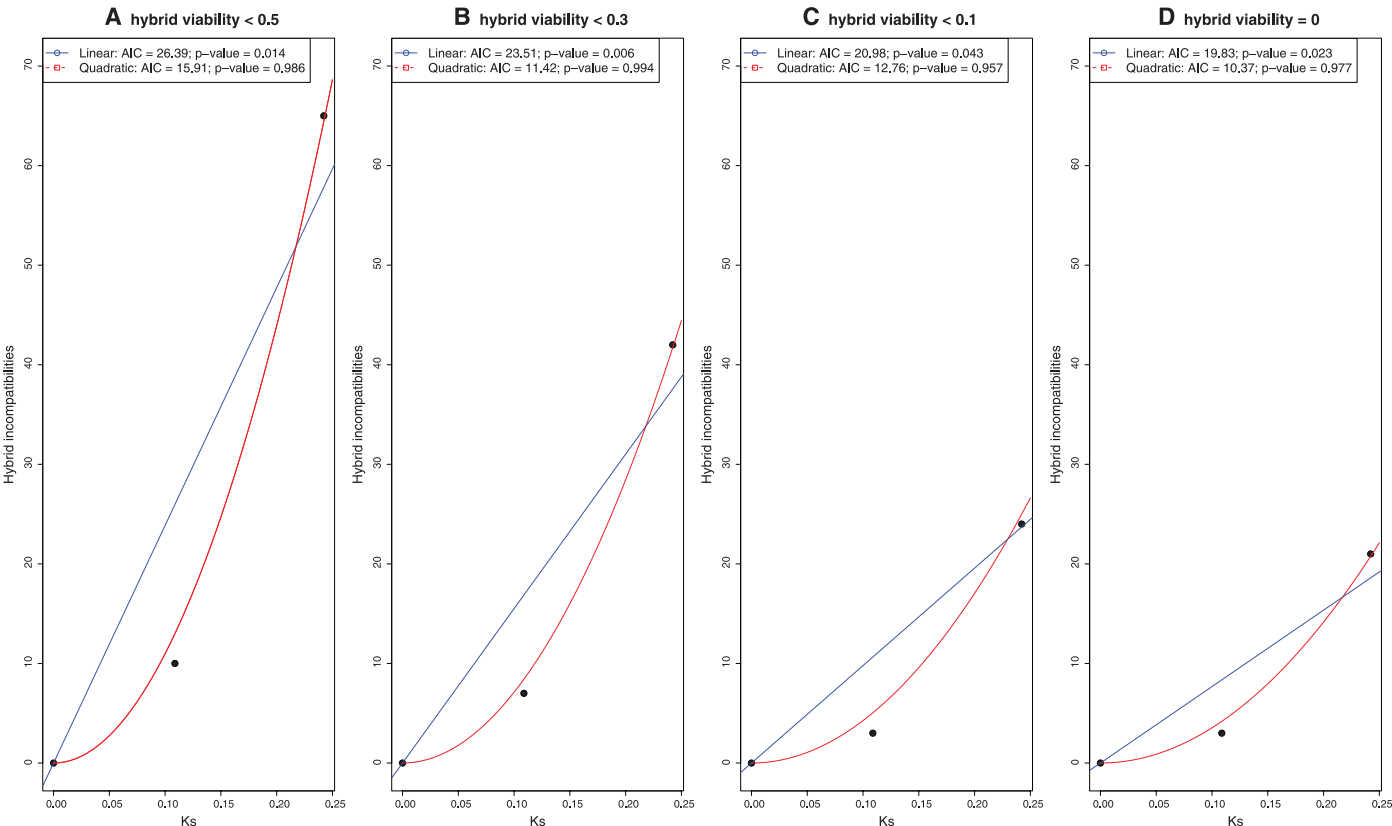


**Fig. 3.** Number of observed and expected hybrid incompatibilities in *san/mel* and *sim/mel* *F*<sub>1</sub> female hybrids. We fitted the linear and quadratic model that had lowest AIC values and forced the models through the origin (the assumption here is that at time zero, when there are no genetic substitutions between populations, there are no incompatibilities). *P* values are the normalized probability that each model is to be preferred over the other one (e.g., the quadratic

model is to be preferred over the linear model and vice versa) according to the evidence ratio of Akaike weights. Deviations are highly significant for the linear model but not for the quadratic model, regardless of how we quantify “viability”; and in all cases the quadratic model explains the data better than the linear model. Different panels represent the four different definitions of “inviability”: (A) Lower than 0.5; (B) lower than 0.3; (C) lower than 0.1; and (D) equal to 0.

patibilities, and the results for all the model comparisons are shown in Fig. 3. These data show that the number of incompatibilities does not accumulate linearly with divergence time and is more consistent with a quadratic increase, as expected if the evolution of those incompatibilities obeys the snowball effect. This result holds regardless of which estimate of divergence time we use (Fig. 1 and figs. S1 to S3). We thus conclude that hybrid incompatibilities between these species accumulate substantially faster than linearly with respect to their divergence time.

In addition to fitting the linear and quadratic models to regions that caused a relative viability lower than 0.5, we used more stringent criteria for inviability, fitting the two models to regions that showed relative viabilities lower than 0.3, 0.1, and 0. The results were similar in all cases (Fig. 1 and figs. S1 to S3) and revealed that, regardless of their size, deleterious epistatic interactions accumulate faster than linearly with divergence time.

Besides counting incompatibilities, our results can be used to identify and isolate genes causing reproductive isolation between species. Deletion mapping in *D. melanogaster*/*D. simulans* hybrids has identified two “hybrid inviability” genes with

function in nuclear transport and whose divergence occurred via natural selection (6, 8, 22).

By confirming a key prediction of the DM theory and showing a snowball effect of the accumulation of genetic incompatibilities causing reproductive isolation, we support the view that postzygotic reproductive isolation often results from deleterious interactions in hybrids between genes that behave normally within species.

#### References and Notes

1. T. Dobzhansky, *Genetics and the Origin of Species* (Columbia Univ. Press, New York, 1937).
2. J. A. Coyne, H. A. Orr, *Speciation* (Sinauer Associates, Sunderland, MA, 2004).
3. H. J. Muller, *Biol. Symp.* **6**, 71 (1942).
4. D. C. Presgraves, *Curr. Biol.* **17**, R125 (2007).
5. N. Phadnis, H. A. Orr, *Science* **323**, 376 (2009).
6. D. C. Presgraves, *Genetics* **163**, 955 (2003).
7. N. J. Brideau *et al.*, *Science* **314**, 1292 (2006).
8. S. Tang, D. C. Presgraves, *Science* **323**, 779 (2009).
9. S. Gourbière, J. Mallet, *Evolution* **64**, 1 (2010).
10. N. Johnson, in *Evolutionary Genetics: Concepts and Case Studies*, C. W. Fox and J. B. Wolf, Eds. (Oxford Univ. Press, New York, 2006), pp. 374–386.
11. H. A. Orr, *Genetics* **139**, 1805 (1995).
12. H. A. Orr, M. Turelli, *Evolution* **55**, 1085 (2001).
13. L. C. Moyle, T. Nakazato, *Genetics* **179**, 1437 (2008).
14. D. I. Bolnick, T. J. Near, *Evolution* **59**, 1754 (2005).
15. L. C. Moyle, B. A. Payseur, *Trends Ecol. Evol.* **24**, 591 (2009).
16. J. A. Coyne, S. Simeonidis, P. Rooney, *Genetics* **150**, 1091 (1998).
17. D. R. Matute, I. A. Butler, J. A. Coyne, *Cell* **139**, 1180 (2009).
18. Materials and methods are available as supporting materials on Science Online.
19. K. Tamura, S. Subramanian, S. Kumar, *Mol. Biol. Evol.* **21**, 36 (2004).
20. W. H. Li, *J. Mol. Evol.* **36**, 96 (1993).
21. K. P. Burnham, D. R. Anderson, *Model Selection and Multimodel Inference: A Practical Information-Theoretic Approach* (Springer, New York, 2002).
22. D. C. Presgraves, L. Balagopal, S. M. Abmayr, H. A. Orr, *Nature* **423**, 715 (2003).
23. We thank D. C. Presgraves, T. D. Price, R. Unckless, D. Kennedy, M. A. Sprigge, and M. Przeworski for discussions and reading of the manuscript; P. Andolfatto, T. Hu, and K. Thornton for sharing data; and A. Harris and J. Gladstone for technical help. Funded by NIH grant R01GM058260 (J.A.C.).

#### Supporting Online Material

www.sciencemag.org/cgi/content/full/329/5998/1518/DC1  
Materials and Methods

Figs. S1 to S3

Tables S1 to S4

References

8 June 2010; accepted 27 July 2010

10.1126/science.1193440

## Hybrid Incompatibility “Snowballs” Between *Solanum* Species

Leonie C. Moyle<sup>1</sup> and Takuya Nakazato<sup>1,2</sup>

Among the reproductive barriers that can isolate species, hybrid sterility is frequently due to dysfunctional interactions between loci that accumulate between differentiating lineages. Theory describing the evolution of these incompatibilities has generated the prediction, still empirically untested, that loci underlying hybrid incompatibility should accumulate faster than linearly with time—the “snowball effect.” We evaluated the accumulation of quantitative trait loci (QTL) between species in the plant group *Solanum* and found evidence for a faster-than-linear accumulation of hybrid seed sterility QTL, thus empirically evaluating and confirming this theoretical prediction. In comparison, loci underlying traits unrelated to hybrid sterility show no evidence for an accelerating rate of accumulation between species.

The Dobzhansky-Muller model of hybrid incompatibility [after (1, 2)] proposes that hybrid sterility and inviability are due to negative genetic interactions between two or more loci [commonly called “Dobzhansky-Muller incompatibilities” (DMIs)] that have accumulated substitutions in diverging lineages. When brought together in hybrids, alleles in each divergent lineage interact dysfunctionally, which results in reduced hybrid fitness (3). The action of DMIs is supported by empirical observation of the segregation of sterility in recombinant populations, and the molecular genetic

description of individual interacting loci underlying hybrid incompatibility phenotypes (4, 5). The Dobzhansky-Muller model (3, 6–9) has produced empirically testable predictions including the “snowball effect”—the number of DMIs accumulating between lineages is expected to “snowball” (increase faster than linearly) with increasing time since lineage divergence (3, 6). Formally, because DMIs are due to gene interactions (epistasis), the number of expected DMIs increases with the square of the number of substitutions differentiating two lineages, when DMIs are due to pairwise epistasis; DMIs due to interactions among more than two loci are expected to accumulate even faster (6). Previous attempts to detect the snowball effect by measuring the strength of reproductive isolation between lineages, rather than the number of genes involved, have failed to find a greater-than-linear

increase in sterility over time (10–12). However, testing this theoretical prediction requires information on the number of DMIs contributing to specific isolating barriers among multiple closely related species, rather than simply their phenotypic effects on hybrid sterility (3, 6).

To evaluate the expected snowball of DMIs, we used data from three quantitative trait loci (QTL) mapping experiments among species in the plant genus *Solanum* (13–15). Each QTL experiment used a unique library of hybrid introgression lines [near-isogenic lines (NILs)] in which all or most of the genome of a wild (undomesticated) *Solanum* species (*Solanum pennellii*, *Solanum habrochaites*, or *Solanum lycopersicoides*) was represented as short individual chromosomal regions serially introgressed into the genetic background of domesticated tomato (*Solanum lycopersicum*). These three experiments are comparable in the mean and distribution of hetero-specific introgression sizes and the generations of crossing used to create the lines, and they have similar statistical power for detecting pollen and seed sterility QTL (Table 1) (15). Each experiment identified the number, genomic location, and phenotypic effect-size of chromosomal regions associated with two separate postzygotic sterility phenotypes (pollen sterility and seed sterility) acting between two species (15). In each population, we also analyzed morphological traits unrelated to hybrid sterility (fruit shape and size of fertile seeds) as an internal control. As a proxy for time since lineage splitting, we estimated pairwise species molecular divergence as the number of synonymous substitutions per synonymous site ( $K_s$ ) at six unlinked loci distributed throughout the genome (15).

<sup>1</sup>Department of Biology, Indiana University, Bloomington, IN 47405, USA. <sup>2</sup>University of Memphis, Memphis, TN 38152, USA.

\*To whom correspondence should be addressed. E-mail: lmoyle@indiana.edu



**Table 1.** Experimental details of three *Solanum* QTL mapping experiments.  $K_s$  is synonymous site divergence between species; genome coverage is the percentage of the wild species' genome represented in introgression lines; gens of crossing are the number of generations of crossing used to generate lines; introgression lengths are the mean and range of heterospecific

introgression sizes, in centimorgans (cM) and as a percentage of the donor species genome (% genome);  $n$  is the experimental population size; min. detectable effect size is the average minimum detectable standardized effect size [ $d$  (22)], across all four traits (SSS, PF, FSH, and SSZ) for each experiment (15).

Species pair	$K_s$	Genome coverage (%)	Gens of crossing	No. of NILs analyzed	Introgression lengths (cM)		$n$	Min. detectable effect size
					Mean (% genome)	Range (% genome)		
<i>S. lycopersicum</i> – <i>S. pennellii</i>	0.0277	98.2	7–10	71	25 (1.98)	2.3–57.2 (0.18–4.54)	382	1.987
<i>S. lycopersicum</i> – <i>S. habrochaites</i>	0.0329	82.4–85.0	5–6	71	48.5 (4.0)	4.5–135.0 (0.35–10.7)	243	2.820
<i>S. lycopersicum</i> – <i>S. lycopersicoides</i>	0.0663	64.2–84.2	7–11	40	42.4 (3.4)	7.5–124.7 (0.61–10.1)	251	1.996

To evaluate evidence for the nonlinear accumulation of DMIs, we compared regression models describing linear and nonlinear relations between molecular divergence (time since lineage splitting) and the minimum number of sterility QTLs observed between species pairs (Fig. 1). Under the snowball prediction, there should be a greater-than-linear increase in DMIs with increasing molecular divergence between species pairs. We evaluated the relative goodness of fit of linear ( $y = a_1x$ ), and two different quadratic models (quad1:  $y = a_1x + a_2x^2$ ; quad2:  $y = a_1x^2$ ) (Table 2). The last two models are nonlinear and consistent with the snowball prediction; we evaluated both because the exact form of nonlinear accumulation can vary with the complexity of gene interactions underlying DMIs [e.g., pairwise versus greater than pairwise (6)], which is not known in this or any other empirical system. Models were evaluated separately for pollen and seed sterility isolating barriers. All models were forced through the origin, because taxa that do not differ by any molecular substitutions are not expected to have accumulated any reproductive isolation loci. Because linear and quad1 models are hierarchically nested, we compared them with parametric statistics; linear and quad2 models were compared with the Akaike Information Criterion (AIC) (15).

For seed sterility, we detected significantly greater-than-linear accumulation of hybrid sterility loci, consistent with a snowball effect. This was true regardless of whether a linear model was compared with either quadratic fit (Table 2). In comparison, a linear model outperformed both nonlinear fits for pollen sterility data (Table 2); therefore, our analysis did not support an accelerating increase in DMI accumulation over time for pollen sterility as an isolating barrier.

The snowball prediction applies specifically to traits determined by epistatic interactions. However, many trait differences between species are not expected to be invariably epistatic; rather, they often contribute additively to interspecific differentiation (16). As such, the accumulation of loci for postzygotic isolation versus nonisolation traits can also be used to assess the unique nonlinearity expected for postzygotic isolation. We assessed the pattern of accumulation

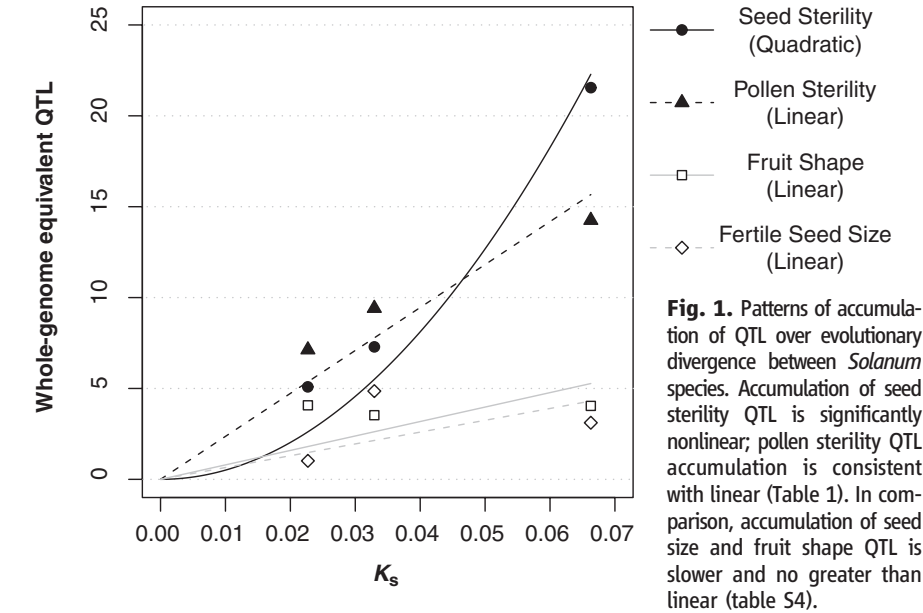


**Fig. 1.** Patterns of accumulation of QTL over evolutionary divergence between *Solanum* species. Accumulation of seed sterility QTL is significantly nonlinear; pollen sterility QTL accumulation is consistent with linear (Table 1). In comparison, accumulation of seed size and fruit shape QTL is slower and no greater than linear (table S4).

**Table 2.** Linear versus nonlinear models for the accumulation of hybrid incompatibility and other QTL between *Solanum* species. SSS, self seed set (seed sterility); PF, pollen fertility (arcsine square-root transformed); FSH, fruit shape; SSZ, fertile seed size. Model comparison 1: linear and quad1 ( $y = a_1x + a_2x^2$ ) models were compared using Zar Eq. 21.4 (23). Where  $P < 0.05$ , the more complex (quadratic) model provides a significantly better fit. Model comparison 2: linear and quad2 ( $y = ax^2$ ) models were compared by using AIC (24); the model that minimizes the AIC is considered the better fit [see (15)]. For results from least-squares regressions for each model (linear, quad1, and quad2) see table S4.

Trait	Model comparison 1: $y = a_1x$ vs. $y = a_1x + a_2x^2$		Model comparison 2: $y = a_1x$ vs. $y = a_1x^2$	
	$F$	$P$ value	AIC (linear)	AIC (exp.)
<i>Isolation QTL</i>				
SSS	345.03	0.0342*	6.2709	5.5647*
PF	13.99	0.1663	4.8492	11.0081
<i>Morphological QTL</i>				
FS	2.29	0.3717	4.7431	7.4321
SSZ	1.94	0.3964	5.2956	7.0262

\*Results indicating better fit for nonlinear model.

of fruit shape (FSH) and seed size (of fertile seeds; SSZ) between the same species pairs. In both cases, we found no evidence for an accelerating accumulation of QTL contributing to species trait differences; for seed size, we also found no evi-

dence for a linear accumulation over time (15). In comparison with sterility traits, therefore, loci for “normal” interspecific quantitative trait differences do not appear to snowball with evolutionary time (Fig. 1).

Although we identified the signal of a snowball effect, it was significant only for seed sterility. The failure to detect a snowball for pollen sterility could be due to several, nonexclusive contributing factors, which we currently cannot differentiate (15). For example, DMIs for pollen sterility might accumulate noncombinatorially [unlike in Orr's (3) original snowball model], which could result in a more linear relation between the number of DMIs and the time since divergence. This could occur, for example, if substitutions contributing to pollen sterility DMIs over time were not independent of each other, as might happen if isolating barriers evolve as the result of genetic conflicts (17). Alternatively, an attenuated snowball for pollen sterility could be due to bias against QTL detection in the cross with the greatest genetic distance, and/or rate heterogeneity in the accumulation of sterility loci (15). Finally, if there is a systematic difference in the complexity of genetic interactions underlying male versus female hybrid sterility, we may have differing abilities to detect them with our introgression line approach, which can detect DMIs due to pairwise epistatic interactions but not DMIs requiring more than one chromosomal segment from each species, i.e., multilocus interactions (4, 15). Current data, although sparse, suggest that DMIs responsible for male sterility might frequently be due to complex multilocus interactions (18–20). In *Solanum*, hybrid introgression lines show progressively more pollen sterility depending on whether they carry one, two, or three conspecific introgressions from the donor species, which suggests that multilocus interactions

are necessary for the expression of some hybrid pollen sterility (21); there is no equivalent increase in seed sterility with number of conspecific introgressions.

Overall, our results indicate that the accumulation of sterility loci follows a different trajectory from the accumulation of loci for other quantitative species differences (Fig. 1), consistent with the unique genetic basis expected to underpin species reproductive isolating barriers. Our analysis examines the accumulation of loci contributing to individually evaluated hybrid sterility traits (pollen sterility and seed sterility); therefore, we explicitly evaluate the accumulation of genetic loci rather than sterility phenotypes, and we do not conflate the accumulation of loci underlying genetically and developmentally distinct isolating barriers [for example, by examining the accumulation of both male and female sterility as a single “total isolation” phenotype (12)]. In doing so, we uncover direct empirical support for the Dobzhansky-Muller model of hybrid incompatibility, and the snowball prediction in particular.

#### References and Notes

1. T. Dobzhansky, *Genetics* **21**, 113 (1936).
2. H. J. Muller, *Biol. Symp.* **6**, 71 (1942).
3. H. A. Orr, *Genetics* **139**, 1805 (1995).
4. J. A. Coyne, H. A. Orr, *Speciation* (Sinauer Associates, Sunderland, MA, 2004).
5. D. C. Presgraves, *Nat. Rev. Genet.* **11**, 175 (2010).
6. H. A. Orr, M. Turelli, *Evolution* **55**, 1085 (2001).
7. M. Turelli, H. A. Orr, *Genetics* **154**, 1663 (2000).
8. A. S. Kondrashov, *Evolution* **57**, 151 (2003).
9. M. Turelli, L. C. Moyle, *Genetics* **176**, 1059 (2007).

10. T. C. Mendelson, B. D. Inouye, M. D. Rausher, *Evolution* **58**, 1424 (2004).
11. N. A. Johnson, in *Evolutionary Genetics, Concepts and Case Studies*, C. W. Fox, J. B. Wolf, Eds. (Oxford Univ. Press, Oxford, 2006), pp. 374–386.
12. S. Gourbière, J. Mallet, *Evolution* **64**, 1 (2010).
13. L. C. Moyle, E. B. Graham, *Genetics* **169**, 355 (2005).
14. L. C. Moyle, T. Nakazato, *Genetics* **179**, 1437 (2008).
15. Materials and methods are available as supporting material on Science Online.
16. T. F. C. Mackay, E. A. Stone, J. F. Ayroles, *Nat. Rev. Genet.* **10**, 565 (2009).
17. R. Unckless, University of Rochester, personal communication.
18. E. L. Cabot, A. W. Davis, N. A. Johnson, C.-I. Wu, *Genetics* **137**, 175 (1994).
19. Y. Tao, Z. B. Zeng, J. Li, D. L. Hartl, C. C. Laurie, *Genetics* **164**, 1399 (2003).
20. A. S. Chang, M. A. F. Noor, *Evolution* **64**, 253 (2010).
21. L. C. Moyle, E. B. Graham; SBE Tri-National Young Investigators, *Mol. Biol. Evol.* **23**, 973 (2006).
22. J. Cohen, *Statistical Power Analysis for the Behavioral Sciences* (Erlbaum Associates, Hillsdale, NJ, 1988).
23. J. H. Zar, *Biostatistical Analysis* (Prentice-Hall, Englewood Cliffs, NJ, ed. 2, 1984).
24. K. P. Burnham, D. R. Anderson, *Model Selection and Multimodel Inference: A Practical Information-Theoretic Approach* (Springer, New York, ed. 2, 2002).
25. M. Fryska, E. Graham, E. Lines, and K. Wolt contributed to collection of the data. C. Muir drew Figure 1. M. Hahn, C. Muir, and M. Turelli provided comments on the manuscript. Supported by National Science Foundation grants DEB-0532097 and DEB-0849157 (LCM).

#### Supporting Online Material

www.sciencemag.org/cgi/content/full/329/5998/1521/DC1

Materials and Methods

Tables S1 to S5

References

1 June 2010; accepted 27 July 2010

10.1126/science.1193063

## The Ecological Significance of Tool Use in New Caledonian Crows

Christian Rutz,<sup>1\*</sup> Lucas A. Bluff,<sup>1†</sup> Nicola Reed,<sup>2†</sup> Jolyon Troschianko,<sup>3</sup> Jason Newton,<sup>4</sup> Richard Inger,<sup>2</sup> Alex Kacelnik,<sup>1</sup> Stuart Bearhop<sup>2</sup>

Tool use is so rare in the animal kingdom that its evolutionary origins cannot be traced with comparative analyses. Valuable insights can be gained from investigating the ecological context and adaptive significance of tool use under contemporary conditions, but obtaining robust observational data is challenging. We assayed individual-level tool-use dependence in wild New Caledonian crows by analyzing stable isotope profiles of the birds' feathers, blood, and putative food sources. Bayesian diet-mixing models revealed that a substantial amount of the crows' protein and lipid intake comes from prey obtained with stick tools—wood-boring beetle larvae. Our calculations provide estimates of larva-intake rates and show that just a few larvae can satisfy a crow's daily energy requirements, highlighting the substantial rewards available to competent tool users.

New Caledonian crows (*Corvus moneduloides*) (hereafter NC crows) use tools for extractive foraging (1, 2). Controlled experiments with captive-bred, juvenile NC crows have recently shown that basic stick tool use is heritable, and hence an evolved adaptation (3). Although we can only speculate about the selective pressures that fostered the evolution of

tool use in NC crows, it is possible to investigate quantitatively how this behavior is maintained under contemporary ecological conditions.

Very little is currently known about the general foraging ecology of NC crows, or the ecological context of their tool use, because of the difficulty of observing wild, free-ranging subjects in their tropical habitats (4, 5). However, long-

term fieldwork has revealed that NC crows exploit two potentially nutritious food sources provided by candlenut trees (*Aleurites moluccana*; Euphorbiaceae): nuts and wood-boring longhorn beetle larvae (*Agrianome fairmairei*; Cerambycidae). In areas where these trees grow, NC crows crack their nuts by dropping them onto hard surfaces (6), and they use stick tools to probe for larvae in decaying, beetle-infested trunks (5, 7). The larva-extraction technique of NC crows relies on exploiting defensive responses of their prey, similar to the well-known “termite fishing” of chimpanzees (8). Crows insert a twig or leaf stem into a burrow, “teasing” the larva by repeatedly poking it with the tool until it bites the tip of the tool with its powerful mandibles and can be levered out (fig. S1 and

<sup>1</sup>Department of Zoology, University of Oxford, South Parks Road, Oxford OX1 3PS, UK. <sup>2</sup>Centre for Ecology and Conservation, School of Biosciences, University of Exeter, Cornwall Campus, Penryn, Cornwall TR10 9EZ, UK. <sup>3</sup>School of Biosciences, University of Birmingham, Birmingham B15 2TT, UK. <sup>4</sup>Natural Environment Research Council (NERC) Life Sciences Mass Spectrometry Facility, Scottish Universities Environmental Research Centre, Rankine Avenue, East Kilbride G75 0QF, UK.

\*To whom correspondence should be addressed. E-mail: christian.rutz@zoo.ox.ac.uk  
†These authors contributed equally to this work.



movie S1) (5, 7). Using motion-triggered video cameras to observe the foraging behavior of wild NC crows at natural larva-fishing sites, we have previously reported [for sample footage, see movie S1; (5)] that (i) tool use indeed plays an important role in accessing this hidden food source (71% of all observed larva extractions by NC crows were immediately preceded by the use of a tool in the same hole; in all remaining cases, larvae were obtained without tools); (ii) extracting larvae with tools requires considerable skill (nutritionally independent, immature NC crows spent considerable time using tools, but were much less successful than local adults); and (iii) even proficient, adult birds take a substantial amount of time to obtain larvae, so this behavior is potentially costly. On this evidence, the proportion of beetle larvae in crow diets provides a

proxy measure of individual tool-use dependence, but assessing activity budgets and dietary composition for these shy forest birds has proved very difficult (4). Here, we used stable isotope techniques ( $\delta^{13}\text{C}$  and  $\delta^{15}\text{N}$ ) (9) to quantify diet composition in a large sample of subjects, and without the need for direct or remote observation of infrequent foraging events (4, 5). This approach, which is schematically illustrated in Fig. 1A, enabled us to examine the ecological significance of tool use in NC crows.

In our dry forest study site on the central west coast of New Caledonia (Gouaro-Déva), we sampled food items that NC crows were known to consume both here and elsewhere on the island (10). The birds' seven main food sources differed highly significantly in their mean isotope signatures [Fig. 1B;  $n = 66$  samples; general linear

models (GLMs):  $\delta^{15}\text{N}$  values,  $F_{6,59} = 100.48$ ,  $P < 0.0001$ ;  $\delta^{13}\text{C}$  values,  $F_{6,59} = 19.96$ ,  $P < 0.0001$ ; for the nutritional composition of food sources, see Fig. 2A and table S1]. Wood-boring beetle larvae were isotopically distinct from all other putative food sources on the  $\delta^{15}\text{N}$  axis ( $P \leq 0.0005$  for all post hoc comparisons), which was most likely a reflection of their unusual xylophagous foraging habits (cerambycid beetle species can hold nitrogen-fixing symbionts in their guts, which will tend to generate products with lower  $\delta^{15}\text{N}$  values).

Bird feathers are metabolically inert after formation and provide an isotopic snapshot of an individual's diet at the time when the keratinous tissue was synthesized (9, 11–13). For stable isotope analyses, we selected several feather types grown at different times in the moult cycle, there-

**Fig. 1.** Foraging ecology of wild New Caledonian (NC) crows. **(A)** Study rationale. NC crows consume a range of foods, but require tools to extract wood-boring beetle larvae from their burrows. These larvae, with their unusual diet, have a distinct isotopic signature that can be traced in the crows' feathers and blood. By comparing the stable isotope profiles of the crows' tissues with those of their putative food sources, the proportion of larvae in crow diet can be estimated, providing a proxy for individual-level tool-use dependence. **(B)** Isotope signatures ( $\delta^{13}\text{C}$  and  $\delta^{15}\text{N}$ ) of feathers (corrected for trophic enrichment; gray cross symbols, error bars represent uncertainty in trophic enrichment factors;  $n = 38$  feather samples for 9 juveniles,  $n = 33$  samples for 7 immatures,  $n = 28$  samples for 6 adults) and blood ( $n = 22$  crows; red cross symbols) from NC crows, and of samples of the birds' putative food sources (colored symbols, means with bidirectional SD;  $n = 66$  samples for 7 food sources). Beetle larvae, with their unusually low  $\delta^{15}\text{N}$  values, are isotopically distinct from all other food sources (for statistics, see main text). Crow tissues lie within the area delineated by the  $\delta^{13}\text{C}$  and  $\delta^{15}\text{N}$  values of the seven putative food sources, indicating adequate sampling of the birds' food base.

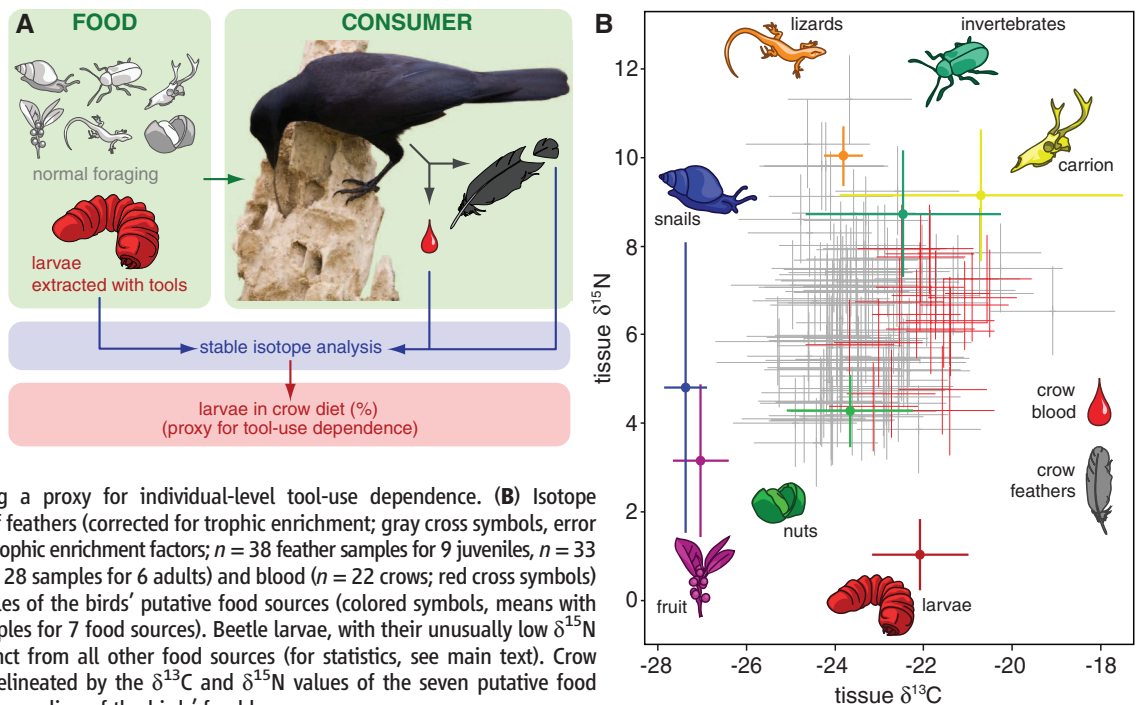
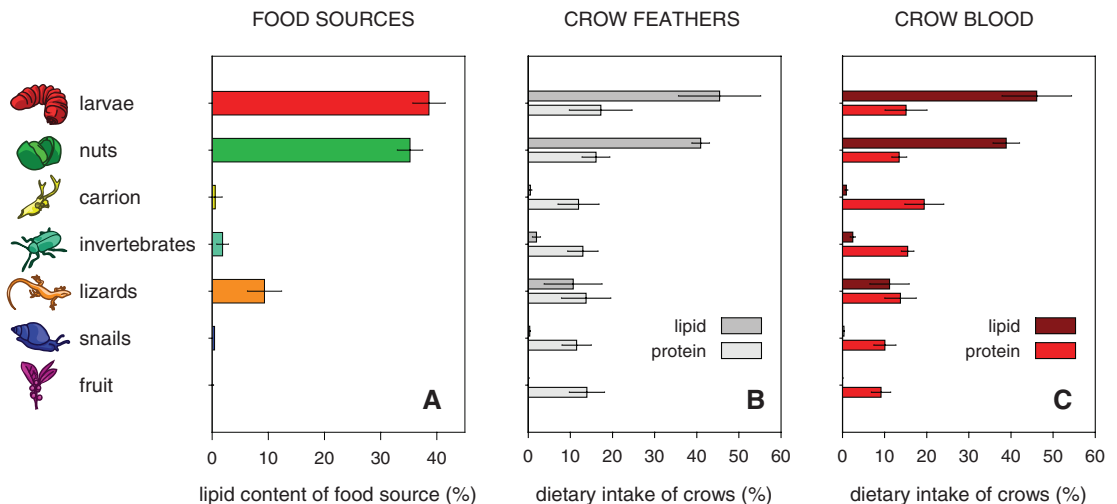


**Fig. 2.** Nutritional significance of seven different food sources for New Caledonian crows. **(A)** Average lipid content of food sources, as estimated through lipid extraction from food items (means  $\pm 1$  SD; color-coding is the same as in Fig. 1B). **(B)** Relative contribution of food sources to crow diet (means  $\pm 1$  SD), in terms of either lipid or protein intake [for details, see (10)], as estimated by Bayesian multiple source isotopic mixing models based on feather samples, and **(C)** blood samples. Sample sizes are the same as in Fig. 1B.



fore representing dietary intake over periods of several weeks to months (10). To obtain complementary estimates at shorter time scales, ranging from days to weeks, we also analyzed the isotopic composition of blood samples that had been taken at the time of trapping (10). With few exceptions, isotope ratios of individual NC crow feathers and blood samples [corrected for trophic enrichment; see (10)] lay within the area delineated by the  $\delta^{13}\text{C}$  and  $\delta^{15}\text{N}$  values of the seven putative food sources and their associated error distributions (Fig. 1B), suggesting that no important dietary components had been missed (10). Because beetle larvae were isotopically distinct from all other relevant food sources, they left a signature in crow tissues that we could use for estimating how much an individual bird relied on tool-assisted foraging (Fig. 1). To estimate diet composition of individual NC crows, we used a recently developed Bayesian multiple source isotopic mixing model (SIAR), which overcomes some limitations of earlier procedures (10, 14).

SIAR analyses revealed that beetle larvae contribute substantially to the diet of wild NC crows, with consistent results for both feather and blood samples (Fig. 2, B and C). Although larvae accounted roughly for the same amount of dietary protein intake (mean  $\pm$  SD; feathers:  $17.23 \pm 7.45\%$ ; blood:  $15.11 \pm 5.00\%$ ) as the other six putative food sources (Fig. 2, B and C), they had the highest lipid content of all foods examined (Fig. 2A;  $38.63 \pm 2.89\%$ ) and contributed disproportionately to the birds' overall lipid intake (feathers:  $45.43 \pm 9.76\%$ ; blood:  $46.13 \pm 8.26\%$ ). The second most important food source, in terms of joint protein and lipid contribution, was candlenuts, which crows crack at communal nut-dropping sites (see above).

To examine further the nutritional significance of beetle larvae for NC crows, we parameterized a simple energy-budget model with our empirical data on individual-level diet composition. The energy content of beetle larvae in our sample ranged from 100 kJ/g for the smallest larvae (width  $\times$  length, 1.0 cm by 3.8 cm) to 299 kJ/g for the largest specimens (1.6 cm by 7.6 cm). Using estimates of the daily energy requirements of NC crows (10), and of the proportion of beetle larvae in their diet (SIAR estimates), we could predict daily larva-consumption rates ( $n = 20$  crows for all estimates; body mass had not been measured for two subjects). Values ranged from  $8.59 \pm 1.74$  larvae (feather data, mean  $\pm$  SD; blood:  $8.72 \pm 1.95$  larvae) for a diet consisting entirely of the smallest larvae, which is highly unlikely, to  $0.55 \pm 0.11$  (blood:  $0.56 \pm 0.13$  larvae) for a diet consisting entirely of the largest larvae, with  $1.80 \pm 0.37$  (blood:  $1.83 \pm 0.41$  larvae) for a diet of mixed-sized larvae. In fact, only  $2.98 \pm 0.28$  larvae of mixed body size would be necessary to satisfy the entire daily energy requirements of an NC crow, illustrating the considerable energetic rewards available to efficient tool users. Sensitivity analyses for these calculations, using individual parameter perturbation (table S2), indicate robust

results for a large parameter space. Our estimates for average larva-intake rates seem comparatively high, but are ecologically plausible (given the high abundance of active larva-fishing sites in our study area at the time) and fall within the range of extrapolations from our video-surveillance data (5, 10, 15). Notably, although our estimates could be reduced if we had inadvertently missed a food source in our diet survey, we would expect the overall nutritional significance of tool use to remain qualitatively unchanged, given the exceptionally high lipid content of beetle larvae (Fig. 2A) and the comparatively even dietary protein contribution across all food sources (Fig. 2, B and C).

Our results suggest that these omnivorous birds use at least one component of their sophisticated tool-use behavior—the use of straight sticks as probes—to obtain a food source that contributes disproportionately to their overall dietary intake of protein and lipids [compare with (16)]. Larva-fishing in NC crows shows an unusual mode of ontogenetic development: Over at least the first 1 to 2 years postfledging, young crows spend much time using stick tools with little or no extraction success, and hence minimal food reinforcement and food intake (3, 5) (but young crows may still receive larvae from competent adults, as illustrated by our stable isotope data and direct observations; fig. S2). The present findings illustrate how the immediate energetic costs of learning complex tool-related skills can be offset by substantial future benefits, once crows have acquired full tool-use competence.

Our technique for assessing diet composition and tool-use dependence in NC crows circumvents laborious field observations (16–20) and enables data collection at the level of the individual subject on a range of temporal scales, from a few days to several months. This sets the scene for efficient, quantitative mapping of tool use within and among NC crow populations (that have access to candlenut trees), for example, to assess seasonal or regional variation in tool-use dependence (16). Larger sample sizes will also enable more detailed investigations of the potential fitness benefits of NC crow tool use. For example, analyses of our feather data have already indicated that NC crow parents may preferentially feed their offspring with tool-derived beetle larvae [ $n = 22$  crows; age-dependent variation in raw  $\delta^{15}\text{N}$  values, general linear mixed model:  $F_{2,19,0} = 4.38$ ,  $P = 0.027$ ; percentage larva contribution to diet, GLMs on arcsine-square-root transformed data: protein,  $F_{2,19} = 6.76$ ,  $P = 0.006$ ; lipid,  $F_{2,19} = 6.13$ ,  $P = 0.009$ ; for details, see (10, 21)]. With the accumulation of bigger longitudinal data sets, it may be feasible to investigate whether particularly proficient tool users, with their privileged access to larvae, produce offspring of superior body condition, and whether a larva-rich diet has lasting effects on future survival and reproduction.

At least in our study site, NC crows successfully exploit two foods provided by candlenut trees—beetle larvae and nuts. Candlenut trees are

thought to have originated in Malesia and were spread by humans throughout the Pacific in recent prehistory (22). In light of our findings, it seems possible that the anthropogenic introduction of this tree species to New Caledonia created foraging opportunities (i.e., lipid-rich, but hidden, larvae) that, presumably in combination with other factors, led to the rapid evolution of tool use in NC crows.

## References and Notes

- G. R. Hunt, R. D. Gray, *Acta Zool. Sinica* **52** (suppl.), 622 (2006).
- L. A. Bluff, A. A. S. Weir, C. Rutz, J. H. Wimpenny, A. Kacelnik, *Comp. Cogn. Behav. Rev.* **2**, 1 (2007).
- B. Kenward, A. A. S. Weir, C. Rutz, A. Kacelnik, *Nature* **433**, 121 (2005).
- C. Rutz, L. A. Bluff, A. A. S. Weir, A. Kacelnik, *Science* **318**, 765 (2007).
- L. A. Bluff, J. Troschianko, A. A. S. Weir, A. Kacelnik, C. Rutz, *Proc. R. Soc. B* **277**, 1377 (2010).
- G. R. Hunt, F. Sakuma, Y. Shibata, *Emu* **102**, 283 (2002).
- G. R. Hunt, *Emu* **100**, 109 (2000).
- J. Goodall, *Nature* **201**, 1264 (1964).
- R. Inger, S. Bearhop, *Ibis* **150**, 447 (2008).
- Materials and methods are available as supporting material on Science Online.
- K. A. Hobson, R. G. Clark, *Condor* **94**, 181 (1992).
- S. Bearhop, S. Waldron, S. C. Votier, R. W. Furness, *Physiol. Biochem. Zool.* **75**, 451 (2002).
- S. F. Pearson, D. J. Levey, C. H. Greenberg, C. Martínez Del Rio, *Oecologia* **135**, 516 (2003).
- A. C. Parnell, R. Inger, S. Bearhop, A. L. Jackson, *PLoS ONE* **5**, e9672 (2010).
- It is worth noting that the most competent, adult tool user according to our video data, a resident breeding male (HC4; 15 larvae extracted in a total of 80 min present at camera sites), had also by far the highest estimated proportion of larvae in its diet among adult crows, based on stable isotope analyses (in terms of protein intake: 23.1%; lipid intake: 52.8%; feather-based SIAR estimates; compare with Fig. 2B).
- S. Tebbich, M. Taborsky, B. Fessl, M. Dvorak, *Ecol. Lett.* **5**, 656 (2002).
- T. Nishida, M. Hiraiwa, *J. Hum. Evol.* **11**, 73 (1982).
- G. Yamakoshi, *Am. J. Phys. Anthropol.* **106**, 283 (1998).
- C. Boesch, H. Boesch-Achermann, *The Chimpanzees of the Tai Forest* (Oxford Univ. Press, Oxford, 2000).
- J. Mann *et al.*, *PLoS ONE* **3**, e3868 (2008).
- Our feather analyses indicated significant age-dependent variation in raw  $\delta^{15}\text{N}$  values and beetle-larva intake (for statistics, see main text), with juvenile crows consuming more larvae (mean  $\pm$  SE; protein,  $22.8 \pm 2.1\%$ ; lipid,  $52.2 \pm 2.3\%$ ) than both immature ( $14.6 \pm 2.0\%$ ;  $43.1 \pm 3.1\%$ ) and adult birds ( $12.0 \pm 2.5\%$ ;  $38.0 \pm 3.8\%$ ). This suggests that parents preferentially feed their offspring with tool-derived food of particularly high energy content, indicating that competent tool users enjoy direct fitness benefits. However, further work is required to corroborate this finding, as we did not observe the same pattern when analyzing blood samples (percentage larva contribution to diet, GLMs on arcsine-square-root transformed data: protein,  $F_{2,19} = 2.26$ ,  $P = 0.132$ ; lipid,  $F_{2,19} = 2.69$ ,  $P = 0.094$ ) [for further details, see (10)].
- A. C. Smith, *Euphorbiaceae. Flora Vitiensis Nova: A New Flora of Fiji* (Pacific Tropical Botanical Garden, Lawai, Hawaii, 1981), vol. 2.
- We thank N. Barré, S. Blancher, and J. Paimbou-Ayouma for logistical support in New Caledonia. Fieldwork was carried out with permissions from the Centre de Recherches sur la Biologie des Populations d'Oiseaux (France) and the Province Sud (New Caledonia), and was in accordance with the University of Oxford's procedures for local ethical review. We are grateful to M. Collett, I. Owens, B. Sheldon, and three referees for comments on the manuscript. The Edward Grey Institute of Field Ornithology (Oxford) kindly allowed



us to dry blood samples in one of their ovens. Supported by the Biotechnology and Biological Sciences Research Council (BBSRC) (BB/C517392/1 to A.K.; BB/G023913/1 to C.R.), the Cogito Foundation (R-120/07 to A.K.), NERC (NE/F021690/1 to S.B.), the Province Sud (New Caledonia; to C.R.), a Rhodes Scholarship (to L.A.B.), the University of Oxford (grant to C.R.), and a Junior Research Fellowship at Linacre College,

Oxford (to C.R.). C.R. is a BBSRC David Phillips Fellow and currently holds a Visiting Fellowship at the Evolution and Ecology Research Centre, University of New South Wales, Sydney.

#### Supporting Online Material

www.sciencemag.org/cgi/content/full/329/5998/1523/DC1  
Materials and Methods

Figs. S1 and S2  
Tables S1 and S2  
References  
Movie S1

10 May 2010; accepted 30 July 2010  
10.1126/science.1192053

# Structural Basis for Activation of Class Ib Ribonucleotide Reductase

Amie K. Boal,<sup>1</sup> Joseph A. Cotruvo Jr.,<sup>2</sup> JoAnne Stubbe,<sup>2,3\*</sup> Amy C. Rosenzweig<sup>1\*</sup>

The class Ib ribonucleotide reductase of *Escherichia coli* can initiate reduction of nucleotides to deoxynucleotides with either a  $\text{Mn}^{\text{III}}_2$ -tyrosyl radical ( $\text{Y}^\bullet$ ) or a  $\text{Fe}^{\text{III}}_2$ - $\text{Y}^\bullet$  cofactor in the NrdF subunit. Whereas  $\text{Fe}^{\text{III}}_2$ - $\text{Y}^\bullet$  can self-assemble from  $\text{Fe}^{\text{II}}_2$ -NrdF and  $\text{O}_2$ , activation of  $\text{Mn}^{\text{II}}_2$ -NrdF requires a reduced flavoprotein, NrdI, proposed to form the oxidant for cofactor assembly by reduction of  $\text{O}_2$ . The crystal structures reported here of *E. coli*  $\text{Mn}^{\text{II}}_2$ -NrdF and  $\text{Fe}^{\text{II}}_2$ -NrdF reveal different coordination environments, suggesting distinct initial binding sites for the oxidants during cofactor activation. In the structures of  $\text{Mn}^{\text{II}}_2$ -NrdF in complex with reduced and oxidized NrdI, a continuous channel connects the NrdI flavin cofactor to the NrdF  $\text{Mn}^{\text{II}}_2$  active site. Crystallographic detection of a putative peroxide in this channel supports the proposed mechanism of  $\text{Mn}^{\text{III}}_2$ - $\text{Y}^\bullet$  cofactor assembly.

Ribonucleotide reductases (RNRs) catalyze the reduction of nucleotides to deoxynucleotides in all organisms, providing the precursors required for DNA synthesis and repair (1). Class I RNRs are composed of two homodimeric subunits:  $\alpha 2$ , which contains the site of nucleotide reduction, and  $\beta 2$ , which contains a metal cofactor required to initiate catalysis in  $\alpha 2$ . Two class I RNRs are found in *Escherichia coli*. The class Ia enzyme supplies deoxynucleotides during normal aerobic growth. In many prokaryotes, including several important human pathogens, the class Ib RNR plays a similar role. The function of the class Ib RNR in *E. coli* is not clear, but it is expressed under iron-limited and oxidative stress conditions (2–4). The class Ia RNRs require a stable diferric-tyrosyl radical ( $\text{Fe}^{\text{III}}_2$ - $\text{Y}^\bullet$ ) cofactor generated from diferrous ( $\text{Fe}^{\text{II}}_2$ )  $\beta 2$  in the presence of  $\text{O}_2$  and a reductant. This process occurs in vitro by self-assembly (5) and in vivo by a biosynthetic pathway (6). By contrast, the identity of the metal cofactor in  $\beta 2$  of the class Ib RNRs (NrdF) has been controversial (7–10). Recent studies, however, have shown in vitro that both  $\text{Fe}^{\text{III}}_2$ - $\text{Y}^\bullet$  and dimanganese(III)- $\text{Y}^\bullet$  ( $\text{Mn}^{\text{III}}_2$ - $\text{Y}^\bullet$ ) cofactors are active in nucleotide reduction (7). Whereas the  $\text{Fe}^{\text{III}}_2$ - $\text{Y}^\bullet$  cofactor in NrdF can be formed by self-assembly from  $\text{Fe}^{\text{II}}$  and  $\text{O}_2$  (8, 9, 11), the  $\text{Mn}^{\text{III}}_2$ - $\text{Y}^\bullet$  cofactor can be generated from  $\text{Mn}^{\text{II}}_2$ -NrdF only in the presence of  $\text{O}_2$  and the flavodoxin-like protein NrdI (7).

We have recently shown that *E. coli*  $\text{Mn}^{\text{II}}_2$ -NrdF can form a complex with NrdI in vitro and in vivo and have proposed that reduced NrdI (NrdI<sub>h</sub>) in this complex generates hydroperoxyl anion ( $\text{HO}_2^-$ ), which channels to the metal site in NrdF (7). Two equivalents of  $\text{HO}_2^-$  would be required to generate the  $\text{Mn}^{\text{III}}_2$ - $\text{Y}^\bullet$  cofactor. In vitro support for this proposal is based on the observations that NrdI, in contrast to most flavodoxins, behaves as a two-electron reductant (11) and that neither  $\text{H}_2\text{O}_2$  nor  $\text{O}_2$  activates cofactor assembly (7, 8). Support in vivo is provided by the conservation of NrdI in all organisms containing a class Ib

RNR and by genetic studies showing that NrdI is essential for *Streptococcus pyogenes* class Ib RNR activity (12). Sequence alignments suggest that the *E. coli* system is representative of most class Ib RNRs, including those from *Corynebacterium ammoniagenes* and the human pathogens *Mycobacterium tuberculosis* and *S. pyogenes*.

The formation of two different active cofactors,  $\text{Fe}^{\text{III}}_2$ - $\text{Y}^\bullet$  and  $\text{Mn}^{\text{III}}_2$ - $\text{Y}^\bullet$ , in NrdF in vitro using the same protein ligands (two His, three Glu, and one Asp) to coordinate the metals (13), but different oxidants, raises the question of how this process is controlled in vivo. These same metal ligands are involved in Fe ligation in the class Ia RNR (14), which cannot form an active  $\text{Mn}^{\text{III}}_2$ - $\text{Y}^\bullet$  cofactor. Here we present the crystal structures of *E. coli* NrdF in the  $\text{Mn}^{\text{II}}_2$  and  $\text{Fe}^{\text{II}}_2$  forms, providing structural insight into how NrdF generates  $\text{Y}^\bullet$  from two different metal cofactors using two different oxidants. We also present structures of NrdF in complex with NrdI<sub>h</sub> and oxidized NrdI (NrdI<sub>ox</sub>). Reaction of the NrdI<sub>ox</sub>-NrdF complex in the crystal with 100 mM dithionite and  $\text{O}_2$  results in trapping of a small molecule best modeled as a peroxide in a channel linking the NrdI flavin to the NrdF metal site, supporting the proposed model of  $\text{Mn}^{\text{III}}_2$ - $\text{Y}^\bullet$  cofactor activation by oxidant channeling.

The 1.65 Å resolution (table S1) crystal structure (15) of  $\text{Mn}^{\text{II}}_2$ -NrdF contains one monomer

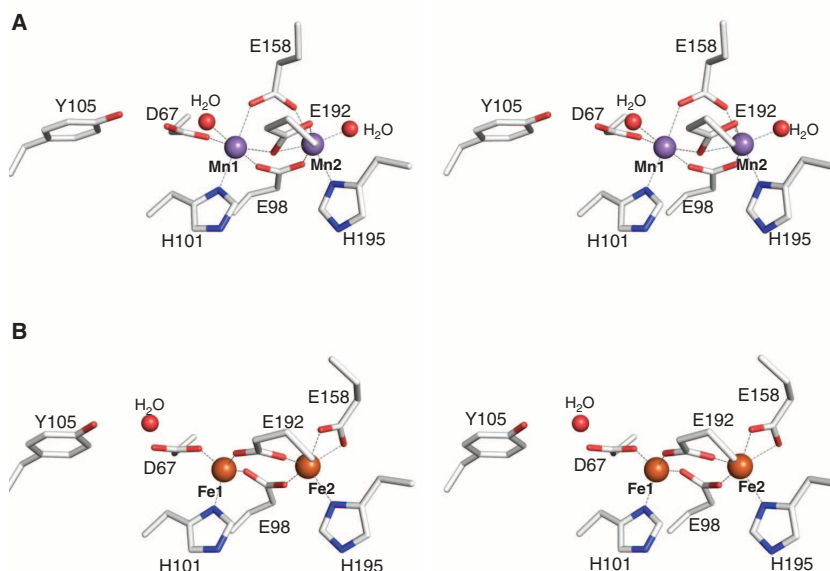


**Fig. 1.** Structures of  $\text{Mn}^{\text{II}}_2$ -NrdF and  $\text{Fe}^{\text{II}}_2$ -NrdF. (A) Stereoview of the  $\text{Mn}^{\text{II}}_2$ -NrdF active site.  $\text{Mn}^{\text{II}}$  ions are shown as purple spheres, water molecules are shown as red spheres, and NrdF side chains are represented in stick format and colored by atom type. (B) Stereoview of the  $\text{Fe}^{\text{II}}_2$ -NrdF active site.  $\text{Fe}^{\text{II}}$  ions, modeled at 0.5 occupancy, are shown as orange spheres. Metal-ligand interactions are highlighted with dashed lines.

<sup>1</sup>Departments of Biochemistry, Molecular Biology and Cell Biology, and Chemistry, Northwestern University, Evanston, IL 60208, USA. <sup>2</sup>Department of Chemistry, Massachusetts Institute of Technology, Cambridge, MA 02139, USA. <sup>3</sup>Department of Biology, Massachusetts Institute of Technology, Cambridge, MA 02139, USA.

\*To whom correspondence should be addressed. E-mail: stubbe@mit.edu (J.S.); amyr@northwestern.edu (A.C.R.)

per asymmetric unit with the other half of the dimer related by crystallographic symmetry. The overall fold closely resembles that of other class I  $\beta 2$  subunits (16) (fig. S1). Anomalous diffraction data are consistent with the presence of two fully occupied  $\text{Mn}^{\text{II}}$  sites (Fig. 1A and fig. S2) with a Mn-Mn distance of 3.7 Å. Mn1 is coordinated by His<sup>101</sup>, Asp<sup>67</sup>, and a terminal water molecule, and Mn2 is coordinated by His<sup>195</sup> and a terminal water molecule. Three glutamate residues (Glu<sup>98</sup>, Glu<sup>158</sup>, and Glu<sup>192</sup>) bridge the two metals in a manner previously not observed in RNRs and related carboxylate-bridged diiron enzymes (Fig. 1A and fig. S2) (17). Thus, each  $\text{Mn}^{\text{II}}$  is six-coordinate so ligand dissociation or reorganization, possibly via loss of the solvent molecule coordinated to Mn2 (17, 18), is necessary for reaction of the cluster with the oxidant. The non-coordinating side-chain oxygen atom of Asp<sup>67</sup> is hydrogen bonded to the hydroxyl group of Tyr<sup>105</sup>, the site of the stable Y•. A similar interaction is observed in the *E. coli* class Ia  $\text{Fe}^{\text{II}}_2$   $\beta 2$  structures (16). In the class Ib  $\text{Fe}^{\text{II}}_2$   $\beta 2$  structures, however, the interaction between Asp<sup>67</sup> and Tyr<sup>105</sup> is mediated by a water molecule. As a result, the Mn1-Tyr OH distance is 5.8 Å as compared to the Fe1-Tyr OH distances of *Salmonella typhimurium* NrdF (6.4 to 7.0 Å) (18), *C. ammoniagenes* NrdF (6.2 to 6.7 Å) (13), and *E. coli*  $\text{Fe}^{\text{II}}_2$ -NrdF (6.7 Å), which was determined to 1.9 Å resolution by soaking apo crystals of NrdF with  $\text{Fe}^{\text{II}}$  (table S1, Fig. 1B, and fig. S2) (19). The shorter Mn1-Tyr OH distance may be associated with the unusual electron paramagnetic resonance spectrum of the Mn-associated Y• relative to the Fe-associated Y• in NrdF (7).

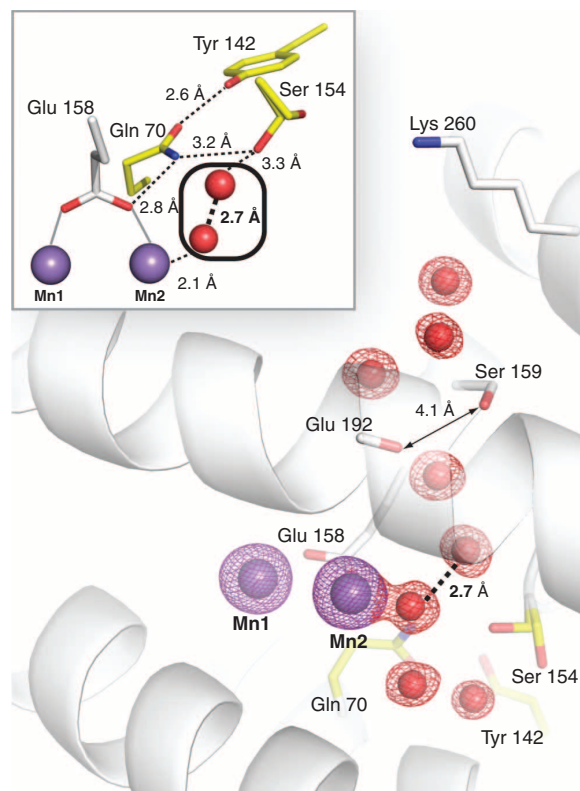
The two  $\text{Mn}^{\text{II}}$  ions are bridged by Glu<sup>98</sup> in a  $\mu$ -1,3 fashion and by Glu<sup>192</sup> in a  $\mu$ -( $\eta^1, \eta^2$ ) arrangement (Fig. 1A and fig. S2). The position of Glu<sup>192</sup> is similar to that observed for the equivalent ligand in the *E. coli* class Ia  $\beta 2$  structure obtained by soaking  $\text{Fe}^{\text{II}}$  into apo crystals (14). The most notable difference between  $\text{Mn}^{\text{II}}_2$ -NrdF and other  $\beta 2$  structures is the orientation of Glu<sup>158</sup>, which bridges the two  $\text{Mn}^{\text{II}}$  ions in a  $\mu$ -1,3 mode, rather than coordinating Fe2 or Mn2 in a monodentate or bidentate fashion (Fig. 1 and fig. S2). Glu<sup>158</sup> is in a short  $\pi$ -helical segment analogous to a conformationally flexible region observed in other  $\beta 2$ s and diiron enzymes and hypothesized to dictate access to the active site (18, 20, 21). The space occupied by the Glu<sup>158</sup> side chain in  $\text{Mn}^{\text{II}}_2$ -NrdF is occupied by two solvent molecules in  $\text{Mn}^{\text{II}}_2$ -NrdF: the coordinated water at Mn2 and a second water that links the coordinated water to the side chain of conserved residue Ser<sup>154</sup> (Figs. 1 and 2). Ser<sup>154</sup> is involved in a conserved hydrogen bonding network that connects Glu<sup>158</sup> to a solvent channel from the protein surface (Fig. 2). The channel opening is located near conserved residue Lys<sup>260</sup>. This channel is better suited to allow access to the metal site by a peroxide oxidant than the channel present in class Ia  $\beta 2$  structures, which is more hydrophobic, smaller, and less solvent exposed, and therefore more appropriate for O<sub>2</sub> passage (fig. S3). The ordered solvent and hydrogen bonding interactions may help constrain the unusual orientation of Glu<sup>158</sup> in  $\text{Mn}^{\text{II}}_2$ -NrdF. Moreover, the location of the two interacting solvent molecules at Mn2 could easily accommodate the proposed HO<sub>2</sub><sup>-</sup> oxidant (22)

(Fig. 2, inset). These waters may dissociate, allowing the oxidant to initially bind terminally to Mn2 in this position, by analogy to the proposal for H<sub>2</sub>O<sub>2</sub> binding to the structurally related Mn catalases (23). By contrast, in both class Ia (fig. S3) and Ib  $\text{Fe}^{\text{II}}_2$  structures, including  $\text{Fe}^{\text{II}}_2$ -NrdF (Fig. 1B), Glu<sup>158</sup> and Phe<sup>162</sup> create a hydrophobic pocket above the Fe2 site opposite His<sup>195</sup> (*E. coli* NrdF numbering), an ideal destination for O<sub>2</sub> before it reacts with the  $\text{Fe}^{\text{II}}_2$  site. This solvent channel likely represents the oxidant route to the metal cluster, and the environment near the active site may reflect different geometric or electrostatic requirements for correctly orienting O<sub>2</sub> and the putative HO<sub>2</sub><sup>-</sup> for reaction with their respective metal centers.

The complex between NrdI<sub>ox</sub> and  $\text{Mn}^{\text{II}}_2$ -NrdF (NrdI<sub>ox</sub>-NrdF) was crystallized and its structure determined to 2.5 Å resolution (table S2). Two NrdI and two NrdF molecules are present in the asymmetric unit (Fig. 3A and fig. S4). One NrdI protein is bound to each NrdF opposite the dimer interface and directly over the solvent-exposed channel to the active site. The location of the C-terminal NrdF residue in this complex (fig. S4) suggests that the NrdI and  $\alpha 2$  binding sites (24) are distinct. The NrdI-NrdF interface, which buries ~800 Å<sup>2</sup> surface area per chain, is largely hydrophobic, with several interprotein hydrogen bonds (fig. S5). The overall fold of NrdF is the same as in the  $\text{Mn}^{\text{II}}_2$ -NrdF structure, and the active site is nearly identical, including the unusual coordination mode of Glu<sup>158</sup> (fig. S6). NrdI adopts a typical flavodoxin-like fold (25), with the isoalloxazine ring of the flavin mononucleotide (FMN) cofactor near the protein surface and enclosed by two loop regions (Fig. 3B). One of these loops provides the closest positive charge on NrdI to the reactive C4a position of the flavin (Arg<sup>92</sup>), whereas the other, the glycine-rich “50s loop,” interacts with the N5 position and displays pronounced redox-dependent conformational changes (see below). The 50s loop comprises residues 50 to 56 (Gly-Thr-Ala-Gly), and as predicted (11), the amide nitrogen atom of Gly<sup>51</sup> is within hydrogen bonding distance of the flavin N5 atom, similar to what is observed in oxidized long-chain flavodoxins (26). The electron density for the NrdI 50s loop is not completely continuous, suggesting conformational flexibility.

The structure of the NrdI<sub>ox</sub>-NrdF complex reveals how NrdF contributes to the electrostatic environment of the FMN binding pocket. Typical flavodoxins carry out single electron transfers partly through destabilization of the reduced FMN, bound in the anionic form (FMN<sup>-</sup>, protonated at N5 and deprotonated at N1), by acidic residues proximal to the isoalloxazine ring (27). The FMN environment in NrdI is more positively charged (Arg<sup>92</sup> and Arg<sup>108</sup>), and in complex with NrdF, three additional charged residues from NrdF (Lys<sup>18</sup>, Arg<sup>25</sup>, and Arg<sup>190</sup>) are located within 12 Å of the FMN C4a position. The presence of positive charges near the O<sub>2</sub>-reactive C4a position is a conserved feature of flavoprotein oxidases, which

**Fig. 2.** The  $\text{Mn}^{\text{II}}_2$ -NrdF solvent-exposed active-site channel terminating at Mn2. A  $2F_o - F_c$  electron density map (red mesh, contoured at  $2\sigma$ ) shows ordered waters in the channel. The Mn anomalous difference Fourier map (purple mesh, contoured at  $12\sigma$ ) is also shown. Residues implicated in channel access are shown as white sticks, and a conserved hydrogen bonding network (illustrated with dashed lines in inset) linking ordered solvent in the channel to Mn2 ligand Glu<sup>158</sup> is shown as yellow sticks. Ser<sup>154</sup> is modeled in two separate rotamer conformations in  $\text{Mn}^{\text{II}}_2$ -NrdF, but in all NrdI-NrdF complex structures, it adopts the rotamer that points into the solvent channel.





reduce  $O_2$  to  $H_2O_2$  as part of their catalytic cycle (28), suggesting that electrostatics may play a similar role in NrdI to favor two-electron reduction of  $O_2$  to a peroxide oxidant.

Complex formation between NrdI and NrdF results in a 10 Å extension of the NrdF active-site channel along the NrdI-NrdF interface toward the flavin ring (Fig. 4A). Solvent access to the channel is prevented by NrdI Phe<sup>86</sup> and other hydrophobic and bulky residues near the flavin. Like the portion of the channel within NrdF, the interfacial region is lined with polar uncharged residues and backbone atoms. The side chains of NrdI residues Asn<sup>83</sup> (completely conserved) and Asn<sup>85</sup> (largely conserved) point into the channel. The position of the highly conserved Lys<sup>260</sup> in NrdF enforces a sharp turn in the channel, leading directly to the  $Mn^{II}_2$  site. Lys<sup>260</sup> is involved in a hydrogen bond network with the strictly conserved residues Tyr<sup>256</sup> and NrdI Glu<sup>110</sup> (figs. S5 and S7). The NrdF portion of the channel is lined by the side chains of Ser<sup>159</sup>, Tyr<sup>197</sup>, and Asn<sup>264</sup> (figs. S7 and S8). Approximately 7 Å from the  $Mn_2$  site, the channel constricts to 4.1 Å (Figs. 2 and 4). This constriction is formed by the carbonyl oxygen of bridging ligand Glu<sup>192</sup> and the side chain of Ser<sup>159</sup>, which follows in sequence space the unusual bridging ligand Glu<sup>158</sup>. Thus, the interactions that define this narrow point of the channel are intimately connected to the  $Mn^{II}_2$  coordination sphere.

As a first step toward investigating the NrdI-mediated activation of the NrdF metallocofactor on the molecular level, we determined two structures of reduced NrdI in complex with NrdF (table S2). For the first structure (NrdI<sub>hq</sub>-NrdF, 2.0 Å resolution), crystals were grown in the presence of 3 mM dithionite in an anaerobic chamber. These crystals were colorless, indicating that the flavin was reduced. For the second structure, which reveals a trapped species best modeled as peroxide (NrdI<sub>hq</sub>-NrdF<sub>perox</sub>, 2.35 Å resolution), NrdI<sub>ox</sub>-NrdF crystals were soaked in 100 mM dithionite outside the anaerobic chamber until the bright yellow color bleached (~2 min). Both structures reveal conformational changes near the FMNH<sup>-</sup> cofactor suggesting reduction of the flavin (Fig. 3C and fig. S9). The most pronounced change involves the NrdI 50s loop, which adopts a more open conformation exposing the isoalloxazine ring to solvent (Fig. 3C). Protonation of the flavin N5 concomitant with reduction breaks the N5 hydrogen bond with the amide nitrogen of Gly<sup>51</sup>, and the carbonyl oxygen of Gly<sup>50</sup> is positioned to accept a hydrogen bond from the FMNH<sup>-</sup> N5H. In addition, NrdF Arg<sup>25</sup> is oriented closer to C4a (6 Å) compared with the NrdI<sub>ox</sub>-NrdF complex, and in one NrdF monomer, it is hydrogen bonded to the backbone carbonyl of NrdI Gly<sup>50</sup>, perhaps locking in place the orientation of the 50s loop. The proximity of a positively charged residue to the reduced FMN may be important in its reaction with  $O_2$  and is consistent with the unusual redox properties of NrdI (29). As in the NrdI<sub>ox</sub>-NrdF structure (Fig. 4A), there is no clear solvent access

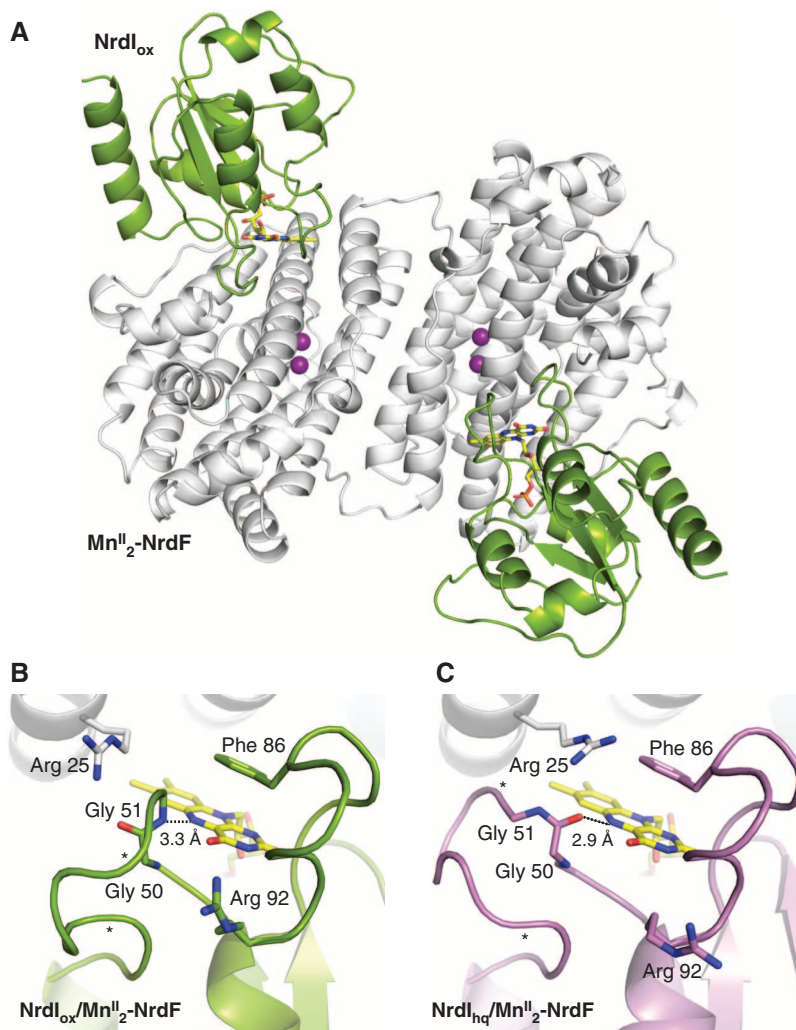


**Fig. 3.** Structures of NrdI-NrdF protein-protein complexes. **(A)** A ribbon diagram of the NrdI<sub>ox</sub>-NrdF structure. NrdI is shown in green and  $Mn^{II}_2$ -NrdF is shown in white. The NrdI FMN cofactor is shown as yellow sticks. **(B)** The NrdI FMN environment in the NrdI<sub>ox</sub>-NrdF structure (NrdI shown in green). **(C)** The NrdI FMN environment in the NrdI<sub>hq</sub>-NrdF structure (NrdI shown in purple). Hydrogen bonding interactions with the FMN N5 position are shown as dashed lines. The electron density for the 50s loop is not completely continuous between the asterisks.

route to the channel. The NrdI<sub>hq</sub>-NrdF structure reveals little conformational change within the complex when compared with NrdI<sub>ox</sub>-NrdF. However, a highly ordered water network is evident within the channel (fig. S8) that extends along the NrdI-NrdF interface to the NrdI FMN cofactor.

Surprisingly, strong (~7σ) unexplained electron density (Fig. 4B) was observed in both active-site channels of the structure obtained from aerobically dithionite-soaked crystals (NrdI<sub>hq</sub>-NrdF<sub>perox</sub>). This density is oblong in shape (Fig. 4C), and a number of small molecules have been modeled in an effort to determine its identity (fig. S10). Modeling as a single water molecule results in strong difference electron density (4.5σ), consistent with a diatomic species. Modeling as dioxygen yields difference density at the edges, suggesting that the O-O bond distance is longer than 1.2 Å. Less difference density was evident with superoxide (O-O bond distance 1.34 Å), with the best fit being a

fully occupied peroxide species with an O-O bond distance of 1.47 Å. Given that the crystals were exposed to 100 mM dithionite, we also considered the possibility that bisulfite, a dithionite breakdown product, could account for the density. Modeling with bisulfite (fig. S10E) yields  $F_o - F_c$  difference density and high B factors, however. Therefore, we modeled the electron density as a peroxide. Peroxide could have been produced by reaction of  $O_2$  with NrdI<sub>hq</sub> or with the dithionite used to reduce NrdI<sub>ox</sub> (30, 31).

The putative peroxide species is lodged at the bend in the active-site channel ~10 Å from the FMN isoalloxazine ring and ~10 Å from the  $Mn_2$  site (Fig. 4B). It is within hydrogen bonding distance of residues from both NrdF and NrdI, as well as solvent molecules in the channel (Fig. 4, C and D). The side chain of the single charged residue in the channel, NrdF Lys<sup>260</sup>, is 3.9 Å from the distal peroxide oxygen atom, consistent with

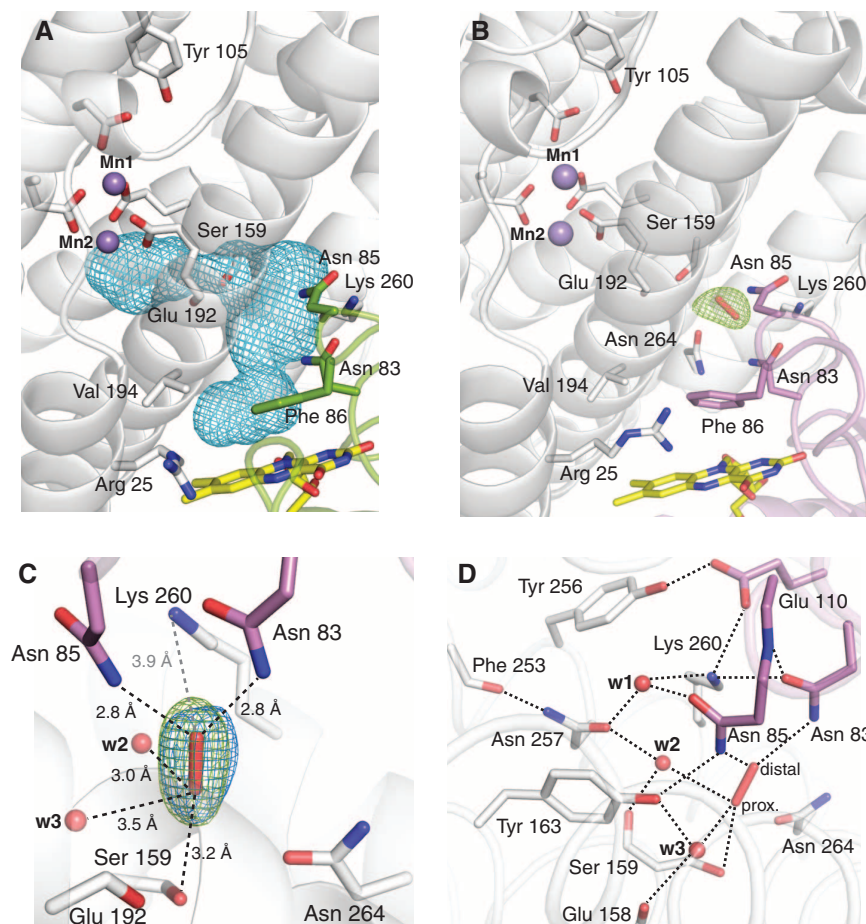


**Fig. 4.** The NrdI-NrdF channel. **(A)** NrdI-NrdF complex formation extends the NrdF active-site channel to the FMN cofactor. The complex channel is depicted as a light blue mesh and was calculated using a 1.4 Å probe radius. Selected NrdI (green) and NrdF (white) residues lining the channel are shown as sticks. **(B)** Observation of a trapped species, best modeled as peroxide, in the NrdI-NrdF channel in a crystal reduced by dithionite in the presence of oxygen (NrdI<sub>hq</sub>-NrdF<sub>perox</sub>). Strong  $F_o - F_c$  electron density (green mesh, contoured at 3.3 $\sigma$ ) is present in the channel after the first refinement cycle. The FMN cofactor (yellow), NrdI side chains lining the channel (purple), NrdF residues in the channel and at the active site (white), and the peroxide (red) are all shown as sticks. **(C)** A magnified view of the modeled peroxide shown in Fig. 3B and hydrogen bonding interactions with residues and solvent in the channel. The final  $2F_o - F_c$  electron density (blue mesh, contoured at 1.8 $\sigma$ ) is superimposed on the initial  $F_o - F_c$  electron density map from Fig. 3A. Water molecules are shown as red spheres. Dashed black lines indicate potential hydrogen bonding interactions. The gray dashed line represents the distance between the modeled peroxide and the nearest charged residue, conserved NrdF residue Lys<sup>260</sup>. The Glu<sup>192</sup> backbone carbonyl group and the side chain of Ser<sup>159</sup> constitute the narrowest point of the active-site channel. The oxygen atom distal to the Mn<sup>II</sup> site interacts strongly with the side chains of NrdI residues Asn<sup>85</sup> (2.8 Å) and conserved Asn<sup>83</sup> (2.8 Å). **(D)** The extended hydrogen bonding network near the putative peroxide binding site. The side-chain orientations of Asn<sup>83</sup> and Asn<sup>257</sup> can be assigned unequivocally based on their interactions with Lys<sup>260</sup> and the backbone amide nitrogen of Asn<sup>85</sup>, and the carbonyl oxygen of Phe<sup>253</sup>, respectively. The interactions of w2 with Asn<sup>257</sup> (2.8 Å) and the backbone carbonyl of Ser<sup>159</sup> (2.7 Å) constrain w2 to act as a hydrogen bond acceptor for the proximal oxygen atom of the modeled peroxide (2.9 Å), suggesting that this oxygen is protonated. The distal oxygen accepts two hydrogen bonds from Asn<sup>83</sup> and Asn<sup>85</sup>. Because no other potential hydrogen bond donor or acceptor exists for this oxygen atom, its protonation state cannot be determined from this analysis.

a role in electrostatic attraction, but not close enough for protonation. It is also protected from protonation by Tyr<sup>163</sup> by an intervening solvent molecule. The modeled peroxide is involved in an extensive hydrogen bonding network in which the proton donors and acceptors can be inferred (Fig. 4D and figs. S11 and S12). The structure suggests that the proximal oxygen atom is protonated, consistent with either H<sub>2</sub>O<sub>2</sub> or HO<sub>2</sub><sup>-</sup> (32). The presence

of the trapped species supports the relevance of the channel for oxidant transport.

The structures of NrdI<sub>ox</sub>-NrdF and NrdI<sub>hq</sub>-NrdF show that complexation results in continuation of the NrdF channel to the NrdI FMN cofactor, delineating an obvious path from the NrdI site of oxidant formation to Mn2. The NrdI<sub>hq</sub>-NrdF<sub>perox</sub> structure offers a crystallographic snapshot of a putative peroxide species within the channel. The

lack of conformational changes at the Mn<sup>II</sup> site in all three NrdI-NrdF complexes, when compared to Mn<sup>II</sup><sub>2</sub>-NrdF, suggests that the requirement for NrdI for Mn<sup>II</sup><sub>2</sub>-NrdF activation, if structural, is subtle. The structures strongly support the proposed mechanism of Mn<sup>II</sup><sub>2</sub>-NrdF activation by NrdI<sub>hq</sub> and O<sub>2</sub> and afford new insight into how reactive small molecules are channeled within complex enzyme systems.

**Note added in proof:** In support of the in vivo relevance of our work, Auling, Lubitz, and co-workers have recently reported isolation of *C. ammoniagenes* NrdF from the native organism containing a Mn<sup>III</sup><sub>2</sub>-Y• cofactor, characterization of the cofactor in detail by EPR spectroscopy, and structural determination of the protein to 1.36 Å resolution (33). Although the crystallized protein contained a Mn<sup>III</sup><sub>2</sub> cluster, the oxidation state of the observed Mn ions remains an open question because of possible photoreduction during data collection.

## References and Notes

1. P. Nordlund, P. Reichard, *Annu. Rev. Biochem.* **75**, 681 (2006).
2. S. Gon, M. J. Faulkner, J. Beckwith, *Antioxid. Redox Signal.* **8**, 735 (2006).
3. J. P. McHugh et al., *J. Biol. Chem.* **278**, 29478 (2003).
4. F. Monje-Casas, J. Jurado, M. J. Prieto-Alamo, A. Holmgren, C. Pueyo, *J. Biol. Chem.* **276**, 18031 (2001).
5. C. L. Atkin, L. Thelander, P. Reichard, G. Lang, *J. Biol. Chem.* **248**, 7464 (1973).
6. C. H. Wu, W. Jiang, C. Krebs, J. Stubbe, *Biochemistry* **46**, 11577 (2007).
7. J. A. Cotruvo Jr., J. Stubbe, *Biochemistry* **49**, 1297 (2010).
8. Y. Huque et al., *J. Biol. Chem.* **275**, 25365 (2000).
9. A. Jordan et al., *Proc. Natl. Acad. Sci. U.S.A.* **91**, 12892 (1994).
10. A. Willing, H. Follmann, G. Auling, *Eur. J. Biochem.* **170**, 603 (1988).
11. J. A. Cotruvo Jr., J. Stubbe, *Proc. Natl. Acad. Sci. U.S.A.* **105**, 14383 (2008).
12. I. Roca, E. Torrents, M. Sahlin, I. Gibert, B. M. Sjöberg, *J. Bacteriol.* **190**, 4849 (2008).
13. M. Högbom, Y. Huque, B.-M. Sjöberg, P. Nordlund, *Biochemistry* **41**, 1381 (2002).
14. W. C. Voegtli et al., *J. Am. Chem. Soc.* **125**, 15822 (2003).
15. See supporting material on Science Online.
16. H. Eklund, U. Uhlin, M. Färnegårdh, D. T. Logan, P. Nordlund, *Prog. Biophys. Mol. Biol.* **77**, 177 (2001).
17. The metal site in the reported structure of the Mn<sup>II</sup><sub>2</sub> form of *C. ammoniagenes* NrdF (13) differs from the *E. coli* Mn<sup>II</sup><sub>2</sub>-NrdF structure and is more similar to the Fe<sup>II</sup><sub>2</sub>-NrdF structures. Given that the *C. ammoniagenes* protein contained 1 Fe/β2 as compared to 0.03 Fe/β2 for the *E. coli* protein and the high sequence identity between *C. ammoniagenes* and *E. coli* NrdFs (66%), it is possible that the crystallized *C. ammoniagenes* protein did not contain two fully occupied Mn<sup>II</sup> sites. Additionally, the presence of two coordinated solvent molecules in a Mn<sup>II</sup><sub>2</sub> or Fe<sup>II</sup><sub>2</sub> β2 as observed in *E. coli* Mn<sup>II</sup><sub>2</sub>-NrdF is unusual. A single solvent molecule is coordinated to the second metal site (Mn2 or Fe2) in class Ia *E. coli* Mn<sup>II</sup><sub>2</sub>-substituted β2 and class Ib *S. typhimurium* and *M. tuberculosis* Fe<sup>II</sup><sub>2</sub>-NrdF (18, 34, 35). However, the solvent molecule in the class Ib NrdF structures likely derives from preparation of Fe<sup>II</sup><sub>2</sub>-NrdF by chemical or photoreduction of the μ-oxo bridged diferric cluster.
18. M. Eriksson, A. Jordan, H. Eklund, *Biochemistry* **37**, 13359 (1998).
19. The *E. coli* Fe<sup>II</sup><sub>2</sub>-NrdF structure was obtained by crystallization of apo-NrdF followed by soaking with Fe<sup>II</sup> ions in cryoprotectant solution. Nonheme Fe<sup>II</sup><sub>2</sub> protein structures are routinely obtained in a similar manner (13, 14) or by crystallizing the Fe<sup>II</sup><sub>2</sub> form followed by chemical or photoreduction (18). As with the Mn<sup>II</sup><sub>2</sub>-NrdF



- structure reported here,  $\text{Fe}^{II}_2\text{-NrdF}$  crystallized with one NrdF monomer per asymmetric unit with the second monomer in the functional  $\beta 2$  subunit related by crystallographic symmetry. Although a fully occupied class Ia  $\text{Fe}^{II}_2\text{-}\beta 2$  structure was obtained by this method (14), the  $\text{Fe}^{II}$  sites in the  $\text{Fe}^{II}_2\text{-NrdF}$  structure reported here are best modeled at 0.5 occupancy. Consequently, the model may represent an average of apo, partially loaded, and fully loaded states. The *C. ammoniagenes*  $\text{Fe}^{II}_2\text{-NrdF}$  structure (13), obtained similarly, contains two  $\beta 2$  dimers in the asymmetric unit with the  $\text{Fe}^{II}$  sites fully occupied in one of the four NrdF molecules with 0.3 to 0.6 occupancy for the other three  $\text{Fe}^{II}$  sites. In the immediate vicinity of the metal site, the *E. coli*  $\text{Fe}^{II}_2\text{-NrdF}$  structure is identical to that of the fully occupied *C. ammoniagenes*  $\text{Fe}^{II}_2\text{-NrdF}$  subunit. This observation supports the conclusion that the unusual features of the *E. coli*  $\text{Mn}^{II}_2\text{-NrdF}$  coordination environment result from  $\text{Mn}^{II}$  in the active site and are not an anomaly of the *E. coli* NrdF protein.
20. M. H. Sazinsky, S. J. Lippard, *J. Am. Chem. Soc.* **127**, 5814 (2005).
  21. M. H. Sazinsky, S. J. Lippard, *Acc. Chem. Res.* **39**, 558 (2006).
  22. The overall charge at the  $\text{Mn}^{II}_2$  site is neutral based on the structure if the Mn-bound solvent molecules are  $\text{H}_2\text{O}$ . If  $\text{H}_2\text{O}_2$  is the oxidant, the charge neutrality of the cluster would be conserved, with a proton being shuttled to one of the ligands upon oxidant binding to  $\text{Mn}^{II}_2$  (36). If the oxidant is  $\text{HO}_2^-$ , there is no obvious proton source near the active site, which may or may not be required to compensate for  $\text{HO}_2^-$  binding.
  23. V. V. Barynin *et al.*, *Structure* **9**, 725 (2001).
  24. M. Uppsten, M. Färnegårdh, V. Domkin, U. Uhlin, *J. Mol. Biol.* **359**, 365 (2006).
  25. M. L. Ludwig, C. L. Luschinsky, in *Chemistry and Biochemistry of Flavoenzymes*, F. Müller, Ed. (CRC Press, Boca Raton, FL, 1992), pp. 427–466.
  26. C. L. Drennan *et al.*, *J. Mol. Biol.* **294**, 711 (1999).
  27. Z. Zhou, R. P. Swenson, *Biochemistry* **34**, 3183 (1995).
  28. A. Mattevi, *Trends Biochem. Sci.* **31**, 276 (2006).
  29. Recent structures of *Bacillus cereus* NrdI in the absence of NrdF exhibit much less drastic conformational changes of the 50s loop upon reduction (37). Although most NrdI homologs possess 50s loops of 7 to 13 residues, typified by *E. coli* NrdI, some contain a short, three-residue 50s loop (usually Gly-Phe-Gly), typified by *B. cereus* NrdI. The shorter, less flexible 50s loop likely contributes to the more flavodoxin-like redox properties of *B. cereus* NrdI, and sequence alignments also reveal that the NrdFs from organisms containing NrdIs with short 50s loops (mainly *Bacillus* and *Staphylococcus*) also contain Gln at the equivalent position of Arg<sup>25</sup> in *E. coli*. Both of these characteristics suggest that NrdI may play a different role in cofactor biosynthesis and maintenance in the former class Ib systems than in *E. coli* (6, 11).
  30. M. Dixon, *Biochim. Biophys. Acta* **226**, 241 (1971).
  31. Reaction of dithionite with  $\text{O}_2$  can also produce  $\text{O}_2^{\cdot -}$ , but the electron density observed is unlikely to be this species. Analysis of the surrounding hydrogen bonding network (Fig. 4D) strongly suggests that at least one oxygen atom is protonated, and trapping of  $\text{HO}_2$  is unlikely ( $\text{pK}_a \sim 4.8$ ). Similarly, we have demonstrated (7) that reaction of NrdI<sub>hq</sub> with  $\text{O}_2$  does not generate appreciable amounts of  $\text{O}_2^{\cdot -}$ . Because high concentrations of dithionite (100 mM) were required to bleach the crystals, we also considered the possibility that the density derives from dithionite itself. Anaerobic soaking with 100 mM dithionite does not produce electron density at this position, however (fig. S14).
  32. Whereas connection of the channel to bulk solvent via a hydrogen bonding network would result in rapid protonation of  $\text{HO}_2^-$  through a proton conduction mechanism, analysis of the hydrogen bonding interactions at possible solvent access routes to the channel suggests that no direct connection exists (figs. S7 and S13). Thus, the structural analysis cannot distinguish between  $\text{HO}_2^-$  and  $\text{H}_2\text{O}_2$ .
  33. N. Cox *et al.*, *J. Am. Chem. Soc.* **132**, 11197 (2010).
  34. M. Atta, P. Nordlund, A. Aberg, H. Eklund, M. Fontecave, *J. Biol. Chem.* **267**, 20682 (1992).

35. M. Uppsten, J. Davis, H. Rubin, U. Uhlin, *FEBS Lett.* **569**, 117 (2004).
36. L. H. Do, T. Hayashi, P. Moënné-Loccoz, S. J. Lippard, *J. Am. Chem. Soc.* **132**, 1273 (2010).
37. A. K. Röhr, H.-P. Hersleth, K. K. Andersson, *Angew. Chem. Int. Ed.* **49**, 2324 (2010).
38. This work was supported by NIH grants GM58518 (A.C.R.) and GM81393 (J.S.), American Cancer Society grant PF-10-148-01-DMC (A.K.B.), and a National Defense Science and Engineering Graduate fellowship to J.A.C. Use of the Advanced Photon Source was supported by the U.S. Department of Energy, Office of Science, Office of Basic Energy Sciences, under Contract No. DE-AC02-06CH11357. Use of the Life Sciences Collaborative Access Team (LS-CAT) Sector 21 was supported by the Michigan Economic Development Corporation and the Michigan Technology Tri-Corridor (grant 085P1000817). Some data were collected at General Medicine and Cancer Institutes Collaborative Access Team (GM/CA-CAT), which has been funded in whole or in part with federal funds from the National Cancer Institute (grant Y1-CO-1020) and the National Institute of General Medical Science (grant Y1-GM-1104). We thank Z. Wawrzak for assistance with data processing and S. Lippard for helpful discussions. Coordinates and structure factors have been deposited in the Protein Data Bank with accession codes 3N37 ( $\text{Mn}^{II}_2\text{-NrdF}$ ), 3N38 ( $\text{Fe}^{II}_2\text{-NrdF}$ ), 3N39 (NrdI<sub>ox</sub>-NrdF), 3N3A (NrdI<sub>hq</sub>-NrdF), and 3N3B (NrdI<sub>hq</sub>-NrdF<sub>perox</sub>).

### Supporting Online Material

www.sciencemag.org/cgi/content/full/science.1190187/DC1

Materials and Methods

Figs. S1 to S14

Tables S1 and S2

References

29 March 2010; accepted 21 July 2010

Published online 5 August 2010;

10.1126/science.1190187

Include this information when citing this paper.

## Bifurcation of Toll-Like Receptor 9 Signaling by Adaptor Protein 3

Miwa Sasai, Melissa M. Linehan, Akiko Iwasaki\*

Endosomal Toll-like receptors (TLRs) 7 and 9 recognize viral pathogens and induce signals leading to the activation of nuclear factor  $\kappa\text{B}$  (NF- $\kappa\text{B}$ )—dependent proinflammatory cytokines and interferon regulatory factor 7 (IRF7)—dependent type I interferons (IFNs). Recognition of viral nucleic acids by TLR9 requires its cleavage in the endolysosomal compartment. Here, we show that TLR9 signals leading to the activation of type I IFN, but not proinflammatory cytokine genes, require TLR9 trafficking from endosomes to a specialized lysosome-related organelle. Furthermore, we identify adaptor protein-3 as the protein complex responsible for the trafficking of TLR9 to this subcellular compartment. Our results reveal an intracellular mechanism for bifurcation of TLR9 signals by selective receptor trafficking within the endosomal system.

Endosomal Toll-like receptors (TLRs) 7 and 9 are used by plasmacytoid dendritic cells (pDCs) for recognition of viral nucleic acids (1). These endosomal TLRs require trafficking by the endoplasmic reticulum (ER) membrane protein UNC93B (2, 3). UNC93B physically interacts with TLR3, TLR7, and TLR9 via the transmembrane domain (2) and transports these TLRs from the ER to the endosome. In

order for TLR9 to signal, the ectodomain of TLR9 must be first cleaved in the endolysosomes by cathepsins (4, 5). Although both TLR7 and TLR9 signal through the adapter protein MyD88 (myeloid differentiation primary response gene 88), two bifurcating pathways emanate from these TLRs. The first pathway leads to the transcriptional activation of proinflammatory cytokines and requires nuclear factor  $\kappa\text{B}$  (NF- $\kappa\text{B}$ ) (6). The second pathway leads to the activation of type I interferon (IFN) genes through phosphorylation of interferon regulatory factor 7 (IRF7) (7). Although both pathways depend on MyD88 (8) and UNC93B (3), the latter pathway also

requires additional molecules (9–15). Retention of multimeric A-type CpG DNA (CpG-A) in early endosome is associated with IFN production in pDCs, whereas rapid translocation of monomeric B-type CpG DNA (CpG-B) to the lysosome is associated with NF- $\kappa\text{B}$  activation (16, 17). These studies suggested that the intracellular location of TLR9 activation could dictate the nature of its downstream signaling. The mechanism by which these two types of signals are mediated through these TLRs, however, remains poorly defined.

To gain an insight into the cell biological basis of TLR9 signaling, we examined adaptor proteins (APs) that could mediate trafficking of TLR9 (18). APs select cargo for inclusion into coated vesicles in the late secretory and endocytic pathways. Of the four adaptors identified for coated vesicles (AP-1, AP-2, AP-3, and AP-4), the AP-3 complex (consisting of four subunits:  $\delta$ ,  $\beta 3\text{A}$ ,  $\mu 3\text{A}$ , and  $\sigma 3$ ) is found on the endosomal membranes and has been shown to recruit its cargo in the endosomes and deliver them to lysosome-related organelles (LROs) (19). LROs share features of late endosome/lysosomes but are functionally, morphologically, and compositionally distinct. To better understand the nature of the endosome from which TLR7 and TLR9 signal, cultured bone marrow (BM) pDCs from wild-type (WT) or AP-3-deficient (*Ap3b1*<sup>−/−</sup>) mice were incubated with CpG-A (TLR9 agonist), vesicular stomatitis virus (VSV), or influenza virus (TLR7 agonists).

Department of Immunobiology, Yale University School of Medicine, New Haven, CT 06520, USA.

\*To whom correspondence should be addressed. E-mail: akiko.iwasaki@yale.edu

AP-3-deficient pDCs failed to secrete IFN- $\alpha$  (Fig. 1A) despite normal to moderately enhanced production of interleukin (IL)-12p40, which is an NF- $\kappa$ B-dependent cytokine (Fig. 1B). Similar observations were made in pDCs from mice that have mutations in AP-3 $\beta$ 1 (pearl mice) or AP-3 $\delta$  (mocha mice), which render the AP-3 complex defective (fig. S1, A and B). This was not due to selective block in IFN protein secretion

but was due to the failure of AP-3-deficient pDCs to activate transcription of IFN genes (fig. S1C). To examine whether this phenotype was restricted to pDCs, we took advantage of the fact that liposome-mediated delivery of CpG-A to conventional DCs and macrophages enables production of type I IFNs through IRF7 activation by TLR9 (17). Upon stimulation with CpG-A coupled to DOTAP (a liposomal transfection reagent)

(Roche Diagnostics, Indianapolis, IN) or with TLR7 agonists poly uridine (poly U) or R848, *Ap3b1*<sup>-/-</sup> BM DCs were also found to have impaired IFN production while maintaining the production of IL-12p40 (fig. S2, A to C). Both cytokine and IFN responses after DOTAP-CpG-A stimulation were largely dependent on TLR9, albeit low levels were detected at higher CpG-A doses (fig. S2D), as reported previously (17). To determine whether the requirement for AP-3 also applies to other TLRs known to engage type I IFN stimulation from the endosome (20, 21), we stimulated BM macrophages (BMMs) from WT or *Ap3b1*<sup>-/-</sup> mice with lipopolysaccharide (LPS) (a TLR4 agonist) or polyinosinic:polycytidylic acid (poly I:C) (a TLR3 agonist). IFN- $\beta$  expression was partially impaired in the absence of AP-3 (fig. S2, E and F), suggesting the involvement of this adaptor complex in signaling from other endosomal TLRs. Next, we examined the in vivo relevance of AP-3 deficiency in TLR9 and TLR7 signaling. AP-3-deficient mice did not have any obvious defects in pDCs or other DC subset development (fig. S3). Mice were injected systemically with CpG-A, which is known to trigger pDCs in the spleen to secrete high amounts of type I IFNs (22). Serum concentrations of IFN- $\alpha$  were undetectable in *Ap3b1*<sup>-/-</sup> mice, whereas they peaked around 5 hours after injection in WT mice (Fig. 1C). In contrast, high amounts of IL-12p40 were detected in both groups, with slightly elevated amounts found in the *Ap3b1*<sup>-/-</sup> group (Fig. 1D). These data demonstrated that the AP-3 complex is required for signaling through TLR7 and TLR9 to induce activation of IFN but not proinflammatory cytokine genes.

Next, we examined whether the defective signaling of TLR9 in *Ap3b1*<sup>-/-</sup> cells could be explained by transcriptional regulation of signaling molecules downstream of TLR9. Quantitative reverse transcription polymerase chain reaction (RT-PCR) comparison of mRNA encoding MyD88, TRAF6, TRAF3, IRAK4, IRAK1, and IKK- $\alpha$  re-

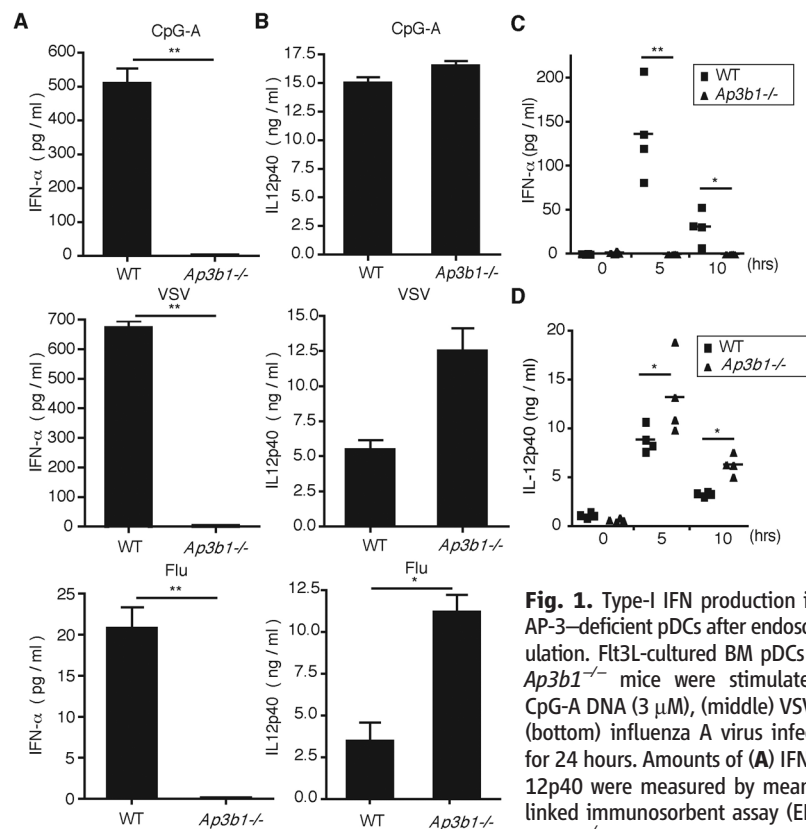


**Fig. 1.** Type-I IFN production is impaired in AP-3-deficient pDCs after endosomal TLR stimulation. Flt3L-cultured BM pDCs from WT and *Ap3b1*<sup>-/-</sup> mice were stimulated with (top) CpG-A DNA (3  $\mu$ M), (middle) VSV (MOI 10), or (bottom) influenza A virus infection (MOI 5) for 24 hours. Amounts of (A) IFN- $\alpha$  and (B) IL-12p40 were measured by means of enzyme-linked immunosorbent assay (ELISA). WT and *Ap3b1*<sup>-/-</sup> mice were injected intravenously

with CpG-A DNA (25  $\mu$ g), and at the indicated time points serum concentrations of (C) IFN- $\alpha$  and (D) IL-12p40 were measured with ELISA. \* $P$  < 0.05. \*\* $P$  < 0.01. Results are mean  $\pm$  SEM ( $n$  = 4 mice) and are representative of [(A) and (B)] four and [(C) and (D)] three independent experiments.

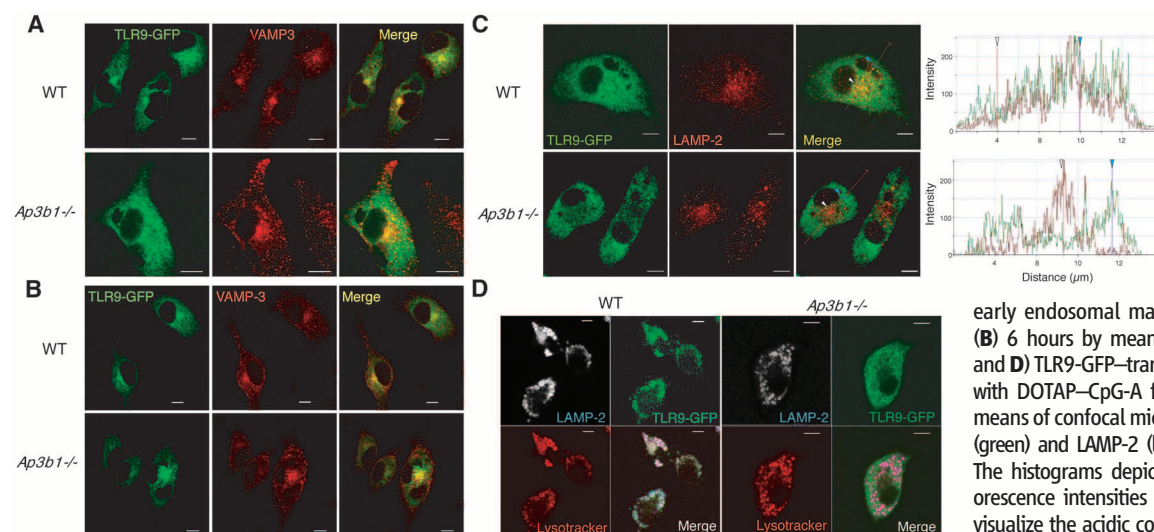


**Fig. 2.** TLR9 fails to enter the acidic LRO compartment in AP-3-deficient cells after CpG-A stimulation. BMM from WT and *Ap3b1*<sup>-/-</sup> mice were transduced with TLR9-GFP retrovirus. Cells were stimulated with DOTAP-CpG-A and analyzed for TLR9-GFP (green) and VAMP-3 (an early endosomal marker) (red) at (A) 3 hours or (B) 6 hours by means of confocal microscopy. (C and D) TLR9-GFP-transduced BMM were stimulated with DOTAP-CpG-A for 6 hours and analyzed by means of confocal microscopy to detect (C) TLR9-GFP (green) and LAMP-2 (late endosomal marker) (red). The histograms depict cross-line scans of the fluorescence intensities of the merged panel. (D) To visualize the acidic compartment, the cells were incubated with LysoTracker (red) followed by staining

for TLR9-GFP (green) and LAMP-2 (white/blue). The data are representative of three independent experiments. Scale bars, 5  $\mu$ m.



The ER transmembrane protein UNC93B associates with TLR3, TLR7, and TLR9 in the ER and facilitates their transport to the endolysosome (2, 3). We next examined whether the defect in TLR9 trafficking in *Ap3b1*<sup>−/−</sup> cells was due to mislocalization of UNC93B. Primary BMM from WT and *Ap3b1*<sup>−/−</sup> mice were cotransduced with retro-

**A**

TLR9-GFP    AP3μ3A-Flag    Merge

Non stimulation

DOTAP-CpG-A  
1 hr

**B**

RAW264.7 TLR9-GFP

AP3μ3A Flag	-			+		
DOTAP-CpG-A	0	1.5	2.5	0	1.5	2.5

(hrs)

1st IP : Flag  
2nd IP : GFP  
WB : GFP

100

150

◀ Cleaved TLR9

1st IP : Flag  
2nd IP : GFP  
WB : Flag

50

150

◀ AP-3μ3A

< Total lysate >

WB : GFP

150

100

◀ Full length TLR9

◀ Cleaved TLR9

(Mr, kDa)

**C**

IRF7-Flag	-	+	+	-	+	+
TRAF3-HA	+	-	+	-	-	+
AP-3μ3A-GFP	-	-	-	+	+	+

1    2    3    4    5    6

IP : Flag  
WB : HA

75

100

◀ TRAF3

IP : Flag  
WB : GFP

75

◀ AP-3μ3A

IP : Flag  
WB : Flag

◀ IRF7

\* IgG heavy chain

< Total lysate >

WB : HA

75

◀ TRAF3

WB : GFP

75

◀ AP-3μ3A

WB : Flag

◀ IRF7

(Mr, kDa)

17 SEPTEMBER 2010 VOL 329 **SCIENCE** [www.sciencemag.org](http://www.sciencemag.org)

data further supported the notion that AP-3 is required to recruit IRF7 to TLR9.

Our data thus far suggested that the failure of TLR9 to induce IFN expression in AP-3-deficient cells is due to the inability of TLR9 to traffic to a specialized LAMP2<sup>+</sup> LRO and engage IRF7. If this is the case, it should be possible to bypass the requirement for AP-3 by targeting TRAF3 to the VAMP3<sup>+</sup> compartment from which TLR9 normally engages NF- $\kappa$ B activation. To accomplish this goal, we searched for a targeting motif that allowed molecules to be specifically recruited to such an endosomal compartment. Phosphoinositides (PIs) are a key component of cell membranes. Every organelle is equipped with a distinct array of PI kinases and PI phosphatases, which produce a specific set of PI species. Phosphatidylinositol 3,5-bisphosphates [PI(3,5)P<sub>2</sub>] are synthesized in the early endosomes (29) and are also found on the membrane of multivesicular bodies (30). Thus, we generated a chimeric molecule in which a PI(3,5)P<sub>2</sub>-binding plextrin homology (PH) domain of centaurin  $\beta$ 2 (31) is fused to the N-terminal end of TRAF3 (PH-TRAF3). PH-TRAF3 associated with the VAMP3<sup>+</sup>LAMP2<sup>-</sup>TLR9<sup>+</sup> endosomes in response to DOTAP-CpG-A stimulation in *Ap3b1*<sup>-/-</sup> cells (Fig. 4B). Combined with our find-

ing that TLR9 localization in VAMP3<sup>+</sup> compartment is sufficient to trigger IL-12p40 production (Figs. 1 and 2), these data suggested that PI(3,5)P<sub>2</sub> decorate the VAMP3<sup>+</sup>LAMP2<sup>-</sup> endosome from which TLR9 signals to activate NF- $\kappa$ B (NF- $\kappa$ B endosome). To determine whether TRAF3 targeting to the NF- $\kappa$ B endosome could overcome the deficient IFN induction seen in *Ap3b1*<sup>-/-</sup> cells, *Ap3b1*<sup>-/-</sup> primary BMM were transduced with PH-TRAF3, and its ability to induce IFN expression after DOTAP-CpG-A stimulation was assessed. We found that targeting of TRAF3 to the NF- $\kappa$ B endosome was sufficient to reconstitute TLR9 signaling for IFN induction in *Ap3b1*<sup>-/-</sup> cells (Fig. 4C). Further, IL-12p40 gene expression was not substantially altered by PH-TRAF3 expression, indicating that the levels of ectopic PH-TRAF3 expression in primary macrophages were not sufficient to affect NF- $\kappa$ B signaling. Collectively, our data indicated that the defective TLR9 signaling in the absence of AP-3 is due to the inability of TLR9 to enter the specialized LRO capable of recruiting TRAF3 and IRF7 to the MyD88 signaling complex.

On the basis of our current study, we propose the following mechanism for TLR9 trafficking and signaling (fig. S13). TLR9 synthesized in the

ER traffics through the Golgi to enter the early endosome—a process facilitated by UNC93B. This VAMP3<sup>+</sup>LAMP2<sup>-</sup> PI(3,5)P<sub>2</sub>-endosome (NF- $\kappa$ B endosome) is proteolytically active, enabling TLR9 to be cleaved and signal through NF- $\kappa$ B to activate proinflammatory cytokine genes. AP-3 complex interacts with cleaved TLR9 in the NF- $\kappa$ B endosome and facilitates its trafficking to the LAMP2<sup>+</sup> LRO compartment, where TLR9 can engage the TRAF3 and IRF7 signaling pathway and induce transcription of IFN genes (IRF7 endosome). This specialized IFN-inducing LRO compartment is probably further downstream of the NF- $\kappa$ B-inducing endosome because transcription of IL-12 p40 occurred as early as 2 hours after CpG-A stimulation in pDCs, whereas mRNA for IFN- $\alpha$  was not detected until 4 to 6 hours (fig. S14). Moreover, intracellular cytokine analysis of pDCs stimulated with CpG-A revealed that cells that secrete IFN- $\alpha$  always also produced TNF- $\alpha$  but not vice versa (fig. S15). Given that AP-3 is dispensable for conventional maturation of endosomes but is required for the formation of LRO in specialized cell types such as melanocytes (melanosomes) and platelets (platelet granules) (19), it is tempting to speculate that pDCs are naturally equipped with an LRO dedicated for IFN production and that DCs and macrophages are capable of generating such LROs when CpG-A is delivered by cationic liposomes. Our data are consistent with the idea that the temporal and spatial coordination of a single receptor could be used to send signals for transcriptional activation of a distinct set of genes and that an adaptor protein can regulate this process.

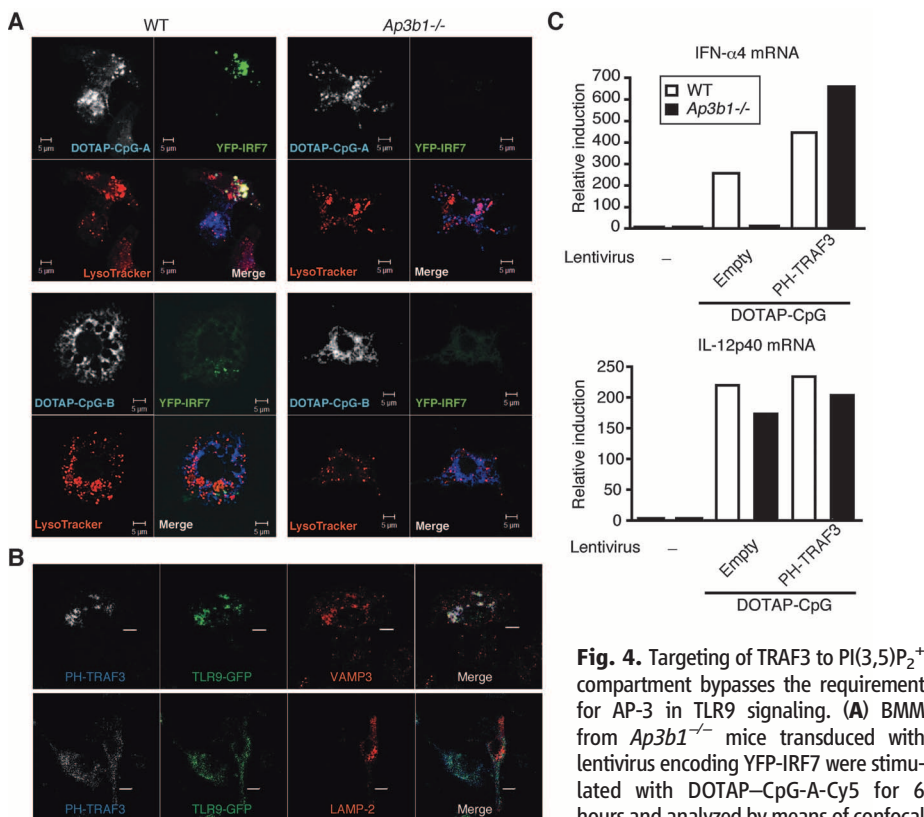


**Fig. 4.** Targeting of TRAF3 to PI(3,5)P<sub>2</sub><sup>+</sup> compartment bypasses the requirement for AP-3 in TLR9 signaling. (A) BMM from *Ap3b1*<sup>-/-</sup> mice transduced with lentivirus encoding YFP-IRF7 were stimulated with DOTAP-CpG-A-Cy5 for 6 hours and analyzed by means of confocal microscopy to detect YFP-IRF7 (green), LysoTracker (red), and CpG-A (white/blue). Scale bars, 5  $\mu$ m. (B) BMM from *Ap3b1*<sup>-/-</sup> mice transduced with retrovirus encoding TLR9-GFP and PH-TRAF3 were stimulated with DOTAP-CpG-A for 4 hours (VAMP-3 staining) or 6 hours (LAMP-2 staining) and analyzed by means of confocal microscopy in order to detect TLR9-GFP (green), VAMP3 (red), or LAMP-2 (red), and PH-TRAF3 (blue). Scale bars, 5  $\mu$ m. (C) BMMs from *Ap3b1*<sup>-/-</sup> mice were transduced with lentivirus encoding TRAF3 or PH-TRAF3. IFN- $\alpha$  and IL-12p40 mRNA expression was assessed by means of quantitative RT-PCR at 12 hours after DOTAP-CpG-A stimulation. Results are representative of four independent experiments.

ing that TLR9 localization in VAMP3<sup>+</sup> compartment is sufficient to trigger IL-12p40 production (Figs. 1 and 2), these data suggested that PI(3,5)P<sub>2</sub> decorate the VAMP3<sup>+</sup>LAMP2<sup>-</sup> endosome from which TLR9 signals to activate NF- $\kappa$ B (NF- $\kappa$ B endosome). To determine whether TRAF3 targeting to the NF- $\kappa$ B endosome could overcome the deficient IFN induction seen in *Ap3b1*<sup>-/-</sup> cells, *Ap3b1*<sup>-/-</sup> primary BMM were transduced with PH-TRAF3, and its ability to induce IFN expression after DOTAP-CpG-A stimulation was assessed. We found that targeting of TRAF3 to the NF- $\kappa$ B endosome was sufficient to reconstitute TLR9 signaling for IFN induction in *Ap3b1*<sup>-/-</sup> cells (Fig. 4C). Further, IL-12p40 gene expression was not substantially altered by PH-TRAF3 expression, indicating that the levels of ectopic PH-TRAF3 expression in primary macrophages were not sufficient to affect NF- $\kappa$ B signaling. Collectively, our data indicated that the defective TLR9 signaling in the absence of AP-3 is due to the inability of TLR9 to enter the specialized LRO capable of recruiting TRAF3 and IRF7 to the MyD88 signaling complex.

#### References and Notes

- Y. J. Liu, *Annu. Rev. Immunol.* **23**, 275 (2005).
- M. M. Brinkmann et al., *J. Cell Biol.* **177**, 265 (2007).
- K. Tabeta et al., *Nat. Immunol.* **7**, 156 (2006).
- S. E. Ewald et al., *Nature* **456**, 658 (2008).
- B. Park et al., *Nat. Immunol.* **9**, 1407 (2008).
- A. Takaoka et al., *Nature* **434**, 243 (2005).
- K. Honda et al., *Nature* **434**, 772 (2005).
- R. Medzhitov et al., *Mol. Cell* **2**, 253 (1998).
- S. Uematsu et al., *J. Exp. Med.* **201**, 915 (2005).
- H. Häcker et al., *Nature* **439**, 204 (2006).
- G. Oganesyan et al., *Nature* **439**, 208 (2006).
- K. Hoshino et al., *Nature* **440**, 949 (2006).
- M. L. Shinohara et al., *Nat. Immunol.* **7**, 498 (2006).
- H. Watarai et al., *Proc. Natl. Acad. Sci. U.S.A.* **105**, 2993 (2008).
- K. Gotoh et al., *J. Exp. Med.* **207**, 721 (2010).
- C. Guiducci et al., *J. Exp. Med.* **203**, 1999 (2006).
- K. Honda et al., *Nature* **434**, 1035 (2005).
- Materials and methods are available as supporting material on Science Online.
- J. S. Bonifacio, L. M. Traub, *Annu. Rev. Biochem.* **72**, 395 (2003).
- M. Matsumoto et al., *J. Immunol.* **171**, 3154 (2003).
- J. C. Kagan et al., *Nat. Immunol.* **9**, 361 (2008).
- C. Asselin-Paturel et al., *Nat. Immunol.* **2**, 1144 (2001).
- E. Latz et al., *Nat. Immunol.* **5**, 190 (2004).
- C. A. Leifer et al., *J. Immunol.* **173**, 1179 (2004).
- Y. M. Kim, M. M. Brinkmann, M. E. Paquet, H. L. Ploegh, *Nature* **452**, 234 (2008).
- E. S. Trombetta, I. Mellman, *Annu. Rev. Immunol.* **23**, 975 (2005).
- E. C. Dell'Angelica, V. Shotelersuk, R. C. Aguilar, W. A. Gahl, J. S. Bonifacio, *Mol. Cell* **3**, 11 (1999).



28. A. A. Peden *et al.*, *J. Cell Biol.* **164**, 1065 (2004).
29. O. C. Ikonomov, D. Sbrissa, A. Shisheva, *Am. J. Physiol. Cell Physiol.* **291**, C393 (2006).
30. M. A. De Matteis, A. Godi, *Nat. Cell Biol.* **6**, 487 (2004).
31. S. Dowler *et al.*, *Biochem. J.* **351**, 19 (2000).
32. We thank R. Medzhitov for critical reading of the manuscript and W. Mothes for helpful discussion.

This work is supported by NIH grants to A.I. (AI054359, AI081884, and AI064705). M.S. is a Japan Society for the Promotion of Science fellow and a recipient of Uehara Memorial Foundation fellowship. A.I. acknowledges support by Gilead Sciences. A.I. is a recipient of the Burroughs Wellcome Investigators in Pathogenesis of Infectious Disease.

#### Supporting Online Material

www.sciencemag.org/cgi/content/full/329/5998/1530/DC1  
Materials and Methods  
Figs. S1 to S15  
References

13 January 2010; accepted 4 August 2010  
10.1126/science.1187029

# Differential Arginylation of Actin Isoforms Is Regulated by Coding Sequence–Dependent Degradation

Fangliang Zhang,<sup>1</sup> Sougata Saha,<sup>1</sup> Svetlana A. Shabalina,<sup>2</sup> Anna Kashina<sup>1\*</sup>

The mammalian cytoskeletal proteins  $\beta$ - and  $\gamma$ -actin are highly homologous, but only  $\beta$ -actin is amino-terminally arginylated in vivo, which regulates its function. We examined the metabolic fate of exogenously expressed arginylated and nonarginylated actin isoforms. Arginylated  $\gamma$ -actin, unlike  $\beta$ -, was highly unstable and was selectively ubiquitinated and degraded in vivo. This instability was regulated by the differences in the nucleotide coding sequence between the two actin isoforms, which conferred different translation rates.  $\gamma$ -actin was translated more slowly than  $\beta$ -actin, and this slower processing resulted in the exposure of a normally hidden lysine residue for ubiquitination, leading to the preferential degradation of  $\gamma$ -actin upon arginylation. This degradation mechanism, coupled to nucleotide coding sequence, may regulate protein arginylation in vivo.

Actin is a major cytoskeletal component in eukaryotic cells. Mammalian  $\beta$ - and  $\gamma$ -actin (1–4) are encoded by different genes and differ substantially at the nucleotide level, but are nearly identical in their amino acid sequences, with only four homologous substitutions near their N termini. N-terminal methionine (M) in the actin sequence is removed immediately after synthesis, exposing the aspartic acid (in  $\beta$ -actin) or glutamic acid (in  $\gamma$ -actin) that can undergo subsequent posttranslational modifications (5). Arginylation, posttranslational addition of arginine (R) to proteins mediated by arginyltransferase (6), affects cytoskeletal proteins (7) and regulates actin (8); however, only  $\beta$ -actin is posttranslationally arginylated on the N terminus in vivo (8). The mechanism for such a differentiation between these two highly similar actin isoforms is unclear.

Although arginylated  $\beta$ -actin is metabolically stable (8), other proteins can be targeted for degradation via N-terminal arginylation (9). To test the possibility that such arginylation-dependent targeting may selectively affect arginylated  $\gamma$ -actin, we tested the metabolic stability of mammalian fusion constructs encoding wild-type and N-terminally arginylated  $\beta$ - and  $\gamma$ -actin [termed M- and R-actin, respectively; see fig. S3A and supporting online material (SOM) text 1 and 2 for further explanations and construct validation] (10).

Exogenously expressed R- $\gamma$ -actin was indeed significantly less abundant than R- $\beta$ -actin or

M-actin isoforms (Fig. 1A and figs. S3 and S4). Measurements of posttranslational degradation in the presence of cycloheximide showed that arginylated  $\gamma$ -actin was degraded significantly faster than other actin species (Fig. 1B and fig. S5). Its levels specifically increased in the presence of proteasome inhibitor MG132 (Fig. 1C), suggesting that selective degradation of  $\gamma$ -actin was at least in part proteasome-dependent.

To examine whether, in addition to the amino acid sequences, differences in  $\beta$ - and  $\gamma$ -actin coding sequences (fig. S6A) could be involved in regulating their differential stability, we produced “converted” actin isoforms, termed  $\beta$ -coded- $\gamma$ -actin ( $\beta$ c- $\gamma$ -actin) and  $\gamma$ -coded- $\beta$ -actin ( $\gamma$ c- $\beta$ -actin), that used the coding sequence of  $\beta$ -actin to produce the amino acid sequence of  $\gamma$ -actin and vice versa (fig. S6B). Such conversion resulted in a reversal of the intracellular levels of arginylated  $\beta$ - and  $\gamma$ -actin (Fig. 2A and figs. S7 and S8). Despite identical amino acid sequences, arginylated  $\gamma$ c- $\beta$ -actin was much less abundant than (less than half of) arginylated  $\beta$ -actin, whereas R- $\beta$ c- $\gamma$ -actin was over fourfold more abundant than R- $\gamma$ -actin. Such codon switching did not significantly affect posttranslational degradation dynamics (Fig. 2C and fig. S9) or intracellular levels of nonarginylated  $\beta$ - and  $\gamma$ -actin (Fig. 2B), indicating that the effect of codon switching was cotranslational and specifically mediated by arginylation. Thus, changes in intracellular level of arginylated actin isoforms after the codon switching resulted from changes in their cotranslational and not posttranslational degradation. This difference was mainly defined by the first 100 nucleotides of the actin coding sequence (fig. S10).

The cotranslational events that contribute to the overall protein stability include translation speed

and/or cotranslational degradation (11). To test whether  $\beta$ - and  $\gamma$ -actin have different translation speeds, we compared the dynamics of accumulation of  $\beta$ - and  $\gamma$ -actin (translated from the constructs that contain identical translation initiation and termination sites) in the presence of proteasome inhibitor MG132 in vivo and in vitro in rabbit reticulocyte lysates. In both tests,  $\gamma$ -actin accumulated more slowly than did  $\beta$ -actin (Fig. 3, A and B, figs. S11 and S12, and table S1). In agreement with this, ribosome translocation speeds measured by incorporation of labeled amino acids into nascent peptides (12) were faster for  $\beta$ - than for  $\gamma$ -actin (Fig. 3C and table S2). Patterns of the ribosome-bound nascent peptides (13) showed at least one prominent low-molecular-weight band in  $\gamma$ -actin that was not present in  $\beta$ -actin (Fig. 3D), suggesting that the ribosome paused during translation of the first short stretch of the  $\gamma$ -actin sequence.

The two major factors that can affect translation speed or dynamics are codon usage and mRNA structure. Analysis of the codon usage in  $\beta$ - and  $\gamma$ -actin revealed no prominent features within the first hundred nucleotides that could explain their difference in translation speeds (fig. S20). However, computational prediction of the folded RNA structure within the 5' region of the actin coding sequence showed a significant difference between  $\gamma$ - and  $\beta$ -actin mRNA within the beginning of their coding sequences (figs. S21 to S25) that probably underlies their different translation speed and dynamics.

To test whether the slow translation of  $\gamma$ -actin is responsible for its preferential cotranslational degradation upon arginylation, we used anisomycin to slow down translation (14) and compared the levels of the normally stable R- $\beta$ -actin with that of nonarginylated M- $\beta$ -actin in anisomycin-treated cells. As expected, increasing doses of anisomycin progressively reduced the levels of both actin species; however, R- $\beta$ -actin levels decreased to a larger extent than did M- $\beta$ -actin levels in a dose-dependent manner (Fig. 3, E and F, and fig. S13). A similar effect was observed for R- $\gamma$  and M- $\gamma$ , whereas no significant difference was seen between nonarginylated actins (fig. S14). Thus, slowing down translation indeed leads to a reduction in the actin levels that is mediated by N-terminal arginylation.

N-terminal arginylation can attract ubiquitin conjugation machinery (15, 16). Such ubiquitination often happens on the Lys nearest to the N terminus and is believed to be an essential feature of the arginylation-dependent N-degron (9). The actin sequence has a Lys residue in position 18 from the N terminus, which is predicted to be buried in the core of the folded actin molecule

<sup>1</sup>Department of Animal Biology, School of Veterinary Medicine, University of Pennsylvania, Philadelphia, PA 19104, USA.

<sup>2</sup>National Center for Biotechnology Information, National Library of Medicine, National Institutes of Health, Bethesda, MD 20894, USA.

\*To whom correspondence should be addressed. E-mail: akashina@vet.upenn.edu

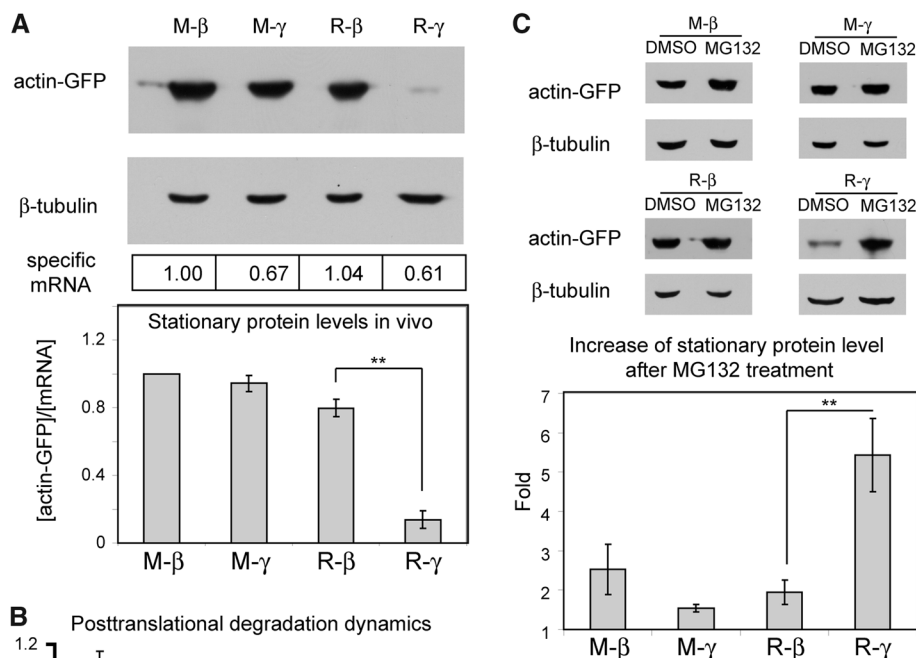


**Fig. 1.** Arginylated  $\gamma$ -actin is selectively degraded. Numbers in all panels represent mean  $\pm$  SEM;  $**P < 0.01$ , Student's  $t$  test. (A) (Top) Representative immunoblots of the lysates of human embryonic kidney (HEK) 293T cells transfected with actin–green fluorescent protein (GFP) constructs and probed with anti-GFP and  $\beta$ -tubulin as loading controls. Boxed numbers at the bottom indicate the specific mRNA levels in each sample (arbitrary units). (Bottom) Quantifications of the stationary protein levels as the amounts of in vivo actin-GFP per mRNA unit, normalized to the level of M- $\beta$ -actin ( $n = 4$  for R- $\beta$  and R- $\gamma$  and 6 for M- $\beta$  and M- $\gamma$ ). (B) Changes in actin protein level over time in the presence of cycloheximide, normalized to zero time point ( $n = 3$  for M- $\beta$  and M- $\gamma$  and 6 for R- $\beta$  and R- $\gamma$ ). (C) (Top) Representative immunoblots showing the stationary protein levels of the actin fusions and  $\beta$ -tubulin loading control in cells treated with dimethyl sulfoxide (DMSO) or MG132. (Bottom) Quantification of the fold change of each fusion protein upon MG132 treatment compared with the DMSO-treated sample ( $n = 3$  for M- $\beta$ , M- $\gamma$ , and R- $\beta$  and 6 for R- $\gamma$ ).

mRNA unit, normalized to the level of M- $\beta$ -actin ( $n = 4$  for R- $\beta$  and R- $\gamma$  and 6 for M- $\beta$  and M- $\gamma$ ). (B) Changes in actin protein level over time in the presence of cycloheximide, normalized to zero time point ( $n = 3$  for M- $\beta$  and M- $\gamma$  and 6 for R- $\beta$  and R- $\gamma$ ). (C) (Top) Representative immunoblots showing the stationary protein levels of the actin fusions and  $\beta$ -tubulin loading control in cells treated with dimethyl sulfoxide (DMSO) or MG132. (Bottom) Quantification of the fold change of each fusion protein upon MG132 treatment compared with the DMSO-treated sample ( $n = 3$  for M- $\beta$ , M- $\gamma$ , and R- $\beta$  and 6 for R- $\gamma$ ).

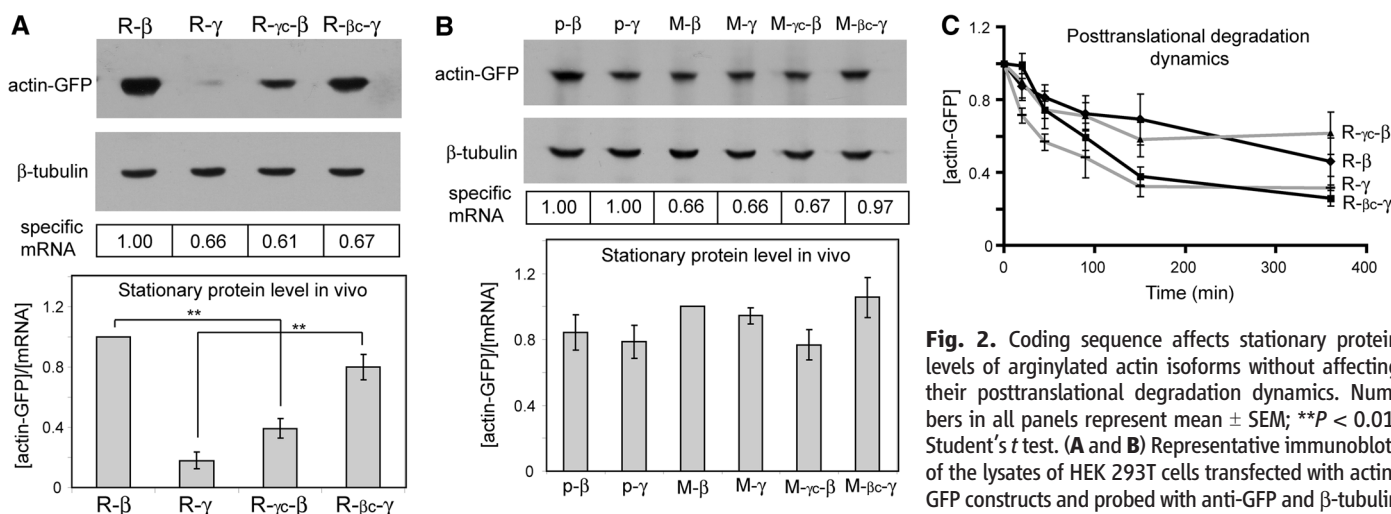


**Fig. 2.** Coding sequence affects stationary protein levels of arginylated actin isoforms without affecting their posttranslational degradation dynamics. Numbers in all panels represent mean  $\pm$  SEM;  $**P < 0.01$ , Student's  $t$  test. (A and B) Representative immunoblots of the lysates of HEK 293T cells transfected with actin-GFP constructs and probed with anti-GFP and  $\beta$ -tubulin as loading controls. Boxed numbers at the bottom

indicate corresponding mRNA levels (arbitrary units). Histograms indicate stationary protein levels of each actin species quantified per mRNA unit and normalized to the level of R- $\beta$ - (A) or M- $\beta$ -actin (B). In (A),  $n = 5$ ; in (B),  $n = 3$  for p- $\beta$  and p- $\gamma$  [the constructs that contain no N-terminal Ub fusion (fig. S2 and SOM text 2)], M- $\gamma$ c- $\beta$ , and M- $\beta$ c- $\gamma$  and 6 for M- $\beta$  and M- $\gamma$ . Double asterisks indicate statistical significance with  $P < 0.01$ . (C) Changes in actin protein levels over time in the presence of cycloheximide, normalized to the protein level at zero time point ( $n = 5$  for R- $\gamma$ c- $\beta$  and R- $\beta$ c- $\gamma$  and 6 for R- $\beta$  and R- $\gamma$ ).

(fig. S15). However, this Lys is probably exposed for potential modifications during translation before the folding can be completed, an effect that is expected to affect  $\gamma$ -actin, translated at a slower rate, much more than  $\beta$ -actin. To test whether Lys<sup>18</sup> (K18) affected degradation of arginylated  $\gamma$ -actin, we replaced this residue with Arg (K18R, the closest Lys homolog) or Leu [K18L, naturally found in a homologous position in the prokaryotic actin homolog MreB (17) (SOM text 2 and fig. S16)]. Such K18L and K18R mutations increased the stationary protein level of R- $\gamma$ -actin by at least 50% without significantly changing its posttranslational degradation dynamics (Fig. 4A and figs. S17 and S18). Moreover, the K18L mutation reduced ubiquitination of R- $\gamma$ -actin (Fig. 4B and fig. S26A). Actin ubiquitination levels also depended on nucleotide coding sequences, and R- $\gamma$ - and R- $\gamma$ c- $\beta$ -actin, the two actin species found to be the least stable, were ubiquitinated to a significantly higher extent than the others (Fig. 4C and fig. S26, B and C).

Thus, differential N-terminal arginylation of actin isoforms in nonmuscle cells is regulated by a degradation mechanism that selectively targets  $\gamma$ -actin, is dependent not only on the amino acid but also on the nucleotide coding sequence, and is linked to cotranslational processing and ubiquitination. Such combination of mechanisms is at least partially proteasome-dependent and results in selective removal of arginylated  $\gamma$ -actin from the intracellular protein pool, so that only arginylated  $\beta$ -actin is found in vivo. Because arginylation regulates actin function at the cell leading edge (8), ensuring that only  $\beta$ - but not  $\gamma$ -actin is arginylated can constitute an important step in this regulation (SOM text 3).

Because Lys<sup>18</sup> involved in cotranslational degradation of  $\gamma$ -actin is normally hidden inside the protein core, it appears likely that this Lys is ubiquitinated before the protein folds, probably



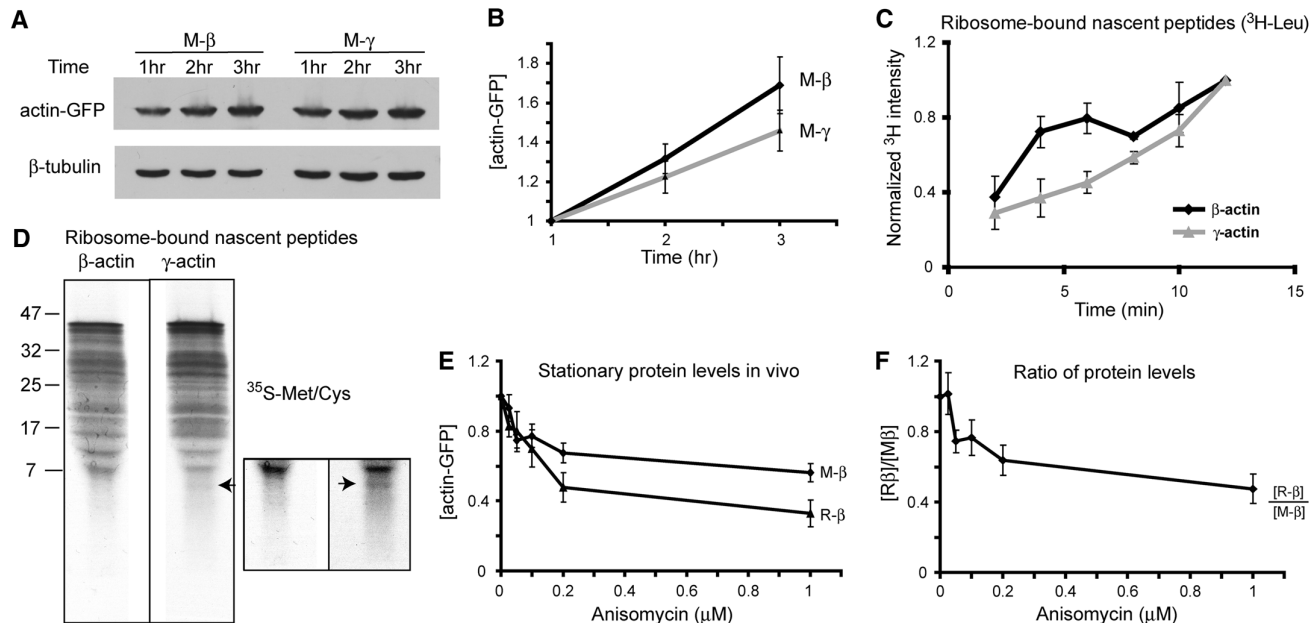
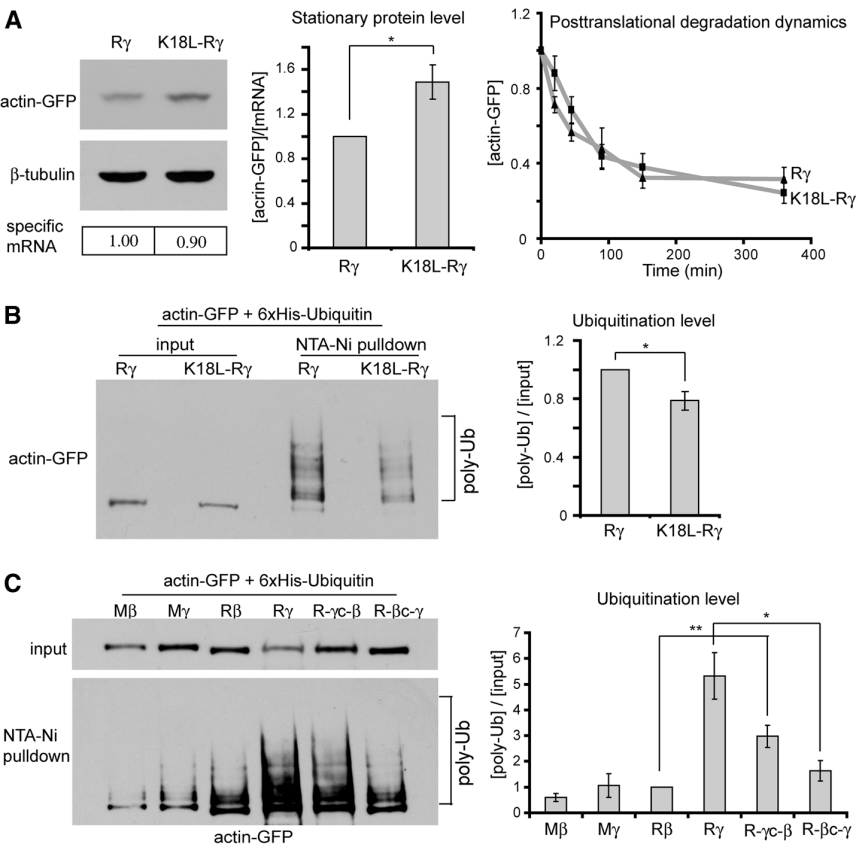


**Fig. 3.** Slower translation of  $\gamma$ -actin is linked to arginylation-mediated degradation. Numbers in all panels represent mean  $\pm$  SEM. **(A)** Representative immunoblots of the lysates of HEK 293T cells transfected with actin-GFP constructs, treated with MG132, and probed with anti-GFP and  $\beta$ -tubulin as loading controls. **(B)** Quantification of protein levels for M- $\beta$ - and M- $\gamma$ -actin adjusted to the starting mRNA level and normalized to the 1-hour time point in each set ( $n = 8$ ). **(C)** Incorporation of  $^3\text{H}$ -Leu into ribosome-bound nascent peptides of  $\beta$ - and  $\gamma$ -actin over time, normalized to the 12-min time point ( $n = 3$ ). **(D)** Pattern of  $^{35}\text{S}$ -labeled nascent peptides. Boxed area represents the bottom part of the same gel, contrasted to emphasize the lower molecular weight

bands by using Adobe Photoshop “brightness/contrast” function applied equally to the entire inset image. Arrow in both images indicates the additional low-molecular-weight band present in  $\gamma$ -actin. Similar results were observed in two independent repeats. **(E)** Stationary protein levels of actin proteins plotted against the increasing concentrations of anisomycin. **(F)** Stationary levels of actin proteins from the experiment shown in **(E)**, quantified by independently performed Western blots by loading M- $\beta$ - and R- $\beta$ -actin side by side and plotted as ratio of  $[\text{R-}\beta]/[\text{M-}\beta]$  against anisomycin concentration. Curves in **(E)** and **(F)** are normalized to the sample with 0  $\mu\text{M}$  of anisomycin in each set ( $n = 3$ ).

**Fig. 4.** Cotranslational degradation of arginylated  $\gamma$ -actin is achieved via a ubiquitin-dependent mechanism. Numbers in all panels represent mean  $\pm$  SEM;  $*P < 0.05$ ,  $**P < 0.01$ , Student’s  $t$  test. **(A)** (Left) Representative immunoblots of the lysates of HEK 293T cells transfected with actin-GFP constructs and probed with anti-GFP and  $\beta$ -tubulin as loading controls; specific mRNA levels (arbitrary units) are indicated below each lane. (Middle) Stationary protein levels generated with each construct quantified per mRNA unit and normalized to the level of arginylated  $\gamma$ -actin ( $n = 4$ ). (Right) Changes in actin protein levels over time in the presence of cycloheximide, normalized to the protein level at zero time point ( $n = 4$  for K18L-R- $\gamma$  and 6 for R- $\gamma$ ). **(B)** (Left) Total actin-GFP levels in cells cotransfected with actin constructs and His-tagged ubiquitin (input) and in the pellet after His-tag precipitation to enrich for ubiquitinated proteins (pull-down). NTA, nitrilotriacetic acid. (Right) Quantification of the ubiquitination levels ( $n = 3$ ). Levels of K18L-R- $\gamma$  mutant are normalized to those of R- $\gamma$ . **(C)** (Left) Representative immunoblots of the input and His-tag-Ub precipitation for the constructs marked on the top. (Right) Quantification of the ubiquitination levels, normalized to those of R- $\beta$  ( $n = 3$ ).



early during translation, targeting actin for degradation in a proteasome-dependent or -independent way. However, replacement of Lys<sup>18</sup> had only a partial effect in reducing the ubiquitination and stabilizing the arginylated  $\gamma$ -actin, suggesting that other Lys residues in the actin sequence or the molecular chaperones involved in cotranslational actin processing may also contribute to this process (18).

In addition to selective degradation, actin isoforms may also be selectively recognized by arginyltransferase, either via the specificity of the enzyme itself or by its spatial segregation toward one actin isoform. However, arginyltransferase has fairly poor substrate specificity (7), and it can efficiently arginylate both N-terminal Asp and  $\gamma$ -actin, respectively (5). Spatial segregation toward one actin isoform is also unlikely, because arginyltransferase appears to have no relevant bias in its intracellular distribution (19, 20). Actin's N-terminal acetylation (5, 21, 22) may also be isoform-biased and regulate its degradation state; however, to date all actin isoforms appear to be equally acetylated. Thus, selective degradation appears to be the most plausible explanation for why only one of the two predominant actin isoforms is arginylated in nonmuscle cells.

For some proteins, N-terminal arginylation targets them for degradation (16, 23), whereas for

others it does not (7, 8). Perhaps arginylation may be a self-regulating modification that ensures selective accumulation of some arginylated proteins and removal of others. This mechanism may be used not only with actin isoforms but also with other closely homologous but selectively arginylated proteins.

#### References and Notes

1. C. A. Otey, M. H. Kalnoski, J. L. Lessard, J. C. Bulinski, *J. Cell Biol.* **102**, 1726 (1986).
2. C. A. Otey, M. H. Kalnoski, J. C. Bulinski, *J. Cell. Biochem.* **34**, 113 (1987).
3. D. Höfer, W. Ness, D. Drenckhahn, *J. Cell Sci.* **110**, 765 (1997).
4. J. Condeelis, R. H. Singer, *Biol. Cell* **97**, 97 (2005).
5. P. A. Rubenstein, D. J. Martin, *J. Biol. Chem.* **258**, 3961 (1983).
6. E. Balzi, M. Choder, W. N. Chen, A. Varshavsky, A. Goffeau, *J. Biol. Chem.* **265**, 7464 (1990).
7. C. C. L. Wong *et al.*, *PLoS Biol.* **5**, e258 (2007).
8. M. Karakozova *et al.*, *Science* **313**, 192 (2006); published online 22 June 2006 (10.1126/science.1129344).
9. A. Varshavsky, *Cell* **69**, 725 (1992).
10. Materials and methods are available as supporting material on Science Online.
11. G. Kramer, D. Boehringer, N. Ban, B. Bukau, *Nat. Struct. Mol. Biol.* **16**, 589 (2009).
12. A. C. Lopo, C. C. Lashbrook, J. W. Hershey, *Biochem. J.* **258**, 553 (1989).
13. A. A. Komar, T. Lesnik, C. Reiss, *FEBS Lett.* **462**, 387 (1999).
14. A. P. Grollman, *J. Biol. Chem.* **242**, 3226 (1967).

15. S. Elias, A. Ciechanover, *J. Biol. Chem.* **265**, 15511 (1990).
16. S. Ferber, A. Ciechanover, *Nature* **326**, 808 (1987).
17. F. van den Ent, L. A. Amos, J. Löwe, *Nature* **413**, 39 (2001).
18. A. L. Goldberg, *Nature* **426**, 895 (2003).
19. R. Rai, A. Kashina, *Proc. Natl. Acad. Sci. U.S.A.* **102**, 10123 (2005).
20. Y. T. Kwon, A. S. Kashina, A. Varshavsky, *Mol. Cell. Biol.* **19**, 182 (1999).
21. J. Vandekerckhove, K. Weber, *Arch. Int. Physiol. Biochim.* **86**, 891 (1978).
22. K. L. Redman, P. A. Rubenstein, *Methods Enzymol.* **106**, 179 (1984).
23. D. K. Gonda *et al.*, *J. Biol. Chem.* **264**, 16700 (1989).
24. We thank R. Dominguez for help with actin structure analysis and the preparation of fig. S15; D. Volgin for helpful suggestions on quantitative polymerase chain reaction; S. Fuchs, Y. Goldman, and J. M. Murray for helpful discussions; and S. Kurosaka for critical reading of the manuscript. This work was supported by NIH grant 5R01HL084419 and W. W. Smith Charitable Trust and Philip Morris Research Management Group awards to A.K. and by the Intramural Research Program of NIH, National Center for Biotechnology Information, to S.A.S.

#### Supporting Online Material

www.sciencemag.org/cgi/content/full/329/5998/1534/DC1

Materials and Methods

SOM Text 1 to 3

Figs. S1 to S26

Tables S1 and S2

References

30 April 2010; accepted 20 July 2010

10.1126/science.1191701

## MiR-16 Targets the Serotonin Transporter: A New Facet for Adaptive Responses to Antidepressants

Anne Baudry,<sup>1</sup> Sophie Mouillet-Richard,<sup>1</sup> Benoît Schneider,<sup>1</sup> Jean-Marie Launay,<sup>2,3\*</sup> Odile Kellermann<sup>1\*</sup>

The serotonin transporter (SERT) ensures the recapture of serotonin and is the pharmacological target of selective serotonin reuptake inhibitor (SSRI) antidepressants. We show that SERT is a target of microRNA-16 (miR-16). miR-16 is expressed at higher levels in noradrenergic than in serotonergic cells; its reduction in noradrenergic neurons causes de novo SERT expression. In mice, chronic treatment with the SSRI fluoxetine (Prozac) increases miR-16 levels in serotonergic raphe nuclei, which reduces SERT expression. Further, raphe exposed to fluoxetine release the neurotrophic factor S100 $\beta$ , which acts on noradrenergic cells of the locus coeruleus. By decreasing miR-16, S100 $\beta$  turns on the expression of serotonergic functions in noradrenergic neurons. Based on pharmacological and behavioral data, we propose that miR-16 contributes to the therapeutic action of SSRI antidepressants in monoaminergic neurons.

**T**ransporters selective for serotonin [5-hydroxytryptamine (5-HT)] (SERTs), noradrenaline (NETs), or dopamine ensure the reuptake of monoamines at the synaptic cleft and thereby sustain the action of therapeutic agents

in the treatment of a variety of psychiatric disorders (1). Dysfunction of serotonergic neurotransmission has been implicated in depression as well as obsessive-compulsive disorder, anxiety, and suicidal behavior (2). Selective serotonin reuptake inhibitors (SSRIs) are beneficial in the treatment of all these neuropsychiatric conditions. A still enigmatic observation is that SSRIs need to be administered for long time periods to yield clinical improvement (3).

The distribution of SERT in the brain mirrors that of serotonergic neuronal cell bodies and innervating fibers (4, 5). Serotonergic raphe neurons project to most parts of the central nervous

system and coordinate the physiology of the whole brain (2). Chronic SSRI antidepressant treatment promotes reductions in SERT binding and protein levels but does not affect SERT mRNA levels (6), suggesting that SSRIs may interfere with SERT translation. This control of translation could be exerted by microRNAs (miRNAs), which have emerged as crucial modulators of gene expression (7, 8). Although the roles of miRNAs in cell fate decision, differentiation, maintenance of cell identity, survival, and neuronal plasticity are being uncovered (9, 10), their targets remain largely unknown.

To investigate whether miRNAs provide a mechanism for adaptive changes in SERT expression in monoaminergic neurons, we first exploited the 1C11 neuroectodermal cell line, which can differentiate into either serotonergic (1C11<sup>5-HT</sup>) or noradrenergic (1C11<sup>NE</sup>) neuronal cells (fig. S1A) (11). 1C11 neuroectodermal cells express transcripts encoding SERT and neurotransmitter-related markers before their choice of cell fate (Fig. 1A and fig. S1B). Because these transcripts remain at roughly constant levels during serotonergic or noradrenergic differentiation, miRNAs may participate in the posttranscriptional mechanisms that prevent illegitimate mRNA translation according to each program.

Using *in silico* computational target prediction, we identified miR-16 as a miRNA with complementarity to the 3' untranslated region of the SERT mRNA (fig. S2A) and then validated miR-16 as a SERT-targeting miRNA with a luciferase assay (fig. S2B). Consistent with a putative role of miR-16 as a negative regulator of SERT

<sup>1</sup>Cellules Souches, Signalisation et Prions, INSERM U747, Université Paris Descartes, 75006 Paris, France. <sup>2</sup>Pharma Research Department, F. Hoffmann-La Roche, CH-4070 Basel, Switzerland. <sup>3</sup>Assistance Publique-Hôpitaux de Paris Service de Biochimie, RTRS Santé Mentale, U942 INSERM Hôpital Lariboisière, Paris, France.

\*To whom correspondence should be addressed. E-mail: jean-marie.launay@lrp.aphp.fr (J.-M.L.); odile.kellermann@parisdescartes.fr (O.K.)



translation, we found that 1C11 neuroectodermal cells expressed a low level of miR-16, which increased along the noradrenergic pathway, whereas the level did not vary along the serotonergic program (fig. S2C).

If the SERT is indeed a target of miR-16, then miR-16 overexpression in 1C11<sup>5-HT</sup> cells should decrease SERT protein levels. During serotonergic differentiation, SERT translation starts at day 2 (12). Functional 5-HT uptake and antidepressant recognition occur at day 4. Among monoamine transporters, only SERT has the capacity

to bind SSRI antidepressants [such as paroxetine and fluoxetine (Prozac)] (13). The SERT further recognizes the cocaine congener [<sup>125</sup>I]-RTI-55, which also binds to NET (12). Using these pharmacological tools, we quantified the level of SERT expression in 1C11<sup>5-HT</sup> cells after transfection with miR-16. miR-16 overexpression reduced the number of [<sup>3</sup>H]-paroxetine or [<sup>125</sup>I]-RTI-55 binding sites by 40% (Fig. 1B). In contrast, the number of [<sup>3</sup>H]-paroxetine and [<sup>125</sup>I]-RTI-55 binding sites remained unchanged when 1C11<sup>5-HT</sup> cells were transfected with miR antisense oligo-

nucleotides (anti-miR-16) (Fig. 1B), suggesting that SERT translation is insensitive to the endogenous basal level of miR-16 in 1C11<sup>5-HT</sup> cells.

1C11<sup>NE</sup> noradrenergic cells selectively implement a functional NET at day 12 of their program (17). Although they express SERT mRNAs, SERT molecules are undetectable (Fig. 1, A and D). Assuming that the up-regulation of miR-16 during noradrenergic differentiation (fig. S2C) may have a role in silencing SERT transcripts, we exposed 1C11<sup>NE</sup> cells to anti-miR-16. Binding was measured with three drugs: [<sup>3</sup>H]-nisoxetine,

**Fig. 1.** miR-16 targets SERT in the 1C11 cell line. (A) Reverse transcription polymerase chain reaction (PCR) analysis of SERT and NET transcripts during serotonergic and noradrenergic differentiation. Glyceraldehyde phosphate dehydrogenase mRNA was used as a control. (B) Overexpression of miR-16 in 1C11<sup>5-HT</sup> cells reduces SERT expression. The level of SERT was determined by [<sup>125</sup>I]-RTI-55 and [<sup>3</sup>H]-paroxetine binding in 1C11<sup>5-HT</sup> day 4 cells untreated (control) or treated with miR-16 or anti-miR-16 at day 2 of serotonergic differentiation. (C to E) miR-16 reduction in 1C11<sup>NE</sup> cells induces SERT expression and SSRI antidepressant binding, while not affecting NET expression. 1C11<sup>NE</sup> cells were treated with miR-16 or anti-miR-16 at day 10 of the noradrenergic program. At day 12, NET and SERT expression were measured in cell homogenates using (C) [<sup>3</sup>H]-nisoxetine, a selective inhibitor of noradrenaline uptake; (D) [<sup>3</sup>H]-paroxetine, a selective inhibitor of 5-HT uptake; and (E) [<sup>125</sup>I]-RTI-55, which recognizes NET and SERT. (F to I) miR-16 reduction in 1C11<sup>NE</sup> cells unlocks the expression of serotonergic markers. Cell extracts from 1C11<sup>NE</sup> day 12 cells untreated (control) or treated with miR-16 or anti-miR-16 at day 10 of differentiation were used to assess (F) TPH activity, (G) 5-HT intracellular content, (H) 5-hydroxyindoleacetic acid (5-HIAA) concentration, and (I) the amount of 5-HT<sub>2B</sub> receptors ([<sup>3</sup>H]-LY 266097 binding). Data are means ± SEM of seven independent experiments, (B) \**P* < 0.01 versus control, (E) \**P* < 0.01, and [(D) and (F) to (I)] \**P* < 0.001 versus control and miR-16.

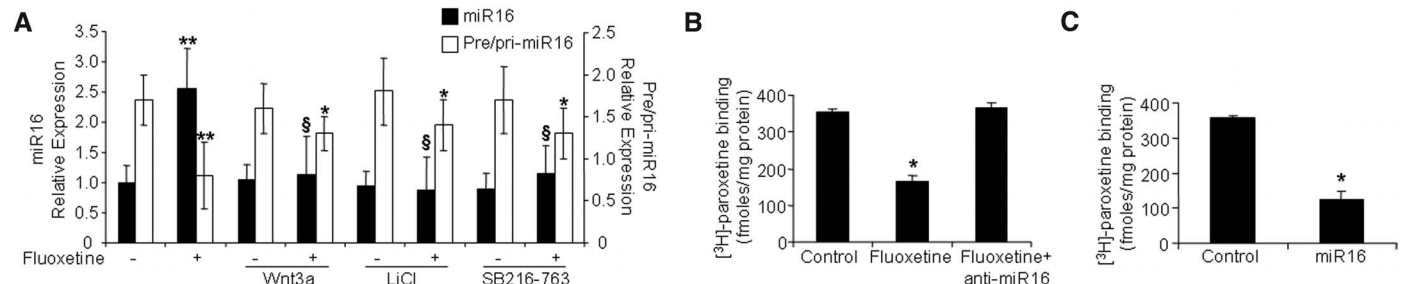
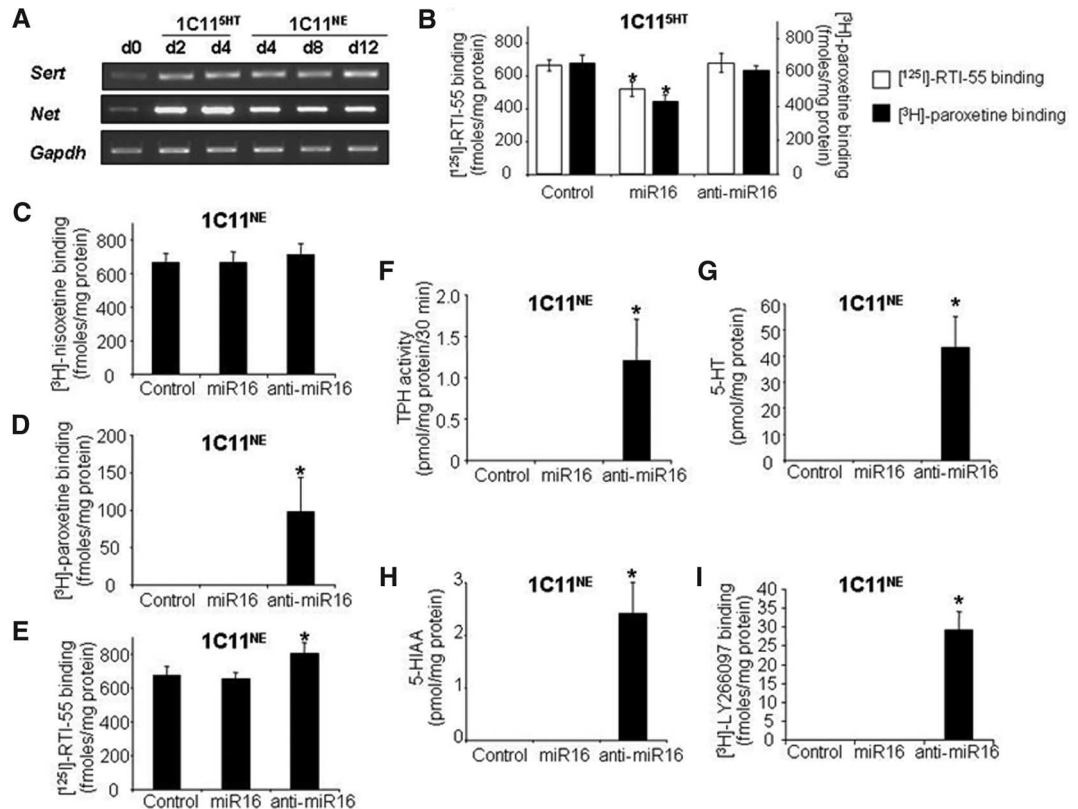


**Fig. 2.** Fluoxetine increases miR-16 levels in raphe by antagonizing canonical Wnt signaling. (A) Mice received chronic stereotaxic injection (2  $\mu$ l/min) of fluoxetine (1  $\mu$ M) into raphe for 3 days in combination or not with activators of the canonical Wnt pathway [Wnt3a (50 ng/ml), LiCl (1 mM), or SB-216763, a selective GSK-3 $\beta$  inhibitor (100 nM)]. The levels of miR-16 and pre/pri-miR-16 in raphe were determined by real-time PCR. Data are means ± SEM (*n* = 7

animals), \*\**P* < 0.01 versus control, \**P* < 0.05, and \$*P* < 0.01 versus fluoxetine alone. (B and C) SERT expression ([<sup>3</sup>H]-paroxetine binding) was determined in raphe extracts of mice perfused (2  $\mu$ l/min) for 3 days into the raphe with fluoxetine (1  $\mu$ M) in the presence or absence of anti-miR-16 (1  $\mu$ l, 2  $\mu$ M) (B) or after direct injection of miR-16 (1  $\mu$ l, 2  $\mu$ M) (C). Data are means ± SEM of seven animals, \**P* < 0.01 versus control.

which is selective for NET; [ $^{125}$ I]-RTI-55, which binds NET and SERT; and [ $^3$ H]-paroxetine, which recognizes SERT only. NET expression was insensitive to a reduction of miR-16 (Fig. 1C). In contrast, anti-miR-16 induced the appearance of paroxetine binding sites in 1C11<sup>NE</sup> cells (Fig. 1D) and increased the number of RTI binding sites to the sum of nioxetine and paroxetine binding sites (Fig. 1E). The number of newly induced RTI sites equaled the number of paroxetine binding sites and may thus be

ascribed to de novo expressed SERT molecules. Hence, the inhibition of miR-16 unlocks SERT protein expression in 1C11<sup>NE</sup> cells and renders noradrenergic cells competent to recognize SSRI antidepressants.

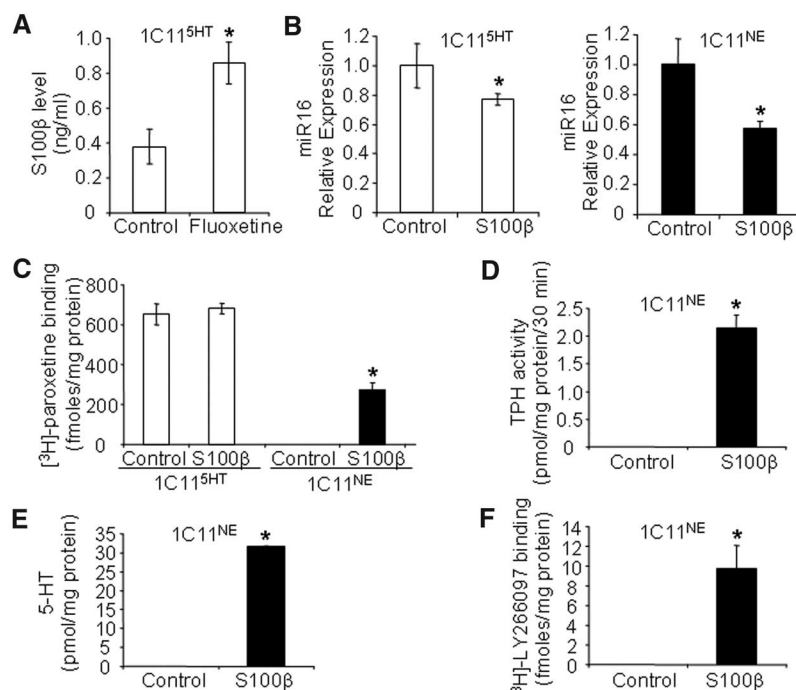
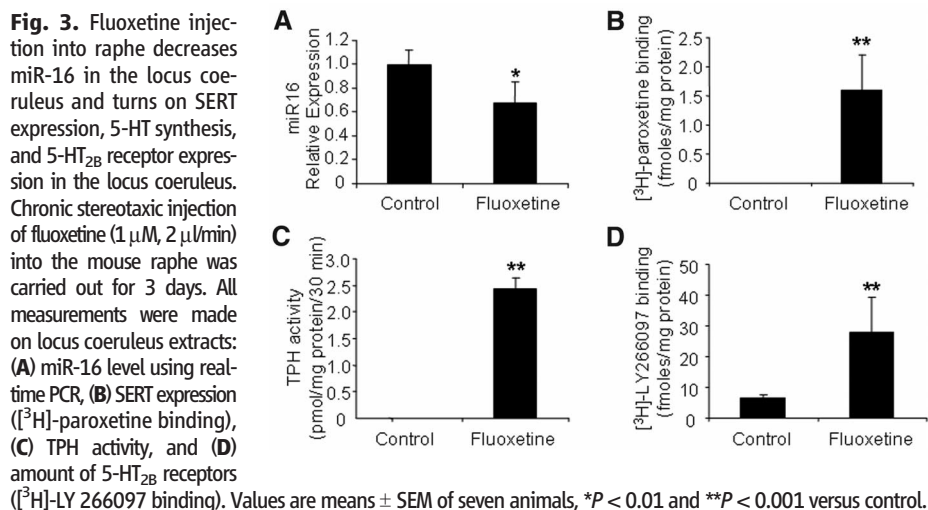
Next, we investigated whether decreasing miR-16 levels in 1C11<sup>NE</sup> cells would promote changes in noradrenergic phenotypic parameters distinct from NET and/or allow the implementation of serotonergic functions, in addition to that of SERT. Neutralization of endogenous miR-16

with anti-miR-16 had no impact on noradrenergic-associated functions in 1C11<sup>NE</sup> cells (fig. S3). In contrast, the cells acquired a complete serotonergic metabolism, as defined by the ability to synthesize, store, and degrade 5-HT, and they expressed 5-HT<sub>2B</sub> receptors (Fig. 1, F to I). These results show that miR-16 acts as a global repressor of the expression of serotonergic-specific functions in 1C11<sup>NE</sup> cells.

We hypothesized that the miR-16-dependent regulation of the SERT shown in the 1C11 cell line may have physiopathological relevance in vivo. We first quantified miR-16 in mouse serotonergic raphe nuclei (2) versus the noradrenergic locus coeruleus (14). As in the 1C11 cell line, lower levels of miR-16 were found in raphe than in the locus coeruleus (fig. S2D). Then we assessed whether SSRI antidepressant treatment could alter the levels of miR-16 in these regions of the mouse brain. When fluoxetine was infused into raphe, we observed a 2.5-fold increase in the level of miR-16 and a twofold reduction in [ $^3$ H]-paroxetine binding in raphe (Fig. 2, A and B). Direct injection of miR-16 into raphe yielded a similar decrease in [ $^3$ H]-paroxetine binding (Fig. 2C). Finally, [ $^3$ H]-paroxetine binding was not affected after the infusion of fluoxetine together with anti-miR-16 (Fig. 2B). These data demonstrate that fluoxetine regulates SERT expression through miR-16 in raphe.

The fluoxetine-induced up-regulation of miR-16 in raphe nuclei may involve a pre/pri-miR-16 enhanced transcription and/or maturation. In raphe versus the locus coeruleus, the level of pre/pri-miR-16 was inversely correlated with the level of miR-16 (compare figs. S2D and S4). In addition, the fluoxetine-mediated increase in miR-16 in raphe was accompanied by a decrease in pre/pri-miR-16 (Fig. 2A), thus supporting the maturation hypothesis. Because canonical Wnt signaling may repress miR-16 maturation (15), we quantified the levels of miR-16 and pre/pri-miR-16 under combined fluoxetine treatment and activation of the Wnt pathway. The up-regulation of miR-16 and the down-regulation of pre/pri-miR-16 triggered by fluoxetine in raphe were both eliminated by either Wnt3a, LiCl, or SB-216763 (Fig. 2A). Chronic fluoxetine treatment actually interfered with canonical Wnt signaling, as inferred from the increase in glycogen synthase kinase-3 $\beta$  (GSK-3 $\beta$ ) activity (fig. S5A). Hence, the SSRI fluoxetine augments the level of miR-16 in raphe by antagonizing Wnt signaling and thereby negatively regulates SERT expression.

When infused into the locus coeruleus, fluoxetine failed to induce any change in miR-16 expression (fig. S6), which is in agreement with the lack of SERT expression in noradrenergic neurons under basal conditions. In contrast, upon infusion of fluoxetine into raphe, we monitored a 30% reduction in miR-16 in the locus coeruleus (Fig. 3A), associated with a decrease in GSK3 $\beta$  activity (fig. S5B). This down-regulation of miR-16 was accompanied by the induction of SERT expression, as well as tryptophan hydroxylase



Fluoxetine induces 1C11<sup>5-HT</sup> cells to release S100 $\beta$ , which decreases miR-16 expression and triggers the implementation of serotonergic markers in 1C11<sup>NE</sup> cells. (A) Treatment of 1C11<sup>5-HT</sup> cells with fluoxetine (50 nM) for 2 days increased the extracellular content of S100 $\beta$ . (B to F) 1C11<sup>5-HT</sup> or 1C11<sup>NE</sup> cells were exposed to S100 $\beta$  (1 nM) for 2 days. (B) The level of miR-16 as analyzed by real-time PCR was decreased in 1C11<sup>5-HT</sup> and 1C11<sup>NE</sup> cells. (C) S100 $\beta$  did not affect SERT expression in 1C11<sup>5-HT</sup> cells, whereas it induced the expression of SERT in 1C11<sup>NE</sup> cells ([ $^3$ H]-paroxetine binding). In 1C11<sup>NE</sup> cells, S100 $\beta$  triggered de novo 5-HT synthesis (detection of TPH activity) (D), 5-HT intracellular content (E), and 5-HT<sub>2B</sub> receptor expression ([ $^3$ H]-LY 266097 binding) (F). Data are means  $\pm$  SEM of seven independent experiments, \* $P$  < 0.01 versus control.



(TPH) activity and 5-HT<sub>2B</sub> receptors (Fig. 3, B to D). Confocal microscopy confirmed that SERT induction occurred in tyrosine hydroxylase-positive neurons (fig. S7). Thus, the locus coeruleus responds to fluoxetine injection in raphe by switching on serotonergic functions. Likewise, in a more clinically relevant paradigm, 20 days after daily intraperitoneal injection of fluoxetine into mice, we measured a 27% decrease of miR-16 associated with an expression of SERT molecules in the locus coeruleus (fig. S8, A and B).

The question then arises of how the response of serotonergic neurons to fluoxetine treatment is relayed to noradrenergic neurons in vivo. Reciprocal connections exist between these two brain-stem monoaminergic nuclei, thus supporting communication between the two systems (16). Recently, the expression of miR-16 in monocytes was shown to be down-regulated by S100 $\beta$  (17), a neurotrophic protein that is up-regulated by fluoxetine treatment (18). We therefore hypothesized that the secretion of S100 $\beta$  increases upon exposure of raphe to fluoxetine and that this protein acts as a paracrine factor to promote the reduction in miR-16 in the locus coeruleus, in turn unlocking the expression of serotonergic functions. We first exposed IC11<sup>5-HT</sup> cells to fluoxetine and observed an accumulation of S100 $\beta$  in the culture medium (Fig. 4A). Although the addition of S100 $\beta$  slightly decreased miR-16 levels in these serotonergic cells (Fig. 4B), it did not affect SERT expression (Fig. 4C), which is in agreement with the lack of impact of miR-16 silencing on SERT in IC11<sup>5-HT</sup> cells (Fig. 1B). A larger decrease (43% of control level) of miR-16 was seen in IC11<sup>NE</sup> cells exposed to S100 $\beta$  (Fig. 4B), which correlated with the appearance of SERT (Fig. 4C). In addition, after S100 $\beta$  treatment, IC11<sup>NE</sup> cells acquired the ability to synthesize and store 5-HT (Fig. 4, D and E) and to express 5-HT<sub>2B</sub> receptors (Fig. 4F). These data thus validate our working hypothesis on an in vitro level. We then measured the level of S100 $\beta$  in raphe upon infusion of fluoxetine. Fluoxetine up-regulated S100 $\beta$  levels in serotonergic nuclei (133% versus control) (Fig. 5A). Further, injection of S100 $\beta$  into the locus coeruleus decreased (by 22.4%) miR-16 levels and turned on the expression of SERT (Fig. 5, B and C). Finally, antibody-mediated neutralization of S100 $\beta$  in the locus coeruleus prevented the decrease in miR-16 levels observed upon infusion of fluoxetine in raphe (Fig. 5D). In addition, the decrease in miR-16 and the onset of SERT expression observed in the locus coeruleus, upon systemic fluoxetine treatment, were both eliminated by small interfering RNA-mediated knockdown of S100 $\beta$  in raphe (fig. S8, A and B). The data from IC11<sup>5-HT</sup> cells (Fig. 4A) and the innervation of the locus coeruleus by raphe fibers (16) strengthen the hypothesis that secretion of S100 $\beta$  by serotonergic neurons, at the locus coeruleus, mediates the action of fluoxetine. Secretion of S100 $\beta$  by glial cells in the raphe is less likely to promote a long-range action on the locus coeruleus.

Finally, we demonstrated the potential benefit of the fluoxetine-induced regulation of miR-16 in two mouse models of depression: the forced swimming test (FST) (fig. S9) and the unpredictable chronic mild stress (UCMS) paradigm (19, 20). Mice exposed to a 6-week UCMS regimen exhibited a deterioration of coat state and reductions in body weight gain, sucrose preference, and loco-

motor activity that were alleviated to the same extent either by chronic infusion of fluoxetine or miR-16 into raphe or by anti-miR-16 into the locus coeruleus (Fig. 5, E to H) (21).

Our study identifies the SERT-targeting miRNA miR-16 as a player in relaying SSRI antidepressant action (fig. S10). Fluoxetine operates directly on serotonergic raphe nuclei by

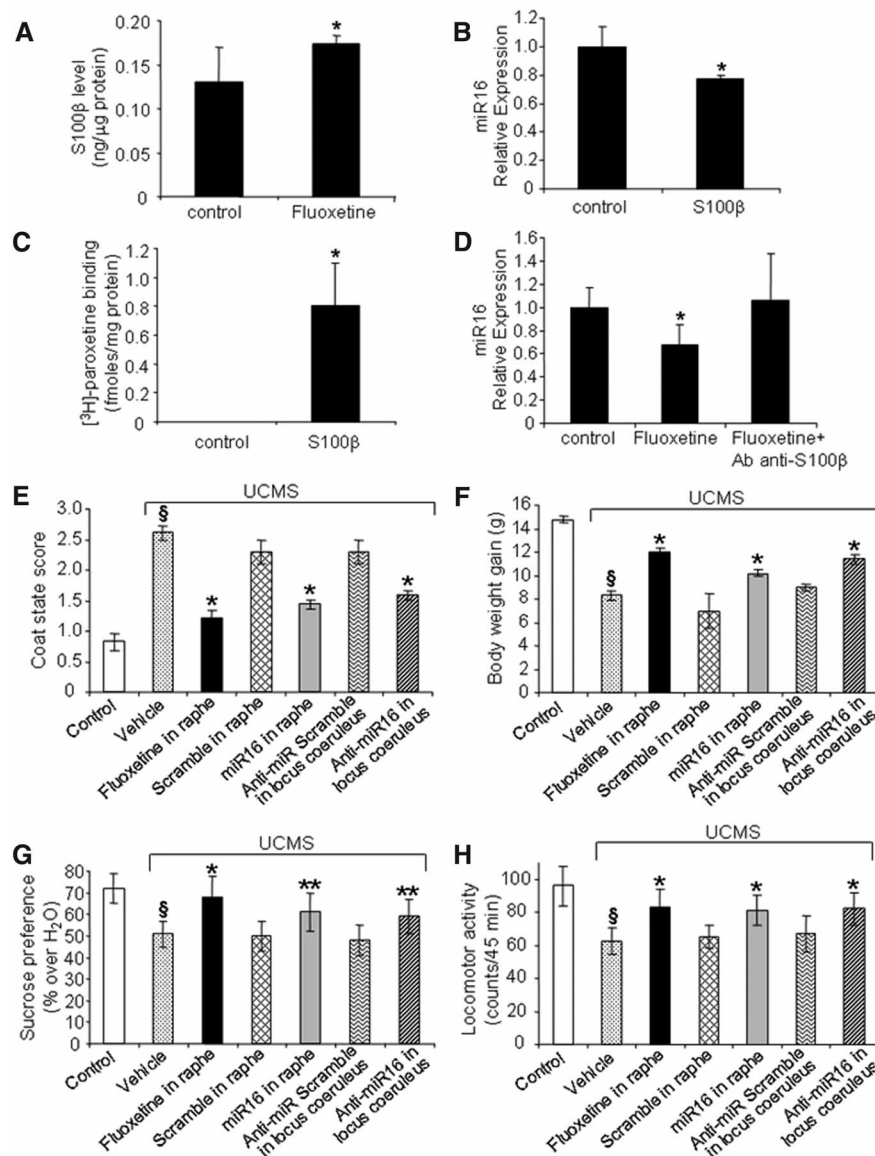


**Fig. 5.** Fluoxetine injection into raphe acts on the locus coeruleus via S100 $\beta$  and induces behavioral responses that are mimicked by increases in miR-16 in raphe or decreases in miR-16 in the locus coeruleus. (A) Chronic stereotaxic injection of fluoxetine (1  $\mu$ M, 2  $\mu$ L/min, 3 days) into mouse raphe induced S100 $\beta$  efflux. (B and C) Stereotaxic injection of S100 $\beta$  (1 nM, 2  $\mu$ L/min, 1 day) into the mouse locus coeruleus decreased miR-16 (B) and induced SERT expression (C) in locus coeruleus extracts as determined by real-time PCR and [ $^3$ H]-paroxetine binding, respectively. (D) Injection of antibodies against S100 $\beta$  (1  $\mu$ g/ml, 24 hours) into the locus coeruleus prevented the down-regulation of miR-16 in this brain structure induced by chronic infusion of fluoxetine into raphe. Data are means  $\pm$  SEM ( $n$  = 7 animals), \* $P$  < 0.01 versus control. (E to H) Six-week UCMS-induced deterioration of the coat state score (E), reduction of body weight gain (F), and decreases in sucrose preference (G) and locomotor activity (H) were alleviated by stereotaxic injection of fluoxetine (1  $\mu$ M, 2  $\mu$ L/min, in the last 5 weeks) or miR-16 (1  $\mu$ L, 2  $\mu$ M, every 36 hours) into mouse raphe or anti-miR-16 (1  $\mu$ L, 2  $\mu$ M, every 36 hours) into the locus coeruleus. The injection of scrambled miRNAs did not yield any improvement in these tests. Data are means  $\pm$  SEM ( $n$  = 6 to 9 mice per group). \$ $P$  < 0.01 versus control, \* $P$  < 0.05, and \*\* $P$  < 0.01 versus vehicle UCMS.

increasing the maturation of miR-16 from its precursor pre/pri-miR-16. Raphe additionally responds to chronic fluoxetine treatment by releasing S100 $\beta$ , which in turn acts on the noradrenergic neurons of the locus coeruleus. By lowering miR-16 levels, S100 $\beta$  unlocks the expression of serotonergic functions in this noradrenergic brain area. Our pharmacological and behavioral data thus posit miR-16 as a central effector that regulates SERT expression and mediates the adaptive response of serotonergic and noradrenergic neurons to fluoxetine treatment.

## References and Notes

- G. E. Torres, R. R. Gainetdinov, M. G. Caron, *Nat. Rev. Neurosci.* **4**, 13 (2003).
- E. C. Azmitia, *Int. Rev. Neurobiol.* **77**, 31 (2007).
- O. Berton, E. J. Nestler, *Nat. Rev. Neurosci.* **7**, 137 (2006).
- Y. Qian, H. E. Melikian, D. B. Rye, A. I. Levey, R. D. Blakely, *J. Neurosci.* **15**, 1261 (1995).
- D. L. Murphy *et al.*, *Neuropharmacology* **55**, 932 (2008).
- S. Benmansour, W. A. Owens, M. Cecchi, D. A. Morilak, A. Frazer, *J. Neurosci.* **22**, 6766 (2002).
- D. P. Bartel, *Cell* **136**, 215 (2009).
- C. M. Croce, *Nat. Rev. Genet.* **10**, 704 (2009).
- K. S. Kosik, *Nat. Rev. Neurosci.* **7**, 911 (2006).
- V. K. Gangaraju, H. Lin, *Nat. Rev. Mol. Cell Biol.* **10**, 116 (2009).
- S. Mouillet-Richard *et al.*, *J. Biol. Chem.* **275**, 9186 (2000).
- J. M. Launay, B. Schneider, S. Loric, M. Da Prada, O. Kellermann, *FASEB J.* **20**, 1843 (2006).
- A. Frazer, *J. Clin. Psychopharmacol.* **17** (suppl. 1), 25 (1997).
- E. J. Nestler, M. Alreja, G. K. Aghajanian, *Biol. Psychiatry* **46**, 1131 (1999).
- G. Martello *et al.*, *Nature* **449**, 183 (2007).
- M. A. Kim, H. S. Lee, B. Y. Lee, B. D. Waterhouse, *Brain Res.* **1026**, 56 (2004).
- N. Shanmugam, M. A. Reddy, R. Natarajan, *J. Biol. Chem.* **283**, 36221 (2008).
- R. Manev, T. Uz, H. Manev, *Eur. J. Pharmacol.* **420**, R1 (2001).
- A. Surget *et al.*, *Neuropsychopharmacology* **34**, 1363 (2009).
- P. Willner, *Psychopharmacology (Berlin)* **134**, 319 (1997).
- Materials and methods and supporting data are available on Science Online.
- We thank P. Weil-Malherbe, V. Mutel, F. d'Agostini, G. Zürcher, E. Borroni, J. L. Moreau, F. Jenck, M. Bühler, and N. Pieron for skillful methodological assistance, and S. Blanquet, M. Briley, and L. Aggerbeck for critical reading of the manuscript. O.K. is a professor at Paris XI University. This work was funded by CNRS, ANR, and INSERM.

## Supporting Online Material

www.sciencemag.org/cgi/content/full/329/5998/1537/DC1

Materials and Methods

Figs. S1 to S10

References

14 June 2010; accepted 4 August 2010

10.1126/science.1193692

# Relating Introspective Accuracy to Individual Differences in Brain Structure

Stephen M. Fleming,<sup>1,\*†</sup> Rimona S. Weil,<sup>1,2,\*</sup> Zoltan Nagy,<sup>1</sup> Raymond J. Dolan,<sup>1</sup> Geraint Rees<sup>1,2</sup>

The ability to introspect about self-performance is key to human subjective experience, but the neuroanatomical basis of this ability is unknown. Such accurate introspection requires discriminating correct decisions from incorrect ones, a capacity that varies substantially across individuals. We dissociated variation in introspective ability from objective performance in a simple perceptual-decision task, allowing us to determine whether this interindividual variability was associated with a distinct neural basis. We show that introspective ability is correlated with gray matter volume in the anterior prefrontal cortex, a region that shows marked evolutionary development in humans. Moreover, interindividual variation in introspective ability is also correlated with white-matter microstructure connected with this area of the prefrontal cortex. Our findings point to a focal neuroanatomical substrate for introspective ability, a substrate distinct from that supporting primary perception.

Our moment-to-moment judgments of the outside world are often subject to introspective interrogation. In this context, introspective or “metacognitive” sensitivity refers

to the ability to discriminate correct from incorrect perceptual decisions (1), and its accuracy is essential for the appropriate guidance of decision-making and action (2, 3). For example, low confidence that a recent decision was correct may prompt us to reexamine the evidence or seek a second opinion. Recently, behavioral studies have begun to quantify metacognitive accuracy following simple perceptual decisions and to isolate variations in this ability: A decision may be made poorly, yet an individual may believe

that his or her performance was good, or vice versa (4–8). Whereas previous work has investigated how confidence in perceptual decisions varies from trial to trial (9, 10), little is known about the biological basis of metacognitive ability, defined here as how well an individual's confidence ratings discriminate correct from incorrect decisions over time. We hypothesized that individual differences in metacognitive ability would be reflected in the anatomy of brain regions responsible for this function, in line with similar associations between brain anatomy and performance in other cognitive domains (11–15).

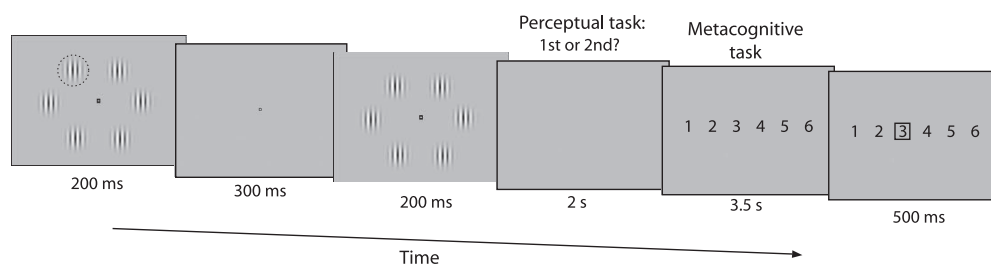
We objectively quantified variability in metacognitive sensitivity between individuals and then related these interindividual differences to brain structure measured with magnetic resonance imaging (MRI). This approach was motivated by observations that individual differences in a range of skills—such as language (11), decision-making (12), and memory (13)—are consistently associated with variation in healthy brain anatomy. Our experimental design dissociated a quantitative measure of metacognitive accuracy,  $A_{roc}$  (which is specific to an individual), from both objective task performance and subjective confidence (which both vary on a trial-by-trial basis). Earlier patient studies describe candidate brain regions in which damage is associated with poor introspective ability: in particular, a prefrontal-parietal network (16–18). Theories of prefrontal

<sup>1</sup>Wellcome Trust Centre for Neuroimaging, University College London, 12 Queen Square, London WC1N 3BG, UK. <sup>2</sup>Institute of Cognitive Neuroscience, University College London, 17 Queen Square, London WC1N 3AR, UK.

\*These authors contributed equally to this work.

†To whom correspondence should be addressed. E-mail: s.fleming@fil.ion.ucl.ac.uk

**Fig. 1. Behavioral task.** Participants completed a two-alternative forced-choice task that required two judgments per trial: a perceptual response followed by an estimate of relative confidence in their decision. The perceptual response indicated whether the first or second temporal interval contained the higher-contrast (pop-out) Gabor patch (highlighted here with a dashed circle that was not present in the actual display), which could appear at any one of six locations around a central fixation point. Pop-out Gabor contrast was continually adjusted with the use of a staircase procedure to maintain ~71% performance. Confidence ratings were



made using a one-to-six scale, with participants encouraged to use the whole scale from one = low relative confidence to six = high relative confidence. The black square in the rightmost panel indicates the choice made in the metacognitive task.



function have emphasized a role for anterior (rostrolateral) prefrontal cortex (PFC) in carrying out second-order operations on internally generated information (19, 20), a process necessary for metacognition. We hypothesized that the local structure of these regions (both gray-matter volume and white-matter integrity) might reflect an individual's metacognitive ability.

We studied 32 healthy human participants while they made a series of visual judgements (21). The difficulty of the visual judgement was varied on a per-participant basis to keep performance at a constant level (71%), near sensory threshold. In addition to asking participants to make these objective perceptual judgements, we also asked them to provide ratings of confidence in their decisions after each trial (Fig. 1). We then used these ratings to determine metacognitive ability at an individual level through the construction of type II receiver operating characteristic (ROC) curves (Fig. 2A) (21–23). The ROC model provided an excellent fit to our data across participants (mean explained variance  $R^2 = 0.97 \pm 0.023$ ). The area between the major diagonal and an individual's ROC curve is a measure of the ability to link confidence to perceptual performance ( $A_{\text{roc}}$ ). We found considerable variation across individuals in metacognitive ability ( $A_{\text{roc}} = 0.55$  to  $0.75$ ), despite underlying task performance being held constant (proportion correct: 70 to 74%); furthermore, these measures were uncorrelated (Pearson's correlation coefficient  $r = -0.21$ ,  $P = 0.24$ ). To establish whether this variability was stable, we split data from each participant into two halves and computed the test-retest reliability of the two sets. This analysis revealed intraparticipant consistency in  $A_{\text{roc}}$  ( $r = 0.69$ ,  $P = 0.00001$ ) (fig. S2).

Having quantified interindividual variability in introspection, we then asked whether this variability in introspective judgements was predicted by variability in brain structure using two distinct measures: gray-matter volume measured from T1-weighted anatomical images and the fractional anisotropy (FA) of white matter measured from diffusion tensor images. Our analysis examined the possible relation between brain structure and four different measures: the metacognitive ability ( $A_{\text{roc}}$ ) of our participants, objective performance on the perceptual task (sensitivity,  $d'$ , and criterion,  $c$ ), and the tendency to use high or low confidence responses on individual trials ( $B_{\text{roc}}$ ) [see supporting online material (SOM) methods section for details]. Having removed the potentially confounding factors (24) of overall brain size and gender (as regressors of no interest), we found that an individual's metacognitive ability ( $A_{\text{roc}}$ ) was significantly correlated with gray-matter volume in the right anterior PFC (Fig. 3A) [Brodmann area (BA) 10; peak voxel coordinates: [24, 65, 18];  $t_{\text{max}} = 4.8$ ;  $P < 0.05$ , corrected for multiple comparisons]. Furthermore, gray-matter volume in this region did not correlate with task performance, as indexed by  $d'$  (Fig. 3B) ( $r = 0.15$ ,  $P = 0.42$ ), or overall confidence ( $B_{\text{roc}}$ ) ( $r = -0.023$ ,  $P = 0.90$ ).

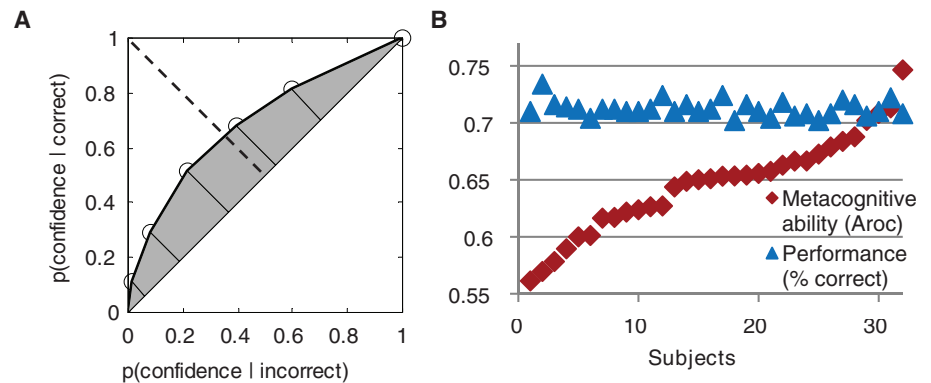


**Fig. 2.** ROC calculation and behavioral performance. (A) Participants' confidence ratings were used to construct a type II ROC function that quantifies the ability to discriminate between correct and incorrect responses cumulated across levels of confidence.  $A_{\text{roc}}$  was calculated as the shaded area between the ROC curve and the major diagonal (21). Mutually perpendicular dotted and solid lines represent the minor and major diagonals, respectively. (B) Plot of the relation between task performance (percentage correct) and  $A_{\text{roc}}$ , with participants ordered by increasing  $A_{\text{roc}}$  value.

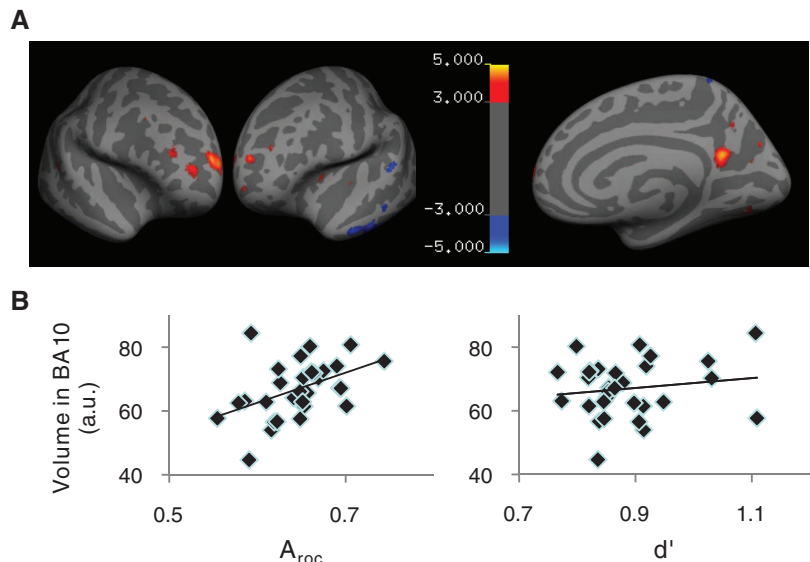


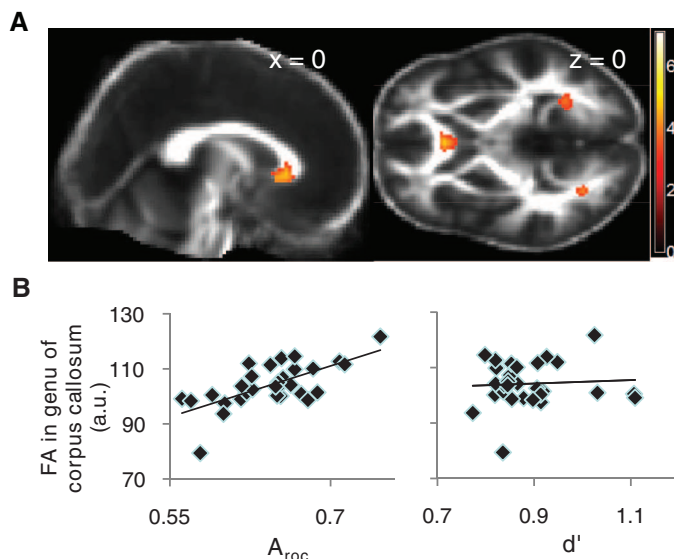
**Fig. 3.** Gray-matter volume correlated with introspective ability. (A) Projection of statistical (T) maps for positive (hot color map: red, orange, yellow) and negative (cool color map: blue) correlations with  $A_{\text{roc}}$  onto an inflated cortical surface (T1-weighted template, thresholded at  $T > 3$  for display purposes). Significant clusters ( $P < 0.05$ , corrected for multiple comparisons) where metacognitive ability correlated with gray-matter volume (see SOM methods) were found in right anterior PFC (BA 10; positive correlation) and the left inferior temporal gyrus (negative correlation), accompanied by contralateral homologous clusters at  $P < 0.001$ , uncorrected. (B) Plot of gray-matter volume in the right BA 10 cluster against both  $A_{\text{roc}}$  and  $d'$  (see SOM methods for full details), indicating that the correlation with metacognitive ability was independent of task performance. a.u., arbitrary units.

Gray-matter volume in a homologous region in the left anterior PFC was also correlated with  $A_{\text{roc}}$  but did not survive correction for multiple comparisons across the brain volume. Details of this and other clusters that did not survive a whole-brain correction are listed in table S2. Thus, variability in introspective judgements of performance on a simple visual-detection task was predicted by variability in the anatomical structure of the anterior PFC (BA 10), independently of both objective performance and level of confidence. Finally, whereas our primary question addressed positive dependence of gray matter on  $A_{\text{roc}}$ , we also found that the left inferior tem-

poral gyrus showed a negative correlation with metacognitive sensitivity (Fig. 3A) (coordinates:  $[-56, -30, -26]$ ;  $t_{\text{max}} = 4.66$ ;  $P < 0.05$ , corrected for multiple comparisons), accompanied by a similar region on the right that did not survive correction for multiple comparisons (see table S2 for full details and coordinates).

After we established that gray-matter volume was predictive of  $A_{\text{roc}}$ , we next analyzed white-matter microstructure. If the structure of the anterior PFC is functionally related to metacognitive performance, we hypothesized that white-matter tracts connected with this region would also show a similar microstructural correlation with

**Fig. 4.** White-matter microstructure correlated with introspective ability. **(A)** Statistical ( $T$ ) map of voxelwise correlations between FA and  $A_{roc}$  thresholded at  $T > 3$  for display purposes and overlaid on sagittal (left) and axial (right) slices of the average FA image across participants, at the  $x$  and  $z$  coordinates indicated. A region within the genu of the anterior corpus callosum showed a correlation between FA and metacognitive ability that was statistically significant after correcting for multiple comparisons ( $P < 0.05$ ). **(B)** Plot of FA in the anterior corpus callosum cluster against both  $A_{roc}$  and  $d'$ , indicating that the correlation with metacognitive ability was independent of task performance.



expression of this behavioral trait. In a whole-brain analysis of white-matter microstructure (21), we found that FA (a measure of white-matter integrity) in the genu of the corpus callosum was positively dependent on  $A_{roc}$  (Fig. 4) ( $P < 0.05$ , corrected for multiple comparisons). This specific subdivision of the corpus callosum contains white-matter fibers connected with the anterior and orbital PFCs in humans (25), consistent with metacognitive ability being dependent not only on anterior prefrontal gray matter but also on reciprocal projections to and from this area. Neither objective performance (stimulus contrast or  $d'$ ) nor overall confidence ( $B_{roc}$ ) correlated with gray-matter volume or white-matter FA elsewhere in the brain ( $P > 0.05$ , corrected for multiple comparisons; see tables S2 and S3 for uncorrected correlations). We note that an absence of structural correlations with these parameters may have been due to our design deliberately minimizing variability in both  $d'$  and  $B_{roc}$  to isolate the neural correlates of introspective ability ( $A_{roc}$ ).

One concern is that the structural covariation that we observed may have been potentially confounded by differences in perceptual ability. Good perceptual ability may be reflected in the staircase procedure converging on consistently low values for stimulus contrast for a given individual. Therefore, we carried out control analyses (table S4) (21) to rule out this alternative explanation. These results demonstrated significant correlations of gray matter and FA with  $A_{roc}$  in the anterior PFC when controlling for changes in task parameters and an absence of correlations with task parameters themselves. Thus, the structure-behavior correlations we observed here are unlikely to be due to low-level differences in performance, but instead relate to underlying differences in individual metacognitive ability.

How might these regions contribute to metacognition? Anterior subdivisions of the PFC have

been implicated in high-level control of cognition (19, 20, 26, 27) and are well placed to integrate supramodal perceptual information with decision output (28), a process thought to be key for metacognitive sensitivity (1). Dorsolateral prefrontal activity increases under conditions in which subjective reports match objective perceptual performance (29), suggesting a computational role in linking performance to confidence. Consistent with prefrontal gray-matter volume playing a causal role in metacognition, patients with lesions to the anterior PFC show deficits in subjective reports as compared with controls, after factoring out differences in objective performance (16). Furthermore, impairing dorsolateral PFC function with theta-burst transcranial magnetic stimulation compromises the metacognitive sensitivity of subjective reports of awareness but leaves underlying task performance intact (30). Together with the present work, these findings suggest a central role for anterior and dorsolateral PFC in metacognitive sensitivity. Our present findings may reflect innate differences in anatomy or, alternatively, may reflect the effects of experience and learning, as has been found in the sensorimotor domain (14, 15). This raises the tantalizing possibility of being able to “train” metacognitive ability by harnessing underlying neural plasticity in the regions that we identify here (31).

Our main finding is a delineation of a noticeably focal anatomical substrate that predicts interindividual variability in metacognitive ability. As with any correlational method, we cannot establish whether the covariation we observed between brain structure and metacognition reflects a causal relation. However, given a wealth of evidence for changes in gray-matter volume within and between individuals associated with a range of skills, we propose that underlying differences in metacognitive ability are similarly dependent on large-scale brain anatomy. Our data provide an in-

tial window to the biological basis of the ability to link objective performance to subjective confidence. The demonstration that this ability may be dependent on local and phylogenetically recent prefrontal anatomy is consistent with a conjecture that metacognitive function has been selected for during evolution (32), facilitating computations that allow us to introspect about self-performance.

## References and Notes

1. A. Cleeremans, B. Timmermans, A. Pasquali, *Neural Networks* **20**, 1032 (2007).
2. J. Metcalfe, *Metacognition: Knowing About Knowing* (MIT Press, Cambridge, MA, 1996).
3. H. C. Lau, *Prog. Brain Res.* **168**, 35 (2007).
4. D. A. Washburn, J. D. Smith, L. A. Tagliatela, *J. Gen. Psychol.* **132**, 446 (2005).
5. C. Kunitomo, J. Miller, H. Pashler, *Conscious. Cogn.* **10**, 294 (2001).
6. R. Szczepanowski, L. Pessoa, *J. Vis.* **7**, 1 (2007).
7. M. Graziano, M. Sigman, A. Rustichini, *PLoS ONE* **4**, e4909 (2009).
8. S. M. Fleming, R. J. Dolan, *Conscious. Cogn.* **19**, 352 (2010).
9. R. Kiani, M. N. Shadlen, *Science* **324**, 759 (2009).
10. A. Kepecs, N. Uchida, H. A. Zariwala, Z. F. Mainen, *Nature* **455**, 227 (2008).
11. M. Carreiras et al., *Nature* **461**, 983 (2009).
12. D. S. Tuch et al., *Proc. Natl. Acad. Sci. U.S.A.* **102**, 12212 (2005).
13. L. Fuentesilla et al., *J. Neurosci.* **29**, 8698 (2009).
14. J. Scholz, M. C. Klein, T. E. J. Behrens, H. Johansen-Berg, *Nat. Neurosci.* **12**, 1370 (2009).
15. B. Draganski et al., *Nature* **427**, 311 (2004).
16. A. Del Cul, S. Dehaene, P. Reyes, E. Bravo, A. Slachevsky, *Brain* **132**, 2531 (2009).
17. A. P. Shimamura, *Conscious. Cogn.* **9**, 313 (2000).
18. J. S. Simons, P. V. Peers, Y. S. Mazuz, M. E. Berryhill, I. R. Olson, *Cereb. Cortex* **20**, 479 (2010).
19. P. C. Fletcher, R. N. A. Henson, *Brain* **124**, 849 (2001).
20. K. Christoff, J. D. E. Gabrieli, *Psychobiology* **28**, 168 (2000).
21. Materials, methods, discussion of ROC model fits, and details of control analyses are available as supporting material on Science Online.
22. S. J. Galvin, J. V. Podd, V. Drga, J. Whitmore, *Psychon. Bull. Rev.* **10**, 843 (2003).
23. D. E. Kornbrot, *Percept. Psychophys.* **68**, 393 (2006).
24. C. D. Smith, H. Chebrolu, D. R. Wekstein, F. A. Schmitt, W. R. Markesbery, *Neurobiol. Aging* **28**, 1075 (2007).
25. H. J. Park et al., *Hum. Brain Mapp.* **29**, 503 (2008).
26. N. D. Daw, J. P. O'Doherty, P. Dayan, B. Seymour, R. J. Dolan, *Nature* **441**, 876 (2006).
27. P. W. Burgess, I. Dumontheil, S. J. Gilbert, *Trends Cogn. Sci.* **11**, 290 (2007).
28. N. Ramnani, A. M. Owen, *Nat. Rev. Neurosci.* **5**, 184 (2004).
29. H. C. Lau, R. E. Passingham, *Proc. Natl. Acad. Sci. U.S.A.* **103**, 18763 (2006).
30. E. Rounis et al., *Cognit. Neurosci.* **1**, 165 (2010).
31. E. B. Titchener, *Lectures on the Experimental Psychology of the Thought-Processes* (Macmillan, New York, 1909).
32. J. Metcalfe, in *Handbook of Metamemory and Memory*, J. Dunlosky, R. A. Bjork, Eds. (Psychology Press, New York, 2008), pp. 27–46.
33. This research was funded by the Wellcome Trust (G.R., R.J.D., Z.N.), the University College London four-year Ph.D. program in neuroscience (S.M.F.), and the Medical Research Council (R.S.W.). We thank T. Sharot, G. Ridgway, and C. Frith for comments on earlier drafts of this manuscript.

## Supporting Online Material

www.sciencemag.org/cgi/content/full/329/5998/1541/DC1

Materials and Methods

SOM Text

Figs. S1 to S4

Tables S1 to S4

References

5 May 2010; accepted 23 July 2010

10.1126/science.1191883



## NEW PRODUCTS



## 8-CHANNEL DECAPPER

The 8-Channel Decapper is designed for handheld capping and decapping of multiple tubes in a 96-well microplate footprint. This handheld decapper is ideal for any laboratory requiring faster, uniform capping that doesn't necessitate a fully-automated system. The reliable Thermo Scientific 8-Channel Decapper is capable of uncapping a column of eight screw-top tubes in just four seconds, enabling researchers to increase the speed of access to samples and their return to storage. The caps are tightened uniformly and at the optimal torque to prevent any spills or leakages, to maintain sample integrity, and to avoid sample loss during cryogenic storage and freeze-thaw cycles. As an ideal mid-point between manual and automated capping, the handheld Thermo Scientific 8-Channel Decapper enables laboratories to decap only a single column as needed and to significantly improve efficiency.

Thermo Fisher Scientific

For info: 800-522-7763 | [www.thermofisher.com/8chcapper](http://www.thermofisher.com/8chcapper)

## FLUORESCENCE IMAGING OPTICAL FILTERS

Four new optical filter sets for fluorescence imaging enable the choice of substantially increased brightness or enhanced contrast when imaging the ubiquitous fluorescent labels fluorescein (FITC) and green fluorescent protein (GFP). These new BrightLine filter sets allow the user to either minimize photobleaching while increasing image contrast, or receive a light boost for a noticeably brighter image, particularly in low-concentration applications such as single-molecule imaging. The single-band filter sets GFP-1828-A and FITC-2024-A offer the highest contrast of filter sets available today, while the GFP-4050-A and FITC-5050-A sets give the user the highest brightness among sets optimized for these fluorophores. The hard-coated filter manufacturing process ensures permanent performance with "no burn-out" even under the most intense illumination conditions. Custom-sized filters are available.

Semrock

For info: 866-736-7625 | [www.semrock.com](http://www.semrock.com)

## DARKBOX ENCLOSURES

Customized darkbox enclosures are designed to block all ambient light for production, testing, or research in the optics field. These mobile structures can be produced to customer-specific requirements, feature sliding or fixed panels on all four sides, and can be large enough to incorporate optical tables, breadboards, or workstations. The enclosures are available with heating and air conditioning, electrical connections, laser ports, and/or computer network (LAN) connections. Multiple tiers of shelving are offered for cameras, spectrometers, reflectors, vibration-damping breadboards, benchtop vibration-isolation platforms, monitor stands, and power supplies. Lighting is also available for assembly, installation, or repositioning.

Kinetic Systems, Inc.

For info: 617-522-8700 | [www.kineticsystems.com](http://www.kineticsystems.com)

## MICROPLATE BLOWDOWN STATION

Designed to quickly and safely remove solvents from 96- or 384-well plates, the Ultravap Blowdown Station is a versatile tool that optimizes microplate sample preparation productivity. The Ultravap achieves high sample throughput through advanced evaporator head technology and an innovative manifold design, which directly injects heated nitrogen into each individual well of the microplate simultaneously. The system is proven to remove most popular chromatography solvents in just minutes. For heat sensitive and thermally labile samples the Ultravap may be operated in a unique two-stage mode combining rapid initial dry-down with carefully controlled final solvent evaporation. The Ultravap has been designed to be simple to install, operate, and maintain. Different drying programs can be retained in the memory eliminating the need to set up the system when changing from one method to another.

Porvair Sciences

For info: +44-(0)-1372-824290 | [www.porvair-sciences.com](http://www.porvair-sciences.com)

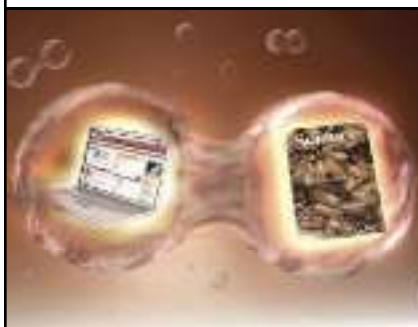
## STORAGE TUBE CAPS

Designed to increase productivity and eliminate expensive tube capping systems, Capcluster sample storage caps offer the unique versatility of single action capping of a single tube, a row of tubes, or a complete 96-tube rack. With a choice of 11 different colors, these caps provide a simple, yet highly effective means of visually differentiating stored samples. Each hydrophobic cap is manufactured from USP Class VI certificated Thermoplastic Elastomer (TPE) and is multipierceable allowing it to be cost effectively used up to 12 times without losing its seal integrity. The TPE caps have high solvent resistance that, in combination with ultralow extractable materials, eliminates the possibility of sample contamination from the tube cap.

Micronic Europe BV

For info: 724-941-6411 | [www.micronicna.com](http://www.micronicna.com)

Electronically submit your new product description or product literature information! Go to [www.sciencemag.org/products/newproducts.dtl](http://www.sciencemag.org/products/newproducts.dtl) for more information. Newly offered instrumentation, apparatus, and laboratory materials of interest to researchers in all disciplines in academic, industrial, and governmental organizations are featured in this space. Emphasis is given to purpose, chief characteristics, and availability of products and materials. Endorsement by *Science* or AAAS of any products or materials mentioned is not implied. Additional information may be obtained from the manufacturer or supplier.



## Science Careers Classified Advertising

For full advertising details, go to  
ScienceCareers.org and click For Employers,  
or call one of our representatives.

### Tracy Holmes

Worldwide Associate Director  
Science Careers  
Phone: +44 (0) 1223 326525

### UNITED STATES & CANADA

E-mail: [advertise@sciencecareers.org](mailto:advertise@sciencecareers.org)  
Fax: 202-289-6742

### Tina Burks

Midwest/West Coast/  
South Central/Canada  
Phone: 202-326-6577

### Elizabeth Early

East Coast & Industry  
Phone: 202-326-6578

### Online Job Posting Questions

Phone: 202-326-6577

### EUROPE & REST OF WORLD

E-mail: [ads@science-int.co.uk](mailto:ads@science-int.co.uk)  
Fax: +44 (0) 1223 326532

### Alex Palmer

Phone: +44 (0) 1223 326527

### Susanne Kharraz Tavakoli

Phone: +44 (0) 1223 326529

### Dan Pennington

Phone: +44 (0) 1223 326517

### Lisa Patterson

Phone: +44 (0) 1223 326528

### JAPAN

#### ASCA Corporation

Jie Chin  
Phone: +81-3-6802-4616  
Fax: +81-3-6802-4615  
E-mail: [careerads@sciencemag.jp](mailto:careerads@sciencemag.jp)

### To subscribe to Science:

In US call 866 434-2227  
In the rest of the world call +1 202 326-6417

All ads submitted for publication must comply with applicable US and non-US laws. *Science* reserves the right to refuse any advertisement at its sole discretion for any reason, including without limitation for offensive language or inappropriate content, and all advertising is subject to publisher approval. *Science* encourages our readers to alert us to any ads that they feel may be discriminatory or offensive.

**Science Careers**

From the journal *Science*



## UNIVERSITÄT BASEL

### Professor in Advanced Biological Imaging

The Biozentrum of the University of Basel in Switzerland invites applications for a Tenure-track Assistant Professorship in Advanced Biological Imaging. The ideal candidate will work at the forefront of advanced imaging, developing and applying fluorescence-based optical methods (e.g. super-resolution light microscopy), to study biological problems. With a strong research record and proven communication skills, the successful candidate will strengthen the research portfolio of the Biozentrum and actively participate in teaching at the undergraduate and post-graduate level. In addition, he/she is invited to interact with other Life Science institutions in Basel as well as the Swiss Nanoscience Institute.

The Biozentrum offers an outstanding scientific environment and an attractive research endowment, while Basel provides a high standard of living and a superb cultural atmosphere. Applications, including CV, list of publications and a short research summary, should be addressed to Prof. Dr. Martin Spiess, Dean, Faculty of Science, University of Basel, Klingelbergstrasse 50, 4056 Basel, Switzerland, and also be provided in electronic form (pdf or zip) to [Dekanat-Philnat@unibas.ch](mailto:Dekanat-Philnat@unibas.ch). For informal enquiries please contact Prof. Dr. Erich A. Nigg ([erich.nigg@unibas.ch](mailto:erich.nigg@unibas.ch), phone: +41-61-267 16 56).

The deadline for receipt of applications is November 30, 2010. The University of Basel is an equal opportunity employer and encourages applications from female candidates.



**550**  
JAHRE  
WISSEN  
BEWEGT  
UNS

## UCLA

### Systems Biology and Physiology and California NanoSystems Institute

The UCLA Department of Integrative Biology and Physiology and the California NanoSystems Institute (CNSI) invite applications for a tenure-track faculty position (Assistant Professor) beginning as early as July 2011. Exceptional candidates will be considered at a higher rank. We seek applicants with expertise in Computational Systems Biology with a focus on understanding properties of physiological systems (see [www.IBP.ucla.edu](http://www.IBP.ucla.edu) for more information and to apply). The successful candidate will be expected to participate in undergraduate and graduate teaching and to establish a vigorous externally funded research program. Review of applications will begin October 15, 2010, but applications received afterwards will be considered until the position is filled. Please use the following job number: **0845-1011-01** in all correspondence. Salary is commensurate with experience.

*UCLA is an Equal Opportunity/Affirmative Action Employer. The Department and CNSI have a strong commitment to the achievement of excellence and diversity among its faculty, staff, and students. Candidates with a history of fostering underrepresented minorities in the sciences are encouraged to apply.*



### Joslin Diabetes Center Harvard Medical School Immunology Research Type 1 Diabetes in Humans

Joslin Diabetes Center is recruiting an investigator in the areas of clinical or translational immunology research relevant to patients with type 1 diabetes. The ideal candidate will develop a vibrant research program. The expected initial academic appointment at Harvard Medical School is Assistant Professor. Initial support will be a start-up package commensurate with the applicant's qualifications; this should be supplanted over time by independent grant support. There will be opportunities to participate in TrialNet. The recruit will also have opportunities to interact with immunologists at Joslin and throughout the Harvard Medical area, and is encouraged to interact with students in and become a faculty member of the HMS Immunology Program. Applicants should forward a letter of interest, CV, and 3 references to:

**Steven E. Shoelson, M.D., Ph.D.**  
Professor of Medicine,  
Harvard Medical School  
Joslin Diabetes Center  
1 Joslin Place, Boston, MA 02215

*Harvard Medical School and the Joslin Diabetes Center are Equal Opportunity/Affirmative Action Employers. Women and minorities are highly encouraged to apply.*



**UC DAVIS**  
SCHOOL OF MEDICINE

**FACULTY POSITION**

**THE CENTER FOR COMPARATIVE MEDICINE**  
Schools of Medicine and Veterinary Medicine  
University of California, Davis

Candidates are sought for a tenure-track position at the level of **ASSISTANT** or **ASSOCIATE PROFESSOR/ASSISTANT** or **ASSOCIATE PROFESSOR IN RESIDENCE** in the Center for Comparative Medicine, a research center at the University of California, Davis, co-sponsored by the Schools of Medicine and Veterinary Medicine and a relevant Instructional and Research (I&R) academic department. The center is engaged in investigative research involving animal models of human disease. We seek individuals with Ph.D., D.V.M. and/or M.D. degrees, postdoctoral experience and a record of publication in high-quality journals. We are soliciting applications from candidates who have enthusiasm for the investigation of human infectious diseases in animal models and the concepts of "One Health". Candidates are expected to have or to establish and maintain a strong extramurally funded research program and to participate in professional and graduate education in their fields. Ample office and laboratory space is available in the Center (including access to BSL2 and BSL3 laboratory space), with state-of-the art facilities, instrumentation, and administrative support. Center research and teaching programs interdigitate with other campus-wide programs and resources in the Schools of Medicine and Veterinary Medicine, the Mouse Biology Program, the California National Primate Research Center, and the Cancer Center. Faculty members will hold an academic appointment in the commensurate department of the School of Veterinary Medicine. The position will provide 0.5 salary support. Review of applications will commence immediately until the position is filled. Priority will be given to applications received by October 1, 2010.

Submit applications with letter of interest, curriculum vitae, concise statement of present and future research plans, summary of teaching experience, up to three representative reprints, and names of four references (including addresses, telephone numbers and e-mail addresses) to: **Recruitment Committee Chair, c/o Center for Comparative Medicine, University of California, Davis, CA 95616.**

*The University of California is an Equal Opportunity/Affirmative Action Employer.*

**Faculty Position**  
**Molecular Biology**  
**Sloan-Kettering Institute**

The Molecular Biology Program of the Sloan-Kettering Institute, Memorial Sloan-Kettering Cancer Center ([www.ski.edu](http://www.ski.edu)), has initiated a faculty search at the Assistant Member level (equivalent to Assistant Professor). We are interested in outstanding individuals who have demonstrated records of significant accomplishment and the potential to make substantial contributions to the biological sciences as independent investigators. Successful applicants will have research interests that move the Program into exciting new areas that complement and expand our existing strengths in the areas of maintenance of genomic integrity, regulation of the cell cycle, and regulation of gene expression. Faculty will be eligible to hold appointments in the Gerstner Sloan-Kettering Graduate School of Biomedical Sciences, the Weill Cornell Graduate School of Medical Sciences, as well as the Tri-Institutional MD/PhD Training Program.

The deadline for applications is **November 1, 2010**. Interested candidates should visit <http://facultysearch.ski.edu> to access the on-line faculty application. Please visit the site as soon as possible, as it contains important information on the required application materials, including deadlines for submission of letters of reference.

Informal inquiries may be sent to **Julie Kwan** at [kwaj@mskcc.org](mailto:kwaj@mskcc.org) or to **Dr. Kenneth Mariani**, Chair, Molecular Biology Program at [kmarians@sloankettering.edu](mailto:kmarians@sloankettering.edu). MSKCC is an equal opportunity and affirmative action employer committed to diversity and inclusion in all aspects of recruiting and employment. All qualified individuals are encouraged to apply.



**Memorial Sloan-Kettering  
Cancer Center**

[www.mskcc.org](http://www.mskcc.org)



**MAKE AN IMPACT**

**Linus Pauling Distinguished Postdoctoral Fellowship**

Pacific Northwest National Laboratory in Richland, Washington, is seeking the next generation of scientists and engineers for its **2011 Linus Pauling Distinguished Postdoctoral Fellowship**. Pauling Fellows will be actively mentored by internationally recognized scientists and equipped with the resources to carry out a research program of their own design. They will have opportunities to contribute to research efforts that advance scientific frontiers and solve pressing challenges for the nation.

Applications open September 1, 2010.  
See <http://www.pnl.gov/pauling/index.stm> to apply.

PNNL is an Equal Opportunity Employer

**Burnett School of Biomedical Sciences**  
**College of Medicine**

**Associate Director**

Burnett School of Biomedical Sciences, College of Medicine seeks an Associate Director to provide leadership to its research enterprise. The school is expanding its research programs in Cancer, Cardiovascular and Metabolic, Neurodegenerative and Infectious diseases into the new 198,000 sq.ft. Burnett Biomedical Science Building. The school will be recruiting more than a dozen new faculty within the next few years. The Burnett School has over 2400 majors and over 14,000 students are enrolled in the courses taught by the school faculty. The school offers MS and PhD degrees and MS/MBA and PhD/MBA programs.

The Associate Director is expected to maintain a highly funded research program in any of the four focus areas of the school and provide leadership to the entire research enterprise and graduate programs of the school. The successful candidate must hold an earned doctorate in a discipline appropriate to the school and must have a distinguished record of scholarly accomplishment meriting appointment with tenure at the rank of professor in the school.

A leadership role in recruiting new faculty will be expected. State of the art research facilities including shared core instrumentation and a large transgenic animal facility are available in the Burnett School. UCF the nation's third largest university, ranked third in innovation and patents, is located in the great metropolitan area of Orlando. The Burnett Biomedical Science building is located in the new Health Science campus at Lake Nona that is home also for the new College of Medicine, Sanford-Burnham Medical Research Institute, Nemours Children's Hospital and VA hospital, the beginnings of an exciting major medical city in Central Florida. Further information is available at <http://www.biomed.ucf.edu>



Please submit nominations or a CV and a list of at least four references to [pk@mail.ucf.edu](mailto:pk@mail.ucf.edu)

*The University of Central Florida is an equal opportunity, equal access, and affirmative action employer. As a member of the Florida State University System, all application materials and selection procedures are available for public review.*

# Positions @ NIH

## THE NATIONAL INSTITUTES OF HEALTH



**Director, Division of Biomedical Technology  
National Center for Research Resources  
National Institutes of Health  
Department of Health and Human Services**



**THE POSITION:** The National Center for Research Resources (NCRR) is seeking exceptional candidates for the position of Director, Division of Biomedical Technology. This individual will lead a program that supports research to discover, create, and develop innovative technologies and provides access to these technologies to the biomedical research community. This research is conducted through grants for technology-driven research and development, the biomedical informatics research network, and biomedical technology research centers. The incumbent will supervise a staff of eleven, including nine scientific professionals in overseeing 50 Biomedical Technology Research Center Grants in five broad technology areas: Imaging, Informatics, Optical and Laser Technology, Technology for Structural Biology and Technology for Systems Biology. At these research centers, interdisciplinary teams create unique, transformative technologies and work to promote their widespread use. These innovations are accomplished through a synergistic interaction of technical and biomedical expertise, both within the centers and through intensive collaborations with other leading laboratories. These research centers span basic, translational and clinical research to create tools that advance science at the molecular level and change scientific approaches to diagnosis and treatment of disease. Additionally, the Division administers the shared instrumentation program which provides institutions with the funds to purchase state of the art technologies, helping researchers remain at the forefront of the biology and medicine. Lastly, the Division supports biomedical researchers through investigator-initiated research projects or large collaborative research projects with other NIH organizations and/or Federal agencies.

The NCRR provides laboratory scientists and clinical researchers with the environments and tools they need to understand, detect, treat, and prevent a wide range of diseases. [www.ncrr.nih.gov](http://www.ncrr.nih.gov) This support enables discoveries that begin at a molecular and cellular level, move to animal-based studies, and then are translated to patient-oriented clinical research, resulting in cures and treatments for both common and rare diseases. This position offers a unique and exciting opportunity for an extremely capable individual to share responsibility in providing strong and visionary leadership to an organization dedicated to enhancing our understanding of health and disease, translating basic research into medical care, and improving human health.

**QUALIFICATIONS REQUIRED:** Applicants must possess a Ph.D., or equivalent degree, as well as senior-level research experience or knowledge of research programs moving research from the basic laboratory sciences into clinical research. Candidates should be outstanding communicators and known and respected as distinguished individuals of outstanding competence. Applicants should also demonstrate the ability to think strategically, work collaboratively, and use a consultative approach to problem solving and decision making.

**SALARY/BENEFITS/OTHER INFORMATION:** Salary is commensurate with experience and a full package of Civil Service benefits is available, including: retirement, health and life insurance, long term care insurance, leave and savings plan (401K equivalent). The National Institutes of Health inspires public confidence in science by maintaining high ethical principles. In addition to the Federal government's code of ethics, we have our own agency specific standards which are described at the NIH Ethics web site. <http://ethics.od.nih.gov/overview.htm> This position is subject to a background investigation.

**HOW TO APPLY:** A Curriculum Vitae, Bibliography, and two letters of recommendation must be received by **November 16, 2010**. Application packages should be sent to the **National Institutes of Health, National Center for Research Resources, ATTN: Sabrina Posley, 6701 Democracy Boulevard, Suite 206, Bethesda, Maryland 20892** or email at [sposley@mail.nih.gov](mailto:sposley@mail.nih.gov).

For further information, please call **(301) 435-0717**. All information provided by candidates will remain confidential and will not be released outside the NCRR search process without a signed release from candidates.



THE UNIVERSITY OF HONG KONG

Founded in 1911, The University of Hong Kong is committed to the highest international standards of excellence in teaching and research, and has been at the international forefront of academic scholarship for many years. The University has a comprehensive range of study programmes and research disciplines spread across 10 faculties and about 100 sub-divisions of studies and learning. There are over 23,400 undergraduate and postgraduate students coming from 50 countries, and more than 1,200 members of academic and academic-related staff.

### Tenure-track Assistant Professor in the Department of Chemistry (Ref.: 20100528)

Applications are invited for tenure track appointment as Assistant Professor in the Department of Chemistry, from July 1, 2011 or as soon as possible thereafter. The post will initially be made on a three-year term with the possibility of renewal upon mutual agreement. Appointment with tenure will be considered during the second three-year contract.

Applicants should possess a Ph.D. degree with a strong background and research record in any discipline of chemistry. Candidates with research interests that can contribute to the broadly defined areas of Analytical/Physical Chemistry, Chemical Biology and Materials Science are especially encouraged to apply. The appointee is expected to develop a vigorous and independent research program and excel in both undergraduate and postgraduate teaching. A suitable start-up fund for research will be provided. Information about the Department can be obtained at <http://chem.hku.hk>.

**Annual salary for Assistant Professorship** will be in the range of HK\$477,360 – 737,700 (subject to review from time to time at the entire discretion of the University) (approximately US\$1 = HK\$7.8). A highly competitive salary commensurate with qualifications and experience will be offered. At current rates, salaries tax does not exceed 15% of gross income. The appointment will attract a contract-end gratuity and University contribution to a retirement benefits scheme, totalling up to 15% of basic salary, as well as leave, and medical/dental benefits. Housing benefits will be provided as applicable.

Interested candidates should send a completed application form together with a C.V. and a research proposal to the Assistant Registrar (Appointments), Human Resource Section, Registry, The University of Hong Kong, Hong Kong. **Further particulars and application forms (152/708)** can be obtained at <http://www.hku.hk/apptunit/>; or from the Appointments Unit (Senior), Human Resource Section, Registry, The University of Hong Kong, Hong Kong (fax: (852) 2540 6735 or 2559 2058; e-mail: [senrapt@hku.hk](mailto:senrapt@hku.hk)). **Closes December 15, 2010.** Candidates who are not contacted within 3 months of the closing date may consider their applications unsuccessful.

**The University is an equal opportunity employer and is committed to a No-Smoking Policy**

Western University  
www.westernu.edu

### Faculty Positions in Anatomy available for 2011

College of Osteopathic Medicine of the Pacific/Northwest Lebanon, Oregon

Western University of Health Sciences, a thriving center for human health care and veterinary medicine education is opening a new site for the College of Osteopathic Medicine of the Pacific – Northwest (COMP-NW) in Lebanon, Oregon with the inaugural class beginning in Fall, 2011. The University's 10 year plan and core values have propelled the institution to be a benchmark University for the development of inter-professional and graduate medical education. The University values a diverse institutional community and is committed to excellence in its faculty, staff and students. Western University seeks applicants of distinguished academic accomplishments who possess a passion for excellence and can illustrate a proven track record of achievements.

The Department of Anatomy provides the preclinical education in gross anatomy, histology, Neuroanatomy, and embryology for the College of Osteopathic Medicine, and invites applications from highly motivated individuals for tenure-track faculty positions in anatomy. These are full-time, 12-month, tenure-track positions at the Assistant Professor/Associate Professor/Professor rank. Successful candidates and faculty will be located at the new site on the COMP-NW campus. Applicants must have a Ph.D. in anatomy or equivalent field and at least 2 years of postdoctoral experience. Preference will be given to master educators who have demonstrated excellence in teaching with significant scholarly activity and/or those with a history of extramural funding and a strong potential to obtain further grant support for their research program. Submit a current curriculum vitae and a cover letter describing your teaching experience and philosophy, your research activity and goals, and how you meet the qualifications for the position. Please include contact information for at least three references. These positions will remain open until filled.

**James F. May, PhD**  
Professor and Chair  
Department of Anatomy  
College of Osteopathic Medicine of the Pacific  
Western University of Health Sciences  
309 E. Second Street, Pomona, CA 91766-1854  
Email Address: [jfmay@westernu.edu](mailto:jfmay@westernu.edu)  
[www.westernu.edu](http://www.westernu.edu)

Western University of Health Sciences is an equal opportunity employer.

BIG DREAMS. BOLD FUTURE.

### Chair

#### Department of Molecular Pharmacology and Physiology

The University of South Florida Health (USF Health) College of Medicine seeks an outstanding scientist and an academic leader for the position of Chair, Department of Molecular Pharmacology and Physiology. The department is comprised of 22 faculty members with research strengths in cell signaling networks, cardiovascular biology, and the neurosciences. Information about the Department can be obtained by visiting: <http://health.usf.edu/medicine/mpp>

USF Health consists of the colleges of Medicine, Nursing, and Public Health and the schools of Biomedical Sciences, Physical Therapy & Rehabilitation Sciences, and a recently approved School of Pharmacy. In partnership with its affiliated hospitals, USF Health's research funding last year was \$232 million. It has strong affiliations with H. Lee Moffitt Cancer Center, the Tampa General Hospital, the All Children's Hospital, the Shriners' Hospital for Children, and the James A. Haley and Bay Pines VA Medical Centers.

**Qualifications and Requirements:** PhD, MD, or MD/PhD; NIH funded investigator with a sustained record of NIH funding; Rank of Professor or is currently being considered for promotion to the rank of Professor; Distinguished record of scholarly activity as evidenced by publications in high impact journals; National and international reputation in his/her discipline as evidenced by the service on NIH study panels and editorial boards; Demonstrated outstanding leadership skills, is a team player, and a change agent; Demonstrated experience in building interdisciplinary programs; Demonstrated commitment to the development and mentoring of faculty, staff, and students; Strong commitment to quality medical and graduate education; Demonstrated success in a leadership position.

**Submission of Application/Nomination:** For full consideration, please submit your application and/or nomination materials by October 1, 2010. The following should be submitted to Ms. **Christine Tam** ([ctam@health.usf.edu](mailto:ctam@health.usf.edu)) by email for consideration: Letter summarizing your qualifications and leadership philosophy; Statement about your future research plans; Curriculum Vitae; Names and contact information of five professional references (References will not be contacted until the advanced stages of screening). **Robert J. Deschenes, PhD, Chair, MPP Search Committee, [rdeschen@health.usf.edu](mailto:rdeschen@health.usf.edu)**

*USF Health is committed to increasing its diversity and will give individual consideration to qualified applicants for this position with experience in ethnically diverse settings, who possess varied language skills, or who have a record of research that support diverse communities or teaching a diverse student population. The University of South Florida is an EO/EA/AA Employer. For disability accommodations, contact Dana Cole at (813) 974-8320 a minimum of five working days in advance. According to FL law, applications and meetings regarding them are open to the public.*

**USF HEALTH**

## NEUROSCIENTIST

The Neuroscience Graduate Program, Department of Neurology and Ernest Gallo Clinic & Research Center at the University of California San Francisco seeks an outstanding neuroscientist to fill a faculty position at the Assistant or Associate Professor level. Applicants will be expected to develop and maintain an independent research program in the area of addiction and/or co-morbid neuropsychiatric disorders. Experience in vitro electrophysiology is required and an approach combining multiple techniques or levels of analysis is encouraged. The successful applicant will also demonstrate a high level of productivity, strong communication and interpersonal skills, and a commitment to work collaboratively with other members of the Gallo Center. Preference will be given to those with a track record in the area of alcohol and substance abuse research. An excellent start-up package and research support will be available to the successful candidate.

Screening of applicants will begin **September 15, 2010**, and will continue until the position is filled. The application must include a cover letter, curriculum vitae, a 2-5 page summary of research interests and goals, and names and contact information (including e-mail addresses) for three references. UCSF seeks candidates whose experience, teaching, research, or community service has prepared them to contribute to our commitment to diversity and excellence.

UCSF is an Equal Opportunity/Affirmative Action Employer. The University undertakes affirmative action to assure equal employment opportunity for underrepresented minorities and women, for persons with disabilities, and for covered veterans. All qualified applicants are encouraged to apply, including minorities and women.

**Send application materials to:**  
[zumwaltm@neurology.ucsf.edu](mailto:zumwaltm@neurology.ucsf.edu)

Neuroscience Search Committee,  
Ernest Gallo Clinic & Research Center  
5858 Horton St., Suite 200  
Emeryville, CA 94608  
[www.galloresearch.org](http://www.galloresearch.org)



The Novo Nordisk Foundation

## Center for Protein Research

The Novo Nordisk Foundation Center for Protein Research, located in central Copenhagen, has been established to promote basic research on human proteins of medical relevance; with the explicit goal to be among the leading laboratories within our focus areas. The Center operates from a significant donation from the Novo Nordisk Foundation, [www.novonordiskfonden.dk/en](http://www.novonordiskfonden.dk/en), as well as other external funding sources. In addition, the University of Copenhagen has made major contributions towards the building of the new Center laboratories, which were opened during 2009. The Center is an integral part of the Faculty of Health Sciences, University of Copenhagen, [www.ku.dk/english](http://www.ku.dk/english), and has a highly international and dynamic environment.

The Center comprises a wide range of expertise and resources in protein production, chemical biology, disease systems biology and mass spectrometry based proteomics as well as having dedicated research groups focused on ubiquitin modified signaling and molecular endocrinology. We are prioritizing basic research but are also open to translational research opportunities within medicine with the aim of generating research results useful to facilitate drug discovery and development.

The Center management team consists of Dr. Michael Sundström (Managing Director), Professor Matthias Mann (Research Director, Proteomics) and Professor Søren Brunak (Research Director, Disease Systems Biology).

## Group Leader in Disease Biology

We are now seeking an excellent and internationally renowned scientist to strengthen our research capabilities – preferably focused on cancer signaling – but also other areas in Disease Biology could be of interest. The successful candidate will establish a research group at the Center, carrying out independent research of highest scientific impact and standard as well as work with us on integrated collaborative projects. It is anticipated that the Group Leader should have the capability to attract significant additional external funding, to complement the Center contribution.

You should have an excellent track-record, international reputation and documented abilities. Our goal is to maintain our highly integrated research environment; thus collaborative interest is essential. In addition, your vision on how the unique environment and resources at the Center will complement your research is of particular interest to us.

The Group Leader will receive excellent resources and support from the Center, consisting of:

- 2-4 million USD (depending on qualifications) in research support, to be spent until the end of 2012
- Additional core funding from 2013, depending on progress and performance
- State of the art facilities and dedicated laboratory and office space
- Laboratory, IT, budget & administrative support are also covered by the Center
- An international environment, with scientists at the highest international level

### Are you interested in becoming a Group Leader at the Center?

Please forward a letter of interest, including a brief CV/biography as well as a summary of planned future research to [contact@cpr.ku.dk](mailto:contact@cpr.ku.dk) preferably before 1 December 2010. Additional information on the Center is found at [www.cpr.ku.dk](http://www.cpr.ku.dk); or contact [michael.sundstrom@cpr.ku.dk](mailto:michael.sundstrom@cpr.ku.dk).



## GRADUATE PROGRAM



## Marine Alliance for Science and Technology for Scotland Graduate School

### Seven Prize PhD Studentships

plus other funded PhD places in marine science across Scotland

The Marine Alliance for Science and Technology for Scotland (MASTS) Graduate School offers a unique environment for the training and development of the next generation of marine scientists in institutions across Scotland. Competition is open to graduates of higher education or those in their final year of a Bachelors or Masters programme.

The work of MASTS will cover nine distinct Joint Research Themes, each concerned with a key component in understanding our marine environment including.

### MASTS Prize Studentships

MASTS is offering seven funded PhD studentships for students from the UK and overseas. These prestigious, competitive awards are intended to attract the brightest students from around the world.

MASTS Prize Students will be registered for a PhD with any suitable qualified member of staff at one or more of the participating universities, but the research may be undertaken within any of the partner institutions:

- |   |                             |
|---|-----------------------------|
| • Edinburgh Napier University                   | • University of Aberdeen    |
| • Heriot-Watt University                        | • University of Glasgow     |
| • Marine Scotland (Science)                     | • University of St. Andrews |
| • Scottish Association for Marine Science (UHI) | • University of Stirling    |
| • University Marine Biological Station Millport | • University of Strathclyde |

The MASTS Graduate School will provide the focus for training, drawing on world-leading experts from across the MASTS partner institutions. They will provide access to masters courses, dedicated seminars on specialised topics, lectures by distinguished visitors, annual summer schools and access to equipment and facilities from across the partnership.

Information on the nine MASTS Joint Research Themes and guidance to applicants may be found at [www.masts.ac.uk](http://www.masts.ac.uk).

Full applications and references must be submitted at [www.masts.ac.uk](http://www.masts.ac.uk) by **13<sup>th</sup> December 2010**.

### Further Funded PhD places in Scotland

Applicants for the ten MASTS Prize studentships may also be considered for the other marine science studentships available within Scotland.





www.ox.ac.uk/jobs

## University Lecturer in Evolutionary Biology

Mathematical, Physical and Life Sciences Division, Department of Zoology in association with Magdalen College

Associated with a Tutorial Fellowship at Magdalen College, under arrangements described in the further particulars, this post is effective from 1 January 2011 or as soon as possible thereafter. The combined University and College salary will be on a scale up to £57,201 per annum, and an additional College housing allowance of £10,250 per annum is available if the successful candidate chooses not to reside in College. Other allowances are detailed in the further particulars.

You will be expected to lead a research programme and group in Evolutionary Biology, give undergraduate lectures and tutorials, supervise graduate students, and carry out examining and administrative duties in the Department and the College. Preferably, you will have a strong background in Evolutionary Biology.

Further particulars, containing details of the application procedure and of the duties, may be obtained from paul.harvey@zoo.ox.ac.uk or by visiting <http://www.zoo.ox.ac.uk/jobs> The closing date for applications is noon on 25 October 2010.

Applications are particularly welcome from women and black and minority ethnic candidates, who are under-represented in academic posts in Oxford.

Committed to equality and valuing diversity



The University of Texas at Austin

## Stem Cell Biology Position The Institute for Cellular and Molecular Biology

The Institute for Cellular and Molecular Biology, Alan Lambowitz, Director, invites applications for a tenure-track/tenured position in Stem Cell Biology. Academic appointments at the level of Assistant, Associate, or Full Professor will be in the Section of Molecular Cell and Developmental Biology.

Candidates should have an outstanding record of research productivity and a research plan based on molecular mechanisms in any area of Stem Cell Biology. Building on a strong existing faculty, the Institute has recruited more than 50 new faculty members over the past ten years. In addition to its highly interactive and interdisciplinary research environment, the Institute provides administrative and financial support for the Graduate Programs in Cell and Molecular Biology, Microbiology, and Biochemistry, as well as state-of-the-art core facilities including DNA and next-gen sequencing, mass spectrometry, electron and confocal microscopy, DNA microarrays, robotics, and mouse genetic engineering. An MD-PhD program with the UT Medical Branch and UT-Austin's new Dell Pediatrics Research Institute enhance the environment for Biomedical Research.

Austin is located in the Texas hill country and is widely recognized as one of America's most beautiful and livable cities.

Applications received before November 1, 2010 will receive first consideration, but applications will be accepted until the position is filled. Please send a single PDF file containing your curriculum vitae, summary of research interests and names of three references to: **MCDB\_stem\_cell@biosci.utexas.edu**. References may also send their letters directly to the same email address.

Homepages • <http://www.biosci.utexas.edu/MCDB/> • <http://www.icmb.utexas.edu/>

*The University of Texas at Austin is an Equal Opportunity Employer.  
Qualified women and minorities are encouraged to apply; a background check will be conducted on applicant selected.*

VANDERBILT  School of Medicine

CHAIR

Department of Cell and Developmental Biology

Vanderbilt University School of Medicine is actively searching for a new Chair for the Department of Cell and Developmental Biology to succeed Dr. Susan Wenthe. Dr. Wenthe, who served as Chair for seven years, has recently vacated the position to become Associate Vice Chancellor for Research. This is an outstanding opportunity for a visionary new department chair to guide a significant research expansion within an existing base of excellence in the Department of Cell and Developmental Biology.

We seek outstanding candidates with Ph.D., M.D., or M.D./Ph.D. degrees that have a demonstrated track record of seminal research accomplishments coupled with outstanding interpersonal skills and leadership ability. The ideal candidate should be able to articulate a compelling vision for the future of research in the field, and a commitment to graduate education. Vanderbilt University School of Medicine is committed to providing the resources needed to execute on that vision.

Review of applications is effective immediately, and the position will remain open until filled. Applicants should submit a cover letter describing their interest along with a full curriculum vitae and names and addresses of three references to:

**Roger D. Cone, Ph.D.**

Chair, Cell and Developmental Biology Search Committee  
c/o Committee Assistant

Vanderbilt University School of Medicine  
702 Light Hall

Nashville, TN 37232-0260

Telephone: 615-936-7085

Fax: 615-343-4075

E-mail: [roger.cone@vanderbilt.edu](mailto:roger.cone@vanderbilt.edu)

*Vanderbilt University is an  
Equal Opportunity/Affirmative Action Employer.*

## ASSISTANT PROFESSOR MOLECULAR BIOLOGY AND BIOCHEMISTRY RUTGERS UNIVERSITY

The Department of Molecular Biology and Biochemistry at Rutgers, The State University of New Jersey, New Brunswick (Busch Campus), invites applicants for a tenure-track **Assistant Professor** position. The position requires a Ph.D. degree or equivalent and involves teaching and research in Molecular Biology. The Department is especially interested in applicants who use biochemical or molecular approaches for research in functional genomics, epigenetics, chromatin structure and function, and control of growth and differentiation but outstanding researchers in other areas will be considered. The Department is an important part of the expanding program in molecular biology within the Division of Life Sciences on the Busch Campus, where the Center for Advanced Biotechnology and Medicine, the Waksman Institute and the Robert Wood Johnson Medical School are also located. We have strong consolidated, interdepartmental graduate programs in molecular biosciences. The position is highly competitive with regard to startup funds, laboratory space and salary.

Please send by e-mail a curriculum vitae, summary of research activities, a research plan, and have three letters of recommendation sent by **December 1, 2010**, to: **Dr. Vincenzo Pirrotta, Chair, c/o Barbara Nowakowski, [barbara@cabm.rutgers.edu](mailto:barbara@cabm.rutgers.edu), Department of Molecular Biology and Biochemistry, Rutgers University, Nelson Laboratories, 604 Allison Road, Piscataway, NJ 08854.**

*Rutgers University is an Equal Opportunity/Affirmative Action Employer. Women and minority candidates are encouraged to apply.*

UT SOUTHWESTERN MEDICAL CENTER AT DALLAS

## ENDOWED SCHOLARS PROGRAM IN MEDICAL SCIENCE

Unique and highly competitive, **THE ENDOWED SCHOLARS PROGRAM IN MEDICAL SCIENCE** is designed to launch the next generation's scientific leaders on their biomedical research careers by providing seed money, research space and startup support for groundbreaking projects. The Endowed Scholars Program gives early-career investigators the chance to take risks, supported by the mentoring of experienced and highly distinguished established researchers at **The University of Texas Southwestern Medical Center at Dallas**.

As one of the foremost research institutions in the world, UT Southwestern, with four Nobel Prizes awarded to its faculty since 1985 and 18 members of the National Academy of Sciences, is poised to lead the way in a new era of scientific discovery in the 21st century. We conduct more than 3,500 research projects annually totaling more than \$400 million. Endowed Scholars have access to exceptional core facilities, which include DNA microarray services; electron microscopy; live-cell imaging; mouse gene knockouts, transgenesis and metabolic phenotyping; high-throughput chemical screening; and structural biology. UT Southwestern also is home to one of the nation's first 7-Tesla magnetic resonance imaging devices for human studies. UT Southwestern has a vibrant graduate school and nearly 4,400 medical, graduate and health professions students, residents and postdoctoral fellows.

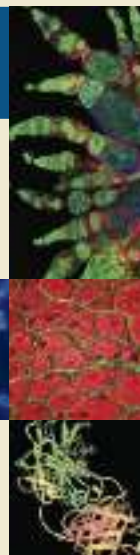
The Endowed Scholars Program, which is fully funded from private endowment, provides more than \$1,000,000 over four years to support the independent research activities, salary and benefits of each scholar. Up to five new scholars are selected each year from top universities, institutions and laboratories around the world. Each scholar is appointed as a tenure-track assistant professor in a UT Southwestern academic department or research center. Positions in both basic science and clinical departments are available.

Potential scholars submit nomination materials to a chair or director of one of UT Southwestern's basic or clinical academic departments or research centers. Those chairs or directors then forward finalists' materials for consideration to the medical center's Endowed Scholars Committee.

For detailed information about nomination materials and currently available positions, please visit our Web page: [utsouthwestern.edu/utsw/home/scholars](http://utsouthwestern.edu/utsw/home/scholars)

*Applications from women and underrepresented minority candidates are strongly encouraged.  
UT Southwestern is an equal opportunity institution.*

**UT SOUTHWESTERN**  
MEDICAL CENTER



### BIOLOGICAL SCIENCES SCHOLARS PROGRAM

#### For Junior, Tenure-Track Faculty

The University of Michigan announces recruitment for the Biological Sciences Scholars Program (BSSP) to continue to enhance its investigational strengths in the life sciences research programs.

Now entering its 14th year, this Program has led to the recruitment of outstanding young scientists in the areas of genetics, microbiology, immunology, virology, structural biology, pharmacology, biochemistry, molecular pharmacology, stem cell biology, cancer biology, physiology, cell and developmental biology, and the neurosciences. The Program seeks individuals with PhD, MD, or MD/PhD degrees, at least two years of postdoctoral research experience, and evidence of superlative scientific accomplishment and scholarly promise. Successful candidates will be expected to establish a vigorous, externally-funded research program, and to become leaders in departmental and program activities, including teaching at the medical, graduate, and/or undergraduate levels. Primary college and department affiliation will be determined by the applicant's qualifications and by relevance of the applicant's research program to departmental initiatives and focus. All faculty recruited via the BSSP will be appointed at the Assistant Professor level.

**APPLICATION INSTRUCTIONS:** Please apply to the Scholars Program through the BSSP website at: (<http://www.med.umich.edu/medschool/research/bssp/>). A curriculum vitae (including bibliography), a three-page research plan, an NIH biosketch, and three original letters of support should all be submitted through the BSSP website. More information about the Scholars Program, instructions for applicants and those submitting letters of recommendation, and how to contact us is located on the BSSP web site: (<http://www.med.umich.edu/medschool/research/bssp/>). The deadline for applications is Friday, October 29, 2010.

*The University of Michigan is an Affirmative Action/Equal Opportunity Employer.*



## ASSISTANT AND ASSOCIATE PROFESSORS THE DEPARTMENT OF EXPERIMENTAL RADIATION ONCOLOGY

The Department of Experimental Radiation Oncology at The University of Texas M. D. Anderson Cancer Center invites applications from researchers using approaches ranging from genetics, cell biology and biochemistry to proteomics and system biology for tenure-track Assistant and Associate Professor positions. The department seeks to complement its existing programs in DNA repair, cell cycle control, growth and proliferation, stem cell biology and epigenetics, especially related to DNA damage response and therapy. Female and minority candidates are encouraged to apply. We offer a very attractive recruitment package, active graduate and post-doctoral training programs, and the unmatched scientific environment of the Texas Medical Center, the world's largest biomedical center. Applicants must have a Ph.D. and/or M.D. degree, and will be expected to develop an internationally recognized, extramurally funded research program. To apply, please send within a single pdf file: (1) Cover Letter; (2) Curriculum Vitae; (3) Short Research Summary (three page maximum); and (4) Contact information for three references by December 15, 2010, to: [exp radonc@mdanderson.org](mailto:exp radonc@mdanderson.org)

**Junjie Chen, Ph.D.**

**Professor and Chair**

**Experimental Radiation Oncology**

**The University of Texas M. D. Anderson Cancer Center  
1515 Holcombe Blvd., Unit 66, Houston, TX 77030**

THE UNIVERSITY OF TEXAS

**MD Anderson  
Cancer Center**

*Making Cancer History®*

M. D. Anderson Cancer Center is an equal opportunity employer and does not discriminate on the basis of race, color, national origin, gender, sexual orientation, age, religion, disability or veteran status except where such distinction is required by law. All positions at The University of Texas M. D. Anderson Cancer Center are security sensitive and subject to examination of criminal history record information. Smoke-free and drug-free environment.

**UK**

UNIVERSITY OF  
**KENTUCKY**

**UK**

## BIOCHEMISTRY FACULTY POSITION

The Department of Molecular and Cellular Biochemistry invites applications for a tenure track faculty position at the Assistant Professor level. The successful candidate must possess a Ph.D., M.D., or equivalent degree and have an active research program using structural methods to address questions of biomedical relevance. We are particularly interested in candidates that use X-ray crystallography as their major technique and whose research interests complement existing departmental programs including, but not limited to the areas of diabetes, cardiovascular disease, neuroscience, and cancer. Preference will be given to candidates with a record of scholarly achievement in membrane protein structural biology.

The successful candidate will benefit from a stimulating and collaborative environment within the department and a strong graduate program. Competitive startup funds and salary as well as access to state-of-the-art facilities including in-house X-ray crystallography equipment, access to the SER-CAT beamline at the Advanced Photon Source in Chicago and appropriate space will be offered in a new 185,000 ft<sup>2</sup> research building.

Evaluation of applicants will begin October 2010. Interested applicants should visit <http://medicine.mc.uky.edu/biochemreference/> to access the online faculty application. Required application materials include a curriculum vitae, a description of your current and future research program, and three letters of reference. Inquires may also be sent to MCBX Faculty Search Committee

at [biochem@uky.edu](mailto:biochem@uky.edu) or call 859-323-5549.

**see blue.**  
*in everything we do*

UNIVERSITY OF KENTUCKY

For further information about the Department, visit: [www.mc.uky.edu/biochemistry](http://www.mc.uky.edu/biochemistry).



The University of Kentucky is an equal opportunity employer and encourages applications from minorities and women



**STANFORD  
UNIVERSITY**

## STANFORD UNIVERSITY DEPARTMENT OF CHEMICAL AND SYSTEMS BIOLOGY

The Department of Chemical and Systems Biology at Stanford University School of Medicine invites applications for two tenure-track positions at the ASSISTANT PROFESSOR level. We are particularly interested in candidates with a strong interdisciplinary record in the broad areas of chemical biology, systems biology, and/or cellular and molecular biology in normal and disease states. Stanford offers an outstanding environment for creative interdisciplinary biomedical research. The main criterion for appointment in the University Tenure Line is excellence in research and teaching.

Candidates should have a Ph.D. and/or M.D. degree and postdoctoral research experience. Candidates should send curriculum vitae, a description of future research plans and the names and addresses of three potential referees by **November 1, 2010** to:

**James Ferrell, Professor and Chair**

**c/o Jean Kavanagh, FAA**

**Department of Chemical and Systems Biology**

**269 Campus Drive, CCSR Bldg Room 4145A**

**Stanford University School of Medicine**

**Stanford CA 94305-5174**

*Stanford University is an Equal Opportunity Employer and is committed to increasing the diversity of its faculty. It welcomes nominations of and applicants from women and minority groups, as well as others who would bring additional dimensions to the university's research, teaching, and clinical missions.*

THE UNIVERSITY OF  
**TENNESSEE**  
KNOXVILLE

**ASSISTANT PROFESSOR:** The Department of Biochemistry and Cellular and Molecular Biology (BCMB) at the University of Tennessee, Knoxville

seeks to fill a tenure-track faculty position at the assistant professor level to begin August 1, 2011, in the following area:

## EXPERIMENTAL PHYSICAL BIOCHEMIST

Working in the area of nucleic acids or membranes. The successful applicant will be expected to develop a first-class, externally funded research program, to provide state-of-the-art training for graduate students and postdoctoral researchers, and to contribute to the teaching mission of the BCMB department at both the undergraduate and graduate levels. Required qualifications include a Ph.D. and postdoctoral experience in experimental molecular biophysics of nucleic acids, membranes, nucleic acid-protein or membrane-protein interactions, evidence of significant scientific productivity, and a commitment to an integrated program of teaching and research. Current research strengths of BCMB relevant to this search include Computational and Molecular Biophysics and Structural Biology. BCMB also has strength in Cell Biology, Genetics, Plant Biology, and Neurobiology. The successful candidate will benefit from interactions with strong research groups within UTK, access to supercomputing facilities (Kraken) and Computational and Physical Sciences programs at Oak Ridge National Laboratories (ORNL), which houses the new Spallation Neutron Source.

The University welcomes and honors people of all races, creeds, cultures, and sexual orientations, and values intellectual curiosity, pursuit of knowledge, and academic freedom and integrity. Interested candidates should send a cover letter, a resume, a description of research experience and of the proposed research program, and arrange for three letters of reference to be sent to: **Engin Serpersu, Chair, Faculty Search Committee, BCMB Department, M407 WLS, University of Tennessee, Knoxville, TN 37996-0840**. Review of applications will begin on **October 1, 2010**, and will continue until the position is filled.

*The University of Tennessee is an EEO/AA/Title VI/Title IX/Section 504/ADA/ADEA institution in the provision of its education and employment programs and services. All qualified applicants will receive equal consideration for employment without regard to race, color, national origin, religion, sex, pregnancy, marital status, sexual orientation, age, physical or mental disability, or covered veteran status.*



**TEMPLE UNIVERSITY**  
**Department of Biology**  
**Assistant/Associate/Full Professor Positions**  
**Neurobiology**  
**Molecular/Cellular/Integrative Biology**  
**Computational Biology**

As part of a significant ongoing expansion, after the addition of eight faculty members in the past three years, the Department of Biology at Temple University (<http://www.temple.edu/biology/>) invites applications for tenure track/tenured positions, at (1) the Assistant/Associate/Full Professor levels in the areas of Neurobiology, and Molecular/Cellular/Integrative Biology, and at (2) the Assistant Professor level in Computational Biology. Outstanding candidates in related areas also will be given full consideration. Candidates at the Assistant Professor level are expected to establish a vigorous, externally funded research program, while candidates for the senior positions are expected to bring productive, well-funded research programs. Candidates should submit their materials online at <http://bio.cst.temple.edu/search>. Review of applications will begin immediately, and will continue until the positions are filled.

*Temple University is an Equal Opportunity, Equal Access, Affirmative Action Employer committed to achieving a diverse community (AA, EOE, m/f/d/v).*



The Departments of Microbiology and Chemical and Biomolecular Engineering at The Ohio State University invite applications for an Assistant or Associate Professor whose research focuses on Environmental Microbiology and Bioenergy. We seek a Molecular Microbiologist whose research will be directed towards molecular characterization of physiological processes used by microorganisms to produce biofuels. Research approaches are expected to include efforts in metabolic engineering and systems biology/synthetic biology. This individual will join a vibrant community that includes, in addition to nearly 50 faculty members in the Microbiology (<http://www.microbiology.osu.edu>) and CBE (<http://www.chbmeng.ohio-state.edu/>) departments, researchers at the Institute for Energy and the Environment (<http://iee.osu.edu/>), the Center for Energy, Sustainability, and the Environment (<http://oaa.osu.edu/documents/CSEproposal.pdf>), and Battelle Memorial Institute (<http://www.battelle.org/>). This hire will interface with a new ARPA-E funded initiative, which represents a collaboration of faculty in Microbiology and CBE with Battelle Memorial Institute. The ideal arrangement will be a 70% appointment in Microbiology and 30% appointment in Chemical and Biomolecular Engineering.

Applicants must have a Ph.D. or equivalent degree and relevant postdoctoral research experience. The successful candidate will be expected to establish and maintain an extramurally funded research program and to actively support our strong commitment to excellence in teaching at both the undergraduate and graduate levels. Applications will be accepted until the position is filled, but priority will be given to applications received by **October 31, 2010**. Application materials, including a letter of intent, curriculum vitae, statement of research and teaching interests, and three letters of recommendation should be sent by e-mail to: [micro.grad@osu.edu](mailto:micro.grad@osu.edu).

Additional questions about this search should be directed to **Dr. F. Robert Tabita, Chair of the Search Committee** ([tabita.1@osu.edu](mailto:tabita.1@osu.edu))

*To build a diverse workforce The Ohio State University encourages applications from minorities, veterans, women and individuals with disabilities. Flexible work options are available. Ohio State is an NSF ADVANCE Institution. EEO/AA Employer.*

*Helen L. and Martin S. Kimmel Center  
 for Biology and Medicine at the Skirball  
 Institute of Biomolecular Medicine*

**NYU Langone Medical Center**

## **FACULTY POSITION**

The Helen L. and Martin S. Kimmel Center for Biology and Medicine at the Skirball Institute of Biomolecular Medicine, NYU Langone Medical Center, invites applications for tenure-track positions at the assistant professor level. We seek applicants with an outstanding record of achievement to join the faculty in the Structural Biology Program at the Skirball Institute. Special priority will be given to applicants who employ X-ray crystallography, electron microscopy or single-molecule techniques to address important mechanistic questions.

The NYU Langone Medical Center offers excellent resources to support new faculty, including generous start-up packages and core facilities for protein expression, X-ray crystallography, electron microscopy, imaging and proteomics. Successful candidates are expected to initiate and maintain vigorous independent research programs that will enrich and be enriched by the highly collaborative environment at the Skirball Institute and throughout the NYU research community.

This is an electronic application process only. Please create your application packet by formatting it as a single PDF document. Use the following page order: 1) cover letter, 2) curriculum vitae, 3) research statement, 4) one recent publication.

Email the application packet to [SBsearch@med.nyu.edu](mailto:SBsearch@med.nyu.edu) by December 1st, 2010. Three letters of reference should be sent independently to [SBsearch@med.nyu.edu](mailto:SBsearch@med.nyu.edu).

*New York University was founded in 1841 and is an equal opportunity affirmative action employer. Women and minority candidates are encouraged to apply.*

**Skirball Institute of Biomolecular Medicine**

<http://skirball.med.nyu.edu>



## POSITIONS OPEN



### Penn State Milton S. Hershey Medical Center Hershey, PA

The Penn State Institute of the Neurosciences invites nominations for the position of **DIRECTOR** of the newly created Penn State Center for Emerging Neurotechnology and Imaging (CENI). The mission of the Center is to be at the cutting edge of neuroscience translational research, particularly as it relates to the application of various neuroimaging modalities, neuroinformatics, and emerging technologies. The Center will focus on translational research to transform and improve treatment paradigms across clinical neuroscience disciplines. The Center is an interdepartmental unit within the Institute of the Neurosciences, and will comprise core faculty within the clinical Departments of Neurosurgery, Neurology, Psychiatry, and Radiology, as well as several basic science and engineering departments at the Penn State Hershey and University Park campuses.

The new Director will be expected to have led successful research efforts that required interdisciplinary collaboration. Experience in working across traditional department boundaries and success in working with several neuroscience disciplines will be highly valued. Penn State University and the Penn State Hershey Medical Center provide extensive opportunities for collaborative and innovative neuroscience research. Considerable resources will be available to the new Director, including new laboratory space, a research-dedicated 3T MR Scanner, a neuropsychophysiology/EEG suite, and the opportunity to recruit new faculty, postdoctoral fellows, and graduate students. The Director is expected to utilize these resources to develop the Center as an innovative, translational neuroscience research facility that will break new ground and attract extramural funding.

The successful candidate will be an M.D., M.D.-Ph.D., Ph.D., or equivalent and be an established investigator at the Associate Professor or Professor level, with a record of research accomplishment and extramural funding. The new Director may have expertise in any field of clinical or basic neuroscience and is expected to be comfortable working across these neuroscience disciplines.

Nominations should include curriculum vitae and be sent to:

**Robert E. Harbaugh, M.D., FACS, FAHA**  
Chair, CENI Director Search Committee;  
Director, Penn State Institute of the Neurosciences;  
Distinguished Professor and Chair,  
Department of Neurosurgery;  
Professor, Department of Engineering Science and  
Mechanics;  
Department of Neurosurgery,  
30 Hope Drive, EC110  
Penn State University,  
M.S. Hershey Medical Center  
Hershey, PA 17033-0850  
Telephone: 717-531-4383, fax: 717-531-3858  
E-mail: rharbaugh@psu.edu

*Penn State is committed to Affirmative Action, Equal Opportunity, and the diversity of its workforce. Equal Opportunity Employer/Affirmative Action/Minorities/Females/Persons with Disabilities/Veterans.*

Website: <http://pennstatehershey.psu.edu/web/neuroscience>.

Wayne State University, School of Medicine, Department of Surgery invites applications for a **FACULTY POSITION** rank to be determined. Applicants must have a Ph.D. degree, a proven track record of productivity and a commitment to cancer research, the ability to work with others in a multidisciplinary setting in order to drive novel approaches linking the laboratory to clinical trials, and the ability to promote an environment of collegiality and collaboration with existing basic and clinical scientists. Send curriculum vitae to: **Donald Weaver, M.D., Professor and Chair, Department of Surgery Wayne State University, 6C/UHC, 4201 St. Antoine, Detroit, MI 48201.** *WSU is an Equal Opportunity/Affirmative Action Employer.*

## POSITIONS OPEN



### TWO FACULTY POSITIONS The University of Kansas

The Department of Pharmaceutical Chemistry at the University of Kansas, invites applications for a full-time tenure-track faculty position at the **ASSISTANT** or **ASSOCIATE** level in Bioanalytical Chemistry for the 2011-2012 academic year. The Pharmaceutical Chemistry Department is affiliated with the Ralph N. Adams Institute for Bioanalytical Chemistry and houses the Macromolecule and Vaccine Stabilization Center. For position details and to apply, go to **website: <http://jobs.ku.edu>** and search for position **00001650**. Screening of applications will begin October 15, 2010. Applications will be accepted until the position is filled.

Bioanalytical Chemistry faculty position. The Department of Chemistry at the University of Kansas is seeking exceptional candidates for a tenure-track position in Bioanalytical Chemistry at the Assistant Professor level expected to begin as early as August 18, 2011. The successful candidate will become a member of the Ralph N. Adams Institute of Bioanalytical Chemistry, which offers a collaborative and cross-disciplinary research environment. For a complete announcement and to apply online, go on **website: <http://jobs.ku.edu>** and search for position **00002056**. Review of applications of applications will begin October 15, 2010, and will continue until no longer needed.

*Equal Opportunity/Affirmative Action Employer.*

### FACULTY POSITION IN IMMUNOLOGY Department of Microbiology-Immunology Northwestern University Feinberg School of Medicine

A tenure-track position is open for a full-time faculty researcher (Ph.D., M.D.-Ph.D., or M.D.) in Immunology. Areas of particular interest include innate and adaptive immunity to microorganisms, lymphocyte activation and differentiation, and immune regulation. Rank is open. All applicants should have substantial peer-reviewed publications that demonstrate research productivity and the ability to perform cutting edge research. Candidates for an **ASSISTANT PROFESSOR** position should have postdoctoral research experience. Candidates seeking appointment at the **ASSOCIATE PROFESSOR** or **FULL PROFESSOR** level should have substantial research productivity and a history of grant support and academic service. Candidates should have an interest in teaching graduate and medical students. Starting date is negotiable.

Application materials will be reviewed as received, but to receive full consideration, should be received by December 15, 2010. Please send a complete curriculum vitae and the name and contact information of at least three references to **e-mail: [immunology@northwestern.edu](mailto:immunology@northwestern.edu)**.

*Northwestern University is an Affirmative Action/Equal Opportunity Employer. Women and minorities are encouraged to apply. Hiring is contingent upon eligibility to work in the United States.*

**CAREER OPPORTUNITY.** Doctor of Optometry (O.D.) degree in 27 months for Ph.D.s in science and M.D.s. Excellent career opportunities for O.D.-Ph.D.s and O.D.-M.D.s in research, education, industry, and clinical practice. This unique program starts in March of each year, features small classes, and has 12 months devoted to clinical care.

Contact the **Admissions Office, telephone: 800-824-5526** at The New England College of Optometry, 424 Beacon Street, Boston, MA 02115. Additional information at **website: <http://www.neco.edu>**. Email: [admissions@neco.edu](mailto:admissions@neco.edu).

## POSITIONS OPEN



### TENURE-TRACK FACULTY POSITIONS Cell Biology and Molecular Genetics

The Department of Cell Biology and Molecular Genetics at the University of Maryland College Park is seeking outstanding candidates to fill two **ASSISTANT PROFESSOR** positions in each of the following research areas:

1. **Functional RNA.** Areas of interest include but are not limited to non-coding RNAs involved in the regulation of gene expression, epigenetics, and development using microbial, plant, insect, and mammalian systems with emphasis on approaches involving cell biology, biophysics, bioinformatics, and/or genomics.

2. **Host-Pathogen Interactions.** Areas of interest include but are not limited to molecular mechanisms of virulence and resistance to pathogens of plants, fungi, insects, or other model organisms with emphasis on approaches involving genetics, cell biology, bioinformatics, and/or genomics.

These appointments will be part of an ongoing campus drive for enhancement in the life sciences. Successful candidates will be expected to maintain a vigorous, externally funded research program and to participate in undergraduate and graduate teaching. Applicants must have a doctorate degree, relevant postdoctoral experience, an outstanding publication record and a commitment to excellence in teaching. Additional information about the department can be found at **website: <http://www.life.umd.edu/CBMG>**.

The University of Maryland, College Park is the flagship campus of the University System of Maryland and one of the most rapidly advancing public research universities in the country. The Department offers outstanding new research facilities and a highly interactive environment, with extensive opportunities to interact with scientists affiliated with other Departments, Centers, and Institutes at the University of Maryland. Close proximity to Washington D.C., Baltimore, and the Maryland Biotechnology Corridor facilitates interactions with an extraordinary range of major research institutions such as NIH, NIST, FDA, and USDA, in addition to providing a rich cultural environment.

Applicants should apply electronically to one of the following at **website: <http://jobs.umd.edu>** specifying either (1) **Functional RNA - Dr. Jonathan Dinman**, Search Committee Chair (position #116703), or (2) **Host-Pathogen Interactions - Dr. Steven Hutcheson**, Search Committee Chair (position #116704). Applications should consist of a single PDF file containing (1) a letter of application, (2) curriculum vitae, and (3) summary of research plans and teaching interests. For full consideration, four recommendation letters should be sent separately. Complete applications should be received by October 31, 2010, but will be accepted until the positions are filled.

*The University of Maryland is an Affirmative Action/Equal Opportunity Employer. Women and members of underrepresented groups are especially encouraged to apply.*

The Department of Ecology and Evolutionary Biology, Tulane University, invites applications for one tenure-track position at the level of **ASSISTANT PROFESSOR**. We encourage applications from **LANDSCAPE** or **ECOSYSTEM ECOLOGISTS** focused on wetland, tropical, and/or plant communities. See **website: <http://www.tulane.edu/~ebio/news/new-positions.php>** for details about the positions, department, and application process. Send letter of application, curriculum vitae, statements of research and teaching interests, selected publications, and names and addresses of three references to: **EEB Faculty Search, Department of Ecology and Evolutionary Biology, 400 Lindy Boggs Center, Tulane University, New Orleans, LA 70118-5698**. Review of applications will begin October 15, 2010, and the search will remain open until the position is filled. An offer of employment is, however, contingent upon authorization of the position. *Tulane University is an Affirmative Action/Equal Employment Opportunity/ADA Employer. Women and minorities are encouraged to apply.*

## Faculty Positions in Gene Regulation and Genomics



The Cecil H. and Ida Green Center for Reproductive Biology Sciences and the Division of Basic Reproductive Biology Research in the Department of Obstetrics and Gynecology at the University of Texas Southwestern Medical Center in Dallas invite applications from outstanding candidates for **three tenure-track assistant professor positions** in signaling, gene regulation, and genome function, especially in the areas of chromatin and transcription, epigenetics, nuclear endpoints of cellular signaling pathways, nuclear receptors, RNA biology, genome organization and evolution, and DNA replication and repair. We are interested in a wide variety of model systems and experimental approaches, including biochemistry, molecular biology, structural biology, animal models, genomics, proteomics, bioinformatics, and computational biology. The Green Center's research programs focus on, but are not limited to, female reproductive biology in a broad sense, including: oocyte maturation, fertilization, development, pregnancy, parturition, stem cells, endocrinology, and oncology, as well as relevant aspects of metabolism, inflammation, immunity, and neurobiology.

**Position 1: Signaling, chromatin, and gene regulation** - a broad search for candidates using a wide array of experimental approaches to address fundamental questions in nuclear signaling, chromatin, transcription, epigenetics, and RNA biology.

**Position 2: Genomic, bioinformatic, computational, and evolutionary approaches to understanding gene regulation** - a more focused search in areas that will connect to broader genomic initiatives on campus.

**Position 3: Molecular biology of female reproductive systems** - a search for candidates using cell-based or physiological models in combination with molecular or genomic approaches to address fundamental questions concerning female reproductive biology.

The Green Center is an endowed basic science research center at UT Southwestern, which promotes and supports cutting-edge, integrative, and collaborative basic research in female reproduction and related areas of biology, as well as strong connections between basic and clinical research. This recruitment is part of a major university- and department-supported renovation and rejuvenation of the Green Center (upwards of 12 million dollars when completed and fully staffed). Successful candidates, who will be housed in a newly renovated state-of-the-art research facility and provided a generous start-up package, are expected to establish scientifically rigorous and externally funded research programs and participate in center, department, and university teaching and training programs. To learn more about the Green Center, visit: <http://www.utsouthwestern.edu/utsw/home/research/greencenter/>.

Candidates must have a Ph.D. or M.D. or equivalent in a relevant field of study, postdoctoral or comparable experience, and a demonstrated record of research excellence. Applicants should send a letter of application, curriculum vitae, and a statement of planned research projects as pdf files to **GreenCenter@UTSouthwestern.edu**, indicating the position of interest (1, 2, or 3) in the subject line. Applicants should also arrange for three letters of reference to be sent directly to the above e-mail address. Review of applications will begin on **October 1, 2010** and continue during the 2010 - 2011 academic year or until the positions are filled, although applicants are encouraged to submit their materials as soon as possible.

*UT Southwestern is an Equal Opportunity/Affirmative Action Employer.*

## University of Colorado School of Medicine

The Department of Biochemistry and Molecular Genetics at the University of Colorado School of Medicine in Denver invites applications for **Assistant Professor** faculty positions. We are broadly interested in candidates focusing in the areas of **biophysics or genomics or biochemistry**. Successful candidates will be expected to establish a vigorous, innovative and independent research program and participate in teaching. They will join a highly interactive, interdisciplinary group of faculty (<http://www.uchsc.edu/sm/bbgn/>), students, and fellows, and enjoy access to state-of-the-art equipment and facilities on our new campus. Candidates must hold a PhD (or equivalent) degree and have a strong record of research accomplishments.

Applicants should submit via [jobsatcu.com](http://jobsatcu.com), a CV, a brief description of research accomplishments and plans, and names of at least three people who can write a letter of reference.

We will begin reviewing applications **November 15, 2010**.

## SANFORD HEALTH

### Vice-President Research Fargo Region

Sanford Health, a non-profit, integrated healthcare system, invites applications for the position of Vice President of Research, Fargo Region. Sanford Health has accelerated the expansion of its health research enterprise, Sanford Research, following receipt of a transformational gift by philanthropist Denny Sanford. Sanford Research engages in medical research to discover, develop, verify and publish knowledge regarding the causes, diagnoses, treatment, prevention or control of certain diseases. Sanford Research strives to coordinate its research efforts with those of Sanford Health's university affiliates. Sanford Health is the largest rural healthcare delivery system in the United States.

Sanford Health's 18,000 employees serve more than two million people in six states. The system includes 30 hospitals with a total of 1,600 beds and employs more than 800 physicians in 70-plus specialty areas. Currently Sanford Research includes more than 160 full-time research staff and has grown to include more than \$30 million in annual research expenditures. The system expects significant growth in research and we seek an individual to lead research initiatives in the Fargo, North Dakota Region.

Sanford seeks an accomplished scientist and innovative research leader with a track record of building and leading multiple research teams. The successful candidate will have had a career as a scientist and administrator with progressive responsibilities in building research programs and additional management functions. It is important that the candidate understand how to integrate research activities within the overall patient care mission of the health system, and to coordinate those research activities with those of Sanford Health's university affiliates. Additional experience with translational research and commercialization would also be of value. Finally, the candidate will have a desire to forge strong research collaborations and business relationships, a demonstrated track record of obtaining extramural funding and the ability to mentor faculty.

Significant institutional support, including modern laboratory space will be provided for program development. A comprehensive compensation package will be tailored to the individual's qualifications. Sanford Health is an Equal Opportunity/Affirmative Action Employer. Applicants should have a PhD, DVM, MD or MD/PhD degrees, and be eligible for academic faculty appointment at the University of North Dakota School of Medicine and Health Sciences. Candidates should submit a detailed curriculum vita, description of research experience and future plans, and at least three letters of recommendation. Application materials should be sent to: **M. Benjamin Perryman, PhD, Sanford Health, 2301 East 60th Street North, Sioux Falls, SD 57104**.

For further information, contact (605) 312-6073 or [ben.perryman@sanfordhealth.org](mailto:ben.perryman@sanfordhealth.org).



## POSITIONS OPEN

### SENIOR POSITIONS in Global Change Science and Adaptation Brown University Center for Environmental Studies and Environmental Change Initiative

Brown University announces a search for two distinguished **SENIOR SCIENTISTS** with broad interests in the science and policy of climate change and global environmental change. We seek outstanding researchers with strong records of interdisciplinary collaboration whose strengths will complement each other and integrate existing research strengths in earth systems history, remote sensing and spatial analysis, conservation biology, ecosystem ecology and biogeochemistry, environmental sociology, demography, and climate change adaptation at Brown and our partner institution, the Marine Biological Laboratory at Woods Hole. Examples of areas of particular interest include regional climate modeling; landscape and ecosystem ecology; predicting environmental and/or socio-economic impacts of energy, water, or land use decisions; environmental risk analysis; and climate change adaptation.

These appointments will be at the rank of **ASSOCIATE PROFESSOR** or **PROFESSOR**, tenured in an appropriate department such as in Geological Sciences, Ecology and Evolutionary Biology, Sociology, Political Science, or Economics. The successful candidate will be expected to contribute to interdisciplinary research programs, teach environmental courses in their area of specialty, and advise undergraduate and graduate students. Requirements include an outstanding record of externally funded research and peer-reviewed publication meriting a tenured departmental appointment, commitment to excellence in graduate and undergraduate education, and potential for intellectual leadership and interdisciplinary collaboration with faculty in the CES/ECI and cooperating departments.

To apply, please send a letter of interest, a current curriculum vitae, and names of five references to: **Search Committee, Center for Environmental Studies, Box 1943, Brown University, Providence, RI 02912-1943**. For further inquiries, please contact e-mail: [patti\\_caton@brown.edu](mailto:patti_caton@brown.edu). Applications must be received by November 15, 2010, in order to receive full consideration, but the search will remain open until the position is closed or filled. *Brown University is an Equal Employment Opportunity/Affirmative Action Employer.*

### ENVIRONMENTAL BIOLOGY Haverford College

Haverford College ([website: http://www.haverford.edu](http://www.haverford.edu)) seeks outstanding candidates for a tenure-track appointment in Environmental Biology at the **ASSISTANT** or **ASSOCIATE PROFESSOR** level, to begin fall 2011. Applicants using molecular and/or computational approaches to study fundamental questions in ecology, biodiversity, and/or plant biology are encouraged to apply. The successful candidate will contribute to a vibrant curriculum in cell and molecular biology, participate in an interdisciplinary Environmental Studies program that engages colleagues at Bryn Mawr and Swarthmore Colleges, and establish a vigorous, externally funded research program involving undergraduate students. Postdoctoral experience required. Apply by submitting a single PDF file containing cover letter, curriculum vitae, and statements of research plans and teaching interests to e-mail: [hc-environbio@haverford.edu](mailto:hc-environbio@haverford.edu). Three formal recommendations, submitted separately by referees, are also required and should be sent to: **Merleen Macdonald, Haverford College, 370 Lancaster Avenue, Haverford, PA 19041**. Review of completed applications begins October 1. Specific questions may be directed to **Karl Johnson**, Chair, Biology Department. Telephone: 610-896-1306. *Haverford is an Equal Opportunity/Affirmative Action Employer committed to excellence through diversity and strongly encourages applications and nominations of persons of color, women, and members of other underrepresented groups.*

## POSITIONS OPEN

### EUKARYOTIC CELL BIOLOGIST Biology

Tenure-track **ASSISTANT PROFESSOR** beginning August 2011 in the Biology Department at Colorado College. Specialization open, but we have particular interest in candidates who use some combination of genetics, molecular biology, biochemistry, bioinformatics, genomics, or microscopy as tools applied to model systems such as eukaryotic microbes (fungi, protozoa) or other organisms appropriate for undergraduates at a liberal arts college (e.g. zebrafish, *Drosophila*, or *C. elegans*). Preference will be given to candidates whose expertise complements existing faculty. Responsibilities include (1) teaching introductory, intermediate, and advanced courses for a new cell and molecular biology track; (2) teaching one or more courses appropriate for non-biology majors; and (3) development of a peer-reviewed research program involving undergraduates. Ph.D. and demonstrated excellence in undergraduate teaching required; postdoctoral experience highly desirable. Colorado College is committed to increasing the diversity of its community and curriculum. Candidates are encouraged to identify the ways in which they can contribute to that goal. Application deadline is September 30, 2010. Send letter of application, curriculum vitae, copies of graduate and undergraduate transcripts, statements of teaching philosophy and research interests, along with three letters of reference to: **Search Committee, Department of Biology, Colorado College, 14 East Cache la Poudre Street, Colorado Springs, CO 80903**. Colorado College is a highly selective liberal arts college with a unique one-course-at-a-time curriculum. *The College is an Equal Opportunity Employer that does not discriminate on the basis of race, color, age, religion, gender, sexual orientation, national origin, or disability in its educational programs, activities, or employment practices.*

### ORGANIC CHEMISTRY Dartmouth College

Applications are invited for a tenured **ASSOCIATE** or **FULL PROFESSOR** faculty position starting July, 2011. The Chemistry Department seeks an individual who has already established a nationally recognized research program in synthetic organic chemistry with biochemical and/or medicinal applications, whose research interests will complement those of the current faculty, and who will excel at teaching in our undergraduate and Ph.D. curriculum. Chemistry with biological or medical applications is one of two targeted areas in the department's long-range plans. We particularly seek candidates who will help lead collaborative research projects both within Chemistry and involving other Dartmouth researchers, including those at Dartmouth's Medical School, Norris Cotton Cancer Center, and Thayer School of Engineering. Candidates will be expected to teach introductory and advanced courses in organic chemistry, as well as graduate courses in their area of research. Applicants should submit curriculum vitae, a description of their current research funding and future plans, a statement of their teaching interests, and names of at least three references. All inquiries and applications will be treated confidentially. Application materials should be sent to: **Chair, Organic Chemist Search Committee, Department of Chemistry, 6128 Burke Laboratory, Dartmouth College, Hanover, NH 03755-3564**. The Committee will begin to consider completed applications on October 15. *With an even distribution of male and female students and over a quarter of the undergraduate student population members of minority groups, Dartmouth is committed to diversity and encourages applications from women and minorities. Dartmouth College is an Equal Opportunity and Affirmative Action Employer.*

Find your future here.  
↓  
**www.ScienceCareers.org**

## POSITIONS OPEN

### TENURE-TRACK FACULTY POSITIONS Physiology

The Department of Physiology at Wayne State University (WSU) School of Medicine invites applications for two tenure-track **ASSISTANT** or **ASSOCIATE PROFESSOR** positions. We seek energetic individuals with research interests in the areas of molecular, cellular, systems, translational physiology, and/or biophysics to strengthen and complement ongoing programs in the Department ([website: http://physiology.med.wayne.edu](http://physiology.med.wayne.edu)). The Department is currently under major expansion and development of its strong multidisciplinary research programs.

Startup packages and salaries are highly competitive. Candidates are expected to establish active extramurally funded research programs and participate in teaching medical/graduate students. Candidates must hold Ph.D., M.D., or equivalent and apply with curriculum vitae, detailed research plan, and names and contact information of three references to e-mail: [wsuphysiologyfacultysearch@med.wayne.edu](mailto:wsuphysiologyfacultysearch@med.wayne.edu). Review of applications will begin after October 1, 2010, and continue until positions are filled.

WSU offers 350 academic programs through 14 schools and colleges to over 31,000 students in metropolitan Detroit. The Detroit metro area combines cosmopolitan attractions with lovely suburban communities as part of a national technology hub. WSU School of Medicine is a state-of-the-art research environment, and is rated by the Carnegie Foundation in the top one third of all U.S. research institutions. WSU was also ranked by Scientist Magazine in 2009 as one of the Top 40 Best Places to Work among all U.S. academic institutions. *WSU is an Equal Opportunity/Affirmative Action Employer.*

### POSTDOCTORAL POSITION Bacterial Pathogenesis

A senior-level Postdoctoral position is currently available to study molecular mechanisms of streptococcal pathogenesis in the laboratory of **Dr. Indranil Biswas**, University of Kansas Medical Center, Kansas City. A doctoral degree in Biochemistry (or related field) with strong background in protein chemistry, molecular biology, and bacterial genetics is required. Applications will be accepted until the position is filled. To view a complete position description and apply online only, go to [website: http://jobs.kumc.edu](http://jobs.kumc.edu) and search for position **J0010449**. Please include a curriculum vitae, list of publications, and contact information for three references. *KUMC is an Equal Opportunity/Affirmative Action Employer.*

## MARKETPLACE

### RECOMBINANT PROTEINS

HIV, SIV, HCV, HBV, Influenza HA, Human Proteins.<sup>™</sup>Ag/Ab:TB, Malaria, Dengue Chagas, Lepto, Toxo, Tp, C-gunya, Sars, W Nile  
[Immunodx@immunodx.com](mailto:Immunodx@immunodx.com) | 1-800-573-1700

Promab Biotechnologies Inc.

### Custom Monoclonal Antibody \$4,200

>3,000 CLONES WILL BE SCREENED

1-866-339-0871

[www.promab.com](http://www.promab.com) [info@promab.com](mailto:info@promab.com)

### Knockout Mice

**Deltagen, Inc.**

Inventory of over 900 lines of knockout mice with targeted gene deletions available to be licensed for research and drug development. Visit [www.deltagen.com](http://www.deltagen.com) to do a BLAST search of our inventory or to download the list of available KO mouse lines.

- GPCRs
- Secreted proteins
- Transporters
- Kinases
- Ion Channels
- Others

[www.deltagen.com](http://www.deltagen.com) (650) 345-7602